



UNIVERSIDAD DE CHILE

FACULTAD DE CIENCIAS FISICAS Y MATEMATICAS

DEPARTAMENTO DE ASTRONOMIA

**ESTUDIO INFRARROJO DEL TORO DE POLVO
EN GALAXIAS CON NUCLEOS ACTIVOS**

**TESIS PARA OPTAR AL GRADO DE DOCTOR EN CIENCIAS
MENCION ASTRONOMIA**

LIZA LUMI VIDELA ALTIERI

PROFESOR GUIA:

Paulina Lira Teillery

MIEMBROS DE LA COMISION:

Almudena Alonso-Herrero

Eduardo Hardy Raskovan

Diego Mardones Perez

José Maza Sancho

Neil Nagar

SANTIAGO DE CHILE

ABRIL 2010

Resumen

En esta tesis doctoral se investigan las condiciones físicas y geométricas de la estructura (denominada toro) responsable del exceso en infrarrojo (IR) observado en la distribución espectral de energía (SED) de galaxias con núcleos activos (AGN). Para ésto, se obtuvieron imágenes en el IR cercano y medio de una muestra estadísticamente significativa de galaxias Seyfert tipo 2 (Sy 2). A partir de estas imágenes se construyó el perfil radial de brillo superficial en cada banda de observación. Este perfil fue modelado utilizando funciones analíticas para cada componente galáctica, de modo de aislar, y luego medir, la emisión nuclear. Utilizando dos modelos distintos de emisión del toro, uno con una distribución continua de polvo, y otro con una distribución grumosa de polvo, se obtiene un rango de valores para los parámetros que describen las condiciones de cada toro.

Los modelos de emisión de un toro grumoso se ajustan mucho mejor a las observaciones que los modelos de un toro continuo. Se encuentra que ni la densidad de columna, ni el tamaño del toro, ni al ángulo de apertura del toro están relacionados con la luminosidad de los objetos de esta muestra. Las densidades de columna derivadas a través de distintos métodos no se encuentran correlacionadas. En particular, aquellas derivadas a partir de los modelos de emisión del toro son, en promedio, mayores que las determinadas a partir de observaciones en rayos X, lo que se opone a resultados previos. No se encuentra correlación entre la presencia o ausencia de regiones de líneas anchas (BLR) detectadas a través de espectropolarimetría y las propiedades del toro, sugiriendo que, de no existir una BLR en aquellos objetos sin detección polarimétrica, las condiciones del toro se mantienen.

La librería de SEDs presentada en este trabajo es el conjunto más completo y de construcción más detallada de galaxias Sy 2 que existe, además de representar una muestra grande y homogénea de imágenes en IR de alta calidad.

Profesor guía: Paulina Lira

A las mujeres

“The greater the sphere of our knowledge,
the larger the surface of its contact with the infinity of our ignorance”

Anonymous quote in *A Short History of Astronomy*, A. Berry

Agradecimientos

Presento mis profundos agradecimientos a Paulina Lira, guía y amiga; a Nelson Larrachea, mi amigo y esposo; y a Micaela, mi hija. A Sonia Duffau, amiga entrañable y dedicada, cuya previa experiencia me sirvió en todo momento, y que aprovecha de agradecer a Paulina por todo el apoyo que le brindó. Agradezco a mi padre, por todo. A mi madre, y a aquellas mujeres que me apoyaron incondicionalmente para lograr terminar este doctorado. Gracias a todas las compañeras y compañeros con quienes compartí este proceso, al departamento por brindarnos apoyo y facilidades para lograr una formación íntegra, y a los profesores que comparten generosamente sus conocimientos y su tiempo con nosotros. Antes de terminar, dedico un cariñoso recuerdo a mi querido amigo Emilio.

Estoy muy agradecida del Centro de Astrofísica FONDAP, de MECESUP, CONICYT y ALMA-SOCHIAS, cuyo apoyo financiero hizo posible este trabajo y toda mi formación.

Contents

1	Introduction	1
1.1	Active Galactic Nuclei	1
1.1.1	Classification of AGN	2
1.1.2	Components of AGN	4
1.2	Unification Model	5
1.2.1	Supporting the UM	6
1.2.2	Opposing the UM	8
1.3	Spectral Energy Distributions	9
1.4	Infrared	11
1.5	The Project	12
2	The Torus	24
2.1	Torus Emission Models	24
2.1.1	Continuous Models	25
2.1.2	Clumpy Models	28
2.2	Previous Attempts at Fitting Torus SEDs	30
2.3	Another Approach	32
3	Data	42
3.1	Sample	42
3.1.1	Extended 12 μm Galaxy Sample	43
3.2	Photometric Observations and data reduction	44
3.2.1	ISSAC visiting run (near-IR)	45

3.2.2	SOFI visitor and service runs (near-IR)	46
3.2.3	ISAAC and Gemini service runs (mid-IR)	47
3.2.4	Data Calibration	49
3.3	Spectroscopic Observations	51
3.3.1	Data Processing (from Wu <i>et al.</i> (2009))	53
4	Construction of SEDs	84
4.1	Separating the Torus from the Galaxy	84
4.1.1	2-D Decomposing Method: Galfit	84
4.1.2	1-D Decomposing Method: Amoeba	85
4.2	Modeling the Surface Brightness Profiles	86
4.2.1	The PSF	89
4.2.2	The Fitting Routine	89
4.2.3	Errors in the fitted components	90
4.2.4	Synthetic Data	91
4.3	Messier 31	92
4.4	Galaxy Fitting Results	94
4.5	Cleaning the <i>Spitzer</i> -IRS Spectra	106
5	Modeling of the SEDs	169
5.1	Continuous Model	170
5.1.1	Results	170
5.2	Clumpy Model	171
5.2.1	Results	171
6	Results & Discussion	273
6.1	AGN Contribution and Luminosity	274
6.2	Column Densities	275
6.3	Receding Torus?	277
6.4	IRAS Colors	278
6.5	Other Properties	279

CONTENTS

vi

6.5.1 Physical Sizes 279

6.5.2 Torus Mass 279

6.6 Concluding Remarks and Future Work 280

Bibliography

296

List of Tables

2.1	Parameters values covered by the Fritz <i>et al.</i> (2006) model.	34
2.2	Range of parameters values included in the Nenkova <i>et al.</i> (2008) database.	34
3.1	Our sample of 52 Seyfert 2 galaxies	55
3.2	Summary of observation runs.	58
3.3	Standard stars observed in SOFI runs.	59
3.4	Zero points for SOFI runs.	60
3.5	Zero points for ISAAC near-infrared run.	61
3.5	Zero points for ISAAC near-infrared run.	62
3.6	Standard stars observed in ISAAC service runs.	63
3.7	Zero points for ISAAC mid-infrared run. Only shown the zero points for galaxies detected in the respective wavelength.	64
3.7	Zero points for ISAAC mid-infrared run. Only shown the zero points for galaxies detected in the respective wavelength.	65
3.8	Standard stars observed in Gemini service run.	66
3.9	Conversion factors for Gemini run.	66
3.10	Aperture size and projected aperture size of extracted <i>Spitzer</i> spectra.	67
3.10	Aperture size and projected aperture size of extracted <i>Spitzer</i> spectra.	68
3.11	Seeing Conditions and Resolution	69

4.1	Relevant fitted parameters of M31 deconvolution process	108
4.2	Percentage contribution of galactic components	109
4.3	Mean percentage contribution of each component	114
4.4	Fitted Parameters in the J band	115
4.5	Fitted Parameters in the H band	117
4.6	Fitted Parameters in the K band	119
4.7	Fitted Parameters in the L band	121
4.8	Fitted Parameters in the M band	122
5.1	Smooth Modeling Parameters Values	173
5.2	Clumpy Modeling Parameters Values	175
5.3	χ^2_{min} Comparison	177
6.1	IRAS fluxes and luminosities	282
6.2	Compiled Data for the modeled galaxies	284

List of Figures

1.1	Megamasers in NGC 4258	14
1.2	Spectral differences between Sy 1 and Sy 2	15
1.3	Broad Wings in Polarized Flux of NGC 1068	16
1.4	Change from type 2 to type 1 Seyfert, NGC 4151	17
1.5	Change from type 2 to type 1 Seyfert, 3C 390.3	18
1.6	Ionization Cones in AGN	19
1.7	Column Densities in Seyfert Galaxies	20
1.8	Intermediate types of Seyfert Galaxies	21
1.9	Spectral Energy Distribution of AGN	22
1.10	Infrared Bands of Observation	23
2.1	Pier and Krolik (1993) SED fitting	35
2.2	Examples of Granato and Danese (1994) torus emission model . .	36
2.3	Torus geometry in Efstathiou and Rowan-Robinson (1995) model.	37
2.4	SEDs fitted with the torus emission model of Efstathiou and Rowan- Robinson (1995)	38
2.5	Torus emission model fitting by Fritz <i>et al.</i> (2006)	39
2.6	Different dust temperatures in clumpy model	40
2.7	Schema of clumpy torus	40
2.8	Torus models of Dullemond and van Bemmelen (2005)	41
3.1	Spectral Energy Distribution for 13 AGNs.	71
3.2	Raw image from ISAAC.	72

3.3	Very large galaxies, lost data.	73
3.4	Large galaxies.	74
3.5	ISAAC near-infrared reduction procedure.	75
3.6	Sky image construction for SOFI data.	76
3.7	Reduction process for SOFI data.	77
3.8	Reducing the mid-infrared data.	78
3.9	Reducing the mid-infrared data.	79
3.10	<i>Spitzer</i> Spectra	80
3.10	Continued	81
3.10	Continued	82
3.11	Projected linear size of the <i>Spitzer</i> -IRS spectral extraction aperture	83
4.1	Sérsic's Law	123
4.2	Moffat versus Gauss to describe the PSF	123
4.3	M 31 model fit	124
4.3	Continued	125
4.4	Component contribution to galaxies profile	126
4.4	Continued	127
4.5	Fitted parameters to galaxies profile	128
4.6	NGC 34 model fit	129
4.7	IRAS 00198-7926 North model fit	130
4.8	IRAS 00198-7926 South model fit	131
4.9	IRAS 00521-7054 model fit	132
4.10	ESO 541-IG12 model fit	133
4.11	IRAS 01475-0740 model fit	134
4.12	NGC 1143/4 model fit	135
4.13	MCG -2-8-39 model fit	136
4.14	NGC 1194 model fit	137
4.15	NGC 1320 model fit	137
4.16	IRAS 03362-1642 model fit	138

4.17	IRAS 04385-0828 model fit	138
4.18	ESO 33-G2 model fit	139
4.19	IRAS 05189-2524 K band raw image	140
4.20	IRAS 05189-2524 model fit	141
4.21	MCG +0-29-23 model fit	142
4.22	NGC 3660 model fit	143
4.23	NGC 4501 model fit	144
4.24	TOL 1238-364 model fit	145
4.25	NGC 4941 model fit	146
4.26	MCG -3-34-64 model fit	147
4.27	NGC 5135 model fit	148
4.28	NGC 5953 model fit	149
4.29	MCG -2-40-4 model fit	150
4.30	IRAS 15480-0344 model fit	151
4.31	NGC 6810 model fit	152
4.31	Continued	153
4.32	NGC 6890 model fit	154
4.33	IC 5063 model fit	155
4.34	Markarian 897 model fit	156
4.35	NGC 7130 model fit	157
4.36	MCG -3-58-7 model fit	158
4.37	NGC 7496 model fit	159
4.38	NGC 7582 model fit	160
4.39	NGC 7590 model fit	161
4.40	NGC 7590 L band profile	162
4.41	CGCG 381-051 model fit	162
4.42	Interband strength ratios of the four main PAH bands at 6.2, 7.7, 11.3, and $17\mu\text{m}$	163
4.43	Noise-free mid-IR templates	164
4.44	Examples of extreme subtracted spectra	165

4.45	<i>Spitzer</i> spectra with subtracted star formation	166
4.45	Continued	167
4.45	Continued	168
5.1	Nuclear IR SEDs with the 20 better fitted smooth models	179
5.1	Continued.	180
5.1	Continued.	181
5.1	Continued.	182
5.1	Continued	183
5.1	Continued	184
5.1	Continued	185
5.2	Preferred values for the smooth model	186
5.3	Best 20 smooth models fitted to NGC 34	187
5.4	Best 20 smooth models fitted to IRAS 00198-7926 South	188
5.5	Best 20 smooth models fitted to IRAS 00198-7926 North	189
5.6	Best 20 smooth models fitted to IRAS 00521-7054	190
5.7	Best 20 smooth models fitted to ESO 541-IG12	191
5.8	Best 20 smooth models fitted to IRAS 01475-0740	192
5.9	Best 20 smooth models fitted to NGC 1068	193
5.10	Best 20 smooth models fitted to NGC 1143	194
5.11	Best 20 smooth models fitted to MCG -2-8-39	195
5.12	Best 20 smooth models fitted to NGC 1194	196
5.13	Best 20 smooth models fitted to NGC 1320	197
5.14	Best 20 smooth models fitted to IRAS 04385-0828	198
5.15	Best 20 smooth models fitted to ESO 33-G2	199
5.16	Best 20 smooth models fitted to IRAS 05189-2524	200
5.17	Best 20 smooth models fitted to MCG +0-29-23	201
5.18	Best 20 smooth models fitted to NGC 3660	202
5.19	Best 20 smooth models fitted to NGC 4388	203
5.20	Best 20 smooth models fitted to NGC 4501	204

5.21 Best 20 smooth models fitted to TOL 1238-364	205
5.22 Best 20 smooth models fitted to NGC 4941	206
5.23 Best 20 smooth models fitted to NGC 4968	207
5.24 Best 20 smooth models fitted to MCG -3-34-64	208
5.25 Best 20 smooth models fitted to NGC 5135	209
5.26 Best 20 smooth models fitted to NGC 5506	210
5.27 Best 20 smooth models fitted to NGC 5953	211
5.28 Best 20 smooth models fitted to MCG -2-40-4	212
5.29 Best 20 smooth models fitted to IRAS 15480-0344	213
5.30 Best 20 smooth models fitted to NGC 6810	214
5.31 Best 20 smooth models fitted to NGC 6890	215
5.32 Best 20 smooth models fitted to IC 5063	216
5.33 Best 20 smooth models fitted to MRK 897	217
5.34 Best 20 smooth models fitted to NGC 7130	218
5.35 Best 20 smooth models fitted to NGC 7172	219
5.36 Best 20 smooth models fitted to MCG -3-58-7	220
5.37 Best 20 smooth models fitted to NGC 7496	221
5.38 Best 20 smooth models fitted to NGC 7582	222
5.39 Best 20 smooth models fitted to NGC 7590	223
5.40 Best 20 smooth models fitted to NGC 7674	224
5.41 Best 20 smooth models fitted to CGCG 381-051	225
5.42 Nuclear IR SEDs with the 50 better fitted clumpy models	226
5.42 Continued.	227
5.42 Continued.	228
5.42 Continued.	229
5.42 Continued	230
5.42 Continued	231
5.42 Continued	232
5.43 Preferred values for the clumpy model	233
5.44 Best 50 clumpy models fitted to NGC 34	234

5.45	Best 50 clumpy models fitted to IRAS 00198-7926 North	235
5.46	Best 50 clumpy models fitted to IRAS 00198-7926 South	236
5.47	Best 50 clumpy models fitted to IRAS 00521-7054	237
5.48	Best 50 clumpy models fitted to ESO 541-IG12	238
5.49	Best 50 clumpy models fitted to IRAS 01475-0740	239
5.50	Best 50 clumpy models fitted to NGC 1068	240
5.51	Best 50 clumpy models fitted to NGC 1143	241
5.52	Best 50 clumpy models fitted to MCG -2-8-39	242
5.53	Best 50 clumpy models fitted to NGC 1194	243
5.54	Best 50 clumpy models fitted to NGC 1320	244
5.55	Best 50 clumpy models fitted to IRAS 04385-0828	245
5.56	Best 50 clumpy models fitted to ESO 33-G2	246
5.57	Best 50 clumpy models fitted to IRAS 05189-2524	247
5.58	Best 50 clumpy models fitted to MCG +0-29-23	248
5.59	Best 50 clumpy models fitted to NGC 3660	249
5.60	Best 50 clumpy models fitted to NGC 4388	250
5.61	Best 50 clumpy models fitted to NGC 4501	251
5.62	Best 50 clumpy models fitted to TOL 1238-364	252
5.63	Best 50 clumpy models fitted to NGC 4941	253
5.64	Best 50 clumpy models fitted to NGC 4968	254
5.65	Best 50 clumpy models fitted to MCG -3-34-64	255
5.66	Best 50 clumpy models fitted to NGC 5135	256
5.67	Best 50 clumpy models fitted to NGC 5506	257
5.68	Best 50 clumpy models fitted to NGC 5953	258
5.69	Best 50 clumpy models fitted to MCG -2-40-4	259
5.70	Best 50 clumpy models fitted to IRAS 15480-0344	260
5.71	Best 50 clumpy models fitted to NGC 6810	261
5.72	Best 50 clumpy models fitted to NGC 6890	262
5.73	Best 50 clumpy models fitted to IC 5063	263
5.74	Best 50 clumpy models fitted to MRK 897	264

5.75	Best 50 clumpy models fitted to NGC 7130	265
5.76	Best 50 clumpy models fitted to NGC 7172	266
5.77	Best 50 clumpy models fitted to MCG -3-58-7	267
5.78	Best 50 clumpy models fitted to NGC 7496	268
5.79	Best 50 clumpy models fitted to NGC 7582	269
5.80	Best 50 clumpy models fitted to NGC 7590	270
5.81	Best 50 clumpy models fitted to NGC 7674	271
5.82	Best 50 clumpy models fitted to CGCG 381-051	272
6.1	Luminosity and Nuclear Contribution	286
6.2	Luminosity and Nuclear Contribution	287
6.3	AGN Luminosity	288
6.4	Extinction	289
6.5	Comparison of Column Density	290
6.6	Luminosity and extinction	291
6.7	Receding Torus	292
6.8	Comparison of $12\mu/25\mu$ Colors	293
6.9	Physical Torus Radii	294
6.10	Luminosity versus Torus Radii	294
6.11	Torus Masses	295

Chapter 1

Introduction

1.1 Active Galactic Nuclei

Galaxies are the largest building blocks in the Universe. They formed very early in the Universe and have varied along with its evolution. In the early 1940s, Carl Seyfert introduced a new class of galaxies: the currently called active galaxies, or galaxies with an Active Galactic Nucleus (AGN), after his observation of a spiral nebula with a star in its center (NGC 1068). With the developing of radio technology in the 60's and the improvement in astronomical observations, another class of luminous AGN was found: galaxies with starlike objects “superimposed” on their central regions, or stars with little nebulosities surrounding them were recognized as quasars.

AGN are variable in every waveband they have been observed. Optical continuum variability of quasars was established even before the emission-line redshifts were understood (Matthews and Sandage, 1963) and variability was one of the first properties of quasars to be explored in detail (Smith and Hoffleit, 1963). A few sources were found to vary significantly on time scales as short as a few days. It was concluded, on the basis of coherence arguments, that much of the radiation must come from a region with a size of $R \lesssim c \cdot \tau$, where τ is the variability timescale, then $R \sim 10^{15}$ cm. This set a major problem: a nucleus comparable in

size with the Solar System emitting more energy than an entire galaxy!

The intrinsically brightest non-transient (i.e., excluding Gamma Ray Bursts) objects ever observed are quasars. The physical process capable of producing such quantities of radiation in such small configurations was unknown until Salpeter (1964) and Zel'Dovich (1964) postulated that this mechanism was accretion onto a supermassive black hole: gravitational potential energy is converted into radiation via viscous dissipation in an accretion disk surrounding the black hole. Only recently, observations of mega-masers have given *direct* observational evidence of the existence of these systems (NGC 4258, Herrnstein *et al.* (1997), as shown in Fig. 1.1).

1.1.1 Classification of AGN

Due to the ever growing number of observed AGNs, and more importantly, to the wide range of observed characteristics, a classification system emerged. They take into account the cosmological evolution observed in AGN and the different characteristics found along the entire electromagnetic spectrum. The most common subclasses are briefly described below.

Seyfert Galaxies

Seyfert galaxies are low-luminosity AGNs ($L \sim 10^{43-45}$ ergs/seg) with a bright nucleus and a host galaxy clearly detectable. Seyfert (Sy) galaxies are now identified spectroscopically by the presence of strong, high-ionization emission lines, with a wide range in ionization levels. In addition to the strong emission lines, weak absorption lines due to stars in the host galaxy are also observed; the absorption lines are relatively weak because the starlight is diluted by the non-stellar 'featureless continuum' ¹. Morphological studies indicate that most if not all Seyferts occur in spiral galaxies.

¹'Featureless Continuum' refers to the non-stellar continuum emission of the AGN, without emission nor absorption lines.

Khachikian and Weedman (1974) were the first to realize that there are 2 distinct subclasses of Seyfert galaxies which are distinguished by the presence or absence of broad wings on the permitted emission lines. It have been observed some cases in which broad emission-line variability is so pronounced that the subclassification changes with time (Penston and Perez, 1984; Risaliti *et al.*, 2005).

Type 1 Type 1 Sy galaxies have two sets of emission lines, superimposed on one another. One set of lines is characteristic by a low-density ($n_e \approx 10^3 - 10^6 \text{ cm}^{-3}$) ionized gas with widths corresponding to velocities of several hundred kilometers per second (i.e., somewhat broader than emission lines in non-AGNs) which are ionized either by photoionization from the central source (Koski, 1978; Ferland and Netzer, 1983; Stasińska, 1984) or by shock excitation from the radio jets emanating from the core (Dopita and Sutherland, 1995). A second set of 'broad lines' are also seen, but in the permitted lines only. These lines have widths of up to 10^4 km s^{-1} ; the absence of broad forbidden-line emission indicates that the broad-line emitting gas is of high density ($n_e \gtrsim 10^9 \text{ cm}^{-3}$). The Sy 1s also show an excess in blue, ultraviolet (UV) and soft X-rays continua.

Type 2 Type 2 Seyfert galaxies show only the "narrow" forbidden lines in their spectra. The AGN continuum is usually so weak (due to obscuration) in these galaxies that it is very difficult to isolate it from the stellar continuum unambiguously. In Fig. 1.2 a comparison of the spectra of a Seyfert 1 and a Seyfert 2 is shown.

Quasars

Quasars owe their name to "Quasi-Stellar Radio Source" (QSRs), since they were discovered as a radio source with a point-like counterpart in optical wavelengths in the early 60s. Their host galaxies are invisible to us because of their distance and because they are overshadowed by the central source. The first QSR was discovered

by Matthews and Sandage (1963). As already pointed out, the light of most if not all quasars is variable over time intervals between a few days and several years, so their diameters must not be much larger than the diameter of the Solar System; yet they are the intrinsically brightest objects known (3C 273 with $z=0.158$, $M_V = -27.5$). The energy output of a typical quasar at cosmological distances is of the order of 10^{47} ergs/sec.

Later, another type of quasi-stellar source was discovered, with almost the same characteristics of QSRs but with much less radio emission, the QSOs (Quasi Stellar Object), which comprise $\sim 90\%$ of the high- z , high-luminosity AGN population.

1.1.2 Components of AGN

From the gathering of information obtained through observations at many different wavelengths and spatial resolution, we have built an idea about the central engine of an AGN which is formed by 4 distinctive regions (listed in order of distance to the central black hole):

- The accretion disk surrounding the black hole (BH). It is responsible for the UV-optical continuum, and has sizes of $100 - 1000 r_g \approx 10^{15}$ cm for a BH mass of $10^8 M_\odot$. The corresponding X-ray emitting region appears to be smaller, only several R_S . Most models of accretion disks in intermediate and luminous AGN adopt the prescription of a geometrically thin, optically thick accretion disk (Shakura and Sunyaev, 1976).
- The Broad Line-emitting Region (BLR) is surrounding the accretion disk, with a typical size of $\sim 10^{16}$ cm, large column densities ($\sim 10^{23}$ cm $^{-2}$) and densities of $\sim 10^{10}$ cm $^{-3}$ (high but not too high to suppress all semi-forbidden emission lines). The BLR is responsible for the wide emission lines seen in type 1 sources. Under the influence of the central BH, the clouds present in this region have typical velocities of several 1000 km/s, reflected in the observed widths of the emitted lines.

- The torus. It is here where most of the infrared (IR) continuum is produced. It obscures the radiation coming from the accretion disk and the BLR, re-emitting it at IR wavelengths with strong dust features. It is thought to be located from 1 to 100 pc from the BH, with an estimated density of $10^4 - 10^6 \text{ cm}^{-3}$ and extremely large column densities ($\gtrsim 10^{24} \text{ cm}^{-2}$). However its geometry and physical conditions are largely unknown and are the subject of this thesis.
- The Narrow Line-emitting Region, localized further away from the central black hole (up to 3 Kpc). The conditions here are very different from that of the BLR, with a typical column density of $\sim 10^{21-22} \text{ cm}^{-2}$, and a low density of $\sim 10^{3-4} \text{ cm}^{-3}$. The velocities associated with the forbidden emission lines coming from this region is of the order of 500 km/s and are characterized by the galactic large scale potential of the host.

1.2 Unification Model

The presence of well collimated radio jets in many AGN and the expectation of a well defined axis of symmetry in a Shakura-Sunyaev accretion disk argues for strong anisotropies in the central engine structure of AGN. This implies that the appearance of a given AGN will depend strongly on the observer's location relative to the system symmetry axis. This is the beginning of the so-called Unification Model (UM). Under the assumption that any description of nature must be made as simple as possible in the absence of evidence to the contrary, the UM postulates that, besides the strong cosmological evolution, all the classes of AGN are the same, but they look different because of the inclination angle of the central engine respects to our line of sight.

The idea that Seyfert 2 galaxies lack broad emission lines because of obscuration of the central source due to an orientation effect goes back at least to 1978, when Osterbrock (1978) suggested that Seyfert type 1 and type 2 are physically

the same, but in Sy 2s the BLR is blocked from our view, probably by dust in a torus surrounding the central source. Antonucci and Miller (1985) found broad lines in the polarized spectra of the Sy 2 galaxy, NGC 1068. This opened the discussion about the unification by orientation in Seyfert galaxies (unlike the unification models proposing an evolutionary sequence, where an object evolves with time into the other). Below we summarize the main arguments supporting and opposing the unified model by orientation.

1.2.1 Supporting the UM

Here we briefly compile the main arguments that support the idea of a Unified Model for Seyfert galaxies. We have to note that there is another unified model (besides the temporal one mentioned above) that refers to radio loud objects (quasars and radio galaxies; see Urry and Padovani (1995) for a review).

The first argument was already mentioned, and refers to the observation of polarized broad wings in Balmer lines in type 2 objects made by Antonucci and Miller (1985) for the first time and shown in Fig. 1.3. The polarized flux is the AGN central emission scattered or reflected by either dust or free electrons. In this case, the polarization was observed to be wavelength independent, which indicates that the scattering particles are free electrons. Other studies of polarized light from AGN include Miller and Goodrich (1990); Tran *et al.* (1992); Tran (2001); Lumsden *et al.* (2001). Very encouraging is the discovery of hidden type 1 nuclei in spectropolarimetry of type 2 quasars candidates (Zakamska *et al.*, 2005). Also, Ruiz *et al.* (1994) and Lutz *et al.* (2002) have found broad components in some spectra of optically classified Seyfert 2 galaxies at IR wavelengths (HeI at $\lambda = 1.083\mu\text{m}$, Pa β at $\lambda = 1.28\mu\text{m}$, and Br α at $\lambda = 4.05\mu\text{m}$), indicating that the obscuration of the BLR is not too high to obscure it at longer wavelengths.

In agreement with this scenario is also the observed variation in classification of some objects: Penston and Perez (1984) observed a “transformation” from type 2 to type 1 in NGC 4151 (shown in Fig. 1.4), and in 3C390.3 (Fig. 1.5).

The so called “ionization cones” have been observed in several galaxies when an excitation map is made, e.g., in $[\text{OIII}]\lambda 5007 / (\text{H}\alpha + [\text{NII}]\lambda\lambda 6548, 6583)$ (Pogge, 1988; Falcke *et al.*, 1998). These are conical structures with sharp edges, implying regions defined by collimation of light from the nuclear source, not by the gas distribution. The observation of ionization cones implies that the ionizing continuum is anisotropic, either because it is emitted anisotropically or because it is beamed somewhere between the central source and the NLR. Some examples from the cited papers are shown in Fig. 1.6.

Differences in X-rays column densities between type 1 and type 2 objects have been observed (Maiolino, 2001; Risaliti *et al.*, 1999), indicating that type 2 objects are on average more obscured than type 1 objects (Fig. 1.7). From this plot it can be deduced that type 2 galaxies are indeed observed through a “dusty” structure. Mas-Hesse *et al.* (1994) found also that the UV emission is obscured in Sy 2 when compared to Sy 1 galaxies.

Osterbrock and Koski (1976) introduced the notation for intermediate Seyfert types 1.5, 1.8 and 1.9 based purely on the appearance of the optical spectrum, with numerically larger subclasses having weaker broad-line components relative to the narrow lines (Fig. 1.8). This would imply that the larger the number of the classification, the larger the amount of obscuration the line of sight has to go through.

All these arguments lead others to propose a toroidal clumpy structure that provides great amounts of collimation and obscuration. Then, the torus described in 1.1.2 would be the obvious key ingredient responsible for the properties described above.

1.2.2 Opposing the UM

On the other hand, there are observations indicating that the differences between type 1 and type 2 Seyfert galaxies could not be explained by an orientation effect only.

Tran (2003) has carried out a spectropolarimetric survey of the Seyfert 2 galaxies present in the CfA (Huchra and Burg, 1992) and 12 μm (Spinoglio and Malkan, 1989; Rush *et al.*, 1993) samples. He detected polarized broad line components (Hidden Broad Line Region, HBLR) in $\sim 50\%$ of his sample and studied the possibility that 2 different types of Seyferts 2 may exist: those with a BLR, and those lacking a BLR. He confirmed that objects without detected broad line component in the polarized spectra (non-HBLR) are systematically weaker than their HBLR counterparts (Tran, 2001; Lumsden and Alexander, 2001). He compared the ionization measure $[\text{OIII}]/\text{H}\beta$ with the IR color $f_{25\mu\text{m}}/f_{60\mu\text{m}}$ and found that the HBLR galaxies tend to occupy the same region that Sy1s, which is different from that occupied by non-HBLR galaxies, being the former more powerful. He also compared the 20 cm flux density, $f_{20\text{ cm}}$, normalized by the flux at 60 μm , $f_{60\mu\text{m}}$, with the same IR colors above, and also found that the HBLR galaxies lay among the Sy1s but both avoid the region inhabited by the weaker non-HBLR galaxies. He also studied the relation between the obscuration (estimated as hard X-ray over $[\text{OIII}]$ emission) and the column density in the 2 types of Sy2s and found no significant difference between them, which would indicate that obscuration would not be the responsible of the polarimetric non-detections. When considering the hard X-rays versus the $[\text{OIII}]$ luminosities, he found again that non-HBLR are intrinsically weaker than HBLR. No difference between the 3 types of Seyfert galaxies is found when the total far-IR luminosity is compared, indicating that no enhanced circumnuclear star formation is observed.

Gathering all these results, Tran (2003) claims that when the difference between HBLR and non-HBLR Sy2s is not properly accounted for, the combined sample of Sy2s will show, for example, a smaller average $L_{[\text{OIII}]}$ than Sy1s

(Maiolino and Rieke, 1995), and a higher $[\text{OII}]/[\text{NeIII}]$ and $[\text{OII}]/[\text{NeV}]$ line-emission ratios than Sy1s, indicating higher excitation spectrum in the later, (Schmitt, 1998). Instead, when the Sy2 populations are separated, the differences, for example, in host galaxy morphology (Malkan *et al.*, 1998) and frequency of companions (Dultzin-Hacyan *et al.*, 1999) disappear. Thus, the positive detection of BLRs appears to be due to the intrinsic strength of the hidden AGN nucleus rather than to the lower level of obscuration or the reduced dominance of the circumnuclear starburst.

Concluding, the HBLR Seyfert 2 galaxies share many similar large-scale characteristics with type 1 Seyfert galaxies, as would be expected if the UM is correct. But, a intrinsically distinct class of Seyfert 2, the non-HBLR, could not be explained as an obscured Seyfert 1.

1.3 Spectral Energy Distributions

AGN are multi-wavelength sources with roughly equal amounts of energy being emitted from the far-infrared (FIR), $\gtrsim 100 \mu\text{m}$, to the hard X-rays ($\gtrsim 10\text{KeV}$), with extensions to the radio and/or γ -rays in $\sim 10\%$ of them (QSRs).

Observing the complete Spectral Energy Distribution (SED) is a difficult, or at least expensive, task given that the majority of AGN vary considerably, particularly at short wavelengths. In addition, the dilution by the host galaxy in weaker and intermediate luminosity AGN makes the determination of the SED more challenging. The number of compiled AGN SEDs in the literature increases constantly, but many of them incorporate data observed over many years (the variability is larger, even by days, for observations at $\lambda \lesssim 1\mu\text{m}$) and often by different groups using different telescopes and instruments.

Three characteristics of the AGN SEDs are present in both radio-loud and radio-quiet AGNs: the bump in the UV (the Big Blue Bump, BBB), the bump in the IR, and an inflection point between the 2 bumps, at $\sim 1.5 \mu\text{m}$. In Fig. 1.9 examples of the SED of a radio-loud (strong radio-emitters AGN) and a

radio-quiet (radio-emitters more powerful than normal galaxies, but less powerful than radio-loud AGN) AGN are shown. It has been observed that the inflection point lines up with the peak of the starlight contribution from the host galaxy. In the lower luminosity Seyfert galaxies, the host galaxy contribution becomes comparable to the emission from the nucleus, flattening the optical-IR part of the SED and resulting in an apparent decrease in the strength of the optical-IR bumps. In order to study the *nuclear* SED, the starlight must be removed.

The BBB dominates the optical-UV emission and often the total energy output of the AGN. It is thought to peak in the far-UV region (as the Shakura-Sunyaev accretion disk model predicts for a BH with $M \sim 10^8 M_{\odot}$). This bump is due to the emission of the accretion disk located at the very center of the AGN.

The near-IR bump peaks somewhere between $\sim 4 - 30 \mu\text{m}$. It is broad and decreases slowly toward the FIR, where a typically very sharp cutoff is seen between $100 \mu\text{m}$ and 1 mm . The bump is attributed to thermal emission from dust at a wide range of temperatures ($\sim 50\text{-}1000 \text{ K}$) and located close to the central engine. This is consistent with the presence of the torus, where part of the soft X-rays, UV and optical radiation coming from the accretion disk is reprocessed and re-emitted at IR wavelengths. On the other hand, cold dust from the host galaxy seems to be responsible for the FIR continuum. The first attempt to determine the physical parameters describing the dusty torus was that of Pier and Krolik (1992), through modeling of the IR part of AGN SEDs using a continuous distribution of dust. A variety of torus emission models will be detailed in Chapter 2.

1.4 Infrared

Many objects in the universe that are too cold to be detected in the optical range of the spectrum can be seen in the infrared (IR). These include interstellar molecules, extrasolar planets, brown dwarfs, cool stars, clouds of dust around bright objects, and infrared galaxies. At near-IR wavelengths dust obscures less than in the optical so it is especially useful when trying to probe areas of our Universe that are surrounded by clouds of gas and dust. For example, the extinction coefficient at $2.2 \mu\text{m}$ is only $\sim 10\%$ of that at $0.5 \mu\text{m}$. As a result, the estimated 15 magnitudes of visual extinction toward the Galactic center is reduced to only 1.5 magnitudes at $2.2 \mu\text{m}$. On the other hand, at mid-IR wavelengths the radiation is generated by dust itself, which is valuable in studying such phenomena as protoplanetary disks, regions of star formation, and the obscured central regions of AGN. Work in cosmology also depends crucially on IR observations: the expansion of the Universe may shift to the IR the UV and optical radiation coming from distant sources.

The problem with IR is that the atmosphere becomes increasingly opaque at $\lambda \gtrsim 1\mu\text{m}$ and not only the astronomical sources radiate in this regime, but also the surrounding ambient and the atmosphere. In the near-IR ($1\text{--}5 \mu\text{m}$) a number of factors (telescope elevation/airmass, clouds, OH emission, water vapor column density) determine the transparency of the sky and the amplitude of fluctuations in the background radiation, both of which affect the performance of the instruments used. In Section 3.2.1 the strategies for observing and reducing data in these bands will be detailed.

The atmospheric absorption in the L and M filters ($\lambda_c \approx 3.78$ and $4.66\mu\text{m}$, respectively) is affected mainly by CO_2 , CH_4 , H_2O , and O_3 . Overall the atmospheric transmission is lower than in the JHK filters. At even longer wavelengths (the “thermal IR” range, $10 - 20\mu\text{m}$) ambient emission becomes as strong as the brightest astronomical source known (Joyce, 1992). In our observations, we found that the typical background is $10^4 - 10^5$ times brighter than the observed

galaxies. Careful techniques have been developed to extend ground-based observations of bright sources to 20-30 μm . Beyond that it is necessary to observe from space-based facilities. The strategies for observing and reducing data obtained in this wavelength range are somewhat different from that of JHK, and the details will be explained in Section 3.2.3.

Our project includes data from two space telescopes: IRAS observations were used to define our sample, and *Spitzer* was used to obtain mid-IR spectroscopy of our targets. These two missions are now briefly described.

In 1983 the Infrared Astronomical Satellite (IRAS) was launched. For \sim ten months IRAS scanned more than 96% of the sky four times, providing the first high sensitivity all-sky map at wavelengths of 12, 25, 60 and 100 microns. IRAS doubled the number of cataloged astronomical sources by detecting $\sim 3.5 \times 10^5$ infrared sources. IRAS discovered, among other important things, a very strong infrared emission coming from interacting galaxies. IRAS also revealed for the first time the central non-active nucleus of our Galaxy, the Milky Way.

The last of NASA's "great observatories" in space was launched in 2003. The *Spitzer Space Telescope* (formerly SIRTF, The Space Infrared Telescope Facility) is much more sensitive than prior infrared missions and it is studying the Universe at a wide range of infrared wavelengths. *Spitzer* concentrates on the study of brown dwarfs, planets, protoplanetary and planetary debris disks, ultraluminous and active galaxies, and deep surveys of the early universe.

1.5 The Project

We are interested in the dusty structure producing the IR bump described in Section 1.3. It is believed that the IR bump is produced by thermal emission of dust at different temperatures located in a structure called "the torus". This structure would cause the obscuration of the BLR observed in type 2 Seyfert galaxies, and hence, is the cornerstone of the Unification Model (see Section 1.2).

In order to study the physical and geometrical characteristics of this structure,

we compiled the nuclear IR SEDs of a sample of type 2 Seyfert galaxies using near- and mid-IR ground-based images. The filters used in these images are shown in Fig. 1.10. The main breakthrough of this work is the number of objects we study, and the detailed treatment of the *nuclear* SED construction. We complement our observations with mid-IR space-based spectra from *Spitzer*.

In Chapter 2 we summarize previous works on this field, either compiling the energy distributions of AGN and/or modeling the IR part of the AGN energy distributions. In Chapter 3 we present the sample we work with and the observations and data reduction. Chapter 4 describes in detail the path from infrared images to the final nuclear IR SEDs of our sample. In Chapter 5 we present the modeling of the nuclear infrared spectral energy distributions, using the continuous model of Fritz *et al.* (2006), and the clumpy model of Nenkova *et al.* (2008). The implications of our results, discussion, concluding remarks, and future work are presented in Chapter 6

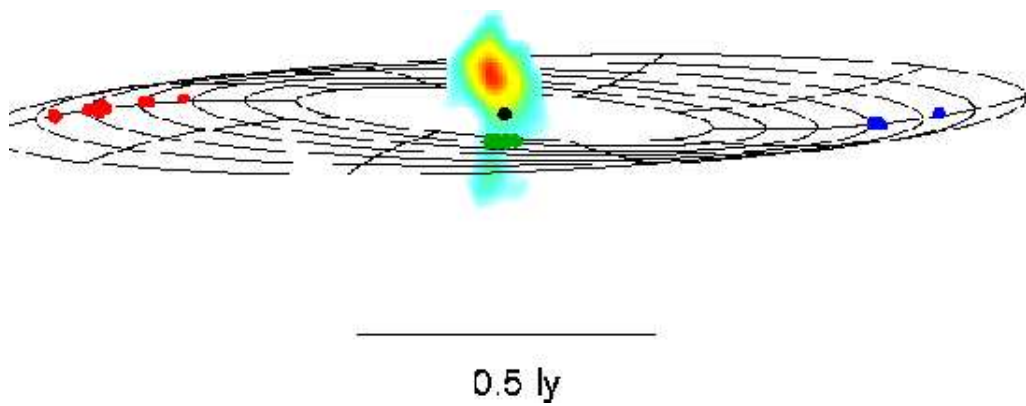
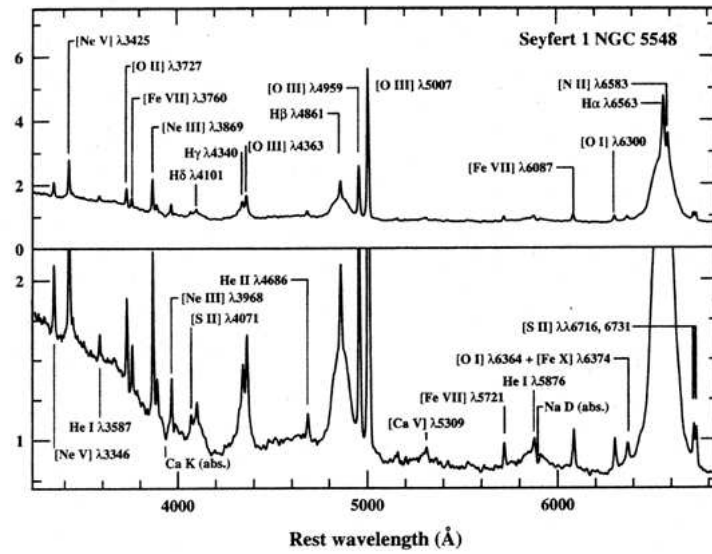
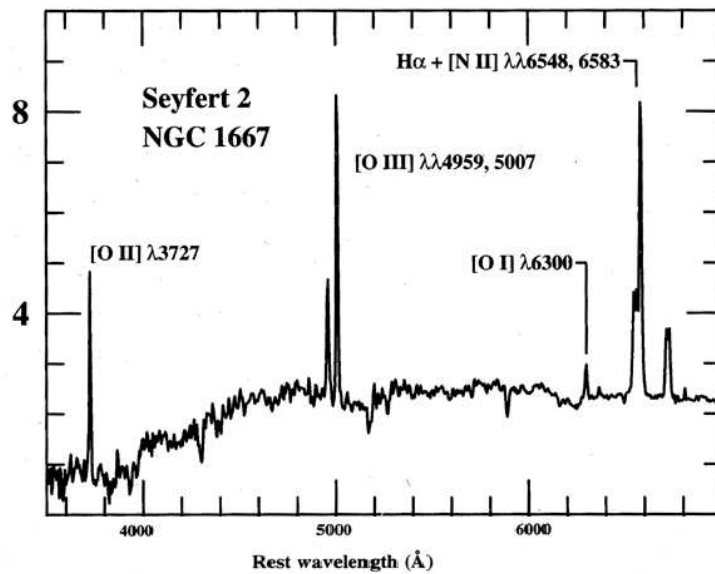


Figure 1.1: This graphic shows the geometrical relationships of the jet emission, the disk of water vapor molecules and the black hole at the center of the galaxy NGC 4258. The pseudo-colors show the relative intensity of radio emission from the jets. The black dot indicates the location of the black hole. The dots in the disk indicate the location of water maser “spots” observed with the VLBA. All components are to scale; the scale bar indicates 5,000 Astronomical Units. Fig. from Herrnstein *et al.* (1997)



(a) Seyfert 1



(b) Seyfert 2

Figure 1.2: Spectral differences between a Seyfert 1 and a Seyfert 2 spectra. In the upper panel of 1.2(a) the optical spectra of NGC 5548 (Sy 1) is shown. The vertical scale is expanded in the lower panel to show the weaker features. The prominent broad and narrow emission lines are labeled, as are strong absorption features of the host galaxy spectrum. 1.2(b) shows the same spectral range for NGC 1667 (Sy2 2). The broad wings in H α and H β lines and the enhancement in continuum emission in the blue part of the spectrum of the Sy 1 are evident. Figs. from Peterson (1997).

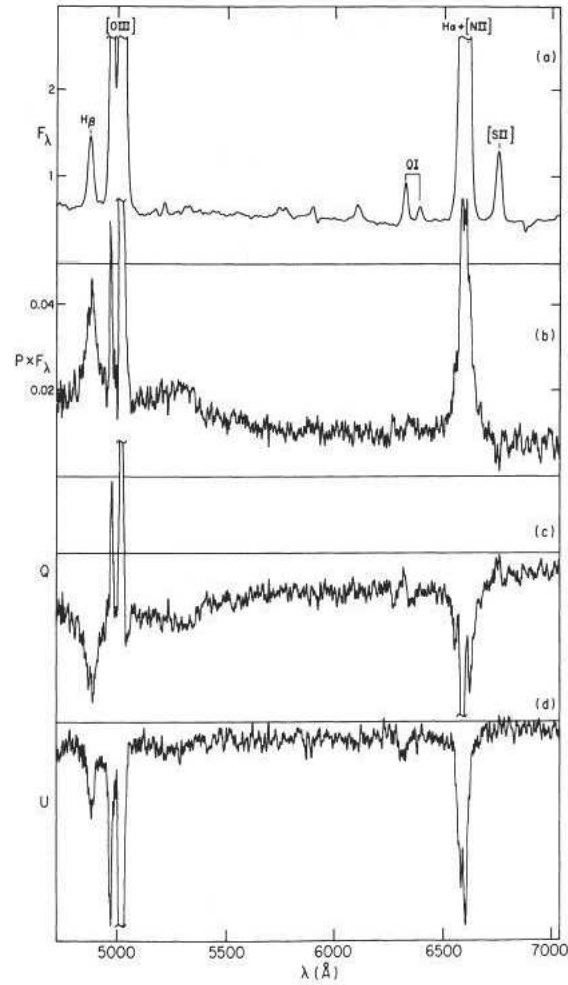


Figure 1.3: Observation of $H\alpha$ and $H\beta$ broad wings in polarized flux of NGC 1068. Panels (a) and (b) show the flux and polarized flux in arbitrary units to be comparable. Panels (c) and (d) show the Stokes parameters spectra. Fig. from Antonucci and Miller (1985).

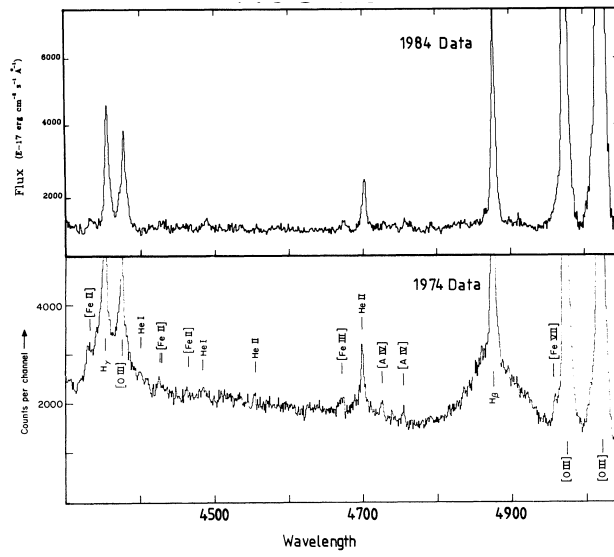


Figure 1.4: Observed changes in the broad component of the Balmer lines between 2 epochs, 1974 and 1984, of type 2 Seyfert NGC 4151. Fig. from Penston and Perez (1984).

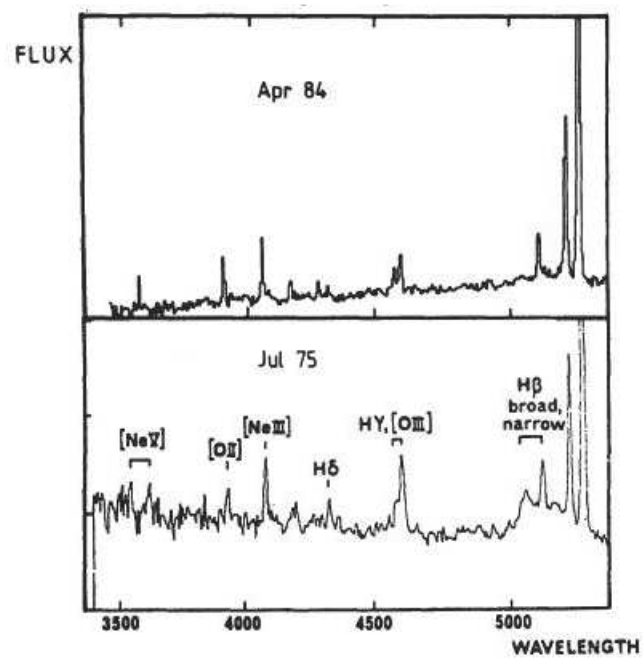


Figure 1.5: Observed changes in the broad component of the Balmer lines between 2 epochs, 1975 and 1984, of type 2 Seyfert 3C 390.3. Fig. from Penston and Perez (1984).

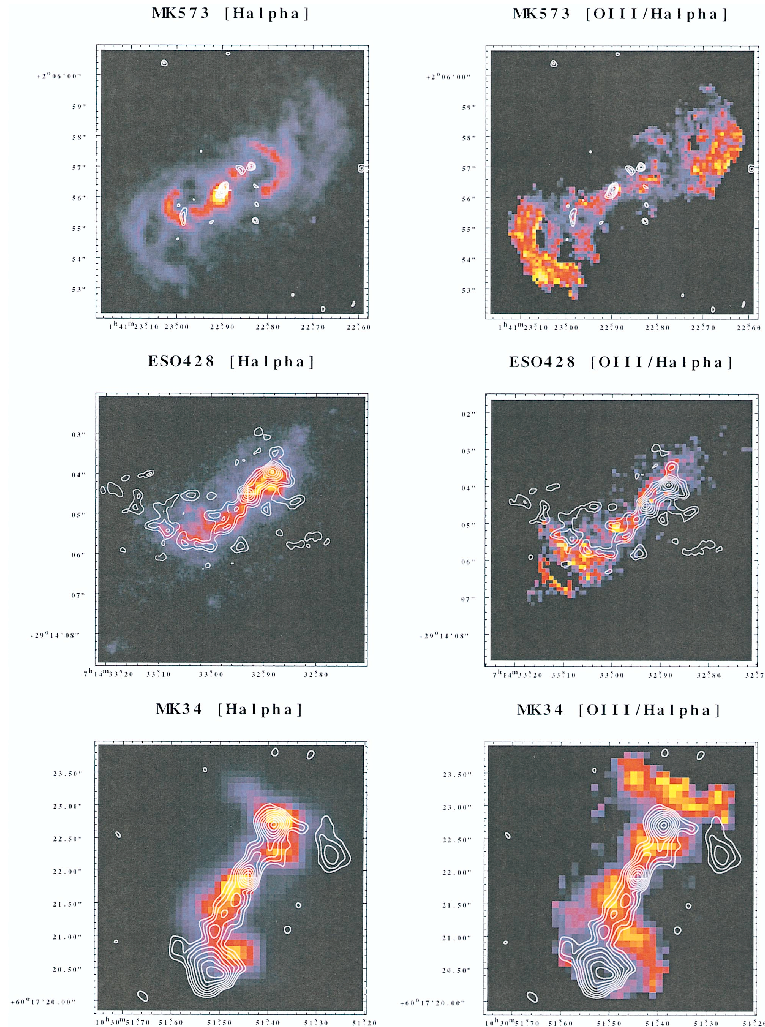


Figure 1.6: $H\alpha$ + $[N II]$ images (left panels) and $[O III]/(H\alpha+[N II])$ excitation maps (right panels) with radio contours overlaid. The coordinates are the B1950 coordinates of the radio maps. North is up, east is to the left. Upper panels show Mrk 573 galaxy, with 2 cm radio contours; middle panels show ESO 428-G14 galaxy, with 2 cm radio contours; lower panels show Mrk 34 galaxy, with 3.5 cm radio contours. Fig. from Falcke *et al.* (1998).

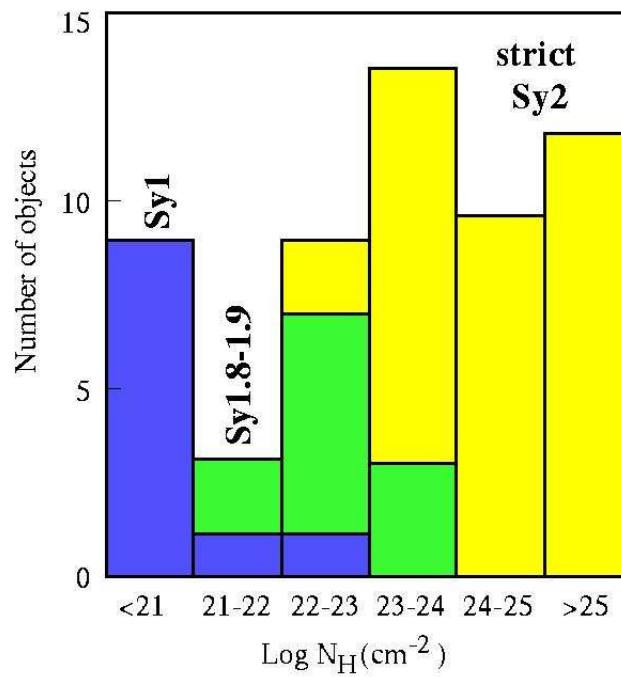


Figure 1.7: Distribution of column densities (determine from absorption of soft X-rays) among Seyfert galaxies. Blue represents type 1 Seyfert galaxies, green represents intermediate types 1.8-1.9, and yellow represents strict type 2 Seyfert galaxies. It is evident the greater absorbing column density of type 2 objects. Fig. from Maiolino (2001).

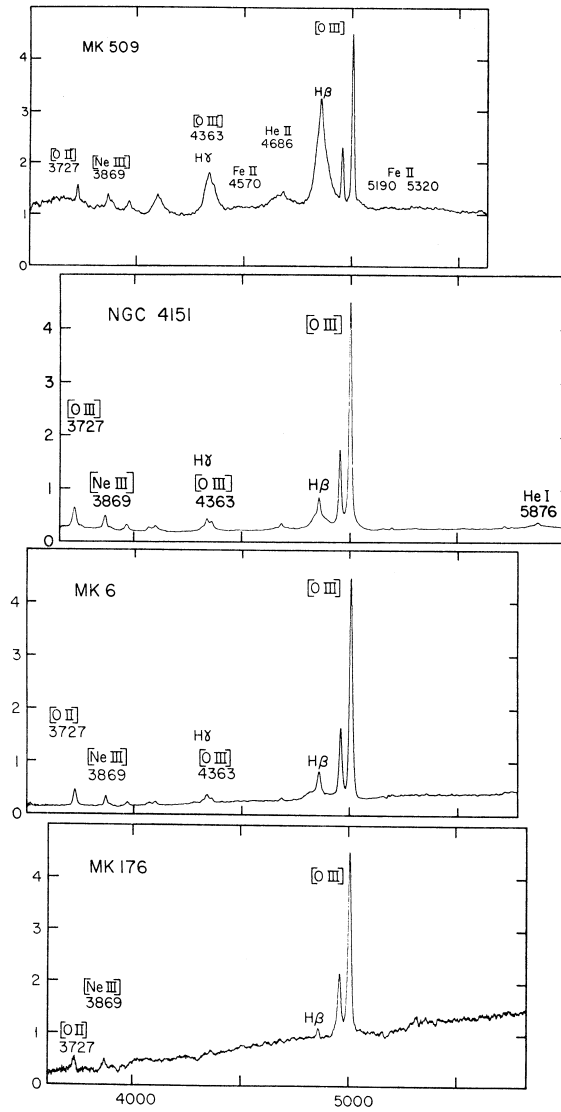


Figure 1.8: Spectra of 4 Seyfert galaxies. Top panel shows MRK 509, a typical Sy 1, with broad Balmer emission lines. In the middle panels intermediate type galaxies NGC 4151 and MRK 6 are displayed, with both broad and narrow profiles. MRK 176, a typical Sy 2, is shown in the bottom panel. Fig. from Osterbrock and Koski (1976).

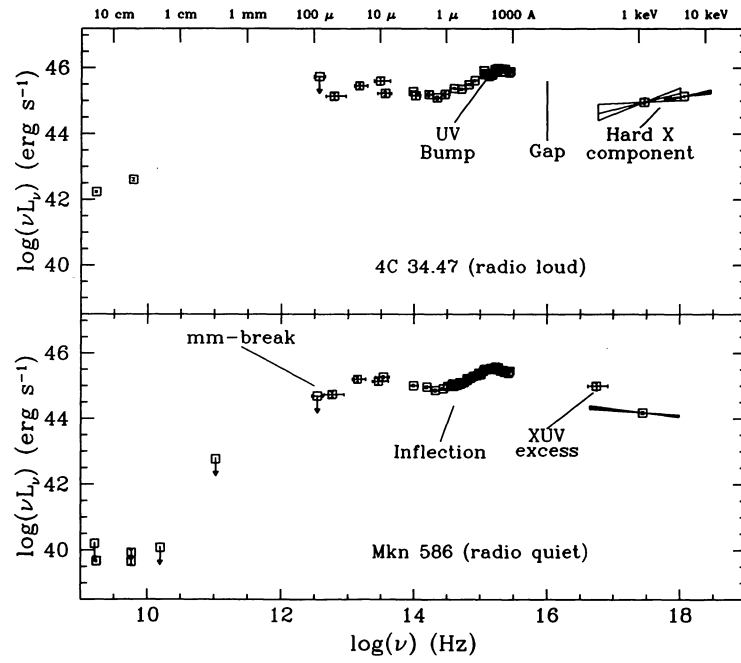


Figure 1.9: Examples of radio-loud (4C 34.47, top panel) and radio-quiet (MRK 586, bottom panel) quasar SEDs. These examples illustrate the main continuum features of AGN SEDs. Fig. from Elvis *et al.* (1994).

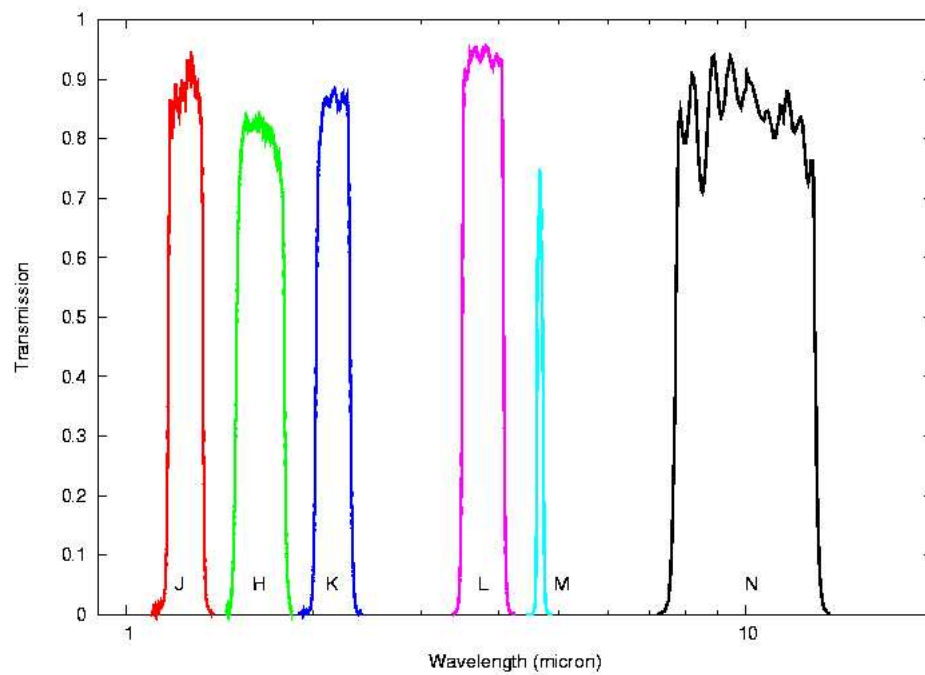


Figure 1.10: Near and mid infrared filters. In order of central wavelength, the infrared bands start with the J band (red, centered at $1.25\mu\text{m}$); H band (green, centered at $1.65\mu\text{m}$); K band (blue, centered at $2.2\mu\text{m}$); L band (magenta, centered at $3.78\mu\text{m}$); M band (cyan, centered at $4.66\mu\text{m}$); and N band (black, centered at $10\mu\text{m}$).

Chapter 2

Knowing Better the Corner Stone

We want to study the corner stone of the unification models of Active Galactic Nuclei (AGN). It is called the “torus” because it would have a doughnut shape with the supermassive black hole, the accretion disk (AD) and the broad emission-lines region (BLR) in its center. This structure was first detected as an excess in the infrared (IR): the dust absorbs part of the soft X-ray, ultraviolet (UV), optical and near-IR radiation emitted by the central engine, and then re-emits it in the near- and mid-IR, producing a bump in the spectral energy distribution (SED) of the AGN, compared to a normal galaxy.

2.1 Torus Emission Models

The first work modeling the emission coming from the torus was done by Pier and Krolik (1992, 1993), and from then many attempts with increasing levels of deepness and complexity have been published. A brief summary of some these works is presented next.

2.1.1 Continuous Models

Pier and Krolik (1992, 1993) were the first to explore the effect of geometry on dust radiative transfer, modeling the torus as a uniform density, geometrically thick, annular ring of dust surrounding a central point source of radiation. They stressed that the torus should be composed by clouds in order to protect the dust grains, but they claimed that the uniform density assumption is good provided the distance between clouds is much less than the size of the torus and the torus does not span too large a range in radius. The optical properties of the dust they used for all of the grains were those described by the extinction curve of Draine and Lee (1984) for an MRN (Mathis *et al.*, 1977) distribution of grain sizes.

The free parameters in this model are: the ratio of the inner radius of the torus to its thickness, a/h ; the Thomson depth in the radial and axial directions (τ_r and τ_z , respectively); and the flux of the nuclear radiation on the inner surface of the torus expressed as an effective temperature, $T_{eff} = (L/4\pi a^2\sigma)^{1/4}$, where L is the nucleus luminosity, σ is the Steffan-Boltzmann constant, and a is the inner radius of the torus. The emission from a given model is also dependent on μ , the cosine of the viewing angle, measured in such a way that $\mu = 0$ for edge-on tori, and $\mu = 1$ for face-on tori.

Pier and Krolik (1992) noted that the thermal bump emitted by the model tori depends only weakly on parameters. Therefore, to first order, only the location of the $9.7 \mu\text{m}$ silicate feature and the peak wavelength were adjusted when fitting the model to an observed SED. Pier and Krolik (1993) compared their model with the well-known Seyfert 2 galaxy NGC 1068, the CfA (Huchra and Burg, 1992) Seyfert galaxies with J, L and N bands photometry, and with a subsample of the PG Quasars (Schmidt and Green, 1983) and found that the preferred models tend to have $a/h \approx 0.3$ for the Seyfert galaxies and perhaps a higher value for the PG quasars, on average. In Fig. 2.1 some examples of their torus emission model fitting are shown, and the extra components needed to obtain a good fit are evident.

The main problems in this work are that the observed far-IR emission covers a much broader range than those reproduced by the models, and the properties of the $10\ \mu\text{m}$ feature, which the models reproduce only for a narrow, finely-tuned range of the parameters (specifically the very shallow emission in type 1 objects and the not so deep absorption in type 2 galaxies).

Granato and Danese (1994) developed a new model for the torus emission. Besides, they observed a sample of type 1 Seyfert galaxies to compare their model with observed *nuclear* SEDs. The main differences between this model and the one previously described is that here the effect of scattering is included and the geometry of the torus is a flared disk. Also, they tested different types (size and composition) and distributions (radial and angular) of dust grains. They found that the broad IR bump might be obtained with models of a thick ($\tau \gtrsim 30$) homogeneous torus with large enough sizes ($R_{\text{out}}/R_{\text{in}} \gtrsim 100$), and suggested that the '10 μm problem' (i.e., model SEDs showing strong emission in type 1 objects, or deep absorption in type 2 objects) could be solved if the silicate grains are depleted by shocks in the innermost regions of the tori. Examples of their emission models are shown in Fig. 2.2. The strong silicate emission feature in type 1 galaxies inclinations is evident, as also the narrow range of the IR emission in type 2 sources inclinations.

Another interesting improvement was that introduced by Efstathiou and Rowan-Robinson (1995), who studied 3 different geometries for the torus (a flared disk, a tapered disk, and an anisotropic sphere, all shown in Fig. 2.3) and explored a range of different density distributions for the gas and dust in the torus. Also, they took into account the different inner radius of each kind of dust grain produced by their different sublimation temperatures. Efstathiou & Rowan-Robinson found that a tapered disk, with an opening angle of $\approx 45^\circ$ and following an r^{-1} density distribution was the best set of parameters to describe the observations. All the other models are inconsistent with the data, either because of the persistent '10 μm problem' or because they predict a too narrow IR continuum. Examples of the fitting results are shown in Fig. 2.4.

Although all these models reproduce the gross features of the observed SEDs, important problems still remained:

- In general, the models cannot generate sufficient emission over the full range of observed IR wavelengths.
- The extreme column densities ($\gtrsim 10^{25} \text{ cm}^{-2}$) found in subsequent X-ray observations greatly exceeded the values allowed by the models: such large column density would produce a very deep $10 \mu\text{m}$ absorption feature in type 2 galaxies, which is not observed.
- Weak emission at $10 \mu\text{m}$ from silicates has been observed in type 1 objects, and models predict that, but only for very restricted values. The absorption feature at $10 \mu\text{m}$ observed in AGN is not as deep as models predict.
- These models do not reproduce the huge range in column densities observed in type 2 objects ($\sim 10^{22} - 10^{25} \text{ cm}^{-2}$).

These problems persisted in all following studies that used homogeneous density distributions for the dust, and it was suggested that clumpiness might alleviate the differences between the observations and the models.

The final continuous model we mention is the one we will compare with our observations. Fritz *et al.* (2006) include most of the successful features of the previous works to model the emission of the torus using a smooth flared disk. They account for the different sublimation temperature of silicate and carbon grains (but do not account for the different sizes), and the dust mixture include almost equal percentage of each specie. The sizes and its distribution are that of Laor and Draine (1993) and MRN, respectively. They adopted a density law that may vary with the angle from the equatorial plane and the distance from the center, and tested not only 'realistic' distributions but also considered models with density increasing toward the outer parts of the torus. In conclusion, they did not invoke particular geometries, nor modified distributions (clumpy) in order to suppress the silicate feature in type 1 sources or to attain wide IR

spectra (examples of their fitting results are shown in Fig. 2.5). The model include the following parameters: R_{max}/R_{min} , the outer to the inner torus radii ratio; τ_{eq} , the optical depth at $9.7 \mu\text{m}$ measured on the equatorial plane; β and γ , the radial and angular exponents describing the dust distribution; Θ , the angle between the polar axis and the torus; and i , the angle between the equatorial plane and the line of sight. The range of values for each parameters is shown in Table 2.1.

2.1.2 Clumpy Models

As was suggested in many previous works, a clumpy structure of the distribution of gas and dust in the torus is more realistic than a continuous one. The fundamental difference between clumpy and continuous density distributions is that radiation can propagate freely between different regions of an optically thick medium when it is clumpy, implying that cold dust may exist near the nucleus, and dust directly illuminated by the central source may exist far from it. The difficulties in modeling such an environment plus the time consuming calculations (and technical limitations) prevented the developing of such approaching until recently.

Nenkova *et al.* (2002) were the first in studying a cloudy distribution for the gas and dust in the torus. In Nenkova *et al.* (2008) they presented the general formalism for handling this clumpy media. They assume that all the clouds are identical and characterize each one by its size (which should be much smaller than the separation between clouds), its opacity (allowing a more manipulable total opacity) and its distribution (angular distribution with the number of clouds declining with the angle increasing away from the equatorial plane of the torus). Also the different dust temperatures in the illuminated surface and the dark side of the cloud are accounted for (Fig. 2.6). The size distribution of the dust grains is that described by MRN, composed by the standard Galactic mixture (53% of silicate and 47% of graphite). Obviously, scattering is took into account, dom-

inating at short wavelengths ($\lambda \lesssim 1 \mu\text{m}$). They argue that the input spectrum makes no difference at wavelengths dominated by dust emission, $\lambda \gtrsim 2 - 3 \mu\text{m}$, but at shorter wavelengths the AGN scattered radiation dominates, reflecting the difference in input radiation in this spectral region. Through the clumpy treatment Nenkova *et al.* (2002) can naturally explain the low and different dust temperatures found close to the nucleus of NGC 1068 (Jaffe *et al.*, 2004; Schartmann *et al.*, 2005). Furthermore, it is found that the X-ray attenuating column density is widely scattered around the column density that characterizes the IR emission, because the IR flux is collected from the entire observed area (averaging over all the clouds), while the X-ray opacity is calculated from one particular line of sight.

The model parameters are the optical opacity of each cloud (τ_V), the number of clouds through the equator (\mathcal{N}_0), angular and radial distribution of the clouds (σ starting at the torus equator, and r^q , respectively), $Y = R_{out}/R_{in}$, and the angle of the line of sight (i , starting from the symmetry axis of the torus)¹. The range of the values of each parameter is shown in Table 2.2. In Fig. 2.7 we show a representation of this kind of torus. Through the investigation of the space parameters, Nenkova *et al.* found that $\mathcal{N}_0 \gtrsim 15$ produces SEDs with a very narrow IR bump, peaking beyond $60 \mu\text{m}$, which has not been observed, and models with $\mathcal{N}_0 \lesssim 2$ never produce an absorption $10 \mu\text{m}$ feature. They also found that $\sigma \approx 30^\circ$ models provide the best match to the behavior of the $10 \mu\text{m}$ feature, while with $\sigma = 60^\circ$ the $10 \mu\text{m}$ feature appears in pronounced absorption at all viewing angles. The radial size of the clumpy torus cannot be constrained by SED measurements, according to them. Only high-resolution observations can discriminate the size of the torus, and these observations are consistent with a torus radial thickness $Y \sim 20 - 30$. They also stress that no modified characteristics for the interstellar medium are needed in order to adequately model AGN observations.

¹Note that the definition of the viewing angles, i , and the torus aperture angle θ and σ are defined in the opposite way in each model

Dullemond and van Bemmél (2005) made a couple of improvements to the clumpy media proposed by Nenkova *et al.* (2002). They used a 2-D Monte-Carlo radiative transfer method to model the clumps as rings around the polar axis (unlike the statistically generalized single clump of Nenkova *et al.*), and include a variation in the size of the clouds, being larger at larger radii, but only with 20 or 40 clouds (an example of these clumpy torus is shown in the lower panel of Fig. 2.8). Also, the mixture of dust is different, being 50% of each type, silicate and graphite.

The main goal of the work of Dullemond & van Bemmél was to compare clumpy and smooth models for the torus. In the smooth tori they tested 2 cases, the first with grains of silicate and carbon with $0.25 \mu\text{m}$ in size and no scattering, and the second with a modified MRN distribution of the grains sizes (extending up to $1 \mu\text{m}$ in size), scattering, and thermal decoupling of the temperatures of silicates and graphite. In the upper panel of Fig. 2.8 examples of their smooth tori are shown.

They found that clumpy models are wider than smooth models for type 2 sources viewing angles, but are a little bit narrower than smooth models at lower viewing angles. The emission feature at $10 \mu\text{m}$ in type 1 object viewing angles is not decreased in clumpy models, but the absorption feature *does* weaken in clumpy models at high inclinations.

2.2 Previous Attempts at Fitting Torus SEDs

As was mentioned in the previous Chapter, the main breakthrough of this work is the number of sources we study, and the detailed treatment of the *nuclear* SED construction. There have been many attempts to model the AGN SEDs using the above summarized models, or others not mentioned, but using either type 1 objects, which can be 'contaminated' by the central source IR emission, which being even more compact than the torus cannot be easily separated, or using type 2 sources, but with no statistically representative samples. Also, many of them

include the host galaxy emission from extended regions of star formation, which can dominate in the near-IR or far-IR, specially when using the first IR detectors which covered a very small area of the sky preventing a good subtraction of the stellar component.

Granato and Danese (1994) for example, compared their emission model to the *nuclear* (i.e. corrected by starlight) SEDs of a sample of 56 Seyfert 1 galaxies. But Pier and Krolik (1993), on the other hand, compared their model to SEDs compiled from the literature, i.e., with no thorough determination of the *nuclear* emission. The fitting process of Fritz *et al.* (2006) suffers the same problem, as they selected photometric measurements of 40 type 1 and 15 type 2 galaxies from the literature taking care only of getting homogeneous apertures.

Moreover, Alonso-Herrero *et al.* (2001) observed a sample of 14 Seyfert 2 galaxies in the J, H, K, L, and M IR-bands. They complemented these observations with archive images from the HST and continuum fluxes obtained with ISO from the literature. As they mentioned, the small field of view of the detectors prevented them to observe the entire galaxy, so they modeled the surface brightness profile of the galaxy as nucleus+bulge, discarding the disk contribution which might induce to a wrong estimation of the nuclear emission. Also, they assumed the nuclear surface brightness profile as a delta function convolved with a Gaussian profile, which might be an inadequate representation of the seeing conditions (as will be shown in 4.2.1).

Alonso-Herrero *et al.* (2003) obtained high-resolution K and L bands images for 34 Seyfert galaxies (roughly, half of them being type 2 sources) from the CfA sample and complemented it with HST and ISO, as in the previous described work. They carefully deconvolved the nuclear emission from the host galaxy and compared the ISO fluxes with observations in radio, in order to determine the level of contamination from circumnuclear star formation. They conclude that the torus emission models (Efstathiou and Rowan-Robinson, 1995) were incapable of reproducing the wide range in observed SEDs shape, in particular the smooth variation of steepness between the almost flat Seyfert 1s and the very

steep Seyfert 2s.

2.3 Another Approach

With the advent of new interferometric facilities, the “direct” observation of the torus in the nearest AGN can be achieved. As part of the ‘snapshot survey’ of the 13 brightest AGN in the mid-IR, Jaffe *et al.* (2004) were the first to directly observe and resolve the torus in an AGN, the nearest type 2 Seyfert NGC 1068, using the MID-infrared Interferometric instrument MIDI at the VLTI. Following this work, Tristram *et al.* (2007) resolved 2 warm structures in the center of the Circinus galaxy, another type 2 object. The results of the completed survey can be found in Tristram *et al.* (2009). In order to model the very high-resolution observations and visibilities obtained with mid-IR interferometry, Schartmann *et al.* (2008) developed a hydrodynamical model of the obscuring torus using a clumpy distribution for the dust and validating such description.

With more observations of NGC 1068, including more *uv* coverage with 16 baselines, Raban *et al.* (2009) found measurements consistent with a compact (0.45×1.35 pc) component composed by hot (~ 800 K) silicate dust with an unusual absorption profile that indicates a silicate composition different from that found in the center of our Galaxy. Tristram *et al.* (2007) found that the distribution of dust in the center of Circinus is better described by a dense and warm ($T \gtrsim 330$ K) disk component with a FWHM radius of 0.2 pc plus a less dense and slightly cooler ($T \lesssim 300$ K) geometrically thick torus-like component with a FWHM radius of 1 pc and a clumpy or filamentary distribution. The disk-like component coincides in orientation and extent with the nuclear maser disk observed by Greenhill *et al.* (2003), and the silicate absorption profile is consistent with that found in the central regions of our Galaxy, unlike that found in NGC 1068.

However, this kind of observations are currently available only for the nearest and brightest objects due to the resolving power needed. The expensive nature of such observations is also an important issue when trying to achieve such resolutions. Therefore, the most affordable way of getting a global idea of the geometrical and physical characteristics of the AGN torus, is the one we propose in this investigation.

Table 2.1. Parameters values covered by the Fritz *et al.* (2006) model.

Parameter	Values	Description
R_{max}/R_{min}	30, 100, 300	Torus size
$\tau_{eq}(9.7\mu\text{m})$	0.1, 0.3, 0.6, 1, 2, 3, 6, 10	Optical depth at torus equator
β	0.5, 0, -0.5, -1	Radial dust distribution exponent
γ	0, 6	Angular dust distribution exponent
Θ	20, 40, 60	Aperture angle of the torus, from symmetry axis
i	0-90 in step of 10	Viewing angle, from equator

Table 2.2. Range of parameters values included in the Nenkova *et al.* (2008) database.

Parameter	Values	Description
τ_V	10, 20, 30, 40, 60, 80, 100, 150, 200, 300, 500	Optical depth of each cloud
\mathcal{N}_0	1-20 in step of 1	Number of clouds at torus equator
σ	15, 30, 45, 60, 75	Aperture angle of the torus, from equator
q	0, 1, 2, 3	Radial cloud distribution exponent
$Y = R_{out}/R_{in}$	10, 30, 100	Torus size
i	0-90 in step of 10	Viewing angle, from symmetry axis

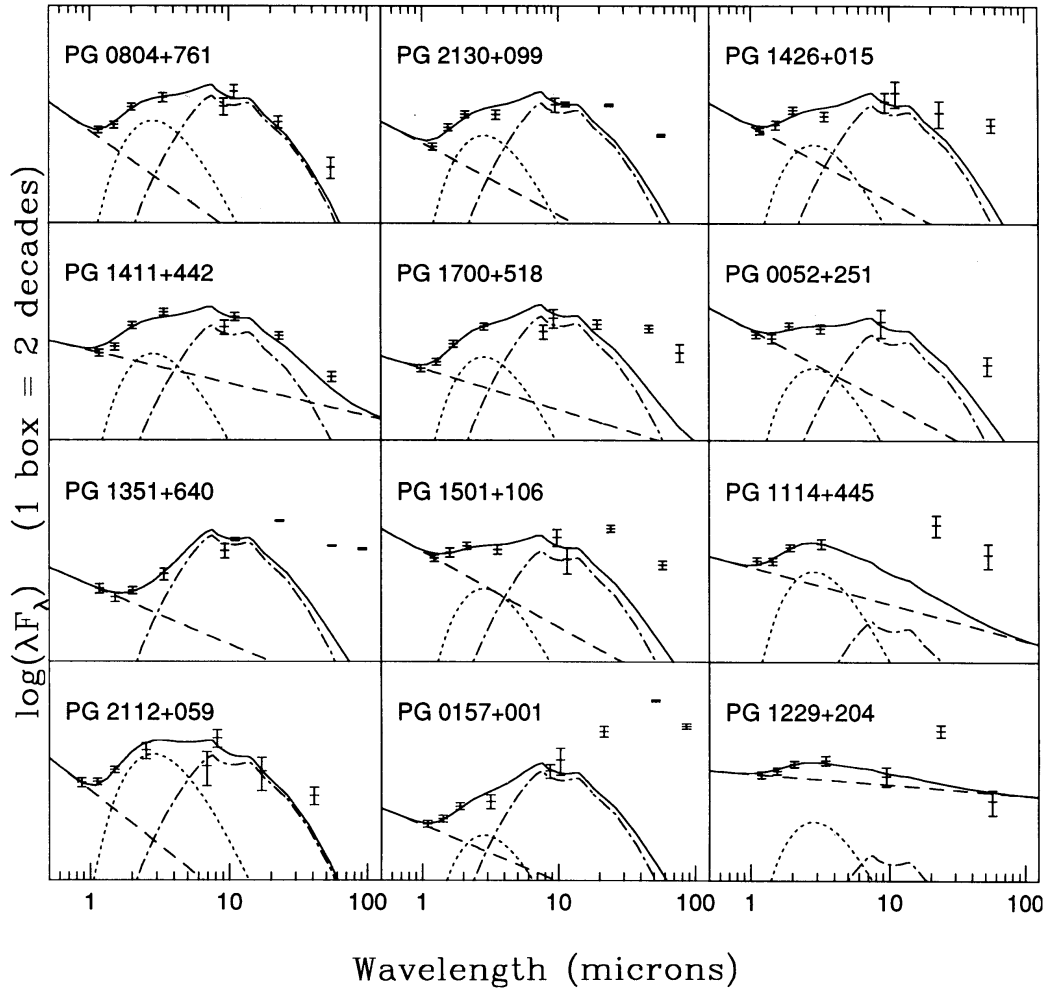


Figure 2.1: Multicomponent torus emission model fits to a subsample of the PG quasars. The dashed line is an extended optical power law (to taken into account the host galaxy contribution), the dotted line is a 1330 K blackbody component (to account for the excess in the near-IR), the dot-dashed line represents the torus, and the solid line is the sum of all these components. Fig. from Pier and Krolik (1993)

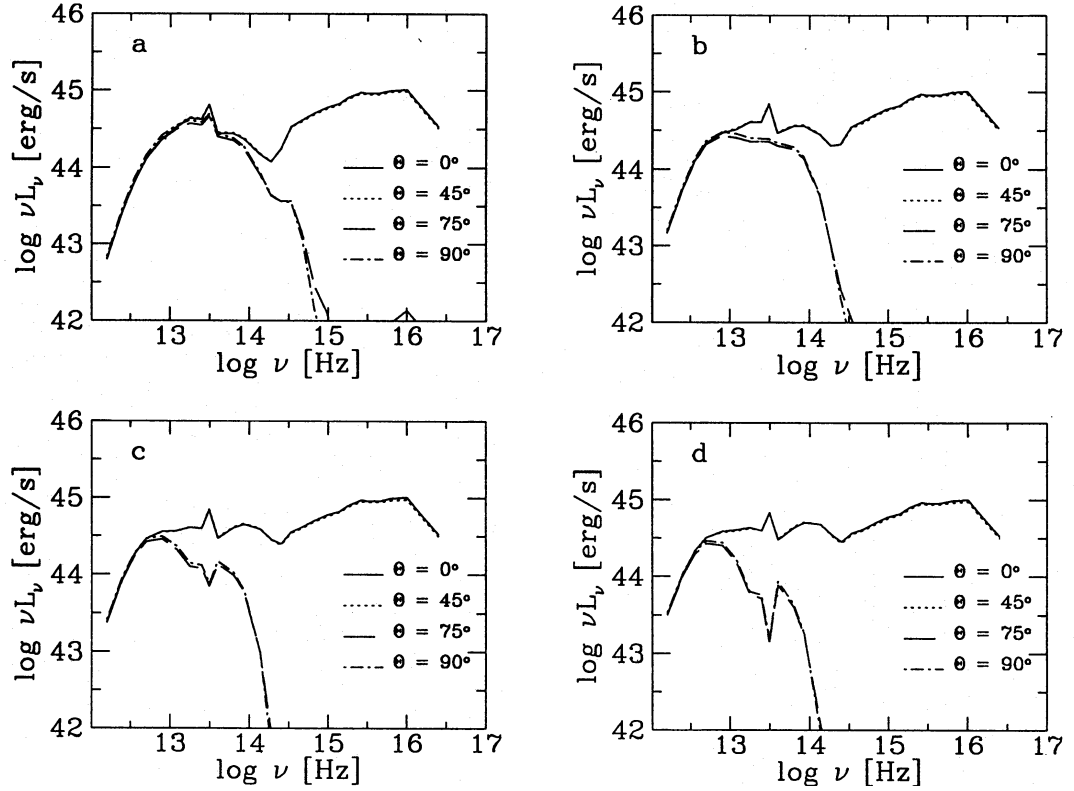


Figure 2.2: Examples of torus emission models with different viewing angles and optical depths. τ_e is the optical depth at the equator of the torus, r_m/r_o is the ratio of the maximum to the minimum radius of the torus, Θ_h is the angle aperture of the torus, $f = \cos \Theta_h$ is the covering factor, and β is the exponent of the radial distribution of dust. (a) $\tau_e = 10$, $r_m/r_o = 1000$, $f = 0.5$ (i.e. $\cos \Theta_h = 60^\circ$), and $\beta = 0$. (b) Same as (a) but with $\tau_e = 30$. (c) Same as (a) but with $\tau_e = 60$. (d) Same as (a) but with $\tau_e = 100$. The strong silicate emission feature in type 1 galaxies inclinations is evident, as also the narrow range of the IR emission in type 2 sources inclinations. It is worth to note that the bimodal behavior has not been seen in the observed SEDs. Fig. from Granato and Danese (1994)

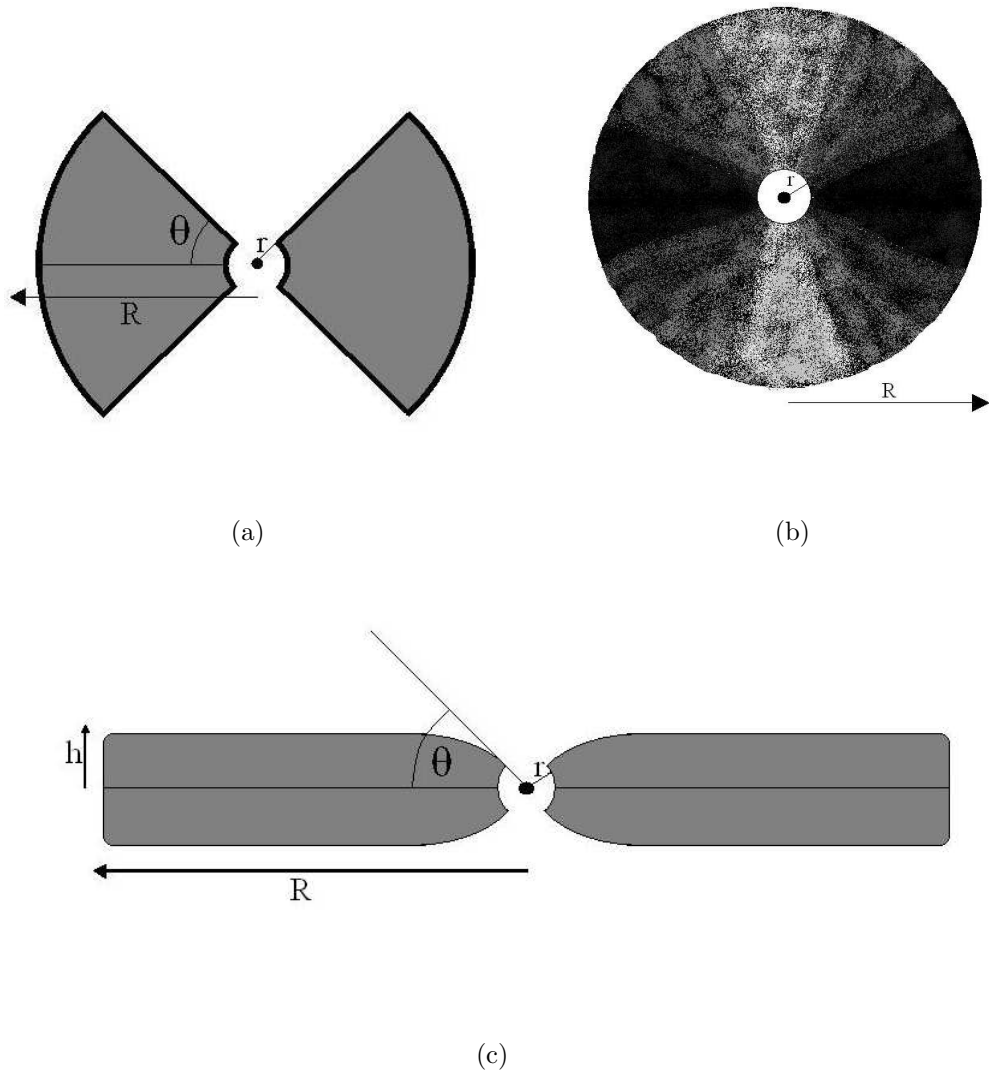


Figure 2.3: Different geometries tested by Efstathiou and Rowan-Robinson (1995) for the torus. (a) Flared disk, (b) anisotropic sphere, and (c) flatered disk.

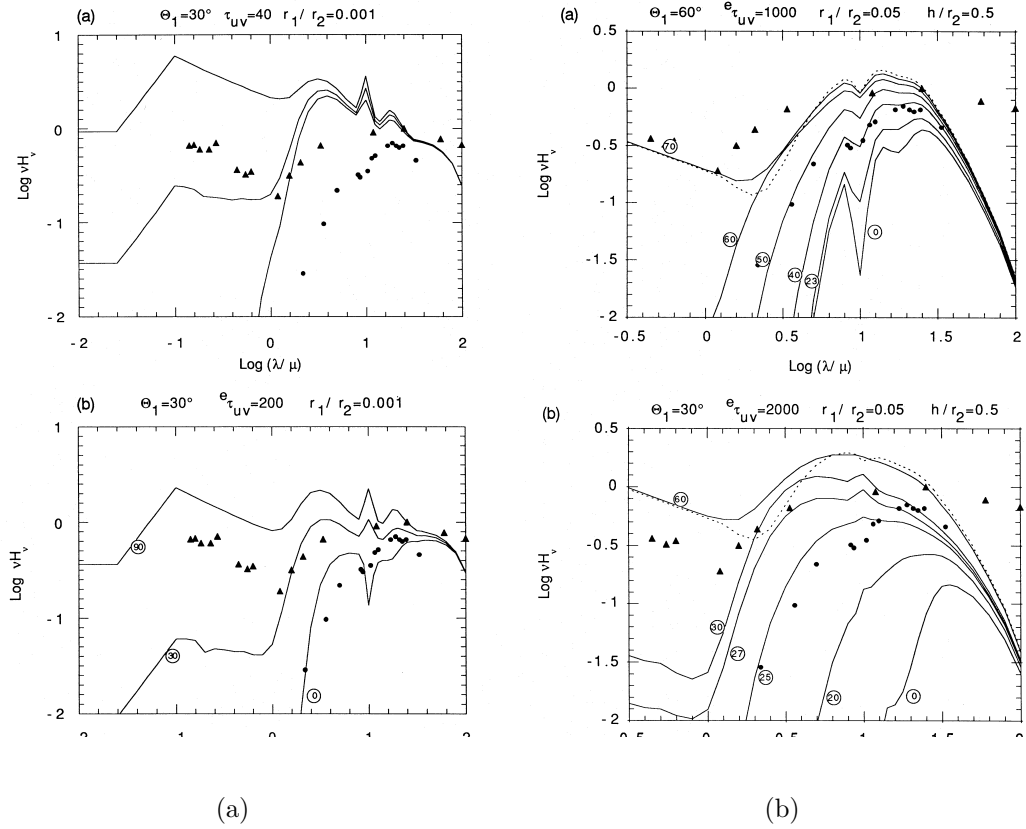


Figure 2.4: Examples of torus emission model fitting by Efstathiou and Rowan-Robinson (1995). The data are 'average' spectra of type 1 sources from Granato and Danese (1994) (triangles) and the prototype NGC 1068 from Rieke and Low (1975) (circles). (a) Flared disk model with $r/R=0.001$, $\Theta = 30^\circ$ and $\tau_{UV}^{eq} = 40$ for the upper panel, and $\tau_{UV}^{eq} = 200$ for the lower panel; (b) flared disk models with $r/R=0.05$, $h/R=0.5$, $\Theta = 60^\circ$ and $\tau_{UV}^{eq} = 1000$ for the upper panel, and $\Theta = 30^\circ$ and $\tau_{UV}^{eq} = 2000$ for the lower panel. Figs. from Efstathiou and Rowan-Robinson (1995).

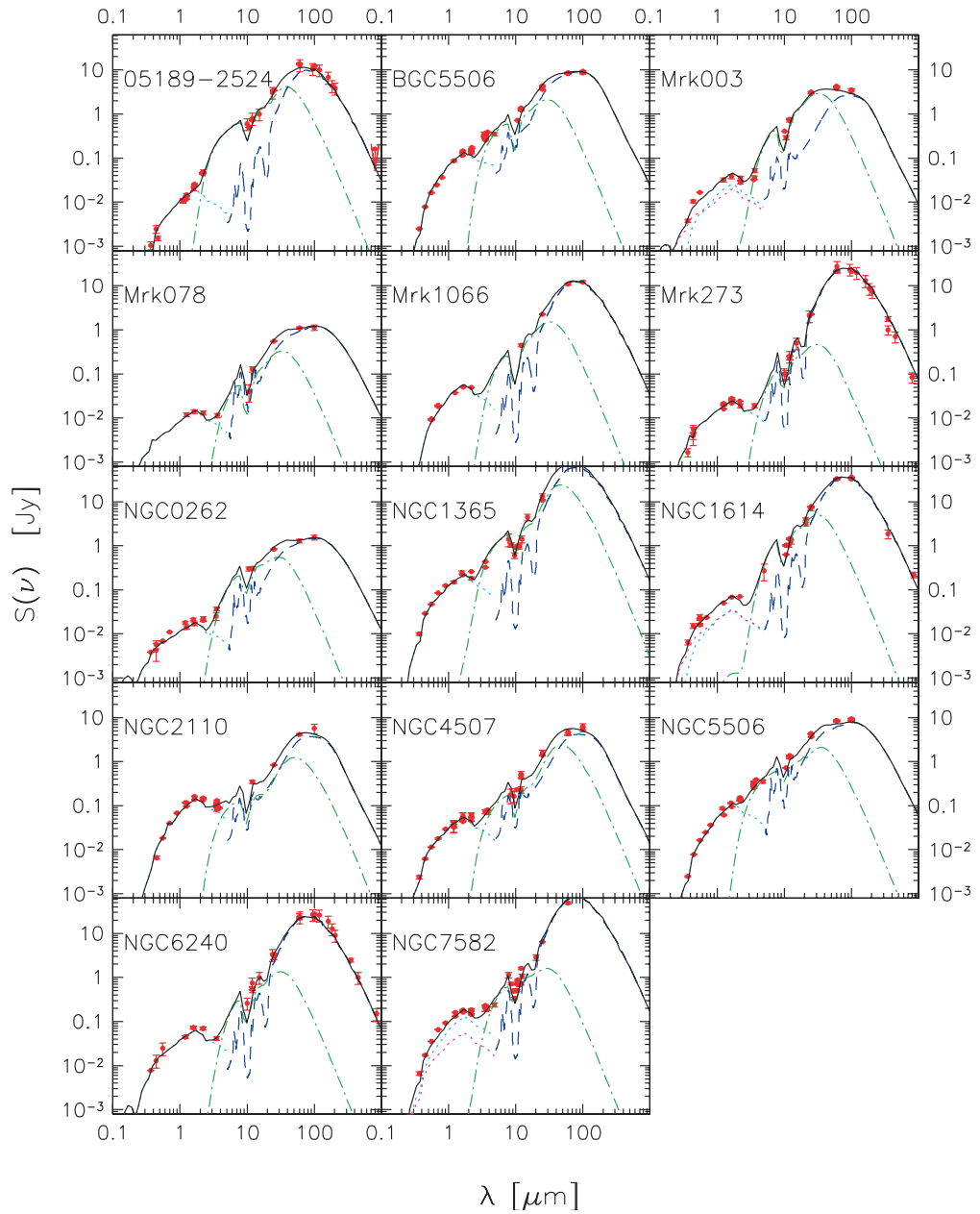


Figure 2.5: Comparison of the best-fitting model with observational data obtained from the literature for 14 type 2 AGNs. Red triangles are the observed data points; the solid black line is the total model SED; the green line is the AGN emission; the blue line denotes the starburst emission; the stellar emission by the host galaxy is shown as dashed lines. Fig. from Fritz *et al.* (2006).

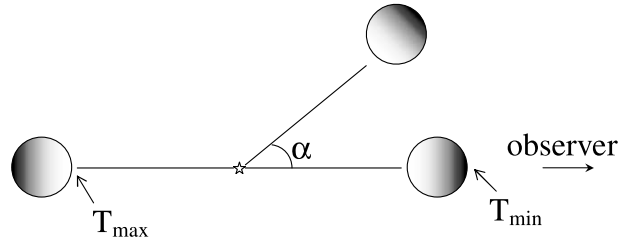


Figure 2.6: Different dust temperatures in the illuminated surface of the cloud and the dark side of the cloud. This is the natural explanation for the observed differences in dust temperatures observed in NGC 1068. Fig. from Nenkova *et al.* (2008).

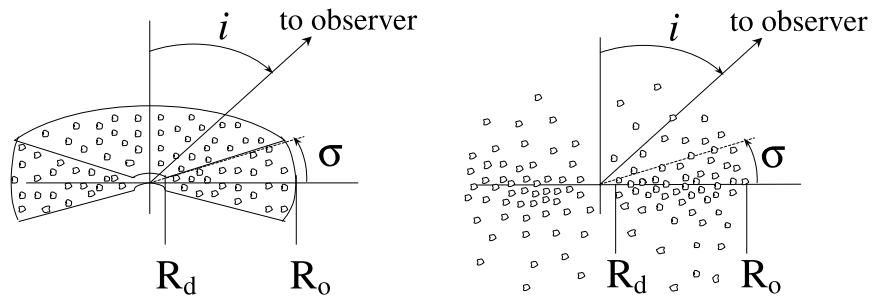


Figure 2.7: Clumpy torus model geometry. Dusty clouds, each with an optical depth τ_V at visual, occupy a toroidal volume from inner radius R_d , determined by dust sublimation, to outer radius $R_o = YR_d$. The radial distribution is a power law r^{-q} , and the total number of clouds along a radial equatorial ray is \mathcal{N}_0 . The angular distribution, characterized by a width parameter σ , has a sharp edge on the left and a smooth boundary (e.g., a Gaussian) on the right. Fig. from Nenkova *et al.* (2008).

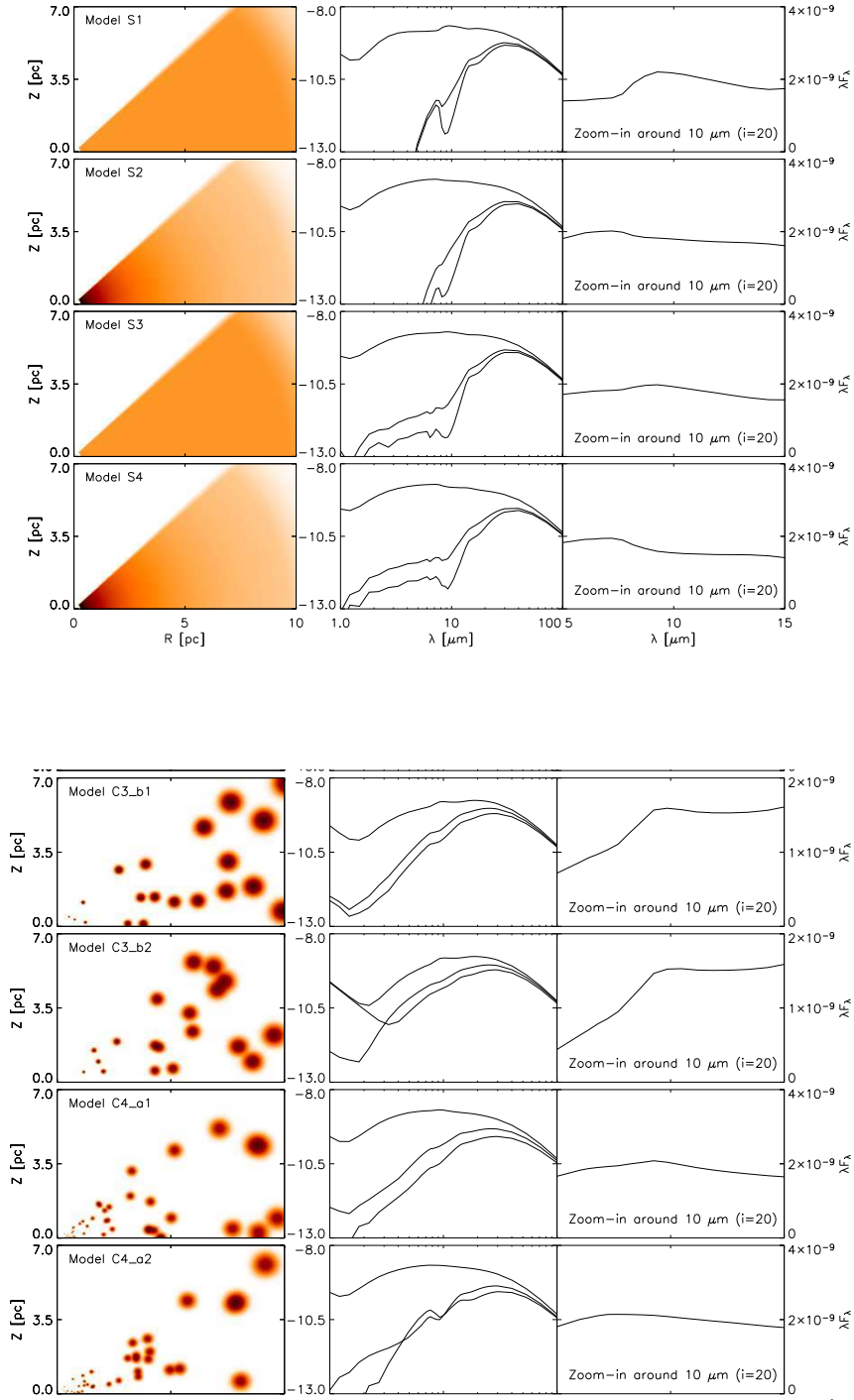


Figure 2.8: Examples of the results of smooth and clumpy models of Dullemond and van Bemmél (2005). Each row represents one model. The left column represents the dust density distribution (as $\rho \cdot R$ in the lower panel). The middle column is the SED of the system at 3 inclinations: 20° , 70° , and 90° . The vertical axis is $\log_{10}(\nu F_\nu)$. The right column is a linear zoom-in of the face-on ($i = 20^\circ$) spectrum around $10 \mu\text{m}$. Figs. from Dullemond and van Bemmél (2005).

Chapter 3

Our Sample, Observations and Data

3.1 Sample

Our sample is formed by all Seyfert 2 galaxies in the southern hemisphere found in the Extended 12 μm Galaxy Sample (Rush *et al.* (1993), hereafter 12GS), comprising 48 Seyfert 2 galaxies listed in table 3.1¹. The redshift and distances (for a $H_0=70$ km/s/Mpc) of each object are listed in Table 3.11.

The most important characteristic of the 12GS for our work is that it includes a fairly unbiased sample of nearby ($z \leq 0.07$) active galaxies (AGNs) that have been observed in many spectral regimes. It is selected in the mid-IR, minimizing possible biases: it includes elliptical, lenticulars and spirals galaxies (allowing us to avoid systematic errors in the decomposition process of the surface brightness profiles); it includes a wide range in galaxy inclinations (allowing us to study not only the nuclear obscuration, but also the importance of the galactic obscuration); and most importantly, it includes a wide range of obscuration properties of the

¹This research has made use of the NASA/IPAC Extragalactic Database (NED) which is operated by the Jet Propulsion Laboratory, California Institute of Technology, under contract with the National Aeronautics and Space Administration.

nuclear source (allowing us to test more generally the nuclear emission models and probing a range of hydrogen columns of $\sim 10^{22} - 10^{25} \text{ cm}^{-2}$).

3.1.1 Extended 12 μm Galaxy Sample

There have been many efforts to obtain a complete and statistically representative sample of AGNs, but most of them are strongly biased in one way or another. For example, the wide range of line strengths and widths found in active galaxies makes emission-line surveys seriously incomplete and biased.

Another important difficulty is that at most wavelengths different classes of active galaxies present very different nuclear continuum emission properties. Thus, for example, samples selected in the ultraviolet are strongly biased against reddened and dusty nuclei and in favor of blue Seyfert 1 nuclei and quasars; samples selected in the far-infrared preferentially select dusty AGNs hosted by dusty galaxies, whose bolometric luminosity is mostly re-radiated by dust grains. clearly, samples selected in the radio will only represent the radio-loud class of objects.

The 12GS overcomes these obstacles by selecting galaxies in the wavelength band that minimizes these effects. In Fig. 3.1, there are plotted 13 energy distributions of representative bright active galaxies, from ultraviolet to far-infrared. All the spectra have been normalized to a unit bolometric flux. Seyfert 2 galaxies are drawn in dot-dashed lines; Seyfert 1's in solid lines; and 3 blue quasars in dashed lines. The wide scatter is evident, even within one class of AGN. In the mid-infrared, however, there is a range of wavelengths (7-12 μm) in which the emission of this diverse set of active galaxies are similar. "The small scatter in this region indicates that the intrinsic fraction of the AGN luminosity emerging in the mid-infrared is roughly constant and is hardly altered by the presence of nuclear dust" (Spinoglio and Malkan (1989)). This is why mid-infrared surveys are ideal for obtaining active galaxies samples which are both, unbiased and complete to a certain flux level. This is the case of the Extended 12 μm Galaxy

Sample, which is complete down to 0.3 Jy.

The 12GS catalog was constructed from IRAS observations, selecting the targets using the following criteria: (i) 12 μm flux density in the FSC-2 (Faint Source Catalog, Version 2) ≥ 0.15 Jy; (ii) either $F_{60 \mu\text{m}} \geq 1/2 F_{12 \mu\text{m}}$ or $F_{100 \mu\text{m}} \geq F_{12 \mu\text{m}}$ (in order to exclude most stars and virtually no galaxies); (iii) 12 μm flux density from ADDSCAN procedure ≥ 0.22 Jy (due to systematic underestimates of the FSC-2 fluxes); and (iv) $|b| \geq 25^\circ$ (to avoid contamination from galactic objects, especially stars). The total number of objects in the sample is 893, all cataloged and with redshifts known. 118 ($\sim 16\%$) are AGN and 63 are type 2 Seyfert galaxies.

The classification of the objects was obtained from existing catalogs of active galaxies (Veron-Cetty and Veron (1991); Hewitt and Burbidge (1991); NASA-IPAC Extragalactic Database, NED). Some objects have been re-classified: ARP 220, is not longer classified as a Seyfert 2 galaxy but a LINER. In order to corroborate the classification of our targets, as future and complementary work, we observed 39 of our galaxies with the RC spectrograph on Blanco Telescope in CTIO, in two runs in August 2007 and February 2008.

3.2 Photometric Observations and data reduction

Some galaxies in our sample have a high quality Spectral Energy Distribution (SED) already determined: NGC 1068, NGC 4388, NGC 4968, NGC 5506, NGC 7172 and NGC 7674. We have observed all the remaining 42 type 2 Seyfert galaxies in the following infrared bands: near-infrared J ($1.25\mu\text{m}$), H ($1.65\mu\text{m}$), and K ($2.2\mu\text{m}$) bands; and mid-infrared L ($3.56\mu\text{m}$), M ($4.66\mu\text{m}$), and N ($10\mu\text{m}$) bands. In table 3.2 the main characteristics of the observing runs are listed.

The observations in near-IR bands followed the usual strategy used in this regime: several images of short integration times (3-20 seconds, in order to avoid

the saturation of the detector and to minimize time fluctuations in the sky brightness) are obtained, positioning the object in different places of the detector in each image, in order to subtract the sky efficiently and to avoid bad pixels.

The reduction of the near-infrared data was done, in part, with the XMOSAIC task of the XDIMSUM package of IRAF ².

The seeing conditions for each analysed observation are summarized in Table 3.11, along with the linear scale (the FWHM of the Point Spread Function).

3.2.1 ISSAC visiting run (near-IR)

The observations with ISAAC in visiting mode were done under non photometric conditions. This was a problem in just one case: there were no stars in the galaxy frame of NGC 424 that would allow us to determine the calibration of the zero point (Z_0) for that particular observation.

The general procedure to reduce the data was:

- Subtraction of the darks. Flat fielding.
- Construction of a sky image. The sky image was obtained through a median average of the object images (4 frames). In order to obtain a better sky image, a mask of the objects in each image is used.
- Subtraction of the sky from each image of the object.
- Registering and shifting of the object images in order to have the center of the galaxy in the same pixel in each image.
- Finally, averaging the object images. Construction of an exposure map in order to calculate the standard deviation.

²IRAF is distributed by the National Optical Astronomy Observatories, which are operated by the Association of Universities for Research in Astronomy, Inc., under cooperative agreement with the National Science Foundation.

The observations with ISAAC in the near-infrared have a especial step in the reduction procedure: after the sky image construction it was necessary to fit two surfaces to each image due to the presence of 2 horizontal wedges introduced by a reading effect. This effect is shown in Fig. 3.2. A similar effect is seen in SOFI raw data, but in ISAAC this wedge is not constant, so the subtraction of the sky does not eliminate it. An example of the reduction process is shown in Fig. 3.5.

We have some cases where the galaxy is bigger than one quadrant of the image. These images are useless because the image of the sky, constructed from the object observations, has flux from the galaxy itself. This translates into an over-subtraction in the sky-subtracted image of the source. Examples of this are shown in Fig. 3.5 and in the left panel of Figs. 3.3 and 3.4. In such cases, we obtained the sky image from another observation close in time (right panel of Fig. 3.4). But not always this was enough to “save” the observation: even when we used the sky constructed from another object, the galaxy is so big that the surface fitting routine is not capable of finding enough “blank space” to fit the surface in the galaxy’s quadrant (right panel of Fig. 3.3 and bottom right panel of Fig. 3.5). The data lost are the near-infrared images of NGC 1097, NGC 1241 and NGC 1386.

3.2.2 SOFI visitor and service runs (near-IR)

For the data obtained with SOFI the observations started with flat fields at twilight, and at the beginning, mid and end of the night we observe a standard star for flux calibration. At the time of SOFI runs we already had the experience of reducing the ISAAC near-infrared data, so we prevented the problems with big galaxies as follow. For small galaxies (galaxies which fit inside one quadrant of the detector) we used a jittering pattern of 6 images shifted in order to avoid bad pixels and to obtain a good sky subtraction. For big galaxies, we used jittering plus an object-sky-object (O-S-O) pattern in order to obtain a good separate image of the sky and then subtract it from the galaxy frames.

When a bright enough star was not present in the galaxy frame, the observation of a known star was included (to determine the PSF).

The general procedure to reduce the data was:

- As the sky is calculated from the galaxy images, the dark is eliminated during sky subtraction. Flat fielding.
- Construction of a sky image. The sky image was obtained either by averaging the sky images in the case of O-S-O pattern observation (3 or 4 images); or through a median average of the object images (6 images). In order to obtain a better sky image, a mask of the objects in each image is used. An example of the complete process to obtain the sky image is shown in Fig. 3.6.
- Subtraction of the sky from each image of the object. In the upper right and bottom left panels of Fig. 3.7 an example of one flat fielded image before and after the sky subtraction is shown.
- Registering and shifting of the object images in order to have the center of the galaxy in the same pixel in each image.
- Finally, averaging the object images. Construction of an exposure map in order to calculate the standard deviation. In the bottom right panel of Fig. 3.7 the reduced image of NGC 7582 in the J band is shown.

3.2.3 ISAAC and Gemini service runs (mid-IR)

Mid-IR detectors are small and therefore the probability of finding a star in the frame of the galaxy is tiny. Then, for all the mid-IR observations, we observed each galaxy followed by a known star to determine the PSF, and/or a standard star also used for flux calibration.

In the mid-IR the atmosphere is very bright, and also it is temporarily and spatially variable. Besides, the telescope contributes emitting and reflecting radiation. So, the observational procedure in the mid-IR is the so called chopping

and nodding technique. Chopping refers to the oscillation of the secondary mirror, in order to observe 2 fields or “beams”: the first beam (A) is centered on the object and the second beam (B) is centered on a hopefully blank part of the sky. Thus there are two measurements: $\text{signal1}=(\text{source}+\text{skyA})$, and $\text{signal2}=\text{skyB}$. Computing $(\text{signal1} - \text{signal2})$ cancels most, but not all, of the sky emission. In practice, because the optical path through the telescope optics is different for the two chop positions, the background is also different ($\text{skyA} \neq \text{skyB}$). Then, to completely remove the background, the telescope is “nodded” to center the beam B on-source and the beam A off-source, and the quantities ($\text{signal3} = \text{skyA}$) and ($\text{signal4} = \text{source} + \text{skyB}$) are obtained, and the background is properly subtracted. In order to save observation time, the off-source beam is not really off-source: in the case of ISAAC mid-infrared observations the off-source beam is centered in the object but it appears as a “negative object” due to the subtraction. Then, in order to obtain the highest signal-to-noise ratio from the image, the negative sources are inverted and added to the positive object. Figure 3.8 shows an example of this technique in M band.

The ISAAC mid-infrared observations were reduced with the ECLIPSE “jitter” pipeline. In a number of cases a reduction by hand was needed because the observing conditions degraded at the end of the integration, so some of the nodding series were discarded.

The Gemini N band data were reduced using the MIDIR task of the GEMINI package within IRAF. The reduction using the pipeline was tested with a reduction by hand, and the results were very similar.

In the Gemini mid-infrared images, the negative object is not useful as with ISAAC, because the “off-source beam” is not guided for active optics, and the image quality is too degraded. An example of a reduced N band image of ESO 253-G3 is shown in figure 3.9.

3.2.4 Data Calibration

A regular calibration procedure was used to transform the obtained count rates of the calibration stars to a flux standard system. The following expression gives us the zero point a_0 :

$$a_0 = V_{std}^* - V_{inst}^* - a_2 X^* - \dots \quad (3.1)$$

where, V_{std}^* is the standard system magnitude of the star in use, V is an example, and can be replaced for the magnitude of any other wavelength-band; V_{inst}^* is the instrumental or measured magnitude of the star; a_2 is the first order extinction coefficient; X^* is the airmass of the observation. In optical calibrations more terms can be included, but those terms are too small compared to the background noise in infrared observations, so we only use the extinction correction.

The determination of the zero point has an error that can be calculated as:

$$\sigma_{a_0}^2 = \sigma_{V_{std}^*}^2 + \sigma_{V_{inst}^*}^2. \quad (3.2)$$

Once the zero point has been determined, we can use it to calibrate the galaxy flux through the same expression used above (Eqn. 3.1):

$$V_{std}^G = a_0 + V_{inst}^G + a_2 X^G + \dots \quad (3.3)$$

The error associated to the calibration procedure is calculated as:

$$\sigma_{V_{std}^G}^2 = \sigma_{a_0}^2 + \sigma_{V_{inst}^G}^2. \quad (3.4)$$

We used different techniques to calibrate the data, depending on the telescope and wavelength. Each technique is detailed below.

SOFI runs (near-IR)

Standard star observations were interspersed with the galaxy imaging. In the SOFI runs the standard stars were selected from Persson *et al.* (1998) and are listed in table 3.3.

In order to improve the zero point determination, more than one star are used, and the different values of the zero point are averaged using the following expression:

$$\bar{X} = \frac{\sum x_i/\sigma_i^2}{\sum 1/\sigma_i^2} \quad (3.5)$$

and the error associated with this average is determine through:

$$\sigma_{\bar{X}}^2 = \frac{1}{\sum 1/\sigma_i^2} \quad (3.6)$$

The standard magnitudes are given by Persson *et al.* (1998), using an aperture of 10 arcseconds in diameter. Due to limited telescope time, only a few standard stars can be observed during the night, so, in order to have a larger number of zero points to average, we used the field stars located near the standard star and the calibrated magnitudes were extracted from the 2MASS catalog ³. The final zero points computed are listed in table 3.4.

ISAAC visiting run (near-IR)

The near-infrared observations with ISAAC were done during non photometric conditions. This implies that the calibration must be done in a different way than with the near-infrared calibration of SOFI data. During non photometric conditions clouds can be present in the sky during the observations, implying that the observation of a standard star can have a different “sky transmission” than the observation of the galaxy. So, in order to get a standard star observed in exactly the same conditions as the galaxy, the standard star must be included in the frame of the galaxy. As it is almost impossible to have a standard star in the same frame as the galaxy, we used the 2MASS calibrated magnitudes of all field stars present in the frame of the galaxy to calculate the corresponding

³This publication makes use of data products from the Two Micron All Sky Survey, which is a joint project of the University of Massachusetts and the Infrared Processing and Analysis Center/California Institute of Technology, funded by the National Aeronautics and Space Administration and the National Science Foundation.

zero points (using Eqn. 3.1). The final zero points used are the average of the individual values determined using Eqns. 3.5 and 3.6, and are listed in table 3.5.

ISAAC service runs (near-IR)

The mid-infrared standard stars were observed, as usual, immediately before or after the observation of each galaxy. Table 3.6 shows the list of standard stars used in these runs. There are some cases when a standard star was observed before and after a galaxy. In these cases we used the average of both derived zero points (using Eqn. 3.1) in order to improve the accuracy. The averages are calculated using Eqns. 3.5 and 3.6. There are other cases when the PSF star is also a standard star, so we used the average of both, the standard star and the PSF star, derived zero points. The standard magnitudes were obtained from van der Blik *et al.* (1996), Simons and Tokunaga (2002), and Tokunaga *et al.* (2002). The final zero points are shown in table 3.7.

Gemini runs (mid-IR)

The galaxies observed with Gemini in the N band ($10\mu\text{m}$) are calibrated using baseline calibration standard stars, listed in table 3.8. The calibration of these observations is different from that of the near-IR and the uncertainties are much larger. In this case we directly scaled the standard star and galaxy fluxes: we calculated a conversion factor from the standard star image in count-rates/Jansky, and then used this ratio to compute the galaxy flux from the galaxy count-rate. The fluxes of standard stars were found in Cohen *et al.* (1999) and references there in. In table 3.9 the conversion factors for each galaxy are listed.

3.3 Spectroscopic Observations

The Infrared Spectrograph (IRS) provides *Spitzer* with low and moderate resolution spectroscopic capabilities from 5.2 to 38.0 μm . The IRS is composed of four

separate modules, with two modules providing $R \sim 60$ -120 spectral resolution over 5.2-38.0 μm (the Short-Low or SL, from 5.2 to 14.5 μm ; and the Long-Low or LL, from 14.0 to 38.0 μm) and two modules providing $R \sim 600$ spectral resolution over 9.9-37.2 μm (the Short-High or SH, from 9.9-19.6 μm ; and the Long-High or LH, from 18.7-37.2 μm). The low-resolution modules employ long slit designs allowing both spectral and one-dimensional spatial information to be acquired simultaneously on the same detector array. Two small imaging sub-arrays (“peak-up arrays”) in the SL module allow objects to be placed accurately into any of the IRS entrance slits and provide images of sources for photometric or structural information. The high-resolution modules use a cross-dispersed echelle design that allows broad spectral coverage in a single exposure.

Staring mode is the basic operating mode of the IRS. In this mode, science targets are placed on one or more of the IRS slits. The Spectral Mapping mode allows an observer to configure a grid of map positions around a central target position and obtain spectra at each position. The observer may specify any combination of slits for single or cluster targets. The individual pointings are arranged so that the science target defines the center of the map.

Buchanan *et al.* (2006) published low-resolution *Spitzer*/IRS spectra for 51 Seyfert galaxies, 20 of which are in our sample. They made a principal component analysis of the continuum shape and spectral features, and their results suggest that the relative contribution of starburst emission may be the dominant cause of variance in the observed spectra, which might be interpreted as evidence against the unified model. The galaxies were observed using the IRS mapping mode, and the spectra were extracted from the central slit placement of each map using a point-source extraction. Since the observations were designed as a spectral map, blind telescope pointing was used. As a result, no effort was made to accurately acquire each target and to ensure that the central slit of each map was indeed well centered on the nucleus. Therefore, the flux calibration is uncertain by typically 20%, but reaching in some cases even 30% or 45%.

Wu *et al.* (2009) published the spectra for 103 AGN of the 12GS, of which 44

are in our sample (the seven remaining lack *Spitzer*/IRS SL spectra) and were kindly provided. We made use of these processed spectra to complement our photometric SEDs. All the spectra are shown in Fig. 3.10. Some processing details, extracted from Wu *et al.* (2009), are described below.

3.3.1 Data Processing (from Wu *et al.* (2009))

All raw data were found in the *Spitzer* archive. For the objects observed with mapping mode, sky subtraction was performed by differencing the on- and off-source observations of the same order in each module (SL and LL). To obtain an accurate SED from the extracted region of the galaxy, one needs to ensure that the same fraction of the source flux at all wavelengths is sampled. Since the Point Spread Function (PSF) changes from 5 to $35\mu\text{m}$, Wu *et al.* (2009) adopted an image convolution method to account for the change in the full width half maximum (FWHM) of the PSF: the 2-dimensional images at each wavelength were degraded to the resolution at the longest wavelength ($35\mu\text{m}$). Then low-resolution spectra were extracted with matched apertures, chosen to encompass the whole nuclear emission. Even though the image convolution method dilutes the fluxes included in the extraction aperture, it does ensure an accurate SED shape, especially for small maps that cannot encompass the extended emission for the source. The extraction aperture used for each galaxy, both in arcseconds and kiloparsecs, are listed in Table 3.3.1, and a histogram with the physical sizes of the extraction apertures of the whole sample is presented in Fig. 3.11. It is important to highlight the large apertures of the spectra, which certainly dilutes and contaminates the nuclear emission probing different scales of the galaxy.

For data obtained with the IRS staring mode, the reduction was done in the following manner. Individual pointings to each nod position of the slit were co-added using median averaging. Then on and off source images were differenced to remove the contribution of the sky emission. Spectra from the final 2-D images were extracted with a point source extraction mode, which scaled the extraction

aperture with wavelength to recover the same fraction of the diffraction limited instrumental PSF. The spectra were flux calibrated using the IRS standard star α Lac, for which accurate template was available. Finally, using the first order of the LL spectrum (LL1, 20–36 μ m) to define the absolute value of the continuum, the flux calibrated spectra of all other low-resolution orders were scaled to it.

Table 3.1: Our sample of 52 Seyfert 2 galaxies. Also shown the targets of our observations, indicating the detector used in each case.

Number	Name	Hubble Type	RA	DEC	J band ^{††}	H band ^{††}	K band ^{††}	L band	M band	N band
1	N34=MK938	Sc	00 11 06.55	- 12 06 26.32	ISA-2	ISA-2	ISA-2	ISA71-B	ISA71-B	
2	F00198-7926	Pec	00 21 52.90	- 79 10 08.00	ISA-2	ISA-2	ISA-2	ISA71-B	ISA71-B	-
3	F00521-7054	E-S0	00 53 56.15	- 70 38 04.16	ISA-2	ISA-2	ISA-2	ISA71-B	ISA71-B	-
4	E541-IG12	Mult	01 02 17.55	- 19 40 08.67	ISA-2	ISA-2	ISA-2	ISA71-B	ISA71-B	-
5	N424=TOL0109	(R)SB(r)0/a	01 11 27.51	- 38 05 01.08	ISA-2	ISA-2	ISA-2	ISA71-B	ISA71-B	-
6	F01475-0740	E-S0	01 50 02.70	- 07 25 48.48	ISA-2	ISA-2	ISA-2	ISA71-B	ISA71-B	-
7	N1068 ^{†**}	(R)SA(rs)b			§	§	§	§	§	§
8	N1097	(R'l)SB(r'l)b	02 46 18.99	- 30 16 28.68	ISA-2	ISA-2	ISA-2	ISA71-B	ISA71-B	-
9	N1125	SAB0	02 51 40.27	- 16 39 03.69	-	-		ISA71-B	ISA71-B	-
10	N1143/4	S0 pec	02 55 10.85	- 00 10 47.20	ISA-2	ISA-2	ISA-2	ISA71-B	ISA71-B	-
11	M-2-8-39	SAB(rs)a	03 00 30.69	- 11 24 54.06	ISA-2	ISA-2	ISA-2	ISA71-B	ISA71-B	-
12	N1194	SA0+	03 03 49.11	- 01 06 13.39	ISA-2	ISA-2	ISA-2	-	-	†
13	N1241	SB(rs)b	03 11 14.90	- 08 55 20.89	ISA-2	ISA-2	ISA-2			-
14	N1320=MK607	Sa sp	03 24 48.72	- 03 02 31.99	ISA-2	ISA-2	ISA-2			†
15	N1386 **	SB(s)0+	03 36 46.40	- 36 00 02.00	ISA-2	ISA-2	ISA-2	-	-	-
16	F03362-1642	Pec	03 38 34.54	- 16 32 15.84	ISA-2	ISA-2	ISA-2			†
17	F04385-0828	S0	04 40 54.96	- 08 22 22.22	ISA-2	ISA-2	ISA-2			†
18	N1667 **	SAB(r)c	04 48 37.14	- 06 19 11.87	ISA-2	ISA-2	ISA-2			GEMI
19	E33-G2	SB0	04 55 58.99	- 75 32 28.06	ISA-2	ISA-2	ISA-2			-
20	F05189-2524	Pec	05 21 01.47	- 25 21 45.38	ISA-2	ISA-2	ISA-2	-	-	GEMI
21	E253-G3	Sa tidal	05 25 18.29	- 46 00 19.60	ISA-2	ISA-2	ISA-2	-	-	GEMI
22	M+0-29-23	SAB(s)b	11 21 12.26	- 02 59 03.45	SOFI(S)	SOFI(S)	SOFI(S)	ISA70-B	ISA70-B	†

Continued on Next Page...

Table 3.1 – Continued

Number	Name	Hubble Type	RA	DEC	J band ††	H band ††	K band ††	L band	M band	N band
23	N3660	SB(r)bc	11 23 32.24	- 08 39 30.21	SOFI(S)	SOFI(S)	SOFI(S)	ISA70-B	ISA70-B	GEMI
24	N4388 ‡	SA(s)b sp	12 25 46.75	+ 12 39 43.51	§	§	§	§	§	†
25	N4501	SA(rs)b	12 31 59.16	+ 14 25 13.60	SOFI(S)	SOFI(S)	SOFI(S)	ISA70-B	ISA-70B	GEMI
26	TOL1238-364	SB(rs)bc	12 40 52.88	- 36 45 21.52	SOFI(S)	SOFI(S)	SOFI(S)	ISA70-B	ISA70-B	GEMI
27	N4941	R)SAB(r)ab	13 04 13.06	- 05 33 5.79	SOFI(S)	SOFI(S)	SOFI(S)	ISA70-B	ISA70-B	†
28	N4968‡**	(R')SAB0	13 07 05.89	- 23 40 39.38	§	§	§			†
29	M-3-34-64	SB?	13 22 24.46	- 16 43 42.90	SOFI(S)	SOFI(S)	SOFI(S)	ISA70-B	ISA70-B	†
30	N5135 **	SB(l)ab	13 25 43.97	- 29 50 02.26	SOFI(S)	SOFI(S)	SOFI(S)	ISA70-B	ISA70-B	†
31	MK463	Merger	13 56 02.87	+ 18 22 19.48	SOFI(S)	SOFI(S)	SOFI(S)	ISA70-B	ISA70-B	†
32	N5506 ‡	Sa pec sp	14 13 14.86	- 03 12 26.94	§	§	§	§	§	†
33	N5953	SAa pec	15 34 33.70	+ 15 11 49.50	SOFI(S)	SOFI(S)	SOFI(S)	ISA70-B	ISA70-B	GEMI
34	M-2-40-4	S(B)c	15 48 24.96	- 13 45 27.94	SOFI(S)	SOFI(S)	SOFI(S)	ISA70-B	ISA70-B	†
35	F15480-0344	S0	15 50 41.51	- 03 53 18.34	SOFI(S)	SOFI(S)	SOFI(S)	ISA71-B	ISA71-B	†
36	F19254-7245	Merger	19 31 21.40	- 72 39 17.96	SOFI(V)	SOFI(V)	SOFI(V)	ISA71-B	ISA71-B	GEMI
37	N6810	SA(s)ab:sp	19 43 34.16	- 58 39 20.54	SOFI(V)	SOFI(V)	SOFI(V)	ISA71-B	ISA71-B	GEMI
38	N6890	R')SA(r:)ab	20 18 18.07	- 44 48 23.36	SOFI(V)	SOFI(V)	SOFI(V)	ISA71-B	ISA71-B	GEMI
39	I5063	SA(s)0+	20 52 02.01	- 57 04 09.12	SOFI(V)	SOFI(V)	SOFI(V)	ISA71-B	ISA71-B	GEMI
40	U11680=MK897	Compact	21 07 43.70	+ 03 52 19.00	SOFI(V)	SOFI(V)	SOFI(V)	ISA71-B	ISA71-B	GEMI
41	N7130=I5135	Sa pec	21 48 19.49	- 34 57 05.98	SOFI(V)	SOFI(V)	SOFI(V)	ISA71-B	ISA71-B	GEMI
42	N7172 ‡	Sa pec sp	22 02 01.68	- 31 52 18.12	§	§	§	§	§	†
43	M-3-58-7	(R')SAB(s)0/a	22 49 37.15	- 19 16 26.39	SOFI(V)	SOFI(V)	SOFI(V)	ISA71-B	ISA71-B	†
44	N7496	(R')SB(rs)bc	23 09 47.26	- 43 25 39.76	SOFI(SV)*	SOFI(SV)	SOFI(SV)	ISA71-B	ISA71-B	-

Continued on Next Page...

Table 3.1 – Continued

Number	Name	Hubble Type	RA	DEC	J band ††	H band ††	K band ††	L band	M band	N band
45	N7582	(R'1)SB(s)ab	23 18 23.50	- 42 22 13.98	SOFI(SV)	SOFI(SV)	SOFI(SV)	ISA71-B	ISA71-B	–
46	N7590	S(r?)bc	23 18 54.60	- 42 14 21.00	SOFI(SV)	SOFI(SV)	SOFI(SV)	ISA71-B	ISA71-B	–
47	N7674†**	SA(r)bc pec	23 27 56.74	+ 08 46 44.52	§	§	§	§	§	†
48	CGCG381-051	SBc	23 48 41.64	+ 02 14 24.02	SOFI(V)	SOFI(V)	SOFI(V)	ISA71-B	ISA71-B	†

†Observed by Gorjian *et al.* (2004).

§SED determined by Alonso-Herrero *et al.* (2003).

**Compton thick source.

‡SED already determined by other.

††(S) Service mode. (V) Visitor mode.

*One bad quadrant made unusable the service images.

Table 3.2. Summary of observation runs.

Period	Observatory	Telescope	Detector	Mode	Observed Bands
2002B	VLT	ANTU (UT1)	ISAAC	Visitor	JHK
2002B	VLT	ANTU (UT1)	ISAAC	Service	LM
2003A	VLT	ANTU (UT1)	ISAAC	Service	LM
2003B	La Silla	NTT	Sofi	Service	JHK
2004A	Gemini	Gemini	T-ReCS	Service	N
2004B	La Silla	NTT	Sofi	Visitor	JHK

Table 3.3. Standard stars observed in SOFI runs.

Date	Star
20031222	GSPC P525-E
	GSPC S312-T
	GSPC S495-E
	GSPC S677-D
20040111	GSPC S121-E
	GSPC S209-D
20040112	GSPC S363-D
	GSPC S840-F
	GSPC S842-E
	GSPC S312-T
	GSPC S264-D
	GSPC S860-D
20040130	GSPC P499-E
20040322	GSPC P499-E
	GSPC P565-C
	GSPC S875-C
20041002	GSPC S071-D
	GSPC S234-E
	GSPC S677-D
20041003	GSPC S071-D
	GSPC S677-D
	GSPC S677-D
	GSPC P530-D
	GSPC S301-D
	GSPC P247-U

Table 3.4. Zero points for SOFI runs.

Date	Band	a_0	σ_{a_0}
20031222	J	23.2023	0.009
	H	22.9427	0.007
	K	22.3443	0.009
20040111	J	23.1916	0.015
	H	23.0348	0.014
	K	22.4060	0.017
20010112	J	23.1144	0.007
	H	22.9592	0.006
	K	22.3824	0.006
20040130	J	22.9974	0.02
	H	22.8325	0.017
	K	22.3131	0.025
20040322	J	23.2381	0.012
	H	22.9124	0.012
	K	22.5092	0.014
20040323	J	23.0163	0.027
	H	22.8622	0.028
	K	22.2946	0.05
20041002	J	23.1286	0.007
	H	22.9761	0.007
	K	22.3874	0.008
20041003	J	23.1599	0.006
	H	23.0023	0.006
	K	22.3938	0.007

Table 3.5. Zero points for ISAAC near-infrared run.

Galaxy	Band	a_0	σ_{a_0}
ESO253-G3	J	24.6942	0.016
	H	24.5767	0.023
	K	23.9602	0.022
IRAS 05189-2524	J	24.7465	0.025
	H	24.5962	0.023
	K	24.0086	0.025
ESO33-G2	J	24.4708	0.013
	H	24.1905	0.016
	K	23.5886	0.014
NGC 1667	J	24.7568	0.016
	H	24.5108	0.017
	K	24.0309	0.020
IRAS 04385-0828	J	24.6105	0.021
	H	24.4131	0.021
	K	23.8991	0.031
IRAS 03362-1642	J	24.5518	0.023
	H	24.3758	0.026
	K	23.8344	0.027
NGC 1320	J	24.6827	0.029
	H	24.4067	0.036
	K	23.9049	0.049
NGC 1194	J	24.7210	0.018
	H	24.4701	0.024
	K	23.9292	0.033
MCG -2-8-39	J	24.4232	0.016
	H	24.1675	0.017
	K	23.7182	0.018
NGC 1143	J	24.1346	0.039
	H	23.6092	0.064

Table 3.5—Continued

Galaxy	Band	a_0	σ_{a_0}
	K	23.0734	0.094
IRAS 01475-0740	J	24.7732	0.013
	H	24.4830	0.014
	K	24.0016	0.013
ESO 541-IG12	J	24.6106	0.040
	H	24.5120	0.055
	K	24.0642	0.082
IRAS 00521-7054	J	24.8040	0.036
	H	24.4340	0.042
	K	23.5445	0.078
IRAS 00198-7926	J	24.3633	0.020
	H	23.9087	0.025
	K	23.0285	0.042
NGC 34	J	24.4596	0.018
	H	24.0201	0.018
	K	23.5917	0.020

Table 3.6. Standard stars observed in ISAAC service runs.

Star
HD 106965
HD 130163
HD 136754
HD 22686
HD 590
HD 2811
HD 1274
HD 210427
HD 205772
HD 161743

Table 3.7. Zero points for ISAAC mid-infrared run. Only shown the zero points for galaxies detected in the respective wavelength.

Galaxy	Band	a_0	σ_{a_0}
IRAS 15480-0344	L	22.427	0.011
	M	19.613	0.052
NGC 7582	L	22.461	0.024
	M	19.633	0.036
NGC 7496	L	22.493	0.016
	M	19.454	*
MCG -3-58-7	L	22.415	0.016
	M	19.705	0.105
NGC 7130	L	22.520	0.007
	M	19.703	*
MRK 897	L	22.486	0.005
IC 5063	L	22.521	0.007
	M	19.744	0.049
NGC 1125	L	22.445	0.013
	M	19.633	0.036
MCG -2-8-39	L	22.479	0.12
	M	19.563	0.039
NGC 1143	L	22.521	0.012
	M	19.707	0.029
IRAS 01475-0740	L	22.563	0.01
	M	19.840	0.009
ESO 541-IG12	L	22.553	0.01
	M	19.840	0.009
IRAS 00521-7054	L	22.563	0.01
	M	19.840	0.009
IRAS 00198-7926	L	22.468	0.013
	M	19.633	0.036
NGC 34	L	22.382	0.021
	M	19.705	0.105

Table 3.7—Continued

Galaxy	Band	a_0	σ_{a_0}
NGC 6890	L	22.489	0.006
	M	19.744	0.049
NGC 6810	L	22.457	0.006
	M	19.744	0.049
IRAS 19254-7245	L	22.465	0.021
	M	19.718	*
MCG -2-40-4	L	22.482	0.011
	M	19.729	*
NGC 5953	L	22.389	0.011
MRK 463	L	22.431	0.011
	M	19.589	0.051
NGC 5135	L	22.486	0.011
	M	19.589	0.051
MCG -3-34-64	L	22.488	0.008
	M	19.668	0.053
TOL 1238-364	L	22.488	0.008
	M	19.668	0.053
NGC 4501	L	22.476	0.011
NGC 3660	L	22.478	0.008
MCG +0-29-23	L	22.484	0.008

*The calibration was done using the intrinsic K-M color of each star and the K standard magnitude.

Table 3.8. Standard stars observed in Gemini service run.

Star
HD 4128
HD 32887
α Canis Mayor
HD 81797
HD 70555
HD 189831
HD 178345
HD 196916
HD 123139

Table 3.9. Conversion factors for Gemini run.

Galaxy	Band	F [counts/Jy]	σ_F
NGC 1667	N	312308.64	604.51
IRAS 05189-2524	N	264010.76	1497.825
ESO 253	N	312308.64	604.51
NGC 3660	N	302404.39	4403.92
TOL 1238-364	N	302404.39	4403.92
NGC 5953	N	270930.47	1061.67
IRAS 19254-7245	N	359875.70	773.63
NGC 6810	N	359875.70	773.63
NGC 6890	N	359875.70	773.63
IC 5063	N	359875.70	773.63
MRK 897	N	340267.78	984.87
NGC 7130	N	359875.70	773.63

Table 3.10. Aperture size and projected aperture size of extracted *Spitzer* spectra.

Object Name	Aperture Size ($''$)	Projected Size (kpc)
NGC 34	20.4×15.3	8.6×6.5
F01475-0740	20.4×15.3	7.7×5.8
NGC1143/4	19.8×16.2	12.2×10.0
M-2-8-39	20.4×15.3	12.6×9.4
NGC1194	20.4×15.3	6.0×4.5
NGC1320	20.4×15.3	3.8×2.9
F04385-0828	20.4×15.3	6.4×4.8
E33-G2	20.4×15.3	7.7×5.8
F05189-2524	10.2 ^b	9.3
M+0-29-23	20.4×15.3	10.8×8.1
NGC3660	20.4×15.3	5.1×3.9
NGC4388	20.4×15.3	3.4×2.6
NGC4501	20.4×15.3	3.4×2.6
Tol1238-364	20.4×15.3	4.7×3.5
NGC4941	10.2 ^b	0.8
NGC4968	20.4×15.3	4.3×3.2
M-3-34-63	20.4×15.3	9.1×6.8
NGC5135	20.4×15.3	6.0×4.5
NGC5506	20.4×15.3	2.6×1.9
NGC5953	20.4×15.3	3.0×2.2
M-2-40-4	20.4×15.3	10.8×8.1
F15480-0344	20.4×15.3	13.0×9.8
NGC6810	20.4×15.3	3.0×2.2
NGC6890	20.4×15.3	3.4×2.6
I5063	10.2 ^b	2.4
MRK 897	20.4×15.3	11.3×8.4
NGC7130	20.4×15.3	6.9×5.2

Table 3.10—Continued

Object Name	Aperture Size (")	Projected Size (kpc)
NGC7172	10.2 ^b	1.9
M-3-58-7	20.4×15.3	13.5×10.1
NGC7496	20.4×15.3	2.6×1.9
NGC7582	20.4×15.3	2.2×1.6
NGC7590	20.4×15.3	2.2×1.6
NGC7674	20.4×15.3	12.6×9.4
CGCG381-051	20.4×15.3	13.5×10.1

^bSpectrum extracted from IRS staring mode. The size of the LL slit is 2 pixel wide, where 1 pixel~5.1".

Table 3.11: Seeing conditions for each observation. Physical resolution of each observation.

Galaxy	Redshift	Distance Mpc	J band PSF		H band PSF		K band PSF		L band PSF		M band PSF		N band PSF	
			["]	[pc]	["]	[pc]	["]	[pc]	["]	[pc]	["]	[pc]	["]	[pc]
NGC 34	0.0192	81.50	0.62	245.0	0.67	266.6	0.62	243.3	0.25	99.02	0.31	121.75		
IRAS 00198-7926	0.0742	306.23	0.96	1423.8	1.03	1529.3	0.95	1406.3	0.43	633.52	0.37	552.35		
IRAS 00521-7054	0.0700	289.52	0.93	1304.6	0.87	1215.3	0.67	934.8	0.32	450.46	0.44	613.90		
ESO 541-IG12	0.0564	234.91	0.70	800.6	0.60	681.0	0.53	598.4	0.34	384.89	0.29	328.29		
IRAS 01475-0740	0.0174	73.92	0.62	223.8	0.57	203.1	0.49	176.6	0.32	115.01	0.44	156.74		
NGC 1143	0.0282	119.15	0.59	340.3	0.53	305.2	0.55	318.9	0.47	271.52	0.53	308.43		
MCG -2-8-39	0.0301	127.06	0.49	299.9	0.48	298.1	0.44	269.9	0.52	321.02	0.54	330.64		
NGC 1194	0.0134	57.04	0.55	151.0	0.54	150.2	0.51	142.0						
NGC 1320	0.0099	42.22	0.53	108.1	0.41	84.8	0.39	79.4						
IRAS 04385-0828	0.0152	64.65	0.51	158.6	0.56	175.8	0.46	144.7						
ESO 33-G2	0.0186	78.97	0.62	236.9	0.63	242.0	0.60	228.4						
IRAS 05189-2524	0.0415	174.17	0.39	327.4	0.42	358.7	0.37	312.4					0.44	367.82
MCG +0-29-23	0.0249	105.39	0.93	473.8	0.80	406.9	0.65	334.0	0.25	126.97	0.33	166.87		
NGC 3660	0.0123	52.39	0.68	173.4	0.74	188.0	0.71	181.0	0.36	91.43			0.36	92.12
NGC 4501	0.0077	32.87	0.90	143.9	0.76	121.9	0.79	126.2	0.50	79.66			0.41	64.98
TOL 1238-364	0.0012	5.14	0.87	21.8	0.75	18.6	0.72	18.0	0.23	5.79	0.22	5.48	0.31	7.65
NGC 4941	0.0037	15.83	0.93	71.3	0.78	59.7	0.78	60.0						

Continued on Next Page...

Table 3.11 – Continued

Galaxy	Redshift	Distance Mpc	J band PSF		H band PSF		K band PSF		L band PSF		M band PSF		N band PSF	
			["]	[pc]	["]	[pc]	["]	[pc]	["]	[pc]	["]	[pc]	["]	[pc]
MCG -3-34-64	0.0172	73.08	0.78	277.0	0.77	273.0	0.80	283.2	0.40	140.37	0.36	127.79		
NGC 5135	0.0137	58.31	0.72	203.5	0.67	188.1	0.62	174.2	0.42	117.62	0.40	112.40		
NGC 5953	0.0066	28.19	0.72	99.0	0.68	93.5	0.71	97.6	0.37	50.27			0.37	49.94
MCG -2-40-4	0.0244	103.30	0.62	310.8	0.63	315.9	0.67	336.8	0.40	201.96	0.34	172.09		
IRAS 15480-0344	0.0304	128.31	0.72	446.1	0.67	419.2	0.71	438.9	0.48	298.56	0.47	294.14		
NGC 6810	0.0066	28.19	0.62	84.2	0.65	89.0	0.59	81.1	0.27	36.39	0.52	70.45	0.31	42.81
NGC 6890	0.0081	34.57	0.59	98.5	0.55	91.7	0.52	87.9	0.42	69.74	0.40	66.41	0.31	52.65
IC 5063	0.0113	48.15	0.71	165.4	0.64	149.3	0.67	156.0	0.33	77.08	0.35	82.22	0.31	73.33
MK 897	0.0264	111.65	0.79	428.7	0.73	392.8	0.72	388.2	0.55	295.16			0.33	176.84
NGC 7130	0.0162	68.87	0.60	199.0	0.60	201.9	0.62	207.7	0.45	151.00	0.34	112.36	0.35	116.89
MCG -3-58-7	0.0316	133.29	0.63	405.7	0.66	424.3	0.66	424.3	0.44	284.46	0.42	268.40		
NGC 7496	0.0055	23.51	0.66	74.8	0.69	79.1	0.56	63.3	0.46	52.43	0.51	58.66		
NGC 7582	0.0053	22.65	0.68	75.0	0.73	80.7	0.67	73.4	0.34	36.81	0.29	31.74		
NGC 7590	0.0050	21.38	0.74	76.4	0.62	64.2	0.62	64.8	0.43	44.73				
NGC 7590	0.0050	21.38	0.77	79.5	0.84	87.1	0.82	85.1						
CGCG381-051	0.0305	128.72	0.79	490.7	0.80	501.4	0.72	447.5						

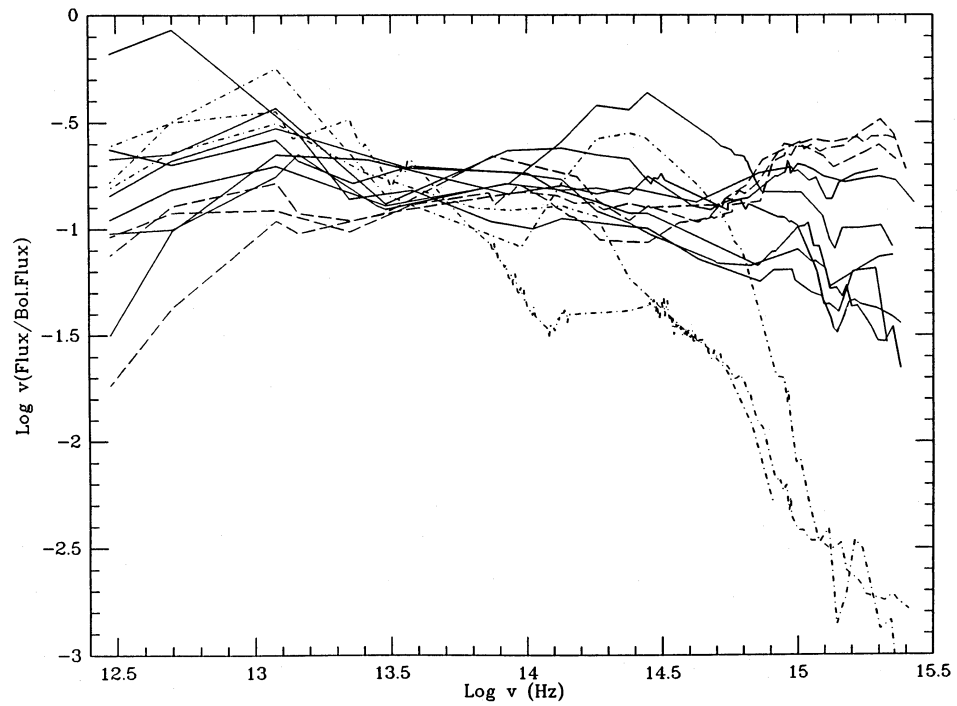


Figure 3.1: Spectral Energy Distribution for 13 AGNs (Fig.1 of Spinoglio and Malkan (1989)). The fluxes have been normalized to unity. Seyfert 2 galaxies are drawn in dot-dashed lines; Seyfert 1's in solid lines; and 3 blue PG quasars in dashed lines. The scatter is minimized in the mid-infrared (7-12 μm) range.

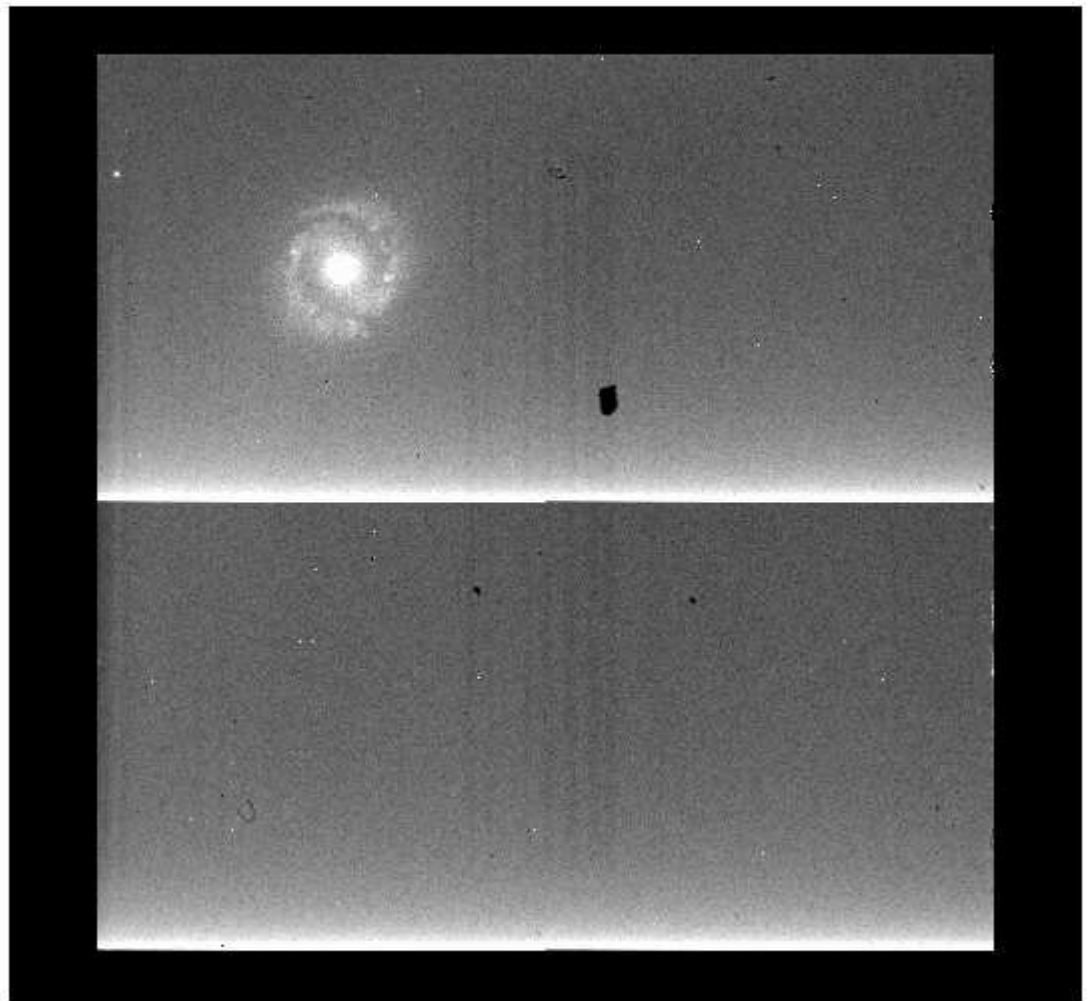


Figure 3.2: Raw image from ISAAC, in the J band, for galaxy NGC 1097. The picture shows the 2 wedges present in raw ISAAC near-infrared images. In order to get rid of them, we fit 2 surfaces to each half of the detector before the determination of the sky image.

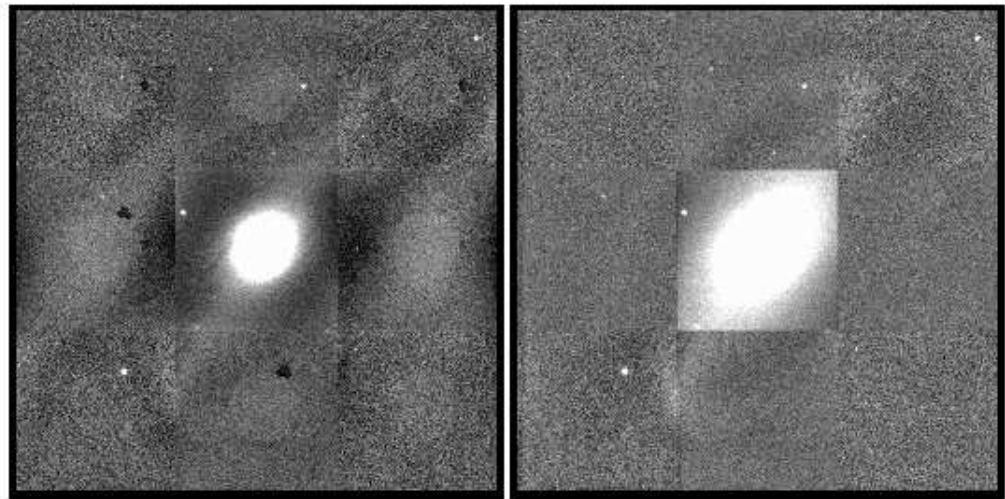


Figure 3.3: J band images of NGC 1097 using ISAAC, an example of lost data. The left panel shows the final combined image using a sky image constructed from the galaxy images. The right panel shows the final combined image using the sky constructed from another object images. In this case, the galaxy is so large, that the surface fitting routine was not able to fit any surface in the quadrant of the galaxy, so the data were lost.



Figure 3.4: J band images of NGC 1667 using ISAAC. This figure shows an example of “saved” data, using a sky image constructed from another object images.

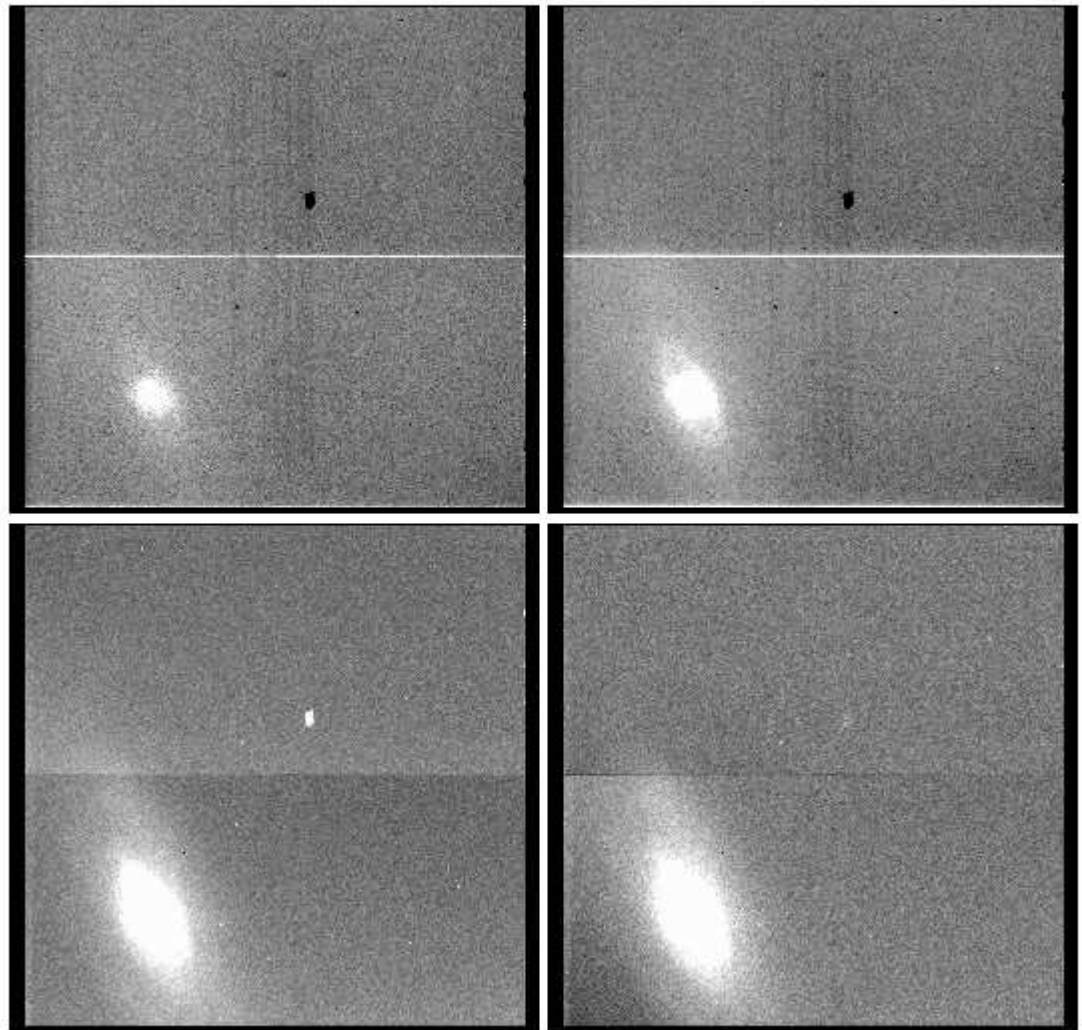


Figure 3.5: J band images of NGC 1386 using ISAAC. In the upper left panel a dark subtracted image is shown. In the upper right panel, the same as shown at left plus the flat fielding correction. The bottom left panel shows the sky subtracted image, where remain the wedges. The bottom right panel shows the surface fitting failure in the quadrant of the galaxy: the bottom left corner of the image is over subtracted, so this data were lost.

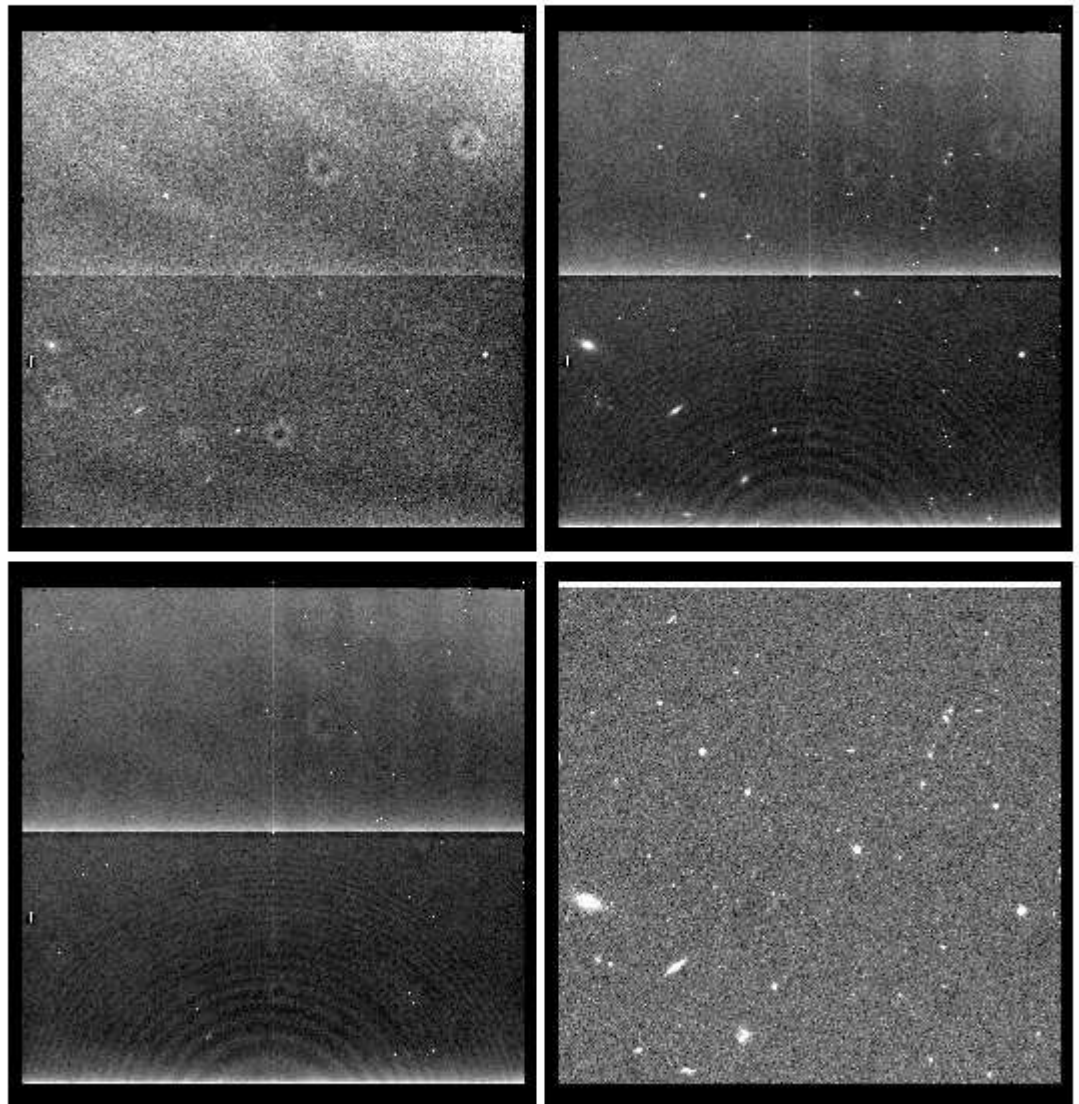


Figure 3.6: Sky image construction for SOFI data. The upper left panel shows a raw sky-dedicated image; the upper right panel shows the same image after flat fielding is applied. In the bottom left panel, the median averaged, final image of the sky; and the bottom right panel shows a sky-dedicated image, flat fielded and sky subtracted, to show that the observed galaxy does not contaminate the combined sky image.

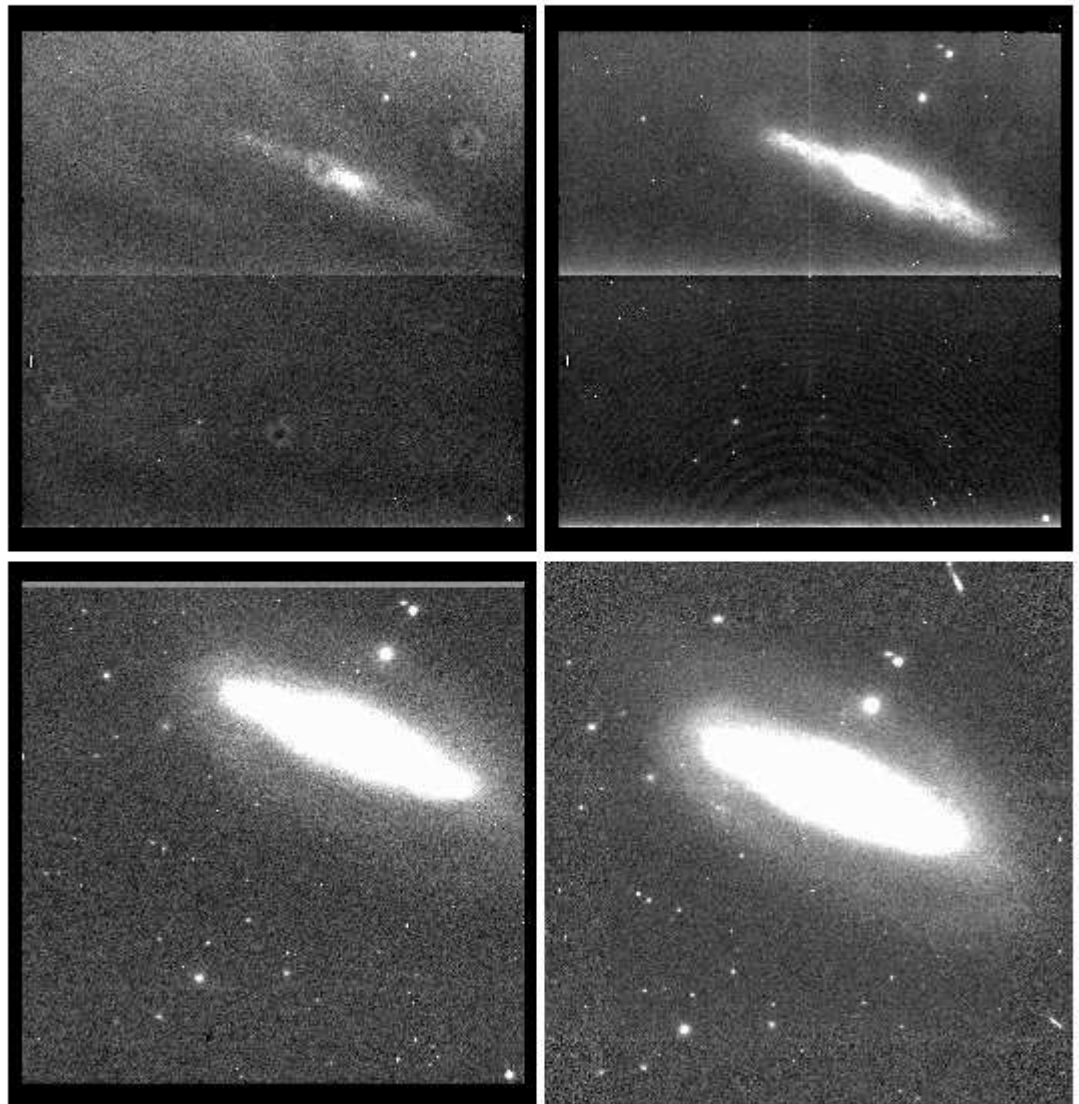


Figure 3.7: Reduction process for an observation in the J band obtained with SOFI. This is an example of a large galaxy with sky-dedicated images: in the upper left panel, a raw image of NGC 7582. In the upper right panel the same image, but flat fielded. In the bottom left panel, the flat fielded image with the sky subtracted. Finally, the bottom right panel shows the final, combined, flat fielded, sky subtracted image.

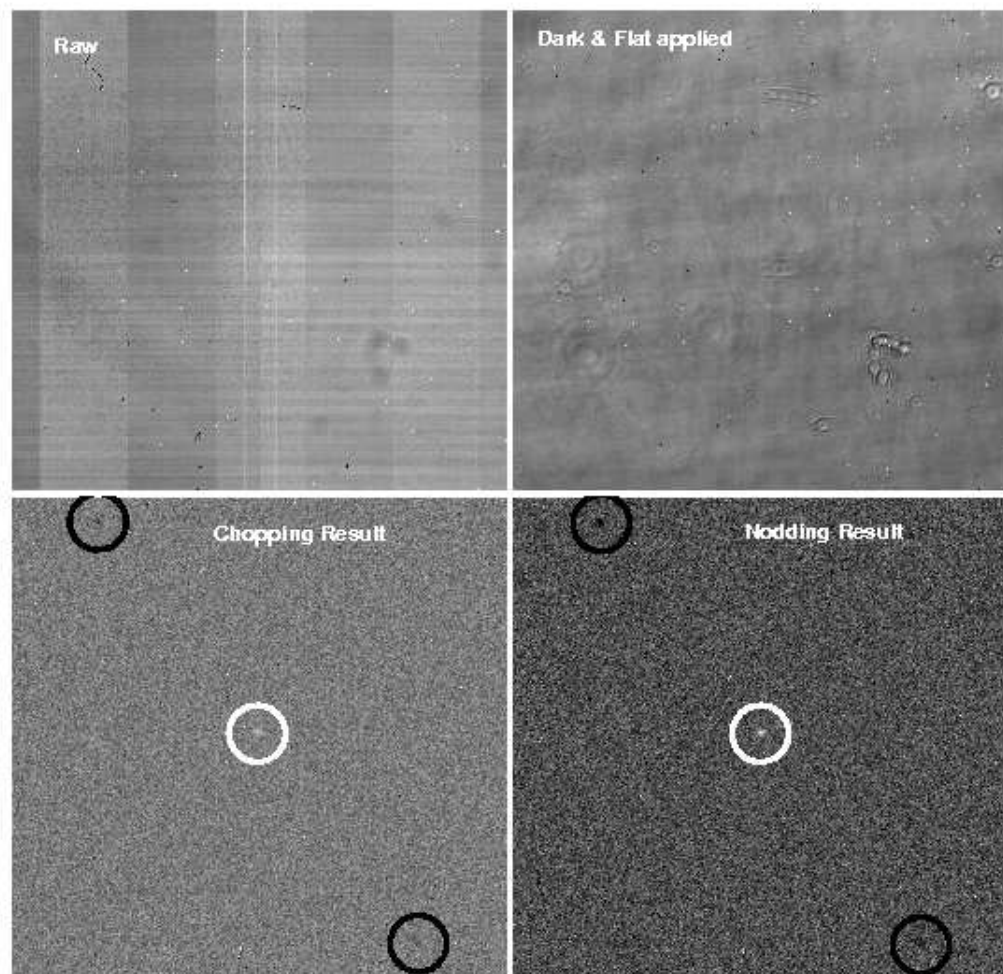


Figure 3.8: M band images of NGC 5135 using ISAAC. The upper left panel shows a raw image. The upper right panel shows the dark subtracted and flat fielded first image. In the bottom left panel the resulting A-B chopping beams subtraction is shown. The bottom right panel shows the resulting (A-B)-(B-A) nodding subtraction. The improvement in background noise and structure is evident in bottom-right respect to bottom-left. The black circles indicate where the negative objects are located, and the white circle indicates where the positive object is located (see text for details).

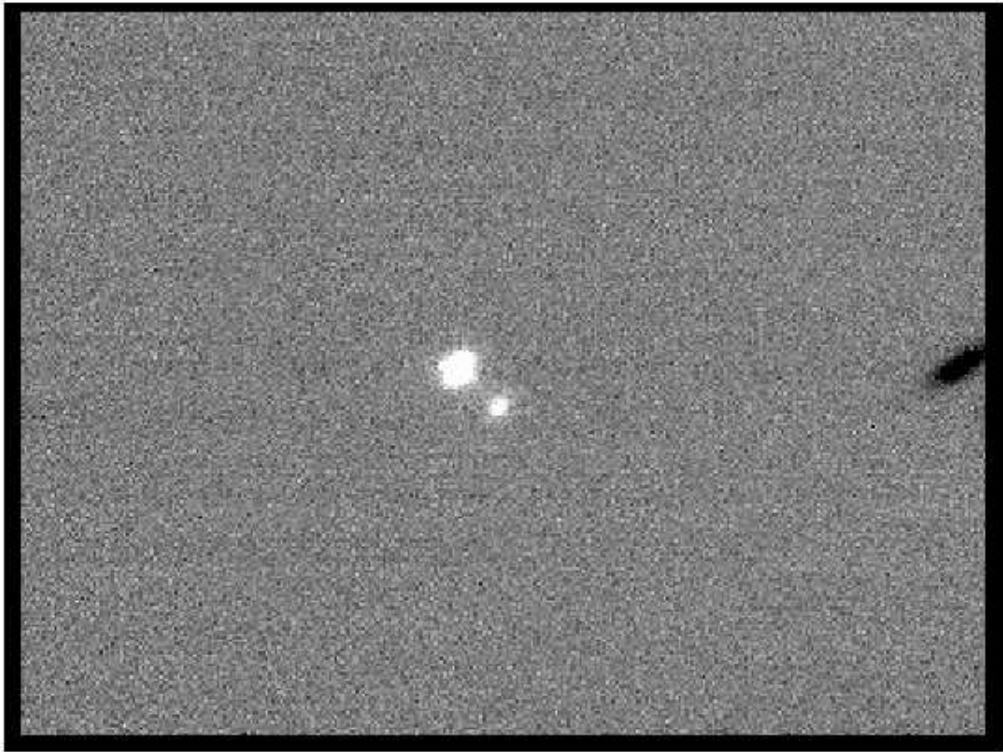


Figure 3.9: N band image of ESO 253-G3 taken with Gemini. In the right edge of the image, the negative object with no guiding is seen and the quality degradation is evident.

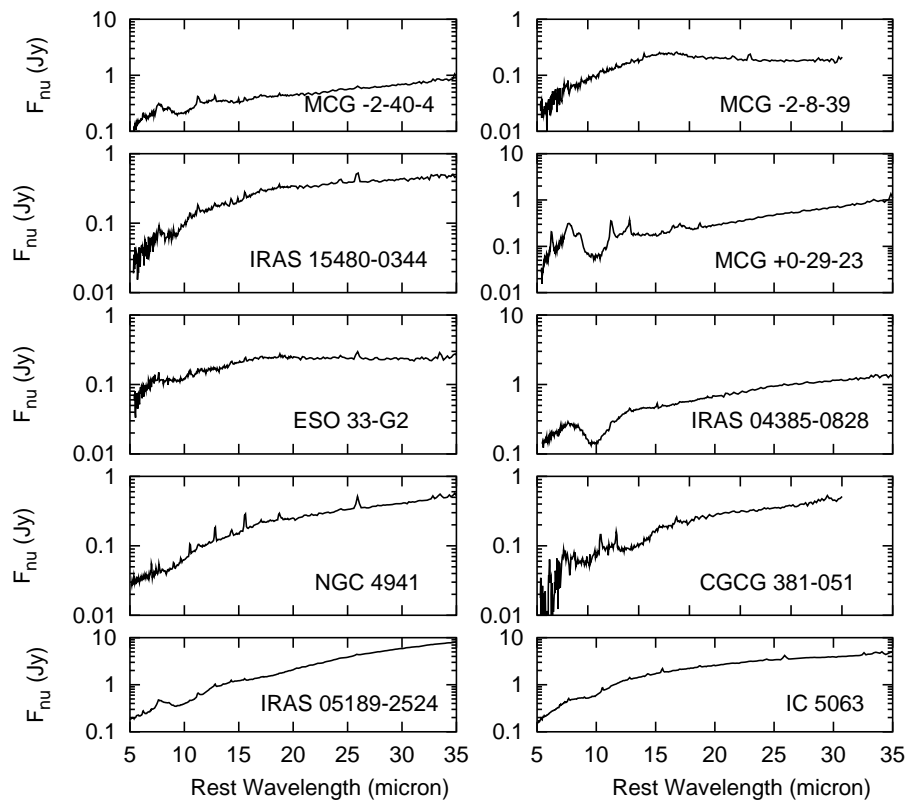


Figure 3.10: *Spitzer* Spectra of some galaxies in our sample. Kindly provided by Wu *et al.* (2009).

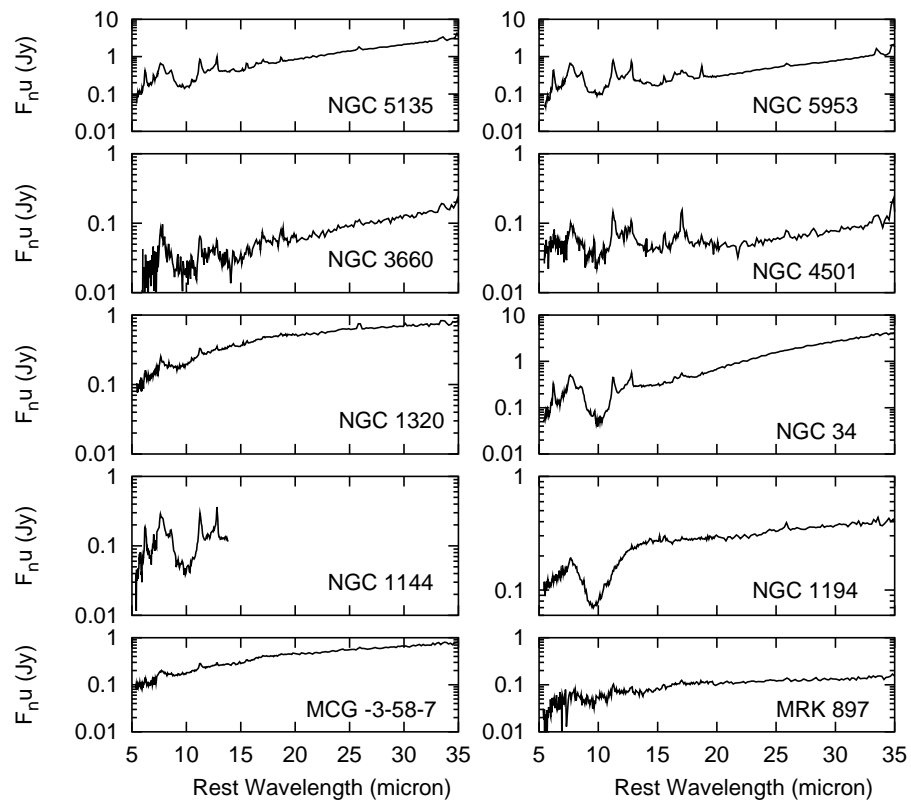


Figure 3.10: Continued

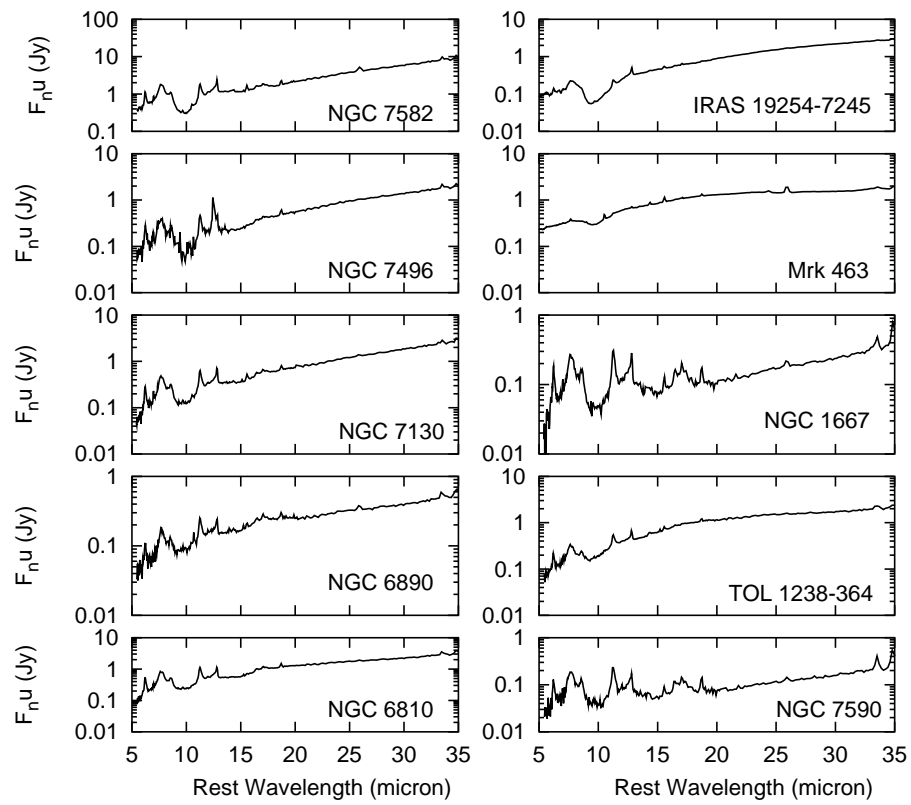


Figure 3.10: Continued

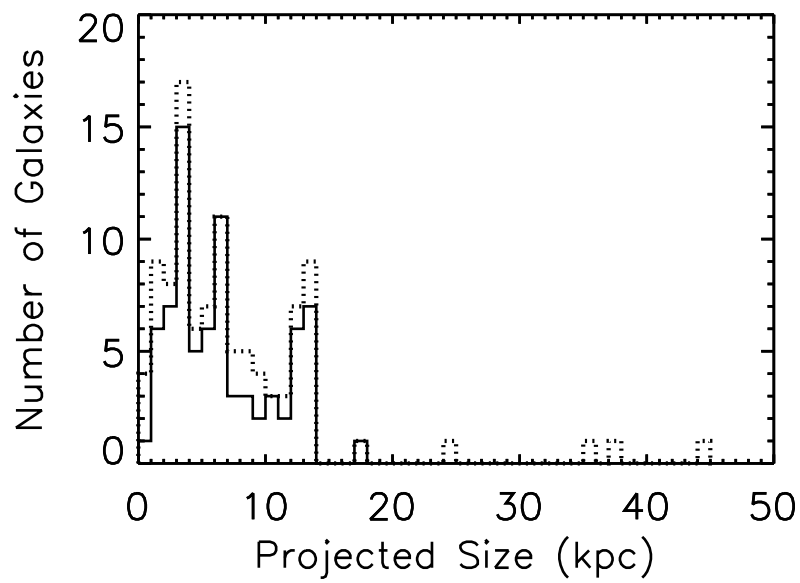


Figure 3.11: A histogram of the projected linear size of the IRS spectral extraction aperture at the distance of the corresponding target of the $12\mu\text{m}$ Seyfert sample. The dotted line indicates the distribution of the whole sample, while the solid line indicates the distribution for those that have been observed using the spectral mapping mode. Fig. from Wu *et al.* (2009).

Chapter 4

Constructing the SEDs

4.1 Separating the Torus from the Galaxy

We have obtain deep infrared (IR) images of a sample of type 2 Seyfert (Sy) galaxies in order to study the dusty structure that would be responsible for the differences seen between type 1 and type 2 Active Galactic Nuclei (AGN). These images cover the entire galaxy but what we need is the emission from the nuclear region only. There are different ways to deconvolve the galaxy into their different components, meaning the bulge, disk, bar, rings, nucleus, etc. One is using the whole image, i.e. using a 2-D approach, and another is using the radial surface brightness profile of the galaxy, i.e., a 1-D method. Both ways have advantages and disadvantages.

4.1.1 2-D Decomposing Method: Galfit

The main advantage of this type of decomposition, compared to 1-D methods, is that no information about all the structures present in the galaxy is lost. But this is also the main disadvantage given our scientific goal.

We tried using Galfit (Peng *et al.*, 2002), a galaxy fitting algorithm that fits 2-D parameterized, axisymmetric, functions directly to images. The minimization engine is based on the Levenberg-Marquardt algorithm (downhill gradient), taken

from Numerical Recipes (Press, 1993) and modified moderately. The models are convolved with the point spread function (PSF) using Fast Fourier Transform (FFT) to take into account the seeing. GALFIT is faster than other similar 2-D galaxy fitting algorithms, but given the big sizes of many of our galaxies, it is much slower than 1-D decomposing methods.

The final data product we are looking for is the nuclear IR spectral energy distribution (SED) of each AGN. This means that we are not interested in the morphology of the galaxy, or the morphology of any structure embedded in the galaxy. We are only interested in obtaining the total emission coming from the nucleus, so keeping information about rings, disk/boxy bulges, etc. is of no immediate benefit. Besides, the ability of GALFIT in modeling the arms of spiral galaxies is still developing. GALFIT is a very useful tool when working with galaxies at intermediate redshift, where the strong local features are diluted.

4.1.2 1-D Decomposing Method: Amoeba

The 1-D methods use the radial surface brightness profile (SBP) of the galaxy, not the image (Kotilainen *et al.*, 1992; Zitelli *et al.*, 1993; Alonso-Herrero *et al.*, 1996; Prieto *et al.*, 2001, 2002). We used the IRAF ¹ task *ellipse* (STSDAS package) on the sky subtracted images to obtain the SBPs. We applied a manual masking to remove contamination from different sources that might distort the isophote fitting, like foreground stars or galaxies. We leave the center coordinates fixed and let vary the other parameters describing the isophotal ellipse, meaning the position angle and the ellipticity. We used a linear radial sampling with steps of 0.5-1 pixel, depending on the size of the galaxy. In cases where the edge of the galaxy is too weak and the ellipse fitting process does not converge, we used the fitted isophotes observed at other wavelengths. In order to take into account the

¹IRAF is distributed by the National Optical Astronomy Observatories, which are operated by the Association of Universities for Research in Astronomy, Inc., under cooperative agreement with the National Science Foundation.

inclination of the galaxy, we corrected the SBP using the mean ellipticity of the last fitted isophotes.

The main advantage of this 1-D description of the galaxy is that the small structures (spiral arms, HII Regions, rings) are diluted, while preserving the more fundamental structures (the bulge, disk, nucleus and bar); and instead of having $\sim 500 \times 500$ pixels for the fitting process, a typical profile has only ~ 200 points to fit. The method used to fit the SBP is the “Downhill Simplex Method in Multidimensions”, described in details in 4.2.2. The analytical functions used to model each component of the galaxy are the same in both 1-D and 2-D methods. Given the characteristics of our scientific goals, we opted for this 1-D deconvolution method.

4.2 Modeling the Surface Brightness Profiles

We want to construct the Spectral Energy Distribution (SED) of the nuclear emission of each galaxy. To observe directly the torus is possible, as mentioned in Chapter 2, but the exposures required are so large that in order to obtain a statistically representative sample we would need “a year of observations”.

As explained in Section 4.1, we use the surface brightness profile (SBP) to separate the emission of the nucleus from that of the galaxy. A spiral galaxy is composed mainly of a disk, a bulge, sometimes a bar, and sometimes an active nucleus. Each physical component has been modeled historically with a specific analytical function. We started our work using only 3 components, a nucleus, a disk and a de Vaucouleurs’s bulge, but experience indicated that the $r^{1/4}$ law was inappropriate to describe the bulge profile, and that sometimes we needed a bar to properly model the galaxy profile. Below we describe each model component.

Nucleus

The nuclear point source is modeled using a Dirac's Delta, defined as:

$$\int_{-a}^a \delta(t) dt = 1, \quad \forall a \in \mathfrak{R}. \quad (4.1)$$

So the nuclear profile is described by:

$$\Sigma_n(r) = \sigma_n \delta(r), \quad (4.2)$$

where σ_n is the nuclear surface brightness.

Disk

The disk is modeled using an exponential law:

$$\Sigma_d(r) = \sigma_d \exp\{-r/r_d\}, \quad (4.3)$$

where σ_d is the surface brightness of the disk at $r = 0$, $\sigma_d = \Sigma_d(r = 0)$, and r_d is the disk scale length.

Bulge

The bulge was first modeled using a de Vaucouleurs law:

$$\Sigma_B(r) = \sigma_B \exp\{-7.6692 \cdot (r/r_B)^{1/4}\}, \quad (4.4)$$

where r_B is the effective radius that encloses half of the total light and σ_B is the effective surface brightness of the bulge, meaning $\sigma_B = \Sigma_B(r_B)$. But the profiles were not well fitted using this function. We decided to use a more general Sérsic's law to describe the bulge, given by:

$$\Sigma_B(r) = \sigma_B \exp\{-b_n \cdot (r/r_B)^{1/n}\}, \quad (4.5)$$

where n is a new parameter to fit and b_n is defined by:

$$\Gamma(2n) = 2\gamma(2n, b_n), \quad (4.6)$$

where Γ is the (complete) gamma function, and $\gamma(2n, x)$ is the incomplete gamma function defined by

$$\gamma(2n, x) = \int_0^x e^{-t} t^{2n-1} dt. \quad (4.7)$$

In Fig. 4.5 different Sérsic profiles are shown, in order to compare the effect of changing the exponent (n). Common values of b_n are $b_1 = 1.678$ and $b_4 = 7.6692$. The most usual analytical expressions for b_n are $b_n = 1.9992 \cdot n - 0.3271$ for $0.5 < n < 10$, and $b_n = 2n - 1/3$ for $n \gtrsim 8$ (Graham, 2001; Graham and Driver, 2005). We use the first approximation given that in the infrared bands the typical values of n are between 0.5 and 4 (Balcells *et al.*, 2003; Hunt *et al.*, 2004; Grosbøl *et al.*, 2004; Kormendy and Kennicutt, 2004).

Bar

There are many galaxies classified as barred in our sample, and also approximately 2/3 of all spiral galaxies classified as non-barred look barred in the infrared (Kormendy and Kennicutt (2004), and references there in). Initially we did not take into account the bar, trying to skip the features produced by it, but the profiles fitted were too far from being considered good fits. Also, omitting a large bar in the decomposition, might overestimate the light attributed to the bulge as noted by Laurikainen *et al.* (2004) and Laurikainen *et al.* (2005). In order to model the bar, we include a second Sérsic's law in our model, introducing 3 new free parameters. There are other functions that describe a bar's profile, but the simplest is the Sersic's one (Freeman, 1966; Prieto *et al.*, 1997; Laurikainen *et al.*, 2005).

Final Model

The final model is the addition of the 3 or 4 components convolved (using Fast Fourier Transform) with the PSF in order to introduce the effect of the seeing:

$$\Sigma(r) = \left[\sigma_n \delta(r) + \sigma_d e^{-\frac{r}{r_d}} + \sigma_B e^{-b_{nB} \left(\frac{r}{r_B}\right)^{1/n_B}} + \sigma_b e^{-b_{nb} \left(\frac{r}{r_b}\right)^{1/n_b}} \right] \otimes PSF(r) \quad (4.8)$$

4.2.1 The PSF

In order to determine the correct parameters that fit the galaxy profile we need a precise representation of the Point Spread Function (PSF) describing the seeing and instrument response of each particular observation. In our near-infrared imaging the PSF is very accurate because it is obtained from a star found in the galaxy frame, which ensures that the galaxy suffers the same distortion as the star. In the mid-infrared imaging instead, the star is observed before and/or after the galaxy and, as the integration is quite long at these wavelengths, the seeing conditions might change significantly, and therefore the PSF we obtain might not describe the same distortions affecting the galaxy.

We obtain the PSF radial profile using the same technique that we used to obtain the galaxy profile (section 4.1.2). Subsequently we modeled this PSF profile using a Moffat function, in order to have a fine enough discretization to fit the galaxy profile more accurately. The Moffat function is similar to a Gaussian, but it fits better the effects of seeing because of its more extended tails, as shown in Fig. 4.5. The Moffat functional expression is:

$$Moff(r) = \frac{peak}{(1 + (r/a)^2)^b} . \quad (4.9)$$

4.2.2 The Fitting Routine

In order to obtain the emission coming from the nucleus, i.e., to achieve a separation of the nuclear emission from the galaxy, we fit the radial SBP using the model described above. The fitting routine uses the “Downhill Simplex Method in Multidimensions” described in Press (1993) and references there in. A *simplex* is the geometrical figure consisting, in N dimensions, of $N + 1$ points (or vertices) and all their interconnecting line segments, polygonal faces, etc. For example, in two dimensions a simplex is a triangle. The minimization process starts with an initial guess ($N + 1$ points defining an initial simplex) given by the user. The algorithm takes a series of steps consisting in contracting, expanding or reflecting the simplex in the point where the function being minimized has its highest value,

until it reaches the termination criteria (at a minimum local, at least) which is, typically, a small variation between one step and the next.

As the algorithm does not assure us that the minimum found is the global minimum, we start the minimization from 4 or 5 extreme different points: the first initial guess includes all the galactic components of the model with a comparable contribution to the total flux. The other initial points have one of the galactic components with zero contribution to the total emission. We also include an iterative process that randomly perturbs the initial point a certain amount of times: tests of the results obtained with different amounts of iterations indicated that 200 iterations was enough to find the global minimum. The model that globally minimizes the χ^2 is the best fitted model, and the percentage contributions of the galactic components are obtained from this particular model and shown in Table 4.2.

The “Downhill Simplex Method” requires only function evaluations, not derivatives, which means that this method is very robust compared to the 2-D GALFIT routine 4.1.1. The problem is that it is not very efficient in terms of the number of function evaluations that it requires, working slowly when a large number of minimizations are necessary, which is not our case.

4.2.3 Errors in the fitted components

The determination of the flux of each fitted component has two main sources of uncertainty: the first coming from the flux calibration (the zero points) and the second coming from the fitting process. The calibration procedure was explained in detail in Section 3.2.4 and the expression for the uncertainty is given in Eqn. 3.4. The confidence limits for the fitted parameters, determined using the fitting routine described previously, are calculated using Montecarlo simulations: the best fitting parameters are perturbed (one at a time) to construct many synthetic data sets. Each of these synthetic data sets has a particular χ_{syn}^2 value, and the first confidence level (corresponding to 1σ error), which occurs 68.3%

of the times, corresponds to all the cases where $\Delta\chi^2 = \chi_{min}^2 - \chi_{syn}^2 \leq 1$. This is a simplification of the real confidence levels because the parameters are not independent, so the confidence levels should be calculated as the projection of the region in a 9-dimension space with $\Delta\chi^2 \leq 1$ into each parameter axis. This calculation is beyond our abilities. The uncertainties in the percentage contribution of each galactic component are computed as the subtraction between the calculated percentage contribution and the maximum or minimum possible contribution. The maximum possible contribution of the bulge, for example, is that of a bulge described by the upper limits of the Σ_B , r_B and n_B , and the minimum contribution is that from a bulge described by the lower limits of the parameters.

4.2.4 Synthetic Data

In order to test our fitting routine we used synthetic data. We constructed SBPs of different “kind” of galaxies: including all the components, with very small or very large contributions, without one or more components, with wrong PSFs, and with different sampling steps (for the galaxy and the PSF star).

The first test was to recover the parameters of the synthetic SBP. We found that our routine gives excellent estimations of the parameters for galaxies composed by 3 or 4 structures with non-negligible contribution to the total emission. In cases when one or more components were not present, the results were also good. Observed examples are all the non-barred galaxies, or a couple of cases where nor disk nor bar is observed. It is important to notice that the first guesses for the presence of the different components are not blind, but instead are based on the morphology seen in the images. Including all the 4 components might give a better χ^2 , because there will be more free parameters, but if the image does not show a bar, for example, it is obvious that it should not be included in the fit.

Then we tested how a change in the PSF (meaning using the wrong PSF to describe the seeing conditions) affects the results. In the cases when we used

a PSF better than the real one (with a narrower FWHM), the results obtained were poor. In the cases where the PSF was worse than real (a broader FWHM), the estimations were pretty good. These tests apply especially to the mid-IR observations: as the integration time is long, the probability of a change in the seeing conditions between the observation of the PSF star and the galaxy is greater.

The truncation of the galaxy profile affects severely the performance of the fitting routine. Fortunately we have very few of these cases, and normally affecting only one of the broad-band images, which means that we could check the results with the profiles not affected and constrain the parameters to have similar values to the non-truncated profiles.

Finally, we find that the sampling step is not so important, providing the PSF is sampled by a finer discretization than the sampling of the galaxy.

4.3 Messier 31

In order to test some of the findings from our SBP fitting procedure we studied Messier 31, the Andromeda galaxy, in the same way that we investigate the objects in our sample.

Images of M31 were taken by IRAC as part of the *Spitzer* General Observer program 3126 in August 2005. Barmby *et al.* (2006) measured the surface brightness profiles by fitting elliptical isophotes to the images using the ELLIPSE task. Profiles in the three longer-wavelength bands (at 4.5, 5.8, and 8.0 μm) were measured using the ellipses fitted to the 3.6 μm image, so that colors could be measured at the same spatial locations from all 4 bands. These profiles were kindly provided by Barmby *et al.* (2006).

Images in J, H, and K bands were obtained from the 2MASS public catalog ².

²This publication makes use of data products from the Two Micron All Sky Survey, which is a joint project of the University of Massachusetts and the Infrared Processing and Analysis Center/California Institute of Technology, funded by the National Aeronautics and Space

The profiles were constructed using ELLIPSE, in the same way we did it for our data. However, M31 is so close to us that the 2MASS images do not cover all the extent of the galaxy: while *Spitzer*-IRAC covers $\gtrsim 4000''$ in radius, the images of 2MASS cover only $\sim 500''$. This had to be considered in the fitting process, which is shown in Fig. 4.3.

Our expectations are that unless there are strong color gradients within each of the structural components of the galaxies (namely, the bulge, disk and/or bar), the scale lengths should remain fairly constant, while the brightness scale factor should decrease from the NIR to the MIR as the stellar populations become less luminous. Also, since the bulge has old stars it is redder than the disk and the bar, and therefore it is expected to be brighter in the mid-IR. Hence, we want to study the variation of the scale lengths fitted to M31 in the different bands, to confirm that they remain the same from the near- to the mid-IR. As can be seen from the images and profiles of galaxies in our sample, in the mid-IR the bulge of the host galaxy is weaker than in the near-IR and the disk is barely detectable. However, because M31 is one of the nearest galaxies, we can detect all the galaxy components in all the IR bands (leaving aside the size of the detectors, which affects the 2MASS images). We fitted the SBPs from $1.25\mu\text{m}$ to $5.8\mu\text{m}$, but did not use the $8.0\mu\text{m}$ SBP because it is dominated by the 10 Kpc ring and individual stellar features. Also, the $5.8\mu\text{m}$ SBP is truncated at $\sim 1300''$ to avoid the deformation produced by the 10 Kpc ring. The resulting fitted parameters are listed in Table 4.1.

It is very interesting to note the bright excess in the central part of the galaxy profiles. This excess is modeled as a bar in the IRAC bands and as a nucleus in the 2MASS bands (due to the difference in pixel scale). Peng (2002) studied in detail the central region of M31 using the *Hubble Space Telescope* (HST). They modeled the center of the galaxy using 6 components in order to account for 3 different peaks of emission in UV and optical images. However the UV peak disappears in the near-IR images and the 2 V-band peaks diminish. So we assume

Administration and the National Science Foundation.

that the nucleus/bar fitted by our process is real, but the pixel scale does not allow a more detailed modeling.

As the disk could not be fitted in the 2MASS profiles, we can compare only the fitted effective radius of the bulge, which is 700 pc in the J band, 862 pc in the H band, 787 pc in the K band, 1140 pc at $3.6\mu\text{m}$, 983 pc at $4.5\mu\text{m}$, and 795 pc at $5.8\mu\text{m}$. The dispersion of these values respect to the mean is between 20 and 30%, and they show that moving toward longer wavelengths does not change the scale length of the galactic structures significantly. Based on this, we can use the scale lengths values fitted in the near-IR to constrain the scale lengths in the mid-IR fits of our sample, where the lower spatial resolution and the weakness of the stellar components might introduce significant degeneracy during the fitting process.

4.4 Galaxy Fitting Results

We found that fitted parameters are generally consistent between observing bands. Although it is not our goal, here we show a brief summary of the fitted parameters. We found a mean nuclear contribution of 8.71% with a standard deviation of 14.58 in the near-IR bands (JHK), and of 47.8% with standard deviation of 30.65 in the longer wavelengths bands (LMN). There are 7 of 105 near-IR fits with null nuclear contribution in the near-IR. The percentage contribution of each component to each galaxy is shown in Table 4.2, the mean percentage contribution is listed in Table 4.3, and the distribution of the fitted nuclear contribution is compared, as a consistency check, with the bulge, bar and disk contributions in Fig. 4.5.

The fitted parameters for the galaxies deconvolved are tabulated in Tables 4.4-4.8, with 2 exceptions: the N band fitting of NGC 6810, which has $\Sigma_{nuc} = 1.24\text{e-}13 \text{ Watts/m}^2/\mu/[\prime]^2$, $\Sigma_{Bul} = 5.04\text{e-}15 \text{ Watts/m}^2/\mu/[\prime]^2$, $r_{eff}^{Bul} = 162.64 \text{ pc}$, and $n_{Bul} = 1.09$, and is the only extended galaxy in the N band. The other exception is MCG -2-40-4, which is the only object with a fitted bar in the L band, with

values of $\Sigma_{bar} = 6.64e-17$ Watts/m²/μ/[″]², $r_{bar} = 2103.41$ pc, and $n_{bar} = 0.65$. The mean, median and standard deviation of the parameters are listed in the 3 lowest rows of each table, and a comparison between the most relevant parameters is shown in Fig. 4.5, in order to check that no correlation is found between them.

In what follows we give details of individual objects. In the mid-IR profiles of all the galaxies we show the fitting result in 2 different scales, the smaller one (left side) showing the central part of the galaxy (mid-IR scale) and the near-IR one (right side), where all the galaxy should be observable.

NGC 34

In this object it is evident how the disk becomes weaker compared to the bulge and nucleus from the J to the L bands. The disk in L band had to be constrained to have similar scale length than in J, H and K bands. In the M-band the disk is not visible, but the bulge maintains its importance. Here we had to restrict the bulge effective radius to have similar values to the other wavelengths. The fits are shown in Fig. 4.6.

IRAS 00198-7926

The near-IR image of this galaxy has 2 objects very close, and it is very difficult to determine which of the two is the Seyfert galaxy, and if the other object is another galaxy or a star. We perform elliptical photometry to the 2 objects in each band. The northern object seems to be the Seyfert galaxy. The fitting results are shown in Fig. 4.7. The southern object has a strange behavior, the effective radius and the exponent of the Sersic's law of the bulge continuously decreases from J to K, as evident in the galaxy fitting procedure (Fig. 4.8). Only one object is detected in the L band image, and it is included in both SEDs (north and south) because it is impossible to determine its correspondence with any of the 2 near-IR objects. Also, the L-band observations seem to suffer from seeing variation, as can be inferred from the fitting results: constraining

the parameters of the bulge to be similar to the near-IR values (we choose the northern values, due to the variable values of the southern bulge) produces a very poorly fitted model. As a result, we considered all the emission observed in this band as coming from the nucleus.

IRAS 00521-7054

This galaxy is classified as an E-S0 and the fits confirm this: in order to obtain a good fit, we needed to exclude the disk component. Because the seeing changed between the observation of the PSF star and the galaxy in the L band, we considered only the external parts of the observed profile to fit the bulge (using the values found in the near-infrared bands) and the nuclear flux was obtained using $F_{nuc} = F_{gal} - F_{bul}$. In Fig. 4.9 we show the fit to the surface brightness profile in each band.

ESO 541-IG12

This is a very “text-book” active galaxy, in spite of being a multiple system. However, in the L-band the Sérsic’s index was constrained to the value obtained in the near-IR fits, and in the M-band the effective radius of the bulge also was constrained to the values obtained in the near-IR and the L-band. The fitting results are shown in Fig. 4.10.

NGC 424

The near-IR observations have no zero point and the mid-IR observations have no PSF star. Therefore this galaxy has no useful data.

IRAS 01475-0740

In order to obtain a reasonable fit to the near-IR profiles the scale length of the disk was constrained to be larger than the effective radius of the bulge. In the

L band, the size and index of the bulge were restricted to have similar values to those found in near-IR fits. In Fig. 4.11 we plot the fits in the different bands.

NGC 1125

This galaxy could only be observed in the L and M bands. The disk and bulge parameters can not be restricted and the degeneration is too high. This galaxy had to be discarded.

NGC 1143/4

This is an interacting system and the disk of the Seyfert is very distorted. Comparing the J, H, and K band images, it is evident that the K band is less contaminated by the tidal tails, giving a good idea of the real parameters of the disk. Using these values to constrain the disk parameters in the J and H bands, the fitting results are consistent in all 3 bands. The fitting results are plotted in Fig. 4.12, being evident the emission excess observable in the outer parts of the galaxy in the J and H bands, excess coming from the stream of material. In the L band the 3 components are discernible, and the parameters are consistent with the near-IR ones only imposing that the disk size were larger than the bulge size. The galaxy is point-like in the M band, so all the emission is considered as nuclear and no fitting is needed.

MCG -2-8-39

This is a very good example of a barred galaxy. The near-IR fits were obtained without any restriction, and the results are consistent. The L band profile was fitted without disk nor bar due to the strong dominance of the bulge in the central region of the galaxy, and the size and index of the bulge had to be constrained using the near-IR values. The fitting results are shown in Fig. 4.13.

NGC 1194

This galaxy has a very extended bulge ($n_B \approx 3.3$). The results were obtained constraining the index value of the K band profile to that found in the J and H band fits. The results are shown in Fig. 4.14.

NGC 1320

This galaxy was fitted limiting the effective radius of the bulge in the K band. The final fits are shown in Fig. 4.15.

IRAS 03362-1642

The fit of this galaxy does not include a nuclear component in the H and K bands. In the J band a weak nucleus is included, with a contribution of 0.65%, which is negligible. The bar is very dominant in all 3 bands. Fig. 4.16 shows the resulting fits.

IRAS 04385-0828

To fit this galaxy it was needed to constrain the bulge Sérsic's index in the J and H bands to that found in the K band because of a distortion of the profiles. The results are shown in Fig. 4.17.

NGC 1667

This galaxy has a very complex morphology, which prevents us to obtain a reliable profile fitting in the 3 bands we observed. These observations were discarded.

ESO 33-G2

To fit this galaxy no restriction was needed in J and H band. In K band the disk scale length was constrained to be larger than the bulge and bar sizes, obtaining consistent results for all the parameters. The fits are shown in Fig. 4.18.

IRAS 05189-2524

In order to obtain a consistent fit to this galaxy, the disk size in the H band was constrained to be larger than the bulge size. In the K band, the first point of the radial profile is lower than the second and third points. This is due to obscuration that can be observed directly in the image, as shown in Fig. 4.19. Therefore this first point is not included in the fitting process. In the N-band profile all the emission comes from the nucleus. The results are plotted in Fig. 4.20.

ESO 253-G3

This object is an interacting system of 2 galaxies and the 2 nuclei are too close to obtain a good modeling of the 2 separated galaxies. These observations were discarded.

MCG +0-29-23

In Fig. 4.21 the fitting results of this very special object are shown. The results barely change from one band to another, and the galaxy looks very extended in the L band. The bulge looks more like a bar than a bulge, both in the images and the Sérsic's index value fitted to this component. In any case, bulge or bar, we are able to determine its contribution to the central emission, even if we are not able to unveil the nature of all the galactic components.

NGC 3660

This galaxy is very large, and due to the small size of the detector the galaxy has been truncated in the J and H bands. In order to determine the real value of the disk parameters we used the K band image and then used these fitted values to constrain the disk parameters values in the J and H band profiles fits, excluding the profile for $r > 45''$. In the L band profile, we skipped the profile for $r > 2''$

because it is mostly sky contribution. We restricted the parameters of the bulge to those obtained in the J, H and K fits. The results are shown in Fig. 4.22.

NGC 4501

This is a huge galaxy compared to the detector. For that reason the flux standard star was used as a PSF star. The only restriction needed to obtain consistent results was that the disk size were larger than the bulge size in the J and H bands. In the L band the change in seeing conditions is evident, and to overcome this problem the bulge was fitted for $r > 3''$, constraining only the Sérsic's index. The nucleus is computed as $F_{nuc} = F_{gal} - F_{bul}$. The galaxy was not detected in the M band. The fitting results are shown in Fig. 4.23.

TOL 1238-364

The fit to this galaxy in the near-IR bands does not include the bump produced by the ending of the flocculent arms (between $16''$ and $23''$). In the J and H bands was needed to impose a disk scale length larger than the bulge size. In the K band the bulge index was constrained to have similar values to those found in the J and H bands. In the L and M bands the bulge and disk parameters were constrained to the values found in the near infrared fits. It seems that seeing conditions changed between the observations in the M band, since the PSF star was not able to fit the nucleus. In this case, as in others, the bulge was fitted and the difference between the galaxy and the bulge was considered as the nucleus. All the results can be seeing in Fig. 4.24.

NGC 4941

This is another very big galaxy, which means that the PSF is not contained in the galaxy frame but comes from the star observed to obtain the calibration in flux. In this case, it seems that the standard star is not a good approximation of the PSF, resulting in a null detection of a nucleus in the 3 near-IR band fits.

However, the galaxy was not detected in both L and M bands, so it may also be that this galaxy has no near- and mid-IR emission associated to the active nucleus. Fitting plots can be found in Fig. 4.25.

MCG -3-34-64

In Fig. 4.26 the results of the fitting process of this barred galaxy are shown. Without special constraints, the near-IR fitted parameters are found to be consistent. In the L and M band the seeing between the observation of the galaxy and the observation of the PSF star seems to vary, resulting in a poor fitting in the L band. In order to fit both profiles, the bulge was fitted with the values found in the near-IR fits and the nuclear contribution was calculated as $F_{nuc} = F_{gal} - F_{bul}$.

NGC 5135

The bar of this galaxy is very strong, and the disk is not seen in the IR images. Between 1'' and 3'' there is a strong star-forming region, dominating the profile at all wavelengths. As we are not interested in these local enhancements we exclude these region from the fit in all the profiles. In Fig. 4.27 we show the fitting results including a close-up of the central region in the K band profile, in order to visualize the expected contributions in the mid-IR scale. The galaxy profile in the M band looks slightly broader than the PSF star, but the bulge component is not able to account for it, so we assume it is produced by a change in the seeing conditions. The nuclear flux is computed though the integration of the galaxy profile for $r \leq 1''$.

NGC 5953

In this case, we exclude the bump observed near $r=6''$ because it is produced by the ending of the flocculent arms of the galaxy. In the L band, the seeing is worse in the observation of the galaxy, compared to that of the PSF star, as can be seen in Fig. 4.28. In this case, we used the results of the J, H and K band fits

to fix the values of the bulge parameters, and estimated the flux of the nucleus as $F_{nuc} = F_{gal} - F_{bul}$.

MCG -2-40-4

This is a very hell behaved barred galaxy. In Fig. 4.29(d) a close-up of the central region of K-band profile is shown, in order to visualize the expected contributions to the profile at the mid-IR scale. Based on this, we find that the bar and the disk are indistinguishable from each for $r \gtrsim 2''$ other, so the fitted component at L-band is a mixture of both structures. The bulge parameters in this band were constrained to the values found in the near-IR fits in order to reliably separate it from the mixed bar-disk component. The M band profile was fitted with the bulge effective radius and Sérsic's index constrained to the values found in the near-IR fits.

IRAS 15480-0344

Barely no restriction was needed to obtain good fitting in near-IR bands. In the L band only a nucleus and a bulge were fitted, and the index of the Sérsic's law was limited by the values found in the near infrared bands. The fitting results can be found in Fig. 4.30.

IRAS 19254-7245

This is an interacting system with the 2 nuclei too close to be able to fit 2 separate galaxies reliably. These data were discarded for this work.

NGC 6810

To obtain a good fit for this galaxy, we do not consider the bumps in the radial profile, because they are produced by 2 large star forming regions. In the L band, one can infer from the narrowness of the nuclear profile that the seeing was better in the observation of the PSF star than in the observation of the galaxy. It is

impossible for the bulge to account for the difference at $r \lesssim 0.5''$. For $r \gtrsim 5''$, a plateau in the galaxy profile appears (in the close-up of K band, Fig. 4.31(d)), due to the 2 star forming regions. Hence, this part of the profile is not included in the fitting process. In the M band it is very clear that the seeing was worse in the observation of the galaxy than in the observation of the PSF star. In this case, we used fixed values for the bulge parameters, similar to the values found at shorter wavelengths, and the nuclear flux was estimated as $F_{nuc} = F_{gal} - F_{bul}$. The extended emission of this galaxy in the N band is an exceptional case, as can be seen in the profile, although there is also a change in seeing conditions. The bulge can be fitted pretty well constraining the values of the parameters to that found in the near-IR and the nucleus can be computed using $F_{nuc} = F_{gal} - F_{bul}$.

NGC 6890

To fit this galaxy we exclude from the fitting the bumps at $r \approx 15''$ and $r \approx 30''$, because they correspond to the ending of the flocculent arms. In the L band, the signal beyond $r \approx 4''$ is sky and it is not fitted. The galaxy in the M and N bands is considered pointlike, so no fit is performed. The fitting results are shown in Fig. 4.32.

IC 5063

This galaxy is classified as SA0, however the best fit found for the profile of this galaxy does not include a disk component, but only a bulge and a nucleus, which gets stronger from shorter to longer wavelengths. In the L band we restricted the values of the parameters of the bulge to be close to the values found in the JHK fits. In the M band a change in seeing is evident, causing the PSF star to be sharper and narrower than the galaxy. The bulge parameters were frozen and only the nucleus was allowed to vary. The results are shown in Fig. 4.33. The galaxy is point-like in the N band, so no fit is needed.

MRK 897

In the L band image the object fell too close to the border of the image, and it was not possible to obtain a more extended profile in order to determine accurately the bulge contribution. Therefore we restricted the bulge parameters to have values similar to the JHK ones. Results are shown in Fig. 4.34.

NGC 7130

The only restriction needed to fit the near-IR bands was that the disk scale length had to be larger than the bulge effective radius. In the L band it seems that the seeing varied between the observations of the galaxy and the PSF star. In order to obtain a reliable nuclear flux, we fit the bulge component between 2'' and 4'' and constrain the parameters to be as more close as possible to the JHK values. However, as the fit to the galaxy is not adequate (mainly the first point), the nuclear flux is estimated as $F_{nuc} = F_{gal} - F_{bul}$. In the M band, the galaxy looks almost point-like so no fit is needed. The fits are shown in Fig. 4.35.

MCG -3-58-7

This galaxy was fitted with all 4 components, as can be seen in Fig. 4.36. The disk size in the K band image was constrained to be larger than the bulge size. In the L band, only a nucleus and a bulge were included, and the index of the bulge was constrained to have a value similar to those obtained at shorter wavelengths.

NGC 7496

In the fitting process of this galaxy, the K band bulge index had to be restricted to the values of the J and H bands. Also, the disk scale length was restricted to be larger than the bulge effective radius. In the L band, only a bulge and a nucleus were included, and the bulge size had to be limited to the values found in the near infrared bands. In the M band a nucleus+bulge model was also used,

with the size and index of the bulge component constrained by the values found at shorter wavelengths. In Fig. 4.37 are the fitting results.

NGC 7582

Our near-IR images show a prominent galaxy and two very weak arms, going out from the central region at a seemingly different inclination angle. In the literature we found that this galaxy has been characterized by an inclination angle of ~ 60 degrees (Morris *et al.*, 1985), corresponding to a disk traced by the very weak arms. The galaxy has a strong star-forming region near the nucleus, also observable in X-rays (Bianchi *et al.*, 2007), and therefore this region near $r \approx 2.5''$ was not included in the fitting process. In Fig. 4.38 are shown the fit results.

NGC 7590

This is a very special case. We observed this galaxy twice in the near-IR, once in service mode and once in visitor mode (the main difference between the two is the pixel scale) with the Sofi detector. Both fitting processes yield consistent results. The point source detected in the near-IR bands contributes at most 0.3% to the total flux. In the L band, no point source was detected, and we postulate that the reason is not a variation in the seeing conditions, but because this galaxy has a very weak AGN. The galaxy was not detected in the M band. The corresponding galaxy fitting results are shown in Fig. 4.39. In Fig. 4.40 the surface brightness profiles of the galaxy and its corresponding PSF star are compared. It is evident that the galaxy is an extended object, without a point source dominating the central region. Besides, after the subtraction of the star forming component (see next section), the *Spitzer*-IRS spectra of NGC 7590 shows no continuum or spectral features attributable to an AGN (Fig. 4.45, last part, bottom-right panel).

CGCG 381-051

This object was not detected in the L and M bands. In the J, H and K bands the fit did not include the region between $r \approx 15''$ and $r \approx 20''$, which correspond to the ending of the galactic arms. In the K band fitting, it was necessary to constrain the index bulge using the value of the H band. In the J band, it was necessary to constrain the value of the bulge size, using the value found in the H band. Although the bulge is small it can be distinguished from the bar in all the images. The fitting results are shown in Fig. 4.41.

4.5 Cleaning the *Spitzer*-IRS Spectra

As the large aperture of *Spitzer*-IRS may include extended emission coming from star formation located close to the nucleus, the spectra of each galaxy should be cleaned before including it into the nuclear SED. The presence of polycyclic aromatic hydrocarbons (PAH), which dominate the mid-IR spectra of star forming regions, allows us to isolate the AGN emission.

Smith *et al.* (2007) used low-resolution *Spitzer*-IRS spectra of a sample of nearby galaxies spanning a large range in star formation properties, to construct 4 templates in order to account for the differences of the PAH feature strengths. Each template corresponds to the mean of the spectra of galaxies located in each quadrant of Fig. 4.42, and are drawn in Fig. 4.43.

In order to get rid of the star formation contaminating the mid-IR spectra of each galaxy, we subtracted the 4 templates described above. Each template was scaled independently by a factor ensuring the disappearance of the PAH features but no oversubtracting the continuum. As can be seen in Fig. 4.43, since the templates differ the most for $\lambda > 20\mu\text{m}$, we decided to exclude this region during the torus emission model fitting of the SEDs because of our inability to determine which template best describes the continuum emission for each particular galaxy for wavelengths longer than $20\mu\text{m}$.

In Fig. 4.5 we show 2 extreme examples of the subtraction process. The first resulting spectra has no PAH features, while the second shows strong PAH residuals. Also, it can be seen that the main differences between the templates start at $\lambda \approx 20\mu\text{m}$. In Fig. 4.45 we show all the resulting spectra, including one case where no subtraction of a star forming template was needed (MCG -2-8-39).

Table 4.1: Values of the relevant fitted parameters in the M31 deconvolution process in each band. The scale lengths are expressed in arcseconds. The bright excess in the central part of the galaxy profiles is modeled as a bar in the IRAC bands and as a nuclear component in the 2MASS bands (due to the differences in pixel scale). The disk is not included in the 2MASS fits because of the covering. See text for details.

Parameter	1.25 μm	1.65 μm	2.20 μm	3.6 μm	4.5 μm	5.8 μm
r_{eff}^{bul}	206.779	227.885	184.575	301.3	258.6	209.28
n_{bul}	2.189	2.276	2.039	2.502	2.355	2.157
r_{disk}	–	–	–	10.735	12.671	26.734
r_{eff}^{bar}	–	–	–	1.150	1.242	0.571
n_{bar}	–	–	–	0.572	0.489	1.222

Table 4.2: Percentage contribution of each galactic component fitted to the surface brightness profile of each galaxy in each band of observation.

Galaxy	Band	Nucleus %	Bulge %	Disk %	Bar %
NGC 34	J	$7.30^{+1.0}_{-1.0}$	$25.46^{+0.9}_{-1.0}$	$67.25^{+2.6}_{-2.5}$	–
	H	$11.43^{+0.4}_{-0.4}$	$25.65^{+0.3}_{-0.4}$	$62.92^{+2.7}_{-2.6}$	–
	K	$18.74^{+2.4}_{-2.4}$	$32.53^{+1.3}_{-1.4}$	$48.73^{+2.4}_{-2.3}$	–
	L	$7.73^{+0.8}_{-0.8}$	$52.83^{+2.1}_{-2.2}$	$39.44^{+9.4}_{-11.5}$	–
	M	$14.44^{+1.1}_{-0.6}$	$85.56^{+6.2}_{-8.2}$	–	–
IRAS 00198-7926	J N	$9.99^{+0.4}_{-0.3}$	$13.75^{+2.1}_{-2.4}$	$76.26^{+22.6}_{-19.7}$	–
	H N	$9.68^{+0.8}_{-0.8}$	$19.31^{+4.3}_{-4.8}$	$71.01^{+37.7}_{-29.8}$	–
	K N	$13.05^{+1.2}_{-1.1}$	$14.00^{+4.0}_{-4.2}$	$72.95^{+40.7}_{-31.7}$	–
	J S	$2.75^{+0.1}_{-0.1}$	$23.17^{+2.5}_{-2.3}$	$74.08^{+13.1}_{-10.6}$	–
	H S	$9.03^{+1.1}_{-1.1}$	$17.65^{+3.7}_{-4.0}$	$73.32^{+20.6}_{-19.0}$	–
	K S	$36.99^{+3.7}_{-3.7}$	$9.11^{+2.9}_{-3.1}$	$53.90^{+16.8}_{-14.3}$	–
	L	$43.83^{+0.3}_{-0.3}$	$56.17^{+12.6}_{-15.4}$	–	–
M	$100.00^{+5.4}_{-5.0}$	–	–	–	
IRAS 00521-7054	J	$63.99^{+2.1}_{-2.2}$	$36.01^{+2.6}_{-2.7}$	–	–
	H	$59.21^{+2.2}_{-2.1}$	$40.79^{+2.8}_{-3.1}$	–	–
	K	$78.49^{+9.0}_{-9.0}$	$21.51^{+1.9}_{-2.1}$	–	–
	L	$0.33^{+1.5}_{-1.3}$	$99.67^{+1947.0}_{-1795.9}$	–	–
ESO 541-IG12	J	$24.28^{+2.4}_{-2.4}$	$43.36^{+1.7}_{-2.0}$	$32.36^{+5.9}_{-5.4}$	–
	H	$44.40^{+4.4}_{-4.4}$	$35.37^{+1.2}_{-1.2}$	$20.23^{+4.1}_{-3.7}$	–
	K	$61.90^{+7.8}_{-7.7}$	$26.70^{+0.9}_{-0.9}$	$11.41^{+2.7}_{-2.4}$	–
	L	$87.81^{+9.1}_{-9.1}$	$12.19^{+1.2}_{-2.1}$	–	–
	M	$76.06^{+6.3}_{-6.2}$	$23.94^{+1.7}_{-17.5}$	–	–
IRAS 01475-0740	J	$15.24^{+0.5}_{-0.5}$	$45.83^{+1.3}_{-1.4}$	$38.93^{+6.1}_{-5.5}$	–
	H	$17.58^{+0.6}_{-0.6}$	$47.59^{+1.6}_{-1.5}$	$34.84^{+7.2}_{-6.4}$	–
	K	$29.97^{+3.8}_{-3.8}$	$40.24^{+2.2}_{-2.4}$	$29.79^{+8.6}_{-7.3}$	–
	L	$74.99^{+7.9}_{-7.8}$	$25.01^{+4.1}_{-11.8}$	–	–

Continued on Next Page...

Table 4.2 – Continued

Galaxy	Band	Nucleus %	Bulge %	Disk %	Bar %
NGC 1144	J	$0.75^{+0.2}_{-0.2}$	$5.91^{+0.5}_{-0.6}$	$93.33^{+16.9}_{-7.5}$	$0.00^{+0.0}_{-0.0}$
	H	$0.61^{+0.2}_{-0.2}$	$6.67^{+0.4}_{-0.5}$	$92.72^{+10.1}_{-0.5}$	–
	K	$1.20^{+0.2}_{-0.2}$	$7.25^{+0.7}_{-0.9}$	$91.55^{+7.2}_{-6.8}$	–
	L	$23.97^{+0.4}_{-0.4}$	$15.46^{+1.5}_{-1.7}$	$60.57^{+12.8}_{-11.3}$	–
MCG -2-8-39	J	$0.75^{+0.4}_{-0.4}$	$31.18^{+1.7}_{-1.7}$	$45.33^{+10.7}_{-9.5}$	$22.74^{+2.4}_{-6.1}$
	H	$0.78^{+0.8}_{-0.8}$	$20.81^{+3.6}_{-7.4}$	$37.50^{+15.5}_{-12.9}$	$40.91^{+2.9}_{-3.2}$
	K	$0.84^{+1.9}_{-0.8}$	$39.39^{+2.8}_{-3.3}$	$40.72^{+15.5}_{-13.0}$	$19.05^{+4.3}_{-7.3}$
	L	$37.98^{+2.5}_{-2.4}$	$62.02^{+0.5}_{-22.7}$	–	–
NGC 1194	J	$0.06^{+0.3}_{-0.1}$	$79.66^{+1.0}_{-1.3}$	$20.27^{+2.4}_{-2.5}$	–
	H	$0.39^{+0.4}_{-0.4}$	$74.47^{+1.0}_{-1.2}$	$25.14^{+3.3}_{-2.9}$	–
	K	$2.97^{+2.0}_{-2.0}$	$73.57^{+1.7}_{-2.0}$	$23.46^{+4.4}_{-4.3}$	–
NGC 1320	J	$0.45^{+0.2}_{-0.2}$	$51.84^{+1.9}_{-2.1}$	$47.70^{+5.8}_{-5.4}$	–
	H	$1.01^{+1.1}_{-1.0}$	$48.05^{+3.2}_{-3.7}$	$50.94^{+7.0}_{-6.6}$	–
	K	$3.64^{+2.2}_{-2.2}$	$59.72^{+2.3}_{-2.3}$	$36.64^{+8.3}_{-7.4}$	–
IRAS 04385-0828	J	$2.66^{+1.1}_{-1.1}$	$17.17^{+1.2}_{-1.7}$	$80.17^{+3.9}_{-3.8}$	–
	H	$9.07^{+1.2}_{-1.2}$	$17.96^{+1.2}_{-1.5}$	$72.97^{+4.7}_{-4.5}$	–
	K	$23.58^{+7.6}_{-7.6}$	$18.31^{+1.5}_{-2.3}$	$58.11^{+4.2}_{-4.1}$	–
ESO 33-G2	J	$1.43^{+1.2}_{-1.2}$	$50.44^{+1.8}_{-1.5}$	$36.86^{+4.8}_{-4.5}$	$11.28^{+1.1}_{-1.7}$
	H	$3.92^{+1.2}_{-1.2}$	$42.67^{+2.1}_{-2.3}$	$43.59^{+10.7}_{-9.5}$	$9.82^{+1.2}_{-2.0}$
	K	$10.10^{+2.0}_{-2.0}$	$46.63^{+1.9}_{-2.1}$	$33.97^{+12.7}_{-10.5}$	$9.30^{+1.3}_{-1.9}$
IRAS 05189-2524	J	$13.96^{+6.9}_{-6.8}$	$39.78^{+1.2}_{-1.6}$	$46.25^{+3.0}_{-3.0}$	–
	H	$36.23^{+13.6}_{-13.6}$	$31.73^{+1.3}_{-1.8}$	$32.03^{+2.9}_{-3.0}$	–
	K	$22.49^{+14.3}_{-3.4}$	$53.31^{+6.2}_{-1.0}$	$24.20^{+0.5}_{-4.7}$	–
MCG +0-29-23	J	$1.61^{+0.3}_{-0.3}$	$29.14^{+1.6}_{-1.7}$	$69.25^{+1.7}_{-1.6}$	$0.00^{+0.0}_{-0.0}$
	H	$1.50^{+0.4}_{-0.4}$	$31.33^{+1.2}_{-1.4}$	$67.16^{+1.9}_{-1.8}$	–
	K	$2.40^{+0.1}_{-0.1}$	$35.28^{+0.7}_{-0.7}$	$62.32^{+4.1}_{-3.9}$	–
	L	$13.30^{+1.7}_{-1.7}$	$51.25^{+3.6}_{-3.8}$	$35.45^{+16.8}_{-13.8}$	–
NGC 3660	J	$1.16^{+0.1}_{-0.1}$	$13.41^{+0.2}_{-0.2}$	$55.71^{+1.7}_{-1.7}$	$29.73^{+0.5}_{-0.6}$
	H	$1.31^{+0.2}_{-0.2}$	$15.19^{+0.3}_{-0.3}$	$51.89^{+2.5}_{-2.3}$	$31.61^{+0.6}_{-0.7}$
	K	$1.68^{+0.3}_{-0.3}$	$15.66^{+1.1}_{-1.2}$	$60.41^{+8.6}_{-8.0}$	$22.26^{+6.6}_{-12.5}$
	L	$28.34^{+1.3}_{-1.3}$	$71.66^{+4.4}_{-11.5}$	–	–

Continued on Next Page...

Table 4.2 – Continued

Galaxy	Band	Nucleus %	Bulge %	Disk %	Bar %
NGC 4501	J	$0.91^{+0.2}_{-0.2}$	$11.37^{+0.4}_{-0.4}$	$87.72^{+1.0}_{-1.0}$	–
	H	$0.82^{+0.1}_{-0.1}$	$13.46^{+0.3}_{-0.3}$	$85.72^{+1.0}_{-1.0}$	–
	K	$0.85^{+0.1}_{-0.1}$	$13.38^{+0.3}_{-0.4}$	$85.76^{+1.5}_{-1.6}$	–
	L	$12.27^{+0.3}_{-0.3}$	$87.73^{+202.7}_{-189.7}$	–	–
TOL 1238-364	J	$2.36^{+0.3}_{-0.3}$	$23.69^{+0.7}_{-0.8}$	$73.94^{+2.0}_{-2.0}$	–
	H	$2.29^{+0.2}_{-0.2}$	$25.75^{+1.0}_{-1.0}$	$71.96^{+2.5}_{-2.4}$	–
	K	$3.13^{+0.6}_{-0.6}$	$28.70^{+1.3}_{-1.6}$	$68.17^{+7.7}_{-7.0}$	–
	L	$36.96^{+3.4}_{-3.6}$	$53.53^{+1.2}_{-9.1}$	$9.51^{+12.0}_{-6.5}$	–
	M	$56.28^{+1.3}_{-0.8}$	$43.72^{+631.5}_{-538.0}$	–	–
NGC 4941	J	–	$20.91^{+0.5}_{-0.5}$	$79.09^{+1.3}_{-1.2}$	–
	H	–	$20.73^{+0.4}_{-0.4}$	$79.27^{+1.7}_{-1.7}$	–
	K	–	$20.96^{+0.8}_{-0.8}$	$79.04^{+6.1}_{-5.9}$	–
MCG -3-34-64	J	$2.35^{+0.3}_{-0.3}$	$34.52^{+0.5}_{-0.6}$	$33.49^{+1.0}_{-1.0}$	$29.64^{+0.4}_{-0.4}$
	H	$1.76^{+0.7}_{-0.7}$	$27.45^{+0.5}_{-0.5}$	$35.10^{+1.7}_{-1.7}$	$35.69^{+0.6}_{-0.6}$
	K	$3.55^{+0.7}_{-0.7}$	$28.62^{+2.3}_{-2.3}$	$33.99^{+11.5}_{-9.8}$	$33.84^{+1.1}_{-1.2}$
	L	$41.70^{+1.4}_{-1.4}$	$58.30^{+1.5}_{-5.5}$	–	–
	M	$67.20^{+1.7}_{-1.6}$	$32.80^{+173.9}_{-130.8}$	–	–
NGC 5135	J	$0.14^{+0.2}_{-0.1}$	$47.77^{+0.8}_{-0.7}$	–	$52.09^{+0.8}_{-1.1}$
	H	$0.14^{+0.0}_{-0.0}$	$54.25^{+0.9}_{-1.1}$	–	$45.61^{+0.9}_{-0.9}$
	K	$1.60^{+0.6}_{-0.6}$	$59.55^{+10.0}_{-5.7}$	–	$38.85^{+16.8}_{-12.1}$
	L	$21.77^{+0.4}_{-0.4}$	$78.23^{+63.8}_{-50.8}$	–	–
	M	$100.00^{+2.2}_{-1.2}$	–	–	–
NGC 5953	J	$1.55^{+0.4}_{-0.4}$	$78.03^{+0.9}_{-0.6}$	$20.42^{+1.0}_{-1.0}$	–
	H	$2.00^{+0.1}_{-0.1}$	$79.07^{+0.5}_{-1.1}$	$18.93^{+1.4}_{-1.6}$	–
	K	$2.01^{+0.1}_{-0.1}$	$88.45^{+2.4}_{-2.3}$	$9.55^{+11.0}_{-6.7}$	–
	L	$4.05^{+0.2}_{-0.2}$	$95.95^{+95.9}_{-86.4}$	–	–
MCG -2-40-4	J	$6.20^{+2.1}_{-2.0}$	$18.75^{+0.8}_{-0.8}$	$60.10^{+1.1}_{-1.2}$	$14.95^{+0.8}_{-0.9}$
	H	$8.88^{+2.6}_{-2.6}$	$17.06^{+0.5}_{-0.6}$	$56.03^{+1.4}_{-1.4}$	$18.04^{+0.8}_{-1.0}$
	K	$20.14^{+5.6}_{-5.5}$	$18.15^{+0.9}_{-1.1}$	$45.57^{+3.8}_{-3.6}$	$16.15^{+0.8}_{-1.0}$
	L	$70.82^{+4.0}_{-3.9}$	$12.35^{+1.7}_{-1.3}$	–	$16.84^{+1.6}_{-1.9}$
	M	$70.36^{+6.1}_{-6.0}$	$29.64^{+23.8}_{-1.0}$	–	–

Continued on Next Page...

Table 4.2 – Continued

Galaxy	Band	Nucleus %	Bulge %	Disk %	Bar %
IRAS 15480-0344	J	$5.07^{+0.4}_{-0.4}$	$63.69^{+0.8}_{-0.8}$	$31.23^{+2.6}_{-2.4}$	–
	H	$6.08^{+1.8}_{-1.8}$	$52.53^{+0.9}_{-0.9}$	$41.39^{+3.7}_{-3.5}$	–
	K	$8.75^{+0.4}_{-0.4}$	$52.13^{+2.5}_{-2.5}$	$39.12^{+13.6}_{-11.5}$	–
	L	$58.86^{+1.7}_{-1.7}$	$41.14^{+7.8}_{-9.0}$	–	–
NGC 6810	J	$1.03^{+0.7}_{-0.7}$	$21.09^{+3.6}_{-4.8}$	$77.88^{+3.6}_{-3.6}$	–
	H	$0.78^{+3.0}_{-0.8}$	$23.12^{+2.9}_{-3.8}$	$76.10^{+3.5}_{-3.3}$	–
	K	$0.81^{+0.3}_{-0.3}$	$27.26^{+2.6}_{-3.2}$	$71.94^{+4.5}_{-4.3}$	–
	L	$3.20^{+0.3}_{-0.3}$	$96.80^{+1.1}_{-3.0}$	–	–
	M	$24.66^{+2.4}_{-2.1}$	$75.34^{+108.6}_{-88.1}$	–	–
	N	$39.4^{+1.8}_{-1.8}$	$60.6^{+33.8}_{-14.5}$	–	–
NGC 6890	J	$0.21^{+0.2}_{-0.2}$	$11.83^{+0.5}_{-0.6}$	$87.96^{+1.5}_{-1.8}$	–
	H	$0.24^{+0.3}_{-0.2}$	$14.65^{+0.5}_{-0.6}$	$85.11^{+1.8}_{-1.9}$	–
	K	$1.15^{+0.7}_{-0.7}$	$13.27^{+0.7}_{-0.7}$	$85.58^{+3.2}_{-3.2}$	–
	L	$41.10^{+2.2}_{-2.2}$	$58.90^{+11.4}_{-1.2}$	–	–
IC 5063	J	$0.58^{+0.5}_{-0.5}$	$99.42^{+0.6}_{-1.0}$	–	–
	H	$0.07^{+0.3}_{-0.1}$	$99.93^{+0.7}_{-1.1}$	–	–
	K	$1.61^{+0.5}_{-0.5}$	$98.39^{+0.9}_{-0.9}$	–	–
	L	$55.58^{+3.2}_{-3.2}$	$44.42^{+0.1}_{-5.0}$	–	–
MRK 897	J	$4.64^{+1.2}_{-1.2}$	$52.34^{+1.7}_{-2.2}$	$43.02^{+3.9}_{-3.6}$	–
	H	$5.98^{+2.6}_{-2.6}$	$58.00^{+1.7}_{-2.1}$	$36.03^{+4.3}_{-4.0}$	–
	K	$6.41^{+0.7}_{-0.6}$	$50.75^{+2.1}_{-2.3}$	$42.83^{+7.5}_{-7.1}$	–
	L	$85.42^{+1.4}_{-1.4}$	$14.58^{+6.1}_{-2.6}$	–	–
NGC 7130	J	$1.19^{+0.3}_{-0.3}$	$43.20^{+2.3}_{-2.6}$	$55.61^{+2.5}_{-2.5}$	–
	H	$1.51^{+0.7}_{-0.7}$	$43.27^{+2.6}_{-2.7}$	$55.22^{+2.7}_{-2.9}$	–
	K	$2.20^{+0.7}_{-0.7}$	$72.59^{+3.0}_{-3.2}$	$25.21^{+4.9}_{-4.5}$	–
	L	$69.64^{+1.9}_{-1.8}$	$30.36^{+23.8}_{-17.5}$	–	–
MCG -3-58-7	J	$7.38^{+1.5}_{-1.5}$	$25.05^{+0.9}_{-1.7}$	$34.68^{+1.8}_{-1.7}$	$32.89^{+1.1}_{-1.2}$
	H	$15.80^{+4.4}_{-4.4}$	$25.32^{+0.8}_{-0.9}$	$28.49^{+2.3}_{-2.2}$	$30.39^{+1.5}_{-1.8}$
	K	$30.97^{+6.7}_{-6.7}$	$28.60^{+1.3}_{-1.5}$	$19.50^{+3.7}_{-3.3}$	$20.93^{+1.2}_{-1.2}$
	L	$88.21^{+3.1}_{-3.0}$	$11.79^{+1.9}_{-2.2}$	–	–

Continued on Next Page...

Table 4.2 – Continued

Galaxy	Band	Nucleus %	Bulge %	Disk %	Bar %
NGC 7496	J	$0.47^{+0.1}_{-0.1}$	$15.05^{+0.5}_{-0.5}$	$25.43^{+2.4}_{-2.3}$	$59.05^{+1.1}_{-1.1}$
	H	$0.65^{+0.4}_{-0.4}$	$17.00^{+0.6}_{-0.6}$	$20.47^{+2.9}_{-2.7}$	$61.87^{+1.4}_{-1.4}$
	K	$1.11^{+1.1}_{-1.1}$	$16.86^{+0.8}_{-0.9}$	$16.21^{+7.0}_{-5.7}$	$65.83^{+3.0}_{-2.8}$
	L	$48.40^{+1.8}_{-1.7}$	$51.60^{+20.9}_{-9.8}$	–	–
	M	$18.88^{+1.7}_{-1.7}$	$81.12^{+2.4}_{-28.2}$	–	–
NGC 7582	J	$0.32^{+0.6}_{-0.3}$	$4.28^{+0.6}_{-1.2}$	$78.04^{+2.8}_{-2.6}$	$17.36^{+1.8}_{-3.4}$
	H	$0.69^{+2.7}_{-0.7}$	$5.03^{+0.4}_{-1.2}$	$65.94^{+3.2}_{-4.9}$	$28.33^{+1.0}_{-6.9}$
	K	$2.66^{+4.4}_{-2.7}$	$6.69^{+0.9}_{-1.3}$	$61.61^{+5.8}_{-5.7}$	$29.04^{+1.9}_{-4.7}$
	L	$79.47^{+2.6}_{-2.6}$	$20.53^{+9.7}_{-7.1}$	–	–
	M	$77.90^{+4.3}_{-4.2}$	$22.10^{+74.4}_{-52.2}$	–	–
NGC 7590	J	–	$10.72^{+0.5}_{-0.5}$	$89.28^{+2.4}_{-2.6}$	–
	H	–	$9.86^{+0.5}_{-0.6}$	$90.14^{+2.3}_{-2.4}$	–
	K	$0.31^{+0.5}_{-0.3}$	$8.79^{+0.8}_{-0.9}$	$90.90^{+4.9}_{-5.0}$	–
	J	$0.03^{+0.1}_{-0.0}$	$9.16^{+1.0}_{-1.6}$	$90.81^{+6.2}_{-0.3}$	–
	H	$0.04^{+0.2}_{-0.0}$	$9.70^{+0.8}_{-1.0}$	$90.25^{+2.8}_{-2.8}$	–
	K	$0.08^{+0.3}_{-0.1}$	$8.75^{+0.9}_{-1.5}$	$91.17^{+4.0}_{-4.0}$	–
CGCG 381-051	J	$7.80^{+1.3}_{-1.3}$	$1.86^{+0.0}_{-1.3}$	$45.30^{+7.3}_{-6.8}$	$45.02^{+2.7}_{-2.9}$
	H	$6.35^{+1.7}_{-1.7}$	$3.85^{+0.0}_{-2.3}$	$49.39^{+8.6}_{-7.8}$	$40.40^{+2.8}_{-3.1}$
	K	$8.73^{+2.1}_{-2.1}$	$4.25^{+0.7}_{-1.3}$	$42.20^{+16.0}_{-13.4}$	$44.80^{+3.3}_{-3.8}$

Table 4.3: Mean percentage contribution of each component fitted to the surface brightness profile of all galaxies in every band of observation. In the last column we indicate the number of fits which include that particular component. The number of observations in each band is: J, H, and K bands, 35 objects; L band, 24 objects; and M band, 9 objects. The standard deviation of the barred component in the mid-IR has no value because there is only one fit with a bar.

Component	Band	Mean Value (%)	Standard Deviation	Number of objects
Nucleus	J	5.74	11.75	34
	H	8.13	13.74	33
	K	12.25	18.23	33
	L	41.78	28.89	24
	M	83.85	30.97	9
Bulge	J	32.9	23.33	35
	H	32.74	22.3	35
	K	34.28	24.57	35
	L	51.48	28.73	24
	M	46.48	26.81	7
Disk	J	56.38	24.43	32
	H	53.48	25.28	32
	K	48.7	26.14	32
	L	36.24	20.95	4
	M	–	–	0
Bar	J	29.6	17.33	11
	H	30.31	16.69	11
	K	28.16	17.58	11
	L	16.84	–	1
	M	–	–	0

Table 4.4: Fitted parameters of the galaxy deconvolution in the J band.

Galaxy	Σ_{nuc}	Σ_{Bul}	r_{eff}^{Bul}	n_{Bul}	Σ_{dis}	r_{dis}	Σ_{bar}	r_{eff}^{bar}	n_{bar}
	Watts/m ² /μ/[$''$] ²	Watts/m ² /μ/[$''$] ²	pc		Watts/m ² /μ/[$''$] ²	pc	Watts/m ² /μ/[$''$] ²	pc	
NGC 34	5.57E-014	2.37E-014	268.68	1.44	1.21E-015	1102.39	–	–	–
IRAS 00198-7926 N	8.99E-015	2.85E-016	1395.56	0.5	8.80E-017	7764.69	–	–	–
IRAS 00198-7926 S	3.41E-015	5.30E-016	2449.66	0.92	1.91E-016	5938.57	–	–	–
IRAS 00521-7054	5.71E-014	4.97E-016	4224.99	1.41	–	–	–	–	–
ESO 541-IG12	4.25E-014	9.90E-016	2459.95	1.07	7.93E-017	5762.66	–	–	–
IRAS 01475-0740	2.20E-014	1.33E-015	465.89	0.87	1.30E-016	1089.46	–	–	–
NGC 1144	1.63E-014	4.09E-015	404.36	0.59	1.57E-015	2478.14	–	–	–
MCG -2-8-39	3.49E-015	2.11E-015	1761.77	1.63	2.60E-017	11482.31	2.41E-017	3215.54	0.16
NGC 1194	1.12E-015	2.51E-014	3877.06	3.34	2.53E-017	7256.34	–	–	–
NGC 1320	7.29E-015	7.74E-015	1596.57	2.29	1.21E-016	3090.79	–	–	–
IRAS 04385-0828	9.46E-015	4.89E-015	288.36	1.5	4.38E-016	1181.64	–	–	–
ESO 33-G2	1.34E-014	5.78E-014	2025.31	3.41	6.51E-017	4157.83	6.54E-017	1271.09	0.16
IRAS 05189-2524	1.18E-013	3.40E-014	481.31	1.38	2.41E-016	3326.93	–	–	–
MCG +0-29-23	1.64E-014	5.46E-015	521.16	0.56	7.77E-016	2130.64	–	–	–
NGC 3660	2.92E-014	1.63E-015	1239.49	1.31	1.40E-016	4152.8	7.00E-017	3540.67	0.19
NGC 4501	1.46E-013	2.68E-015	1010.33	0.83	5.59E-016	6482.69	–	–	–
TOL 1238-364	5.91E-014	3.14E-015	74.76	0.86	7.07E-016	174.44	–	–	–
NGC 4941	–	2.58E-014	373.75	2.42	1.49E-016	2642.36	–	–	–
MCG -3-34-64	2.98E-014	6.82E-015	542.08	0.91	6.66E-017	4722.84	2.14E-016	2115.18	0.32
NGC 5135	8.88E-015	1.26E-016	6753.57	0.3	–	–	1.21E-014	3299.05	2.3
NGC 5953	7.11E-014	2.37E-014	638.24	1.71	9.27E-017	3325.15	–	–	–
MCG -2-40-4	1.48E-013	4.97E-016	1727.8	0.17	7.24E-016	3034.92	8.45E-015	681.1	1.07
IRAS 15480-0344	3.38E-014	1.11E-014	1816.43	2.01	4.45E-017	6419.7	–	–	–
NGC 6810	4.54E-014	3.34E-014	386.77	1.75	5.65E-016	2472.34	–	–	–

Continued on Next Page. . .

Table 4.4 – Continued

Galaxy	Σ_{nuc}	Σ_{Bul}	r_{eff}^{Bul}	n_{Bul}	Σ_{dis}	r_{dis}	Σ_{bar}	r_{bar}	n_{bar}
	Watts/m ² /μ/[$''$] ²	Watts/m ² /μ/[$''$] ²	pc		Watts/m ² /μ/[$''$] ²	pc	Watts/m ² /μ/[$''$] ²	pc	
NGC 6890	5.05E-015	1.14E-014	422.35	1.85	9.50E-016	1466.5	–	–	–
IC 5063	1.03E-014	1.50E-014	4185.54	2.64	–	–	–	–	–
MRK 897	8.72E-015	5.48E-015	898.55	1.5	1.38E-016	2316.74	–	–	–
NGC 7130	3.98E-014	1.88E-015	2494.16	0.95	2.95E-016	4086.82	–	–	–
MCG -3-58-7	2.17E-013	5.40E-017	3269.81	0.17	1.68E-016	3670.46	1.37E-015	1557.36	0.56
NGC 7496	2.51E-014	1.35E-014	1668.66	2.9	3.23E-017	5004.84	8.52E-017	4863.51	0.34
NGC 7582	3.38E-014	7.86E-016	711.57	1.08	2.02E-016	4142.04	3.45E-017	2252.21	0.16
NGC 7590	4.38E-016	9.34E-015	248.77	1.79	4.53E-016	1634.61	–	–	–
NGC 7590	–	1.25E-014	289.19	1.97	4.73E-016	1789.05	–	–	–
CGCG 381-051	1.48E-014	1.88E-016	705.18	0.73	1.77E-016	3238.83	1.16E-016	4280.99	0.28
Mean	4.07E-014	1.02E-014	1519.93	1.43	3.52E-016	3791.60	2.25E-015	2707.67	0.55
Median	2.36E-14	5.18E-15	954.44	1.40	1.77E-16	3325.15	1.01E-16	2733.87	0.30
Std.Dev.	5.02E-14	1.31E-14	1496.75	0.84	3.78E-16	2397.43	4.33E-15	1353.06	0.67

Table 4.5: Fitted parameters of the galaxy deconvolution in the H band.

Galaxy	Σ_{nuc}	Σ_{Bul}	r_{eff}^{Bul}	n_{Bul}	Σ_{dis}	r_{dis}	Σ_{bar}	r_{eff}^{bar}	n_{bar}
	Watts/m ² /μ/[$''$] ²	Watts/m ² /μ/[$''$] ²	pc		Watts/m ² /μ/[$''$] ²	pc	Watts/m ² /μ/[$''$] ²	pc	
NGC 34	1.17E-013	2.94E-014	225.22	1.27	1.45E-015	1070.78	–	–	–
IRAS 00198-7926 N	6.67E-015	2.26E-016	1722.19	0.48	5.03E-017	8907.86	–	–	–
IRAS 00198-7926 S	8.22E-015	2.37E-016	2108.19	0.53	1.50E-016	5671.34	–	–	–
IRAS 00521-7054	7.53E-014	2.40E-015	3003.81	1.87	–	–	–	–	–
ESO 541-IG12	9.49E-014	7.59E-016	2505.51	1	4.44E-017	6810.42	–	–	–
IRAS 01475-0740	2.24E-014	1.35E-015	462.3	1.03	1.39E-016	799.17	–	–	–
NGC 1144	1.10E-014	3.57E-015	421.69	0.68	1.04E-015	2478.14	–	–	–
MCG -2-8-39	2.14E-015	1.45E-017	2698.1	0.16	1.16E-017	17106.42	1.85E-015	1971.21	1.83
NGC 1194	4.73E-015	2.26E-014	3288.03	3.37	3.68E-017	4109.35	–	–	–
NGC 1320	1.66E-014	5.78E-015	1357.08	2.12	1.01E-016	3238.17	–	–	–
IRAS 04385-0828	1.98E-014	3.20E-015	316.57	1.5	3.24E-016	1175.37	–	–	–
ESO 33-G2	3.55E-014	2.73E-014	1585.03	2.92	7.21E-017	3924.28	4.74E-017	1470.17	0.17
IRAS 05189-2524	2.56E-013	1.63E-014	523.53	1.26	2.08E-016	2609.19	–	–	–
MCG +0-29-23	1.40E-014	5.03E-015	521.16	0.58	6.20E-016	2043.78	–	–	–
NGC 3660	2.43E-014	1.53E-015	1310.61	1.45	8.42E-017	4465.21	5.61E-017	3510.19	0.19
NGC 4501	1.05E-013	2.37E-015	1043.8	0.94	4.03E-016	6474.72	–	–	–
TOL 1238-364	5.06E-014	2.33E-015	76	0.85	4.65E-016	176.93	–	–	–
NGC 4941	–	1.84E-014	298.54	2.22	1.04E-016	2656.94	–	–	–
MCG -3-34-64	2.32E-014	2.06E-016	2093.92	0.29	8.15E-017	4347.28	8.57E-015	538.54	0.99
NGC 5135	3.75E-014	2.85E-015	3584.57	1.78	–	–	7.36E-017	6795.98	0.28
NGC 5953	5.74E-014	2.06E-014	646.44	1.8	6.73E-017	3148.85	–	–	–
MCG -2-40-4	2.08E-013	1.25E-014	651.06	1.34	5.58E-016	2959.8	3.79E-016	1497.43	0.17
IRAS 15480-0344	3.84E-014	5.13E-015	1517.84	1.57	6.10E-017	5237.78	–	–	–
NGC 6810	2.48E-014	2.00E-014	511.14	1.8	4.18E-016	2484.64	–	–	–

Continued on Next Page...

Table 4.5 – Continued

Galaxy	Σ_{nuc}	Σ_{Bul}	r_{eff}^{Bul}	n_{Bul}	Σ_{dis}	r_{dis}	Σ_{bar}	r_{bar}	n_{bar}
	Watts/m ² /μ/[$''$] ²	Watts/m ² /μ/[$''$] ²	pc		Watts/m ² /μ/[$''$] ²	pc	Watts/m ² /μ/[$''$] ²	pc	
NGC 6890	4.01E-015	2.13E-014	554.76	2.54	6.58E-016	1473.2	–	–	–
IC 5063	1.91E-015	1.77E-014	3854.05	2.81	–	–	–	–	–
MRK 897	9.43E-015	4.04E-015	1001.39	1.5	6.26E-017	2955.47	–	–	–
NGC 7130	3.38E-014	1.53E-015	2404.01	0.98	1.95E-016	4173.64	–	–	–
MCG -3-58-7	3.38E-013	4.75E-017	4529.91	0.19	1.03E-016	3819.09	8.18E-016	1628.44	0.46
NGC 7496	2.50E-014	8.09E-015	1778.08	2.83	1.48E-017	5590.7	5.91E-017	4839.57	0.34
NGC 7582	5.02E-014	5.93E-016	634.7	0.97	1.57E-016	3431.57	3.19E-017	2213.77	0.16
NGC 7590	6.93E-016	9.61E-015	268.46	2	3.34E-016	1626.32	–	–	–
NGC 7590	–	9.32E-015	253.95	1.95	3.80E-016	1615.95	–	–	–
CGCG 381-051	1.04E-014	7.60E-016	580.37	1.18	1.24E-016	3550.85	8.85E-017	4199.87	0.29
Mean	5.40E-014	8.15E-015	1421.53	1.46	2.75E-016	3875.26	1.20E-015	2866.52	0.49
Median	2.46E-14	3.81E-15	1022.59	1.40	1.39E-16	3238.17	8.11E-17	2092.49	0.29
Std.Dev.	7.77E-14	8.90E-15	1200.79	0.82	3.22E-16	3119.73	2.65E-15	1930.17	0.53

Table 4.6: Fitted parameters of the galaxy deconvolution in the K band.

Galaxy	Σ_{nuc}	Σ_{Bul}	r_{eff}^{Bul}	n_{Bul}	Σ_{dis}	r_{dis}	Σ_{bar}	r_{eff}^{bar}	n_{bar}
	Watts/m ² /μ/[$''$] ²	Watts/m ² /μ/[$''$] ²	pc		Watts/m ² /μ/[$''$] ²	pc	Watts/m ² /μ/[$''$] ²	pc	
NGC 34	4.78e-14	3.10e-14	292.39	2.21	3.32e-16	1134	–	–	–
IRAS 00198-7926 N	5.72e-15	9.54e-17	1558.88	0.26	3.52e-17	8670.32	–	–	–
IRAS 00198-7926 S	2.81e-14	6.64e-17	2197.27	0.24	1.03e-16	5537.72	–	–	–
IRAS 00521-7054	1.19e-13	4.76e-16	2821.34	1.19	–	–	–	–	–
ESO 541-IG12	1.27e-13	8.68e-16	2346.06	1.38	1.87e-17	6901.53	–	–	–
IRAS 01475-0740	1.96e-14	4.72e-16	444.38	0.89	4.94e-17	852.93	–	–	–
NGC 1144	8.02e-15	1.40e-15	398.58	0.6	4.36e-16	2252.85	–	–	–
MCG -2-8-39	1.48e-15	1.43e-15	2075.93	2.08	7.46e-18	14445.29	7.36e-18	2550.26	0.16
NGC 1194	1.83e-14	1.29e-14	3312.92	3.5	1.06e-17	5934.49	–	–	–
NGC 1320	2.58e-14	2.55e-15	1817.63	2.3	3.23e-17	3203.37	–	–	–
IRAS 04385-0828	3.85e-14	1.97e-15	247.61	1.27	1.68e-16	1084.47	–	–	–
ESO 33-G2	4.59e-14	2.84e-14	1684.57	3.36	3.26e-17	3445.71	2.16e-17	1477.83	0.17
IRAS 05189-2524	4.04e-13	2.85e-13	388.42	1.98	2.65e-16	2718.97	–	–	–
MCG +0-29-23	1.29e-14	2.63e-15	526.27	0.46	3.25e-16	1926.26	–	–	–
NGC 3660	1.36e-14	1.10e-15	1442.68	1.83	4.60e-17	4411.87	1.98e-17	1137.89	0.16
NGC 4501	4.82e-14	2.01e-15	1109.13	1.33	1.80e-16	7110.56	–	–	–
TOL 1238-364	3.89e-14	1.42e-15	79.99	1	1.91e-16	186.4	–	–	–
NGC 4941	–	6.53e-15	299.31	2.1	4.50e-17	2485.03	–	–	–
MCG -3-34-64	1.50e-14	7.75e-17	2054.95	0.33	2.44e-17	4549.23	2.53e-15	506.65	0.9
NGC 5135	4.52e-14	1.75e-15	3663.72	1.92	–	–	3.13e-17	6555.69	0.26
NGC 5953	1.25e-14	4.59e-15	683.34	1.81	7.05e-18	3364.79	–	–	–
MCG -2-40-4	2.48e-13	1.22e-14	545.89	1.49	2.99e-16	2709.39	1.93e-16	1617.62	0.17
IRAS 15480-0344	2.81e-14	3.33e-15	1536.5	1.72	2.89e-17	5436.84	–	–	–
NGC 6810	1.37e-14	1.92e-14	367.64	1.84	2.33e-16	2200.37	–	–	–

Continued on Next Page...

Table 4.6 – Continued

Galaxy	Σ_{nuc}	Σ_{Bul}	r_{eff}^{Bul}	n_{Bul}	Σ_{dis}	r_{dis}	Σ_{bar}	r_{bar}	n_{bar}
	Watts/m ² /μ/[$''$] ²	Watts/m ² /μ/[$''$] ²	pc		Watts/m ² /μ/[$''$] ²	pc	Watts/m ² /μ/[$''$] ²	pc	
NGC 6890	8.38e-15	1.36e-14	395.54	2.51	3.29e-16	1401.14	–	–	–
IC 5063	5.19e-15	3.22e-15	3956.77	2.72	–	–	–	–	–
MRK 897	5.60e-15	2.43e-15	763.22	1.34	5.76e-17	2354.63	–	–	–
NGC 7130	1.89e-14	1.09e-15	2874.8	1.24	3.52e-17	4387.33	–	–	–
MCG -3-58-7	4.58e-13	5.95e-16	1602.59	0.59	4.35e-17	3864.32	2.29e-17	3832.01	0.17
NGC 7496	1.96e-14	4.79e-15	1652.7	2.9	3.04e-18	8550.75	2.86e-17	4847.55	0.34
NGC 7582	6.51e-14	2.26e-16	823.58	0.93	6.36e-17	3619.34	1.65e-17	2491.59	0.16
NGC 7590	6.41e-16	3.68e-15	211.45	1.68	1.72e-16	1578.64	–	–	–
NGC 7590	2.71e-15	2.68e-15	215.6	1.6	1.73e-16	1634.61	–	–	–
CGCG 381-051	8.68e-15	3.50e-16	854.95	1.3	3.07e-17	4630.46	5.41e-17	4243.55	0.31
Mean	5.93e-14	1.34e-14	1330.78	1.59	1.22e-16	3954.31	2.93e-16	2926.06	0.28
Median	1.96E-14	2.22E-15	982.04	1.55	4.94E-17	3364.79	2.58E-17	2520.92	0.17
Std.Dev.	1.07E-13	4.86E-14	1082.08	0.83	1.24E-16	2936.15	7.88E-16	1903.60	0.23

Table 4.7: Fitted parameters of the galaxy deconvolution in the L band. Only MCG -2-40-4 has a fitted bar in this waveband, with values of $\Sigma_{bar} = 6.64e-17$ Watts/m²/μ/[$''$]², $r_{bar} = 2103.41$ pc, and $n_{bar} = 0.65$

Galaxy	Σ_{nuc}	Σ_{Bul}	r_{eff}^{Bul}	n_{Bul}	Σ_{dis}	r_{dis}
	Watts/m ² /μ/[$''$] ²	Watts/m ² /μ/[$''$] ²	pc		Watts/m ² /μ/[$''$] ²	pc
NGC 34	2.88e-14	1.02e-14	162	1.24	9.71e-17	979.9
IRAS 00198-7926 N	6.60e-14	6.32e-16	1261.95	0.51	–	–
IRAS 00198-7926 S	6.60e-14	6.32e-16	1261.95	0.51	–	–
IRAS 00521-7054	1.70e-16	8.04e-16	3088.03	1.9	–	–
ESO 541-IG12	4.38e-13	3.30e-16	2152.46	1.4	–	–
IRAS 01475-0740	5.87e-14	1.62e-16	379.88	1	–	–
NGC 1144	2.08e-14	3.72e-16	329.26	0.87	1.01e-16	2148.88
MCG -2-8-39	1.20e-14	2.92e-16	1749.45	2	–	–
NGC 1194	–	–	–	–	–	–
NGC 1320	–	–	–	–	–	–
IRAS 04385-0828	–	–	–	–	–	–
ESO 33-G2	–	–	–	–	–	–
IRAS 05189-2524	–	–	–	–	–	–
MCG +0-29-23	2.43e-14	3.99e-16	551.82	0.36	3.84e-17	1813.85
NGC 3660	1.71e-14	4.06e-16	1262.35	2	–	–
NGC 4501	1.48e-14	2.82e-16	983.24	1.2	–	–
TOL 1238-364	1.01e-13	3.88e-16	70.77	1.3	1.02e-17	185.15
NGC 4941	–	–	–	–	–	–
MCG -3-34-64	1.04e-13	1.39e-15	453.51	1.1	–	–
NGC 5135	5.10e-14	6.13e-16	3412.12	2.3	–	–
NGC 5953	4.12e-15	7.02e-16	601.34	1.9	–	–
MCG -2-40-4	3.89e-13	1.49e-15	570.93	1.5	–	–
IRAS 15480-0344	4.74e-14	1.67e-16	2027.93	1.5	–	–
NGC 6810	3.35e-14	6.13e-15	404.54	1.9	–	–
NGC 6890	5.46e-14	1.02e-15	594.98	2.3	–	–
IC 5063	2.27e-13	1.17e-15	3812.04	2.9	–	–
MRK 897	3.38e-13	3.01e-16	660.38	0.25	–	–
NGC 7130	4.53e-14	1.43e-16	1539.24	1.3	–	–
MCG -3-58-7	5.85e-13	3.90e-17	1809.38	0.4	–	–
NGC 7496	3.18e-14	8.63e-16	1618.51	3.18	–	–
NGC 7582	7.25e-13	3.25e-16	779.65	1.2	–	–
NGC 7590	–	–	–	–	–	–
NGC 7590	–	–	–	–	–	–
CGCG 381-051	–	–	–	–	–	–
Mean	1.39e-13	1.17e-15	1261.51	1.44	6.17e-17	1281.95
Median	5.10E-14	4.06E-16	983.24	1.30	6.78E-17	1396.88
Std.Dev.	1.98E-13	2.22E-15	1016.17	0.77	4.47E-17	881.04

Table 4.8: Fitted parameters of the galaxy deconvolution in the M band.

Galaxy	Σ_{nuc}	Σ_{Bul}	r_{eff}^{Bul}	n_{Bul}
	Watts/m ² /μ/[$''$] ²	Watts/m ² /μ/[$''$] ²	pc	
NGC 34	1.46e-14	7.45e-15	225.22	1.83
IRAS 00198-7926 N	9.53e-14	–	–	–
IRAS 00198-7926 S	9.53e-14	–	–	–
IRAS 00521-7054	–	–	–	–
ESO 541-IG12	2.51e-13	3.54e-16	2106.9	1.4
IRAS 01475-0740	–	–	–	–
NGC 1144	–	–	–	–
MCG -2-8-39	–	–	–	–
NGC 1194	–	–	–	–
NGC 1320	–	–	–	–
IRAS 04385-0828	–	–	–	–
ESO 33-G2	–	–	–	–
IRAS 05189-2524	–	–	–	–
MCG +0-29-23	–	–	–	–
NGC 3660	–	–	–	–
NGC 4501	–	–	–	–
TOL 1238-364	5.95e-14	1.79e-16	74.26	1.2
NGC 4941	–	–	–	–
MCG -3-34-64	1.30e-13	4.30e-16	503.11	1
NGC 5135	3.32e-14	–	–	–
NGC 5953	–	–	–	–
MCG -2-40-4	1.82e-13	1.29e-15	641.04	1.5
IRAS 15480-0344	–	–	–	–
NGC 6810	2.69e-14	2.59e-15	338.94	1.9
NGC 6890	–	–	–	–
IC 5063	–	–	–	–
MRK 897	–	–	–	–
NGC 7130	–	–	–	–
MCG -3-58-7	–	–	–	–
NGC 7496	1.67e-13	8.29e-15	1618.51	3.1
NGC 7582	4.85e-13	1.53e-16	779.65	1.2
NGC 7590	–	–	–	–
NGC 7590	–	–	–	–
CGCG 381-051	–	–	–	–
Mean	1.40e-13	2.59e-15	785.95	1.64
Median	9.53E-14	8.60E-16	572.07	1.45
Std.Dev.	1.36E-13	3.36E-15	713.13	0.67

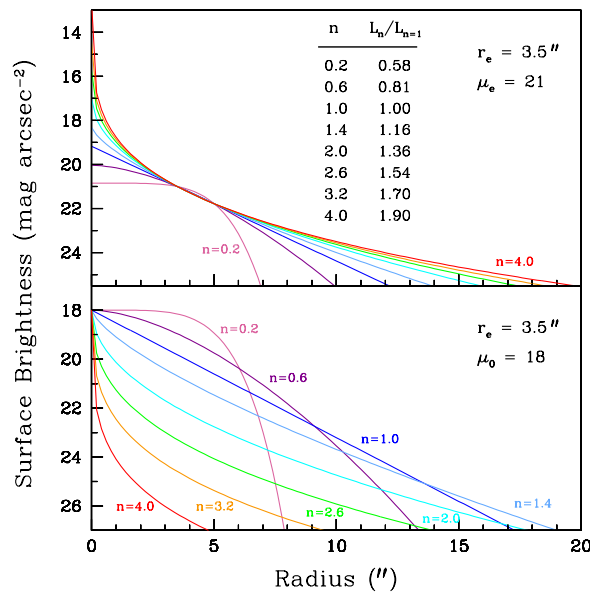


Figure 4.1: Sérsic profiles for different values of n . The top panel shows profiles with $\mu_e = 21$ mag arcsec $^{-2}$ and $r_e = 3.5''$ for values of n in the range $0.2 < n < 4$. The table lists the relative light contributions of the different profiles normalized to the $n = 1$ case. The bottom panel shows the same profiles except for a constant CSB of $\mu_0 = 18$ mag arcsec $^{-2}$. Fig. 2 from MacArthur *et al.* (2003).

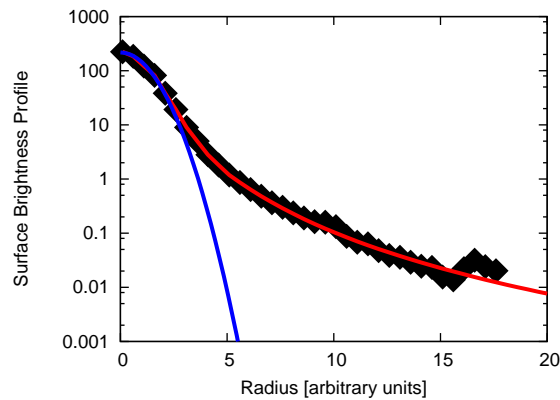


Figure 4.2: Example of the Moffat fitting of a PSF star. The observed data are the black diamonds and the Moffat profile is represented by the red line. A Gaussian profile is shown for comparison (blue).

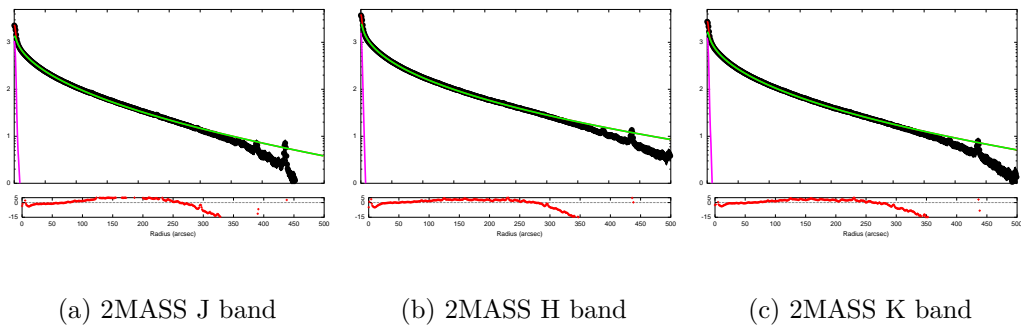


Figure 4.3: Radial surface brightness profile fitting of J, H, and K bands, and $3.6\mu\text{m}$, $4.5\mu\text{m}$, and $5.8\mu\text{m}$ of galaxy Messier 31. The abscissas show $\text{Log}(\text{counts}/\text{pix}^2)$ and the ordinates show the distance from the center in arcseconds. The percentage residues are shown in the bottom panels. The model (red) is composed by a nuclear PSF (pink), a bulge (green), a bar (yellow) and a disk (blue). The black points corresponds to the observation. The brightness excess in the central part of the galaxy is modelled as a bar in the IRAC bands and as a nuclear component in the 2MASS bands. See text for details.

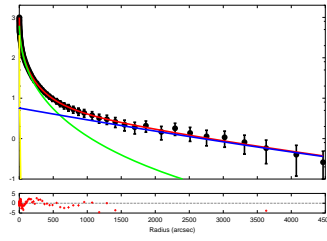
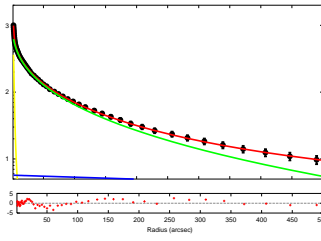
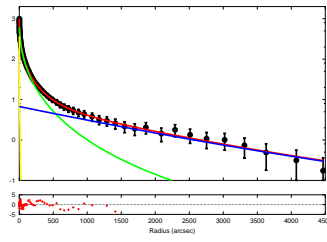
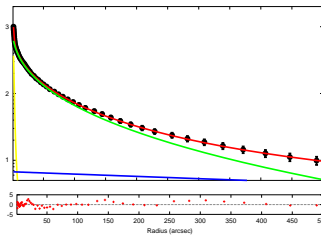
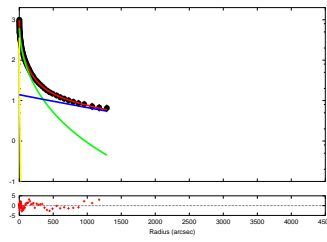
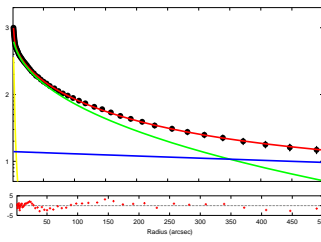
(d) IRAC 3.6 μm (e) IRAC 3.6 μm , detail(f) IRAC 4.5 μm (g) IRAC 4.5 μm , detail(h) IRAC 5.8 μm (i) IRAC 5.8 μm , detail

Figure 4.3: Continued

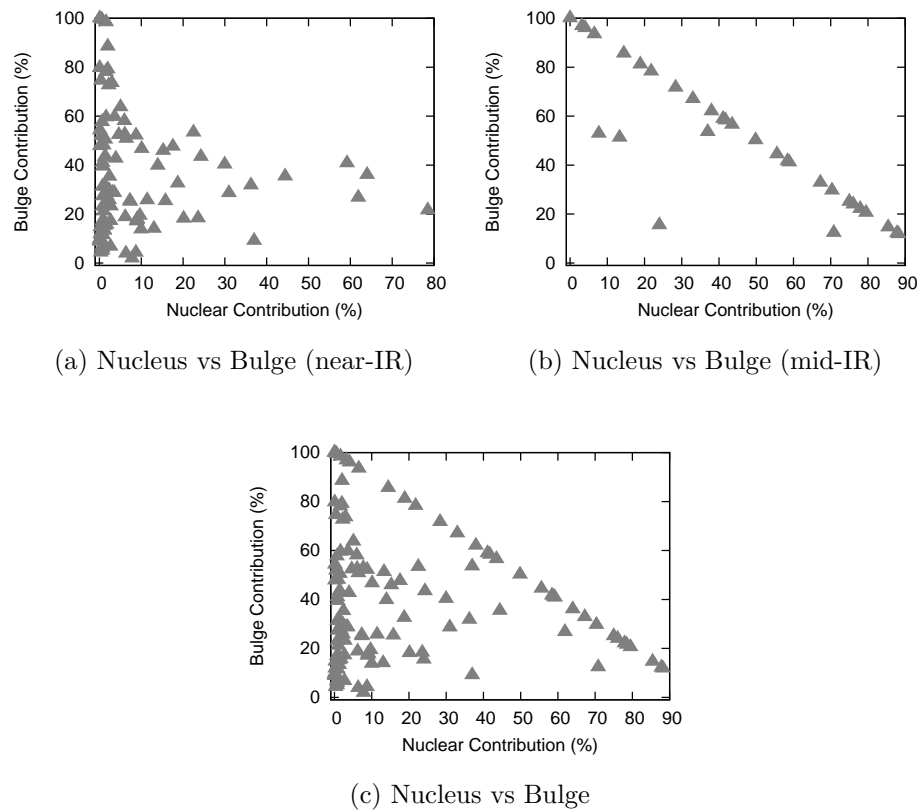
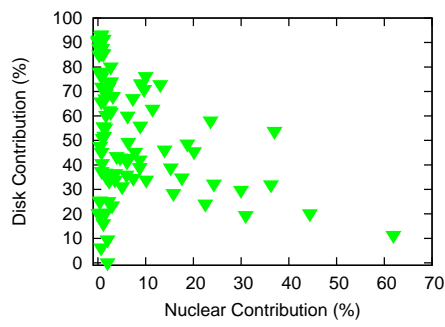
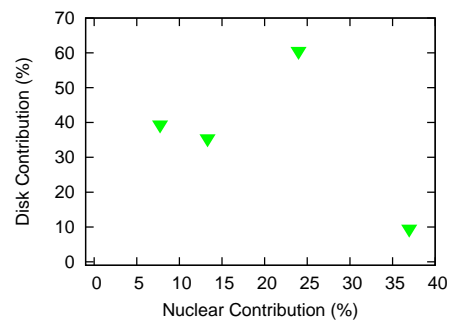


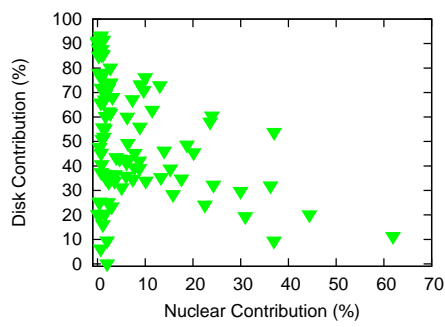
Figure 4.4: Comparison of the distributions of percentual contribution of the nucleus with the contribution of the bulge and disk. The differentiation between near-IR and mid-IR bands fits has been done, corresponding to 105 and 33 respectively.



(d) Nucleus vs Disk (near-IR)



(e) Nucleus vs Disk (mid-IR)



(f) Nucleus vs Disk

Figure 4.4: Continued

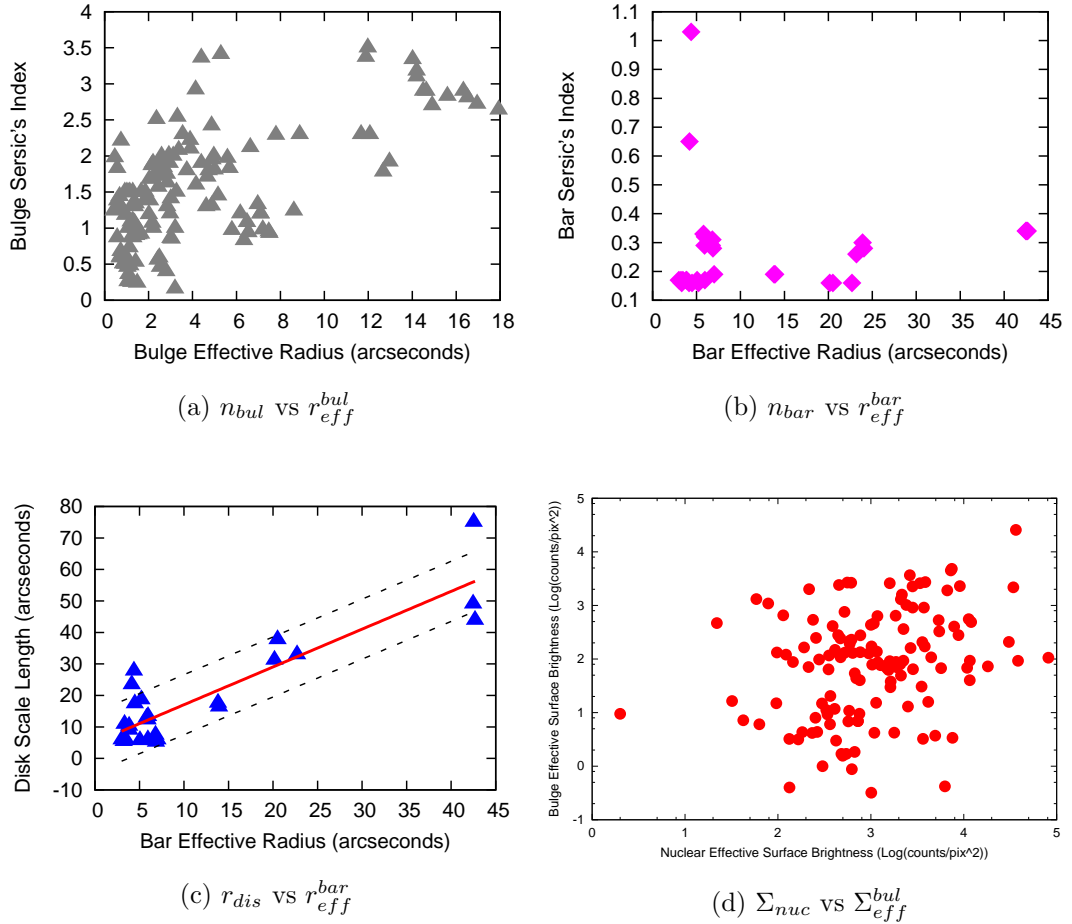


Figure 4.5: Relevant comparison of fitted parameters. It is thought that the Sérsic's effective radius is correlated with the Sérsic's index, but we did not find a clear relation neither between the bulge nor the bar parameters (top panels). It is found that the size of the bar is related with the size of the disk (bottom left panel). The solid red line is the best straight line fitted, with a slope of 1.2, a position coefficient of 5.05, and a RMS of 7.9, (the dashed lines correspond to one RMS of the fitted line). The surface brightness of the nucleus (Eqn. 4.2) could be correlated with the central surface brightness of the bulge (bottom right panel), but no trend is evident.

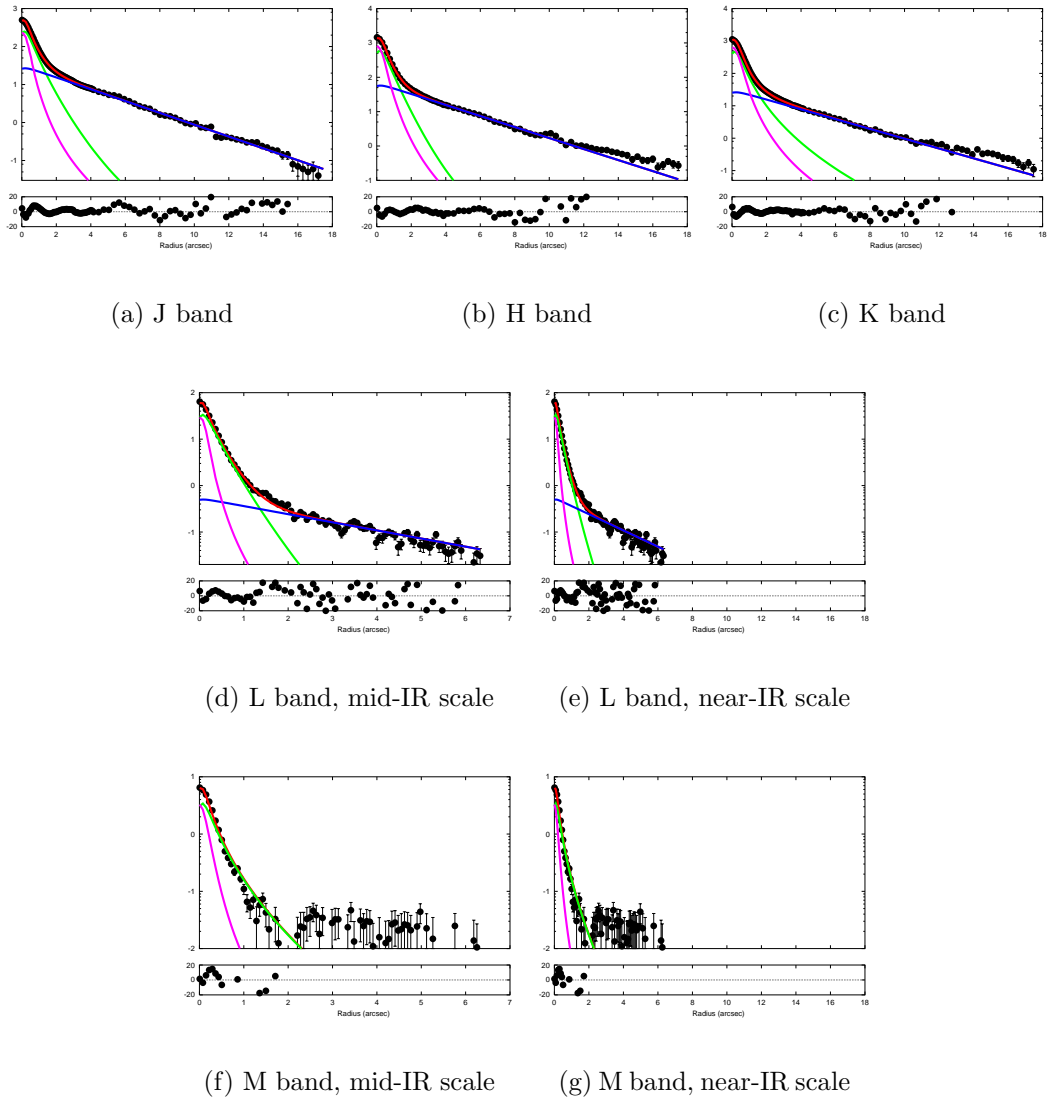
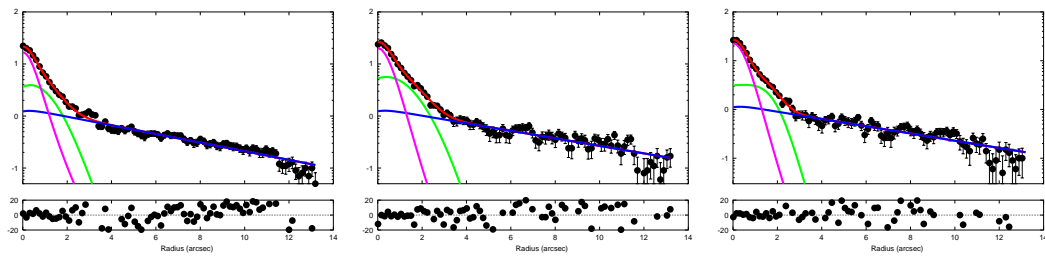


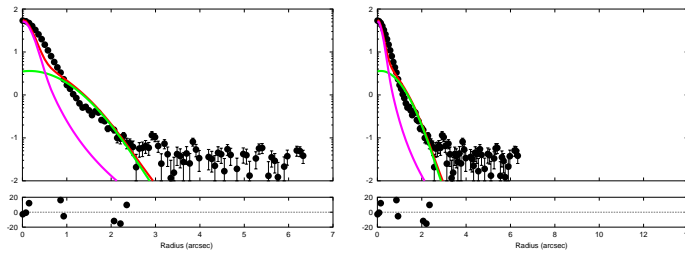
Figure 4.6: Radial surface brightness profile fitting of J, H, K, L and M bands observations of NGC 34. The abscissas show $\text{Log}(\text{counts}/\text{pix}^2)$ and the ordinates show the distance from the center in arcseconds. The residuals in percentage are shown in the bottom panels. The different physical components of the model are the nucleus (pink), the bulge (green) and the disk (blue). The sum of these is the final model (red) and the black points corresponds to the observation. The mid-IR profiles (L, M and N whenever available) are plotted in 2 scales: a detailed scale showing the central part of the galaxy (left side), and a global scale, showing the complete galaxy (right side).



(a) J band

(b) H band

(c) K band



(d) L band, mid-IR scale

(e) L band, near-IR scale

Figure 4.7: Radial surface brightness profile fitting of J, H, K and L bands of IRAS 00198-7926 North. The axis and colors are the same as in Fig. 4.6. This seems to be a multiple system, and the Northern source seems to be the Seyfert nucleus. The L band model fit result is discarded (see text) and all the emission is considered as nuclear.

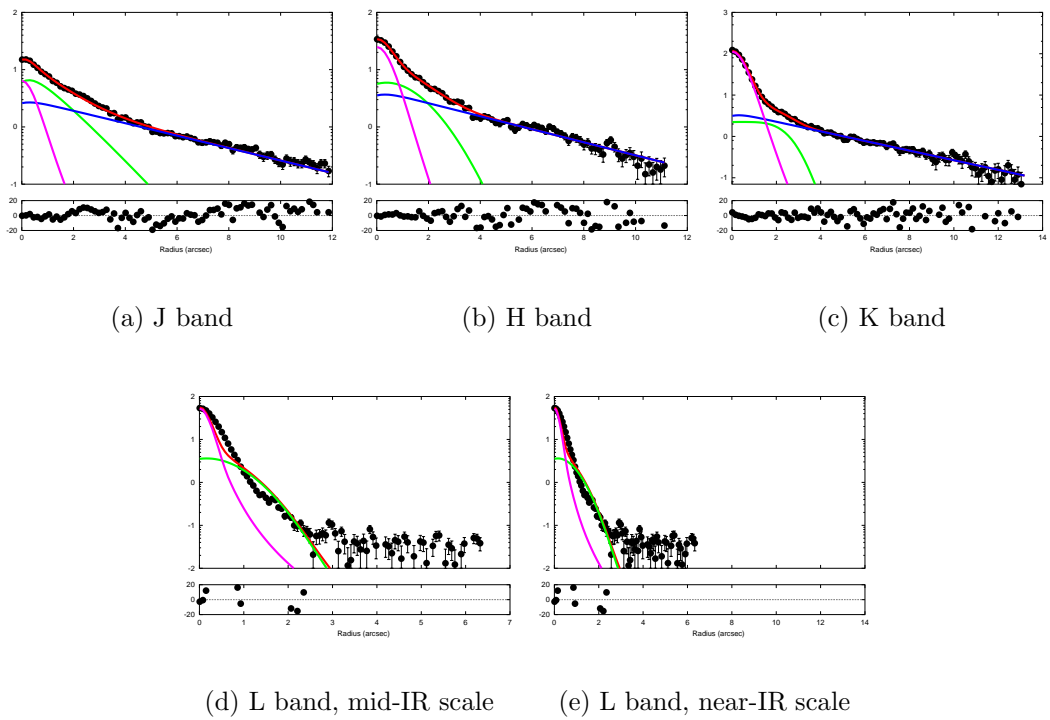
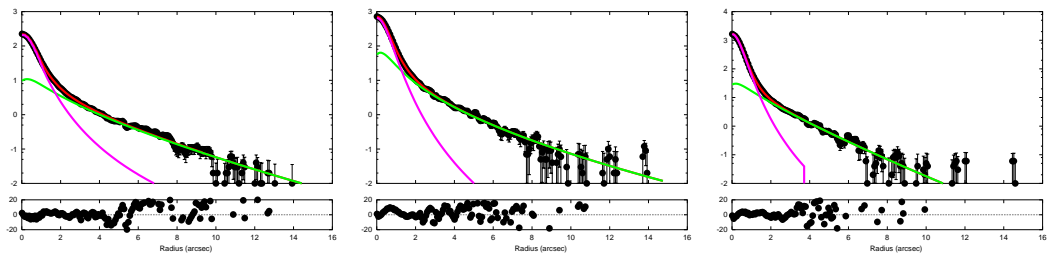


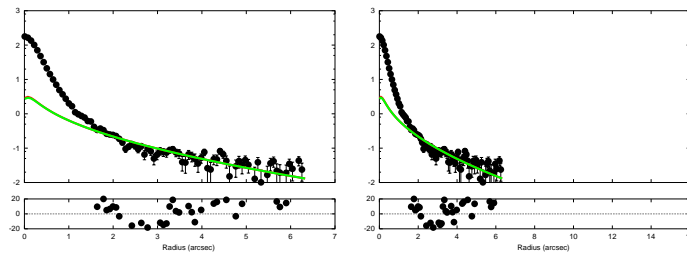
Figure 4.8: Radial surface brightness profile model fit of J, H, K and L bands of IRAS 00198-7926 South. The axis and colors are the same as in Fig. 4.6. See text for details.



(a) J band

(b) H band

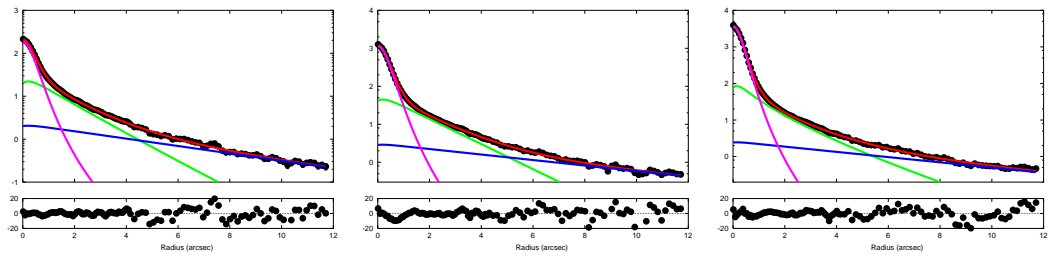
(c) K band



(d) L band, mid-IR scale

(e) L band, near-IR scale

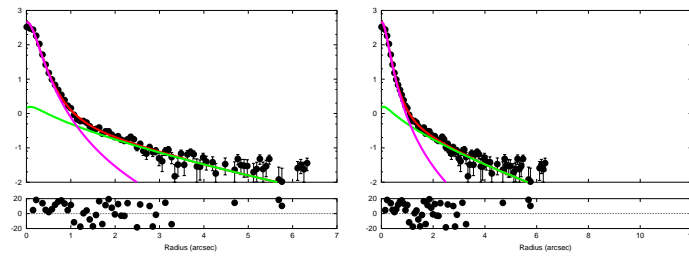
Figure 4.9: Radial surface brightness profile model fit of IRAS 00521-7054 in the J, H, K and L-bands. The axis and colors are the same as in Fig. 4.6. As the seeing conditions changed between the observation of the PSF star and the galaxy, the bulge is fitted to the outer parts of the observed L-band profile and the nuclear flux is computed as $F_{nuc} = F_{gal} - F_{bul}$.



(a) J band

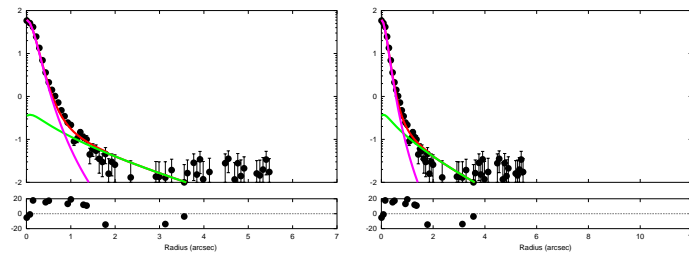
(b) H band

(c) K band



(d) L band, mid-IR scale

(e) L band, near-IR scale



(f) M band, mid-IR scale

(g) M band, near-IR scale

Figure 4.10: Radial surface brightness profile model fit of J, H, K, L and M bands of ESO 541-IG12. The axis and colors are the same as in Fig. 4.6. See text for details.

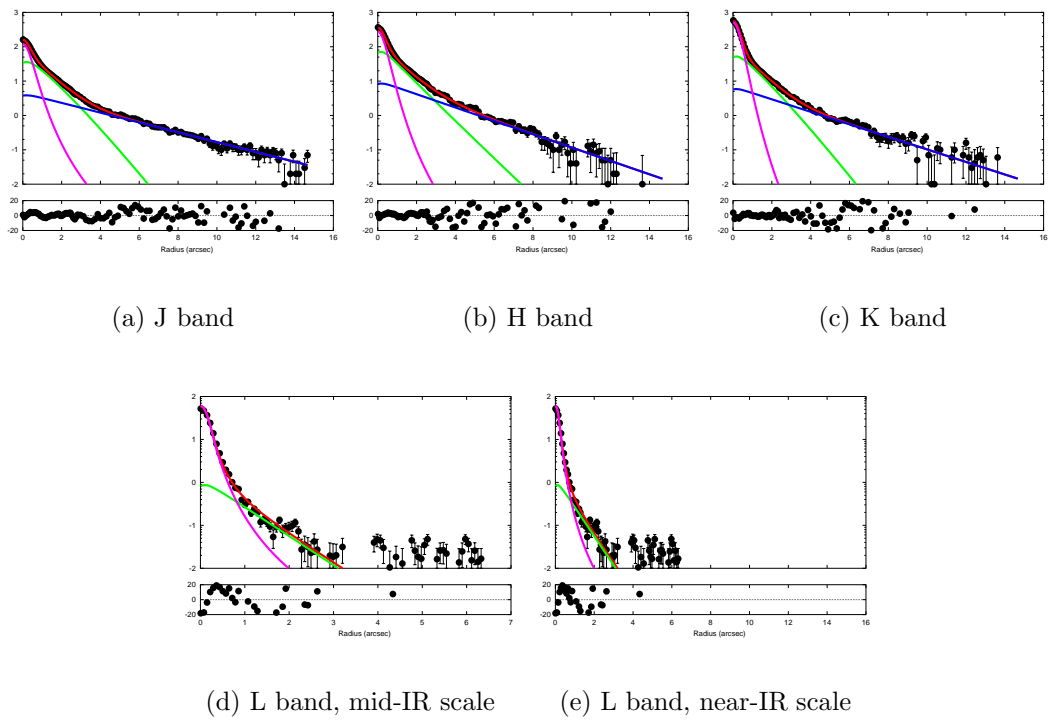


Figure 4.11: Radial surface brightness profile model fit of J, H, K and L bands of galaxy IRAS 01475-0740. The axis and colors are the same as in Fig. 4.6.

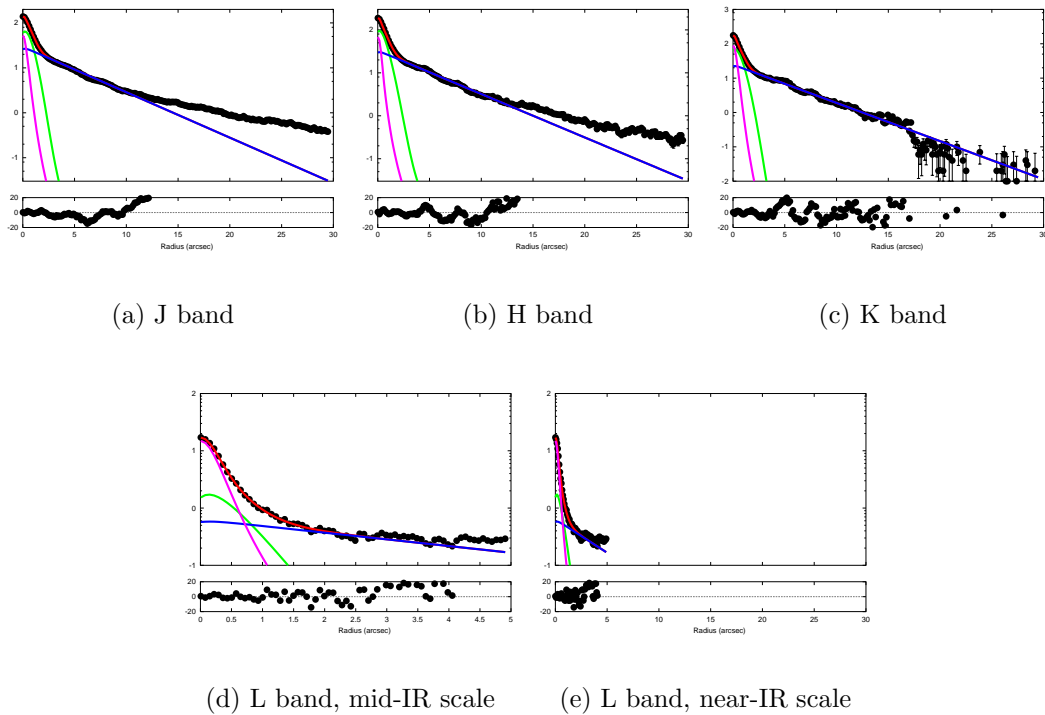
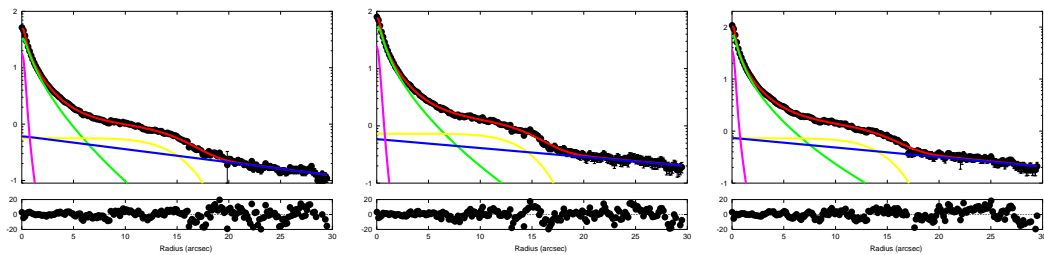


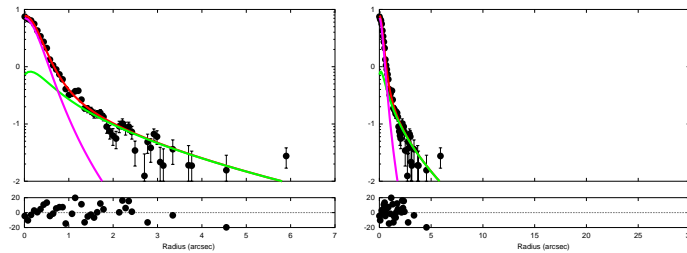
Figure 4.12: Radial surface brightness profile model fit of J, H, K, and L bands of NGC 1143/4. The axis and colors are the same as in the previous figures. The emission excess observed in the outer parts of the galaxy in the J and H bands come from the stream of material. The galaxy is point-like in the M band, so all the emission is considered as nuclear and no fitting is needed.



(a) J band

(b) H band

(c) K band



(d) L band, mid-IR scale

(e) L band, near-IR scale

Figure 4.13: Radial surface brightness profile fitting of J, H, K and L bands of MCG -2-8-39. The axis and colors are the same as in the previous figures, with the addition of the bar component (yellow). It is very clear that this is a barred galaxy, as classified.

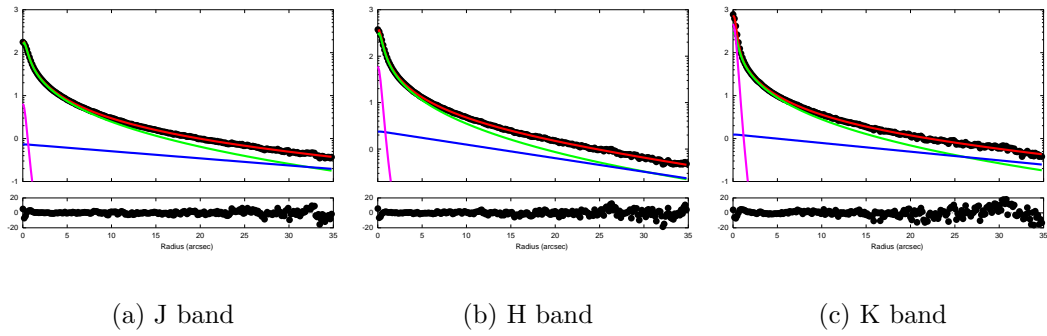


Figure 4.14: Results of the fitting process to the radial surface brightness profile of J, H and K bands of NGC 1194. The axis and colors are the same as in the previous figures.

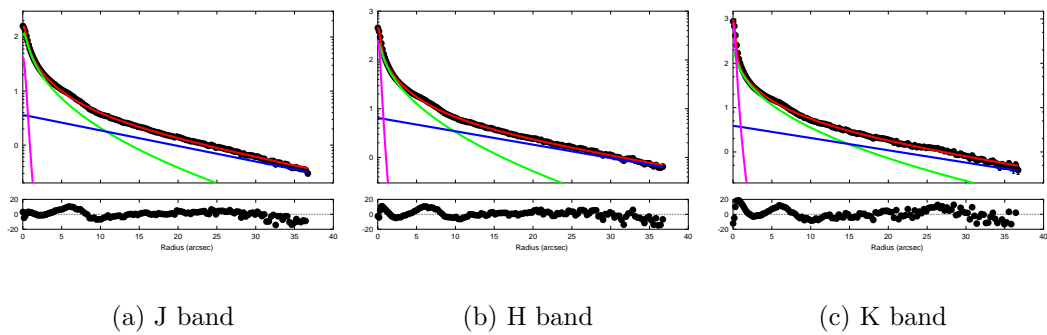


Figure 4.15: Radial surface brightness profile fitting of J, H and K bands of galaxy NGC 1320. The axis and colors are the same as in the previous figures.

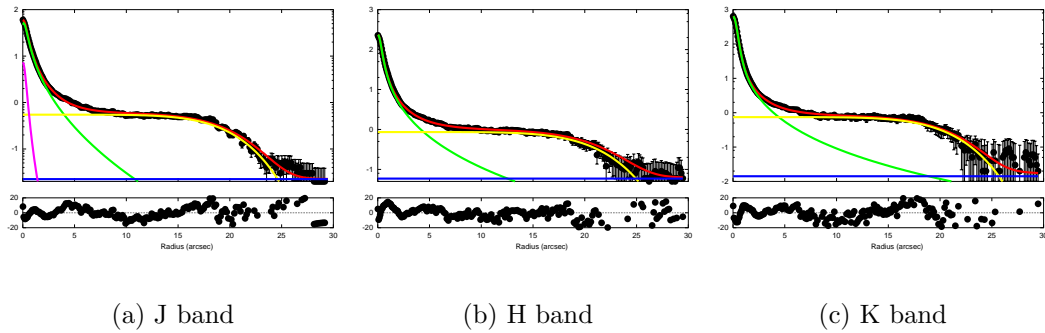


Figure 4.16: Radial surface brightness profile fitting results of J, H and K bands of IRAS 03362-1642. The axis and colors are the same as in the previous figures. In this case, only in the J band a nuclear component was fitted, although very weak. This galaxy is classified as barred, with a very dominant bar, and the fits corroborate it.

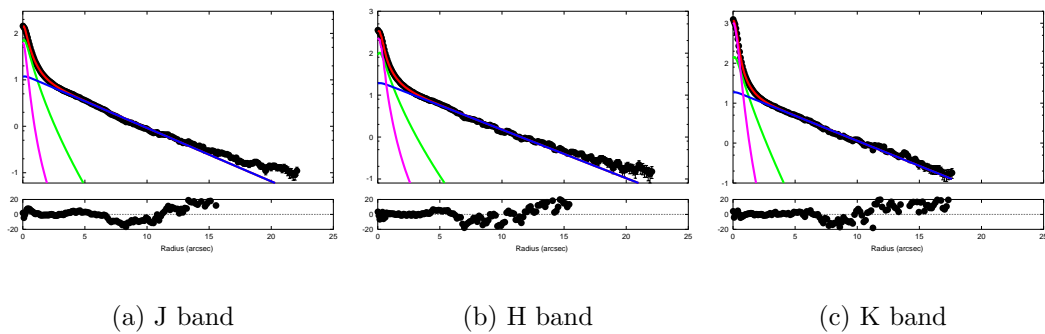


Figure 4.17: Radial surface brightness profile fitting results for J, H and K bands of IRAS 04385-0828. The axis and colors are the same as in the previous figures.

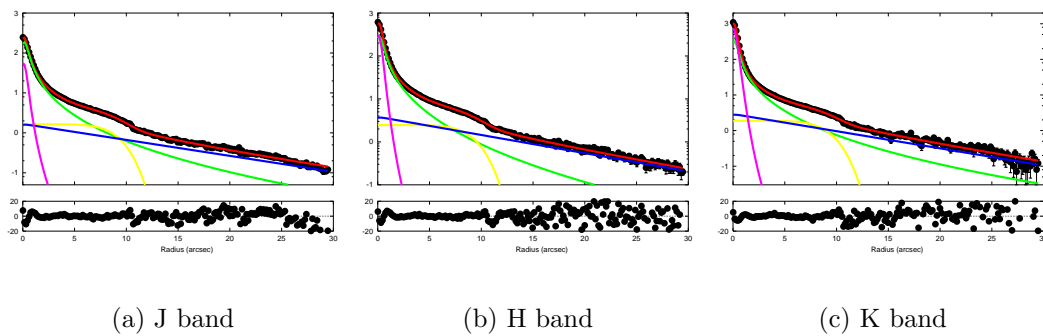


Figure 4.18: Radial surface brightness profile fitting of J, H and K bands of galaxy ESO 33-G2. The axis and colors are the same as in the previous figures. A rather weak bar is fitted to the profiles, agreeing with the optical classification.

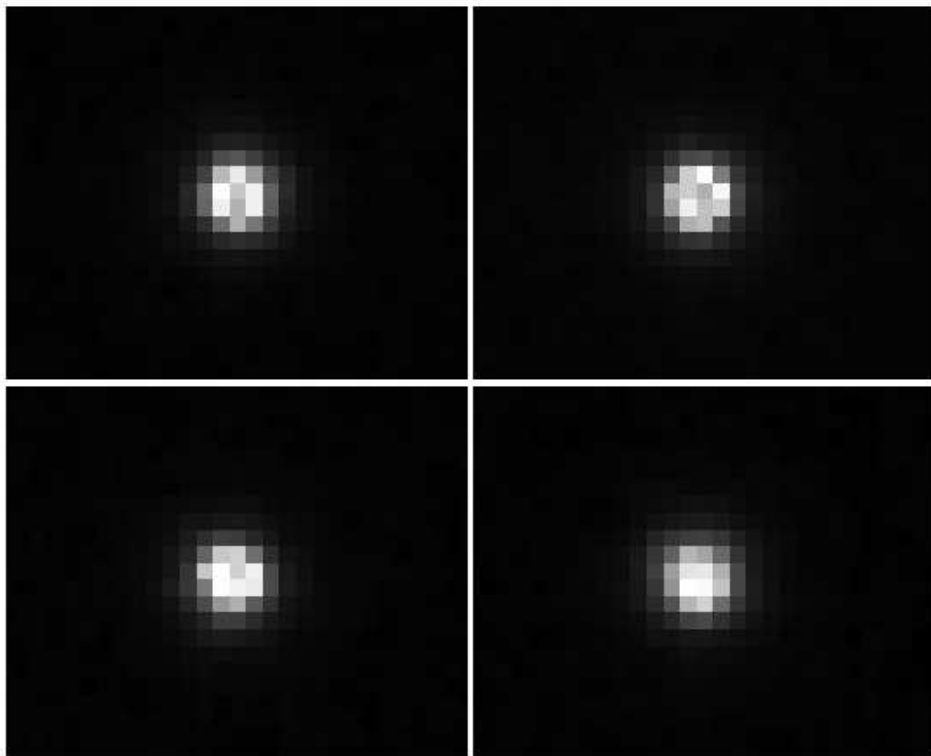


Figure 4.19: Four raw images in the K band of galaxy IRAS 05189-2524. The obscured central pixels are evident.

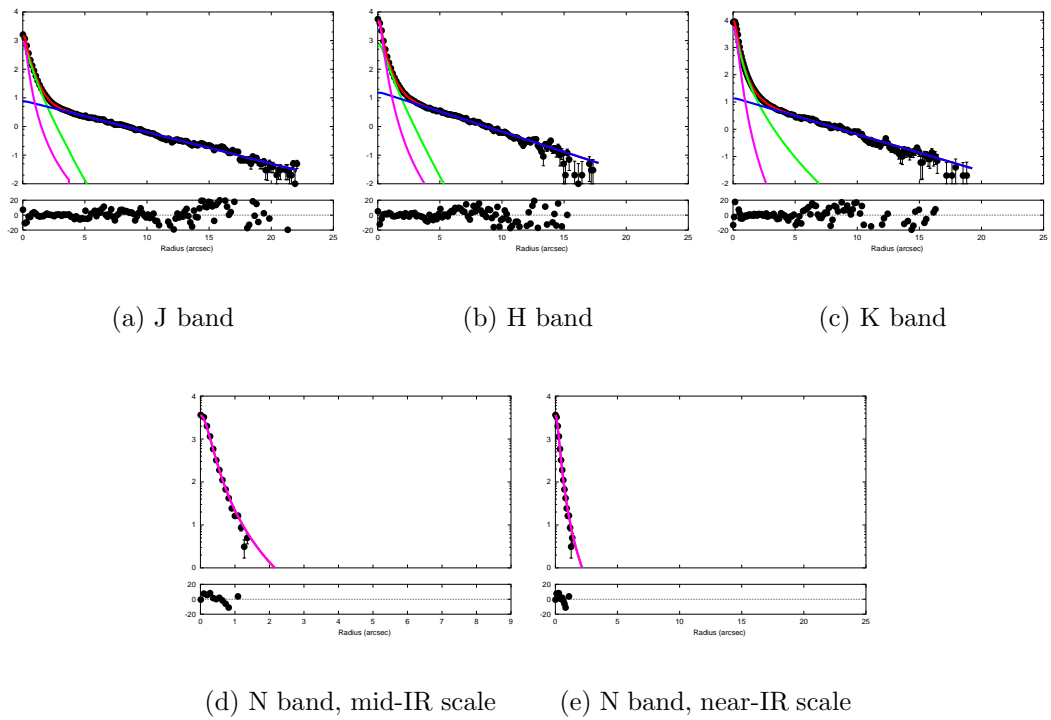
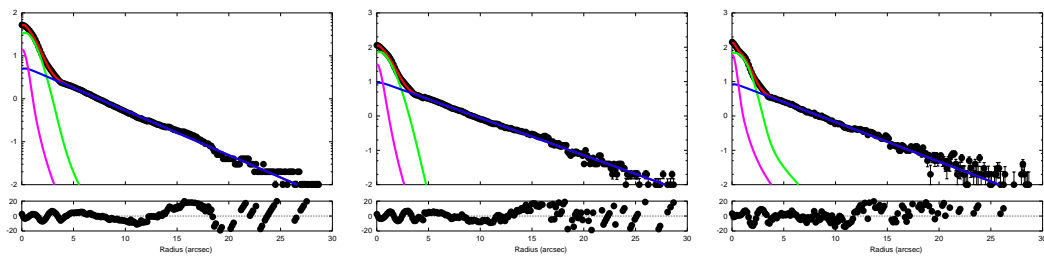


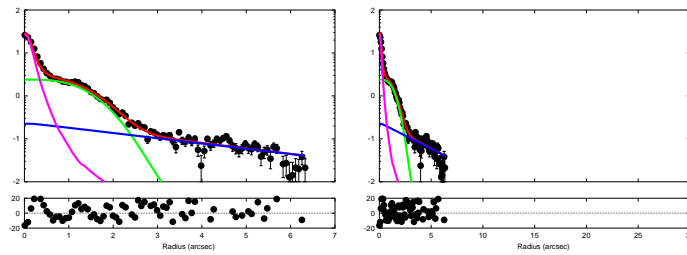
Figure 4.20: Radial surface brightness profile fitting of J, H, K, and N bands of IRAS 05189-2524. The axis and colors are the same as in the previous figures. It is clear that the N-band observation corresponds completely to nuclear emission.



(a) J band

(b) H band

(c) K band



(d) L band, mid-IR scale

(e) L band, near-IR scale

Figure 4.21: Radial surface brightness profile fitting of J, H, K and L bands of MCG +0-29-23. The axis and colors are the same as in the previous figures. The parameters values barely change from one band to another, and all the 3 components are clearly seen even in the L-band profile.

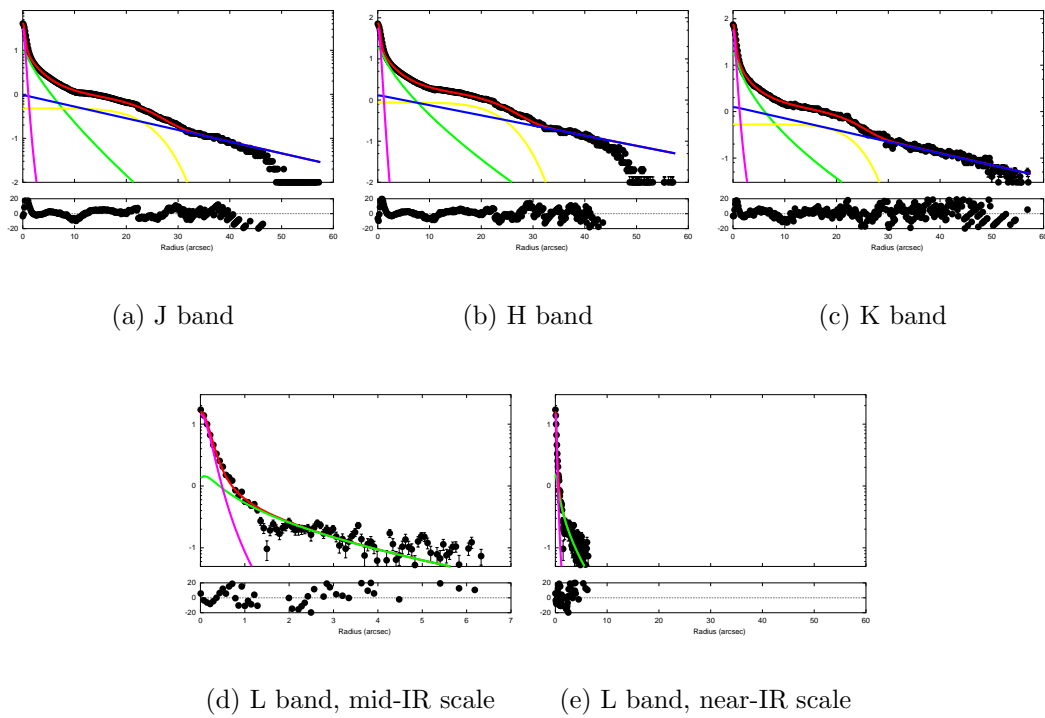
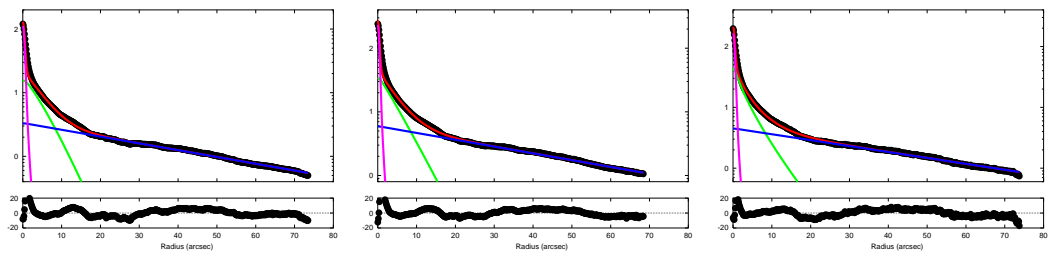


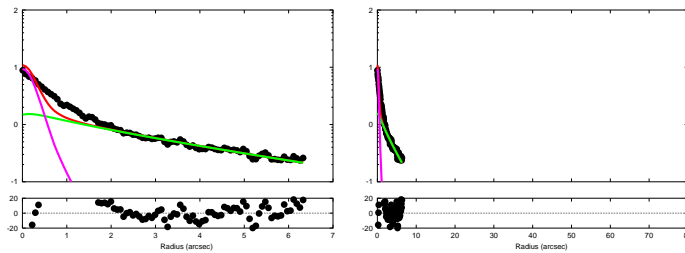
Figure 4.22: Radial surface brightness profile fitting of J, H, K and L bands of NGC 3660. The axis and colors are the same as in the previous figures. This galaxy is very big, and due to the small size of the detector the disk has been truncated in the J and H band. See text for details.



(a) J band

(b) H band

(c) K band



(d) L band, mid-IR scale

(e) L band, near-IR scale

Figure 4.23: Radial surface brightness profile fitting of J, H, K, and L bands of NGC 4501. The axis and colors are the same as in the previous figures. The nuclear contribution is computed as $F_{nuc} = F_{gal} - F_{bul}$ due to the change in seeing conditions between the observation of the galaxy and the PSF star.

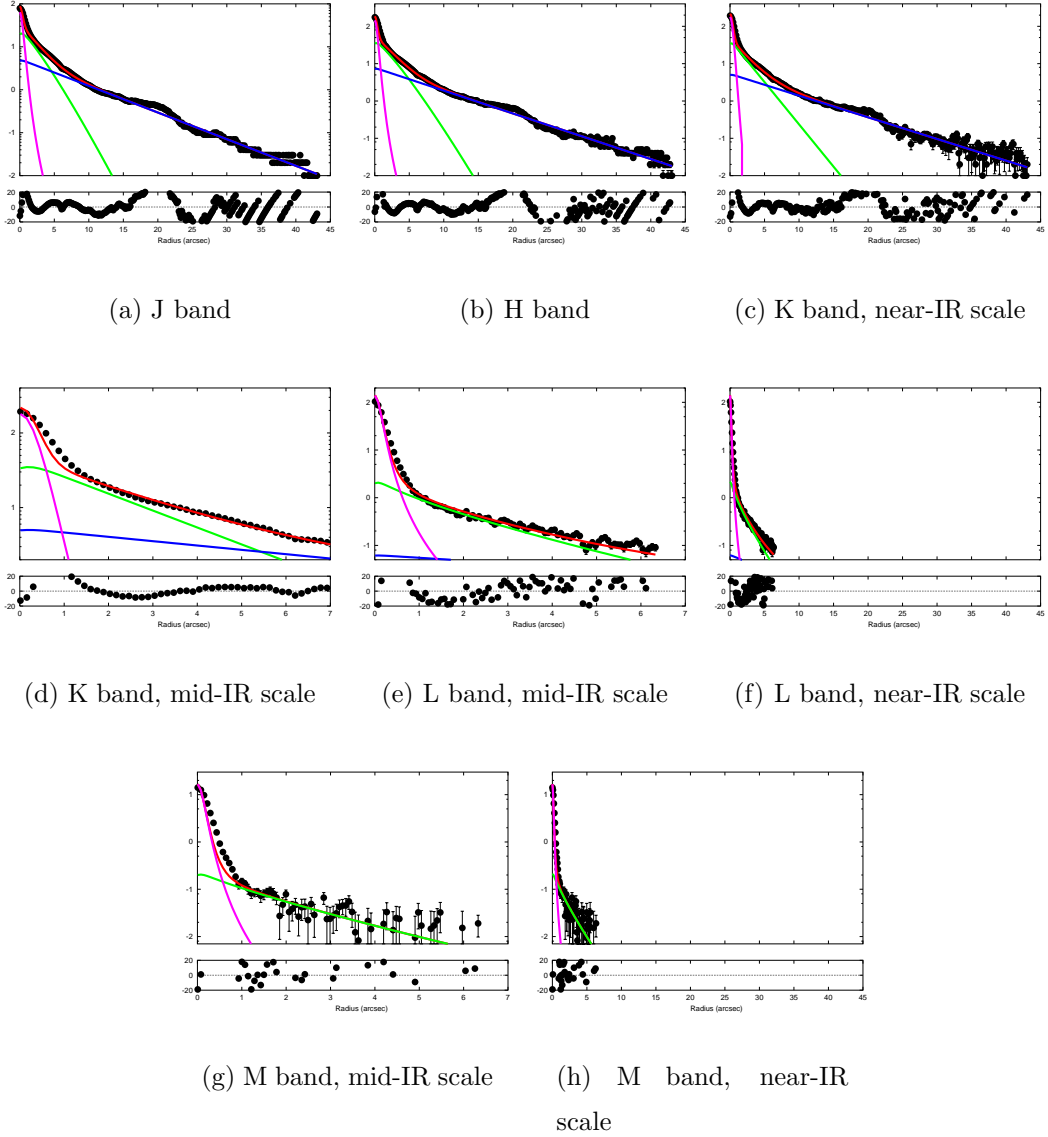


Figure 4.24: Radial surface brightness profile fitting of J, H, K, L and M bands of TOL 1238-364. The axis and colors are the same as in the previous figures. In the near-IR bands we do not fit the bump produced by the end of the flocculent arms (between 16'' and 23''). A close-up into the central region of K-band profile is shown (d), in order to visualize which components should be expected at mid-IR scale. The nuclear contribution in M band is computed as $F_{nuc} = F_{gal} - F_{bul}$.

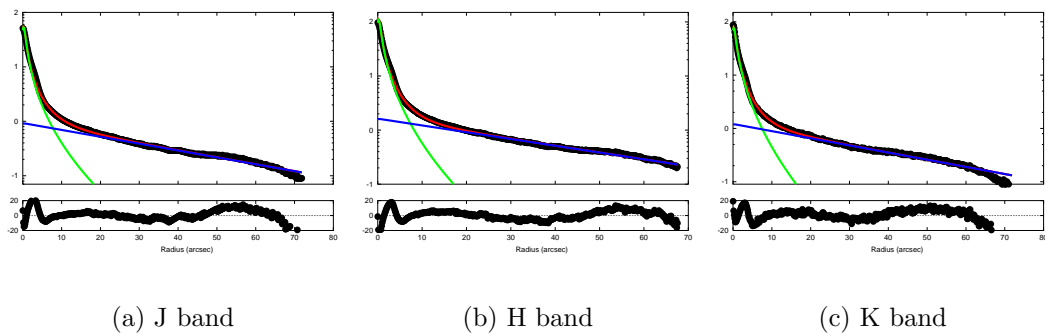
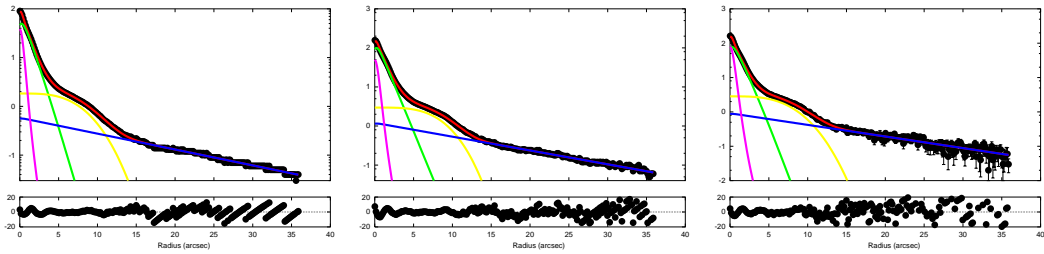


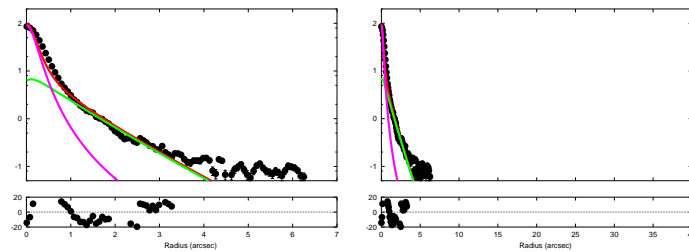
Figure 4.25: Radial surface brightness profile fitting of J, H, and K bands of galaxy NGC 4941. The axis and colors are the same as in the previous figures. No nucleus is fitted in any of the 3 bands (see text).



(a) J band

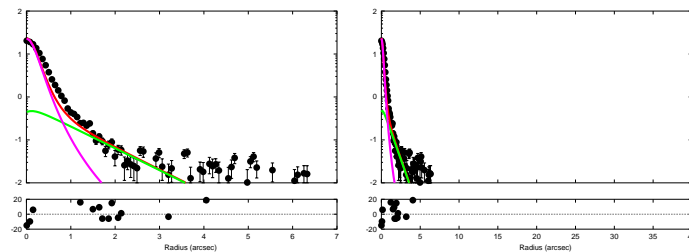
(b) H band

(c) K band



(d) L band, mid-IR scale

(e) L band, near-IR scale



(f) M band, mid-IR scale

(g) M band, near-IR scale

Figure 4.26: Radial surface brightness profile fitting of J, H, K, L and M bands of MCG -3-34-64. The axis and colors are the same as in the previous figures. The nuclear contribution is calculated as $F_{nuc} = F_{gal} - F_{bul}$ in the mid-IR observations, due to a probable change in seeing conditions.

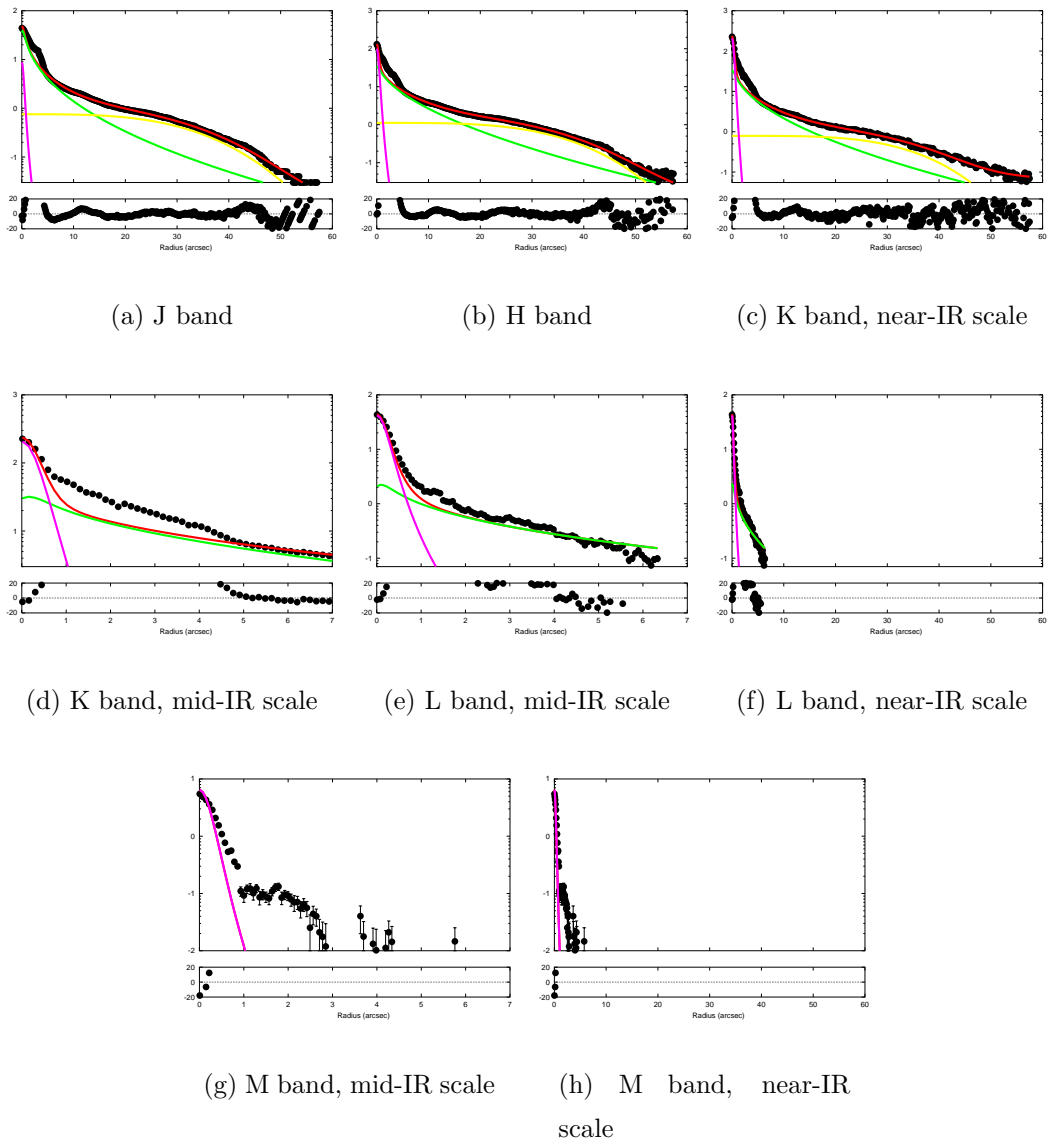
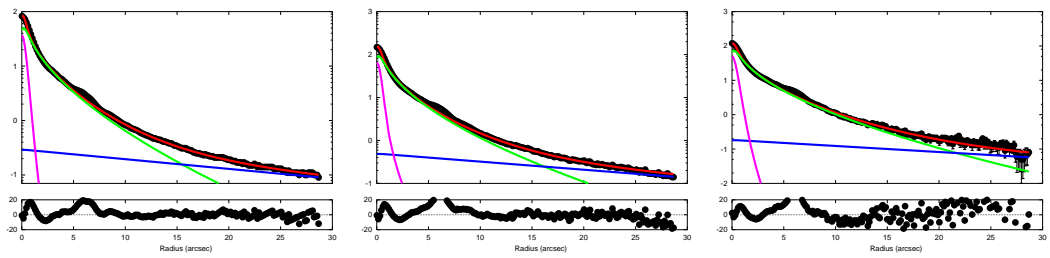


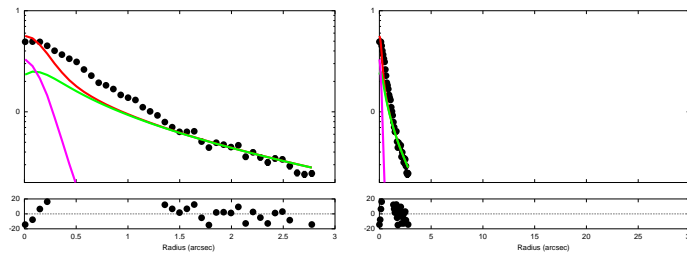
Figure 4.27: Radial surface brightness profile fitting of J, H, K, L and M bands of NGC 5135. The axis and colors are the same as in the previous figures. The fit skips the region between $1''$ and $3''$, avoiding the strong star-forming structure. (d) is a close-up of the central region in the K band profile, in order to visualize the expected contributions in the mid-IR scale. The M band profile looks broader than the PSF star, and we assume it is produced by a change in the seeing conditions, so the nuclear flux is computed through the integration of the galaxy profile until $r = 14 \text{ pix} = 1''$.



(a) J band

(b) H band

(c) K band



(d) L band, mid-IR scale

(e) L band, near-IR scale

Figure 4.28: Radial surface brightness profile fitting of J, H, K and L bands of galaxy NGC 5953. The axis and colors are the same as in the previous figures. As can be seen in (d), the seeing is very bad in the observation of the galaxy, compared to that of the PSF star, so $F_{nuc} = F_{gal} - F_{bul}$.

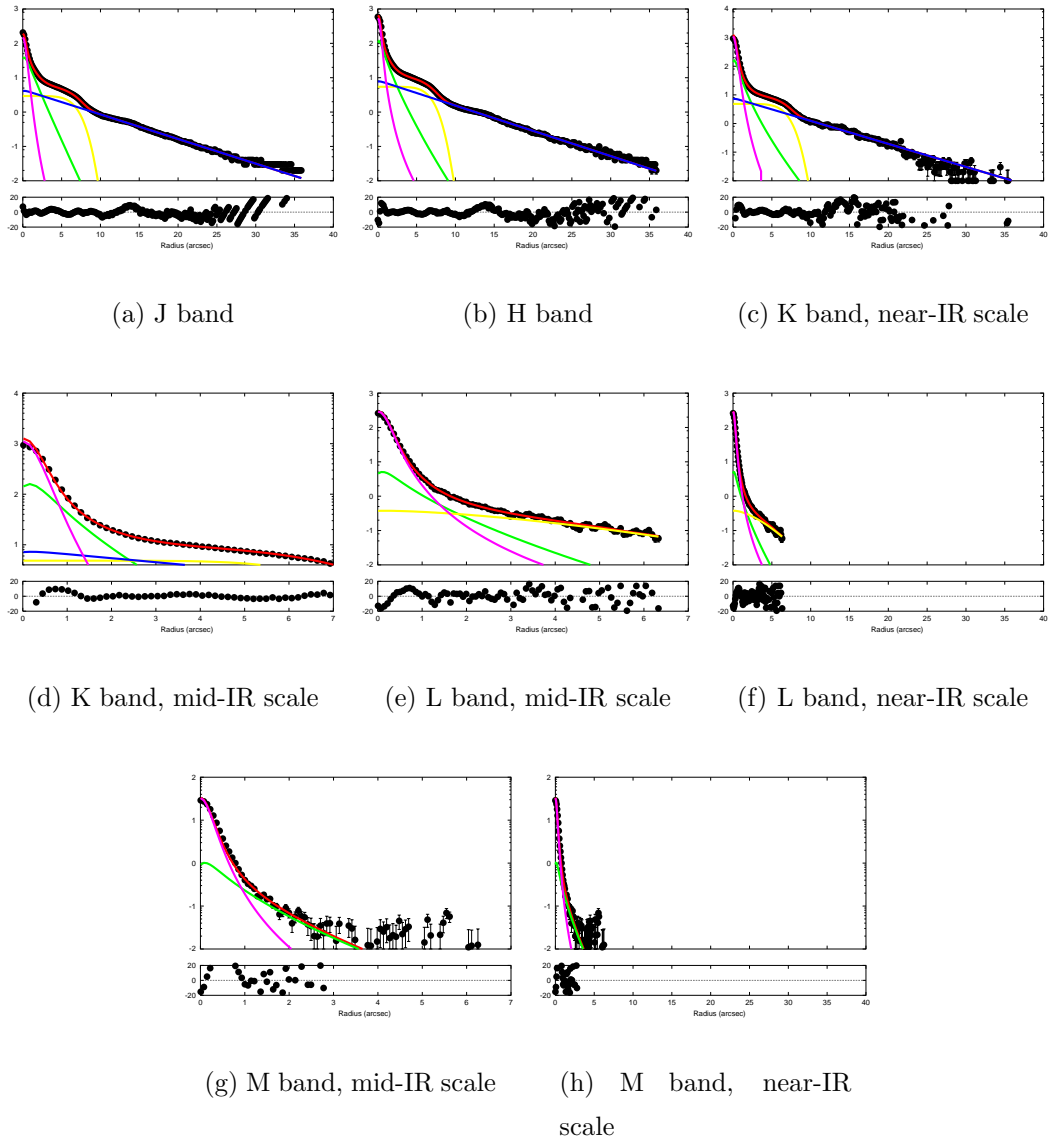


Figure 4.29: Radial surface brightness profile fitting of J, H, K, L and M bands of galaxy MCG -2-40-4. The axis and colors are the same as in the previous figures, except for the yellow curve in (e) and (f), which in these cases represent a mixture of bar and disk (see text for details).

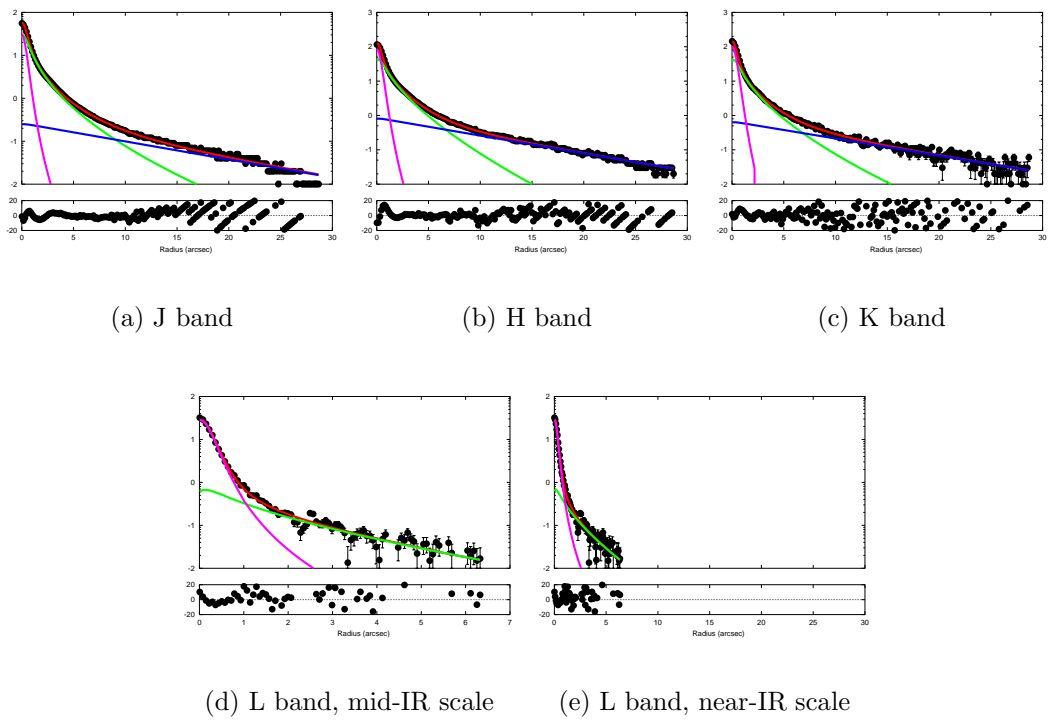


Figure 4.30: Radial surface brightness profile fitting of J, H, K, and L bands of IRAS 15480-0344. The axis and colors are the same as in the previous figures.

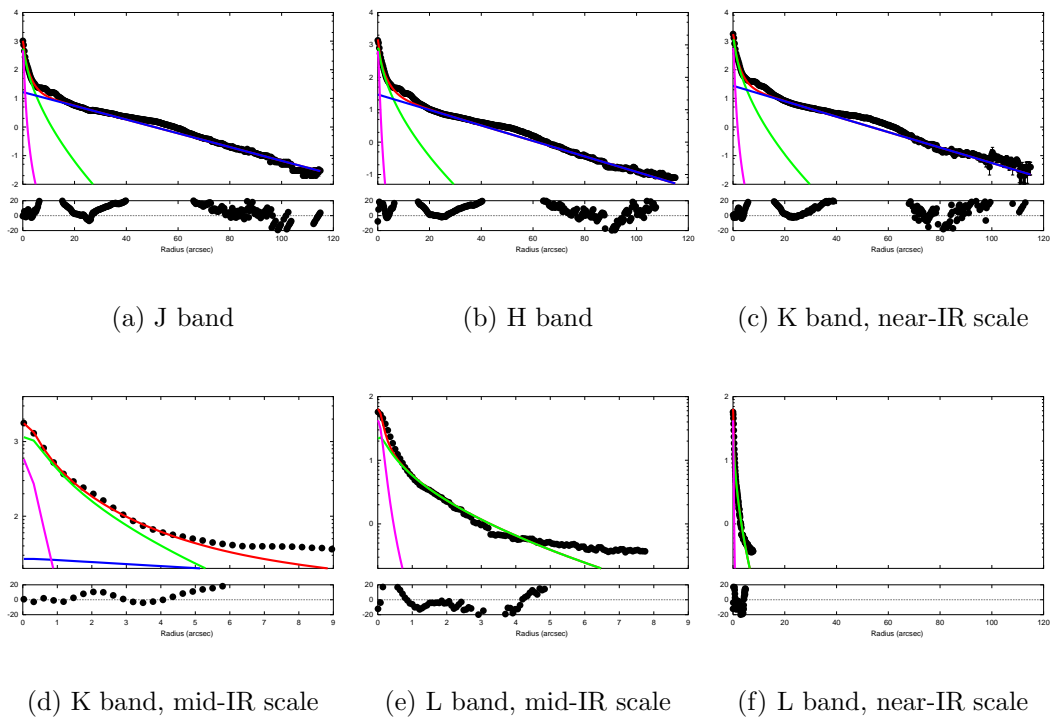
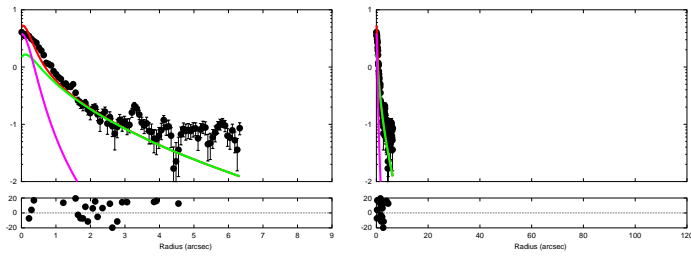
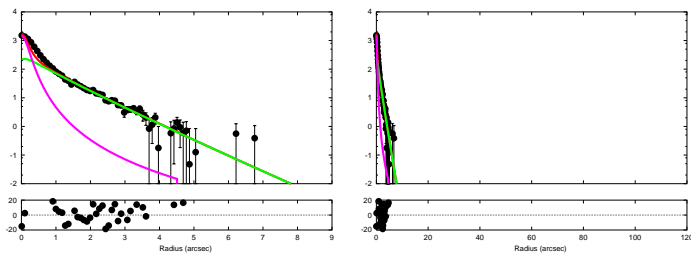


Figure 4.31: Surface brightness profile fitting of J, H, K, L, M and N bands of NGC 6810. The axis and colors are the same as in the previous figures. The close-up in K (d) band allows to discard the emission beyond $r=6''$ in the L band. The emission beyond $r=4''$ in the M band comes from the sky. This is an exceptional case of the N band observations, the bulge can be fitted in spite of the change in seeing conditions.



(g) M band, mid-IR scale

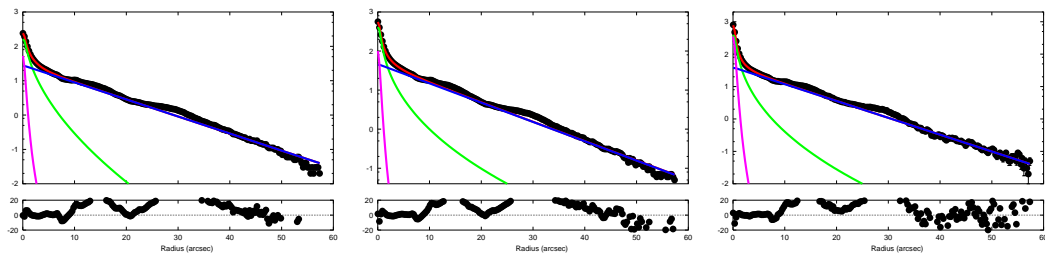
(h) M band near-IR scale



(i) N band, mid-IR scale

(j) N band, near-IR scale

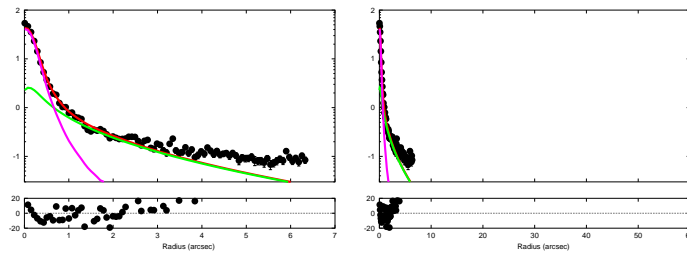
Figure 4.31: Continued



(a) J band

(b) H band

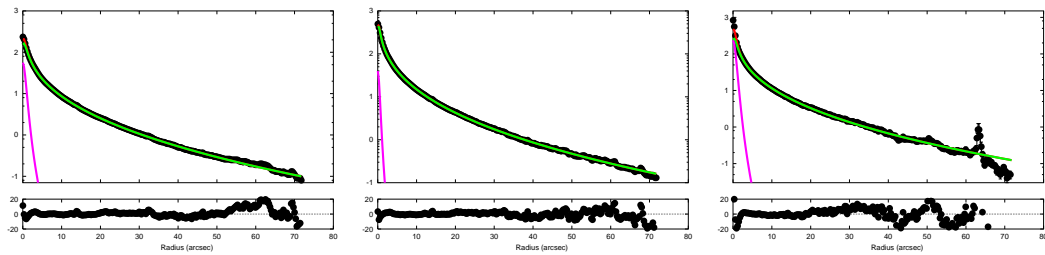
(c) K band



(d) L band, mid-IR scale

(e) L band, near-IR scale

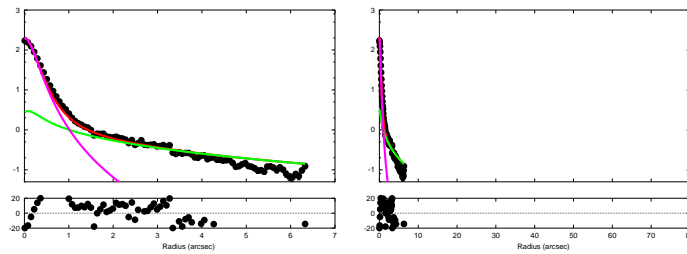
Figure 4.32: Radial surface brightness profile fitting of J, H K, and L bands of NGC 6890. The axis and colors are the same as in the previous figures. The bumps at $r \approx 15''$ and $r \approx 30''$, are exclude from the model fit since they correspond to the end of the flocculent arms.



(a) J band

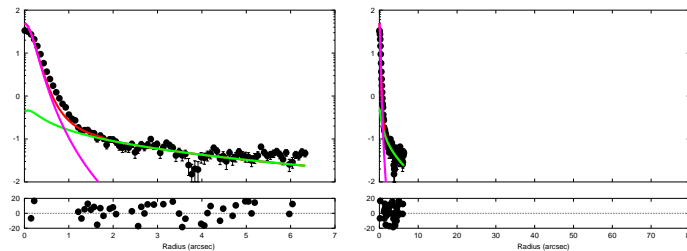
(b) H band

(c) K band



(d) L band, mid-IR scale

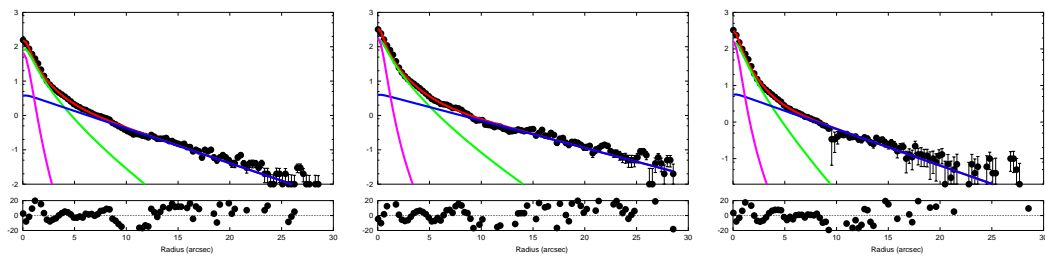
(e) L band, near-IR scale



(f) M band, mid-IR scale

(g) M band, near-IR scale

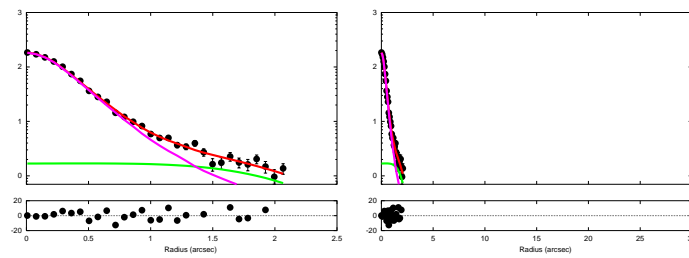
Figure 4.33: Radial surface brightness profile model fit of J, H, K, L, and M bands of IC 5063. The axis and colors are the same as in the previous figures. This galaxy is classified as SA0 and the preferred fits are consistent.



(a) J band

(b) H band

(c) K band



(d) L band, mid-IR scale

(e) L band, near-IR scale

Figure 4.34: Radial surface brightness profile model fit of J, H, K, and L bands of Markarian 897. The axis and colors are the same as in the previous figures.

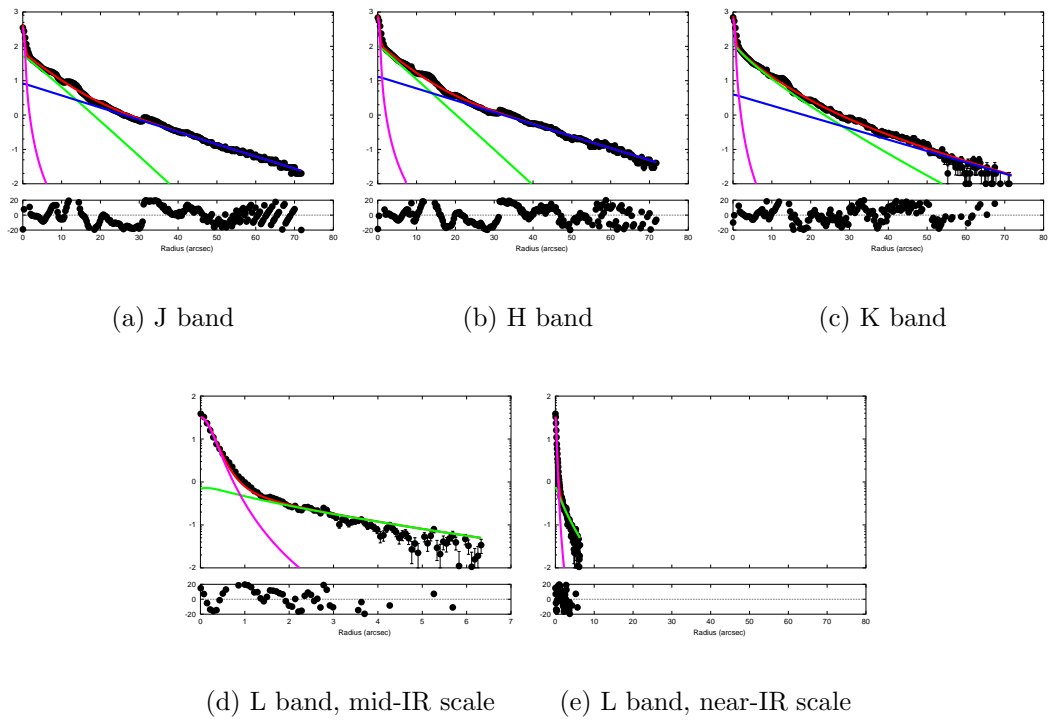


Figure 4.35: Radial surface brightness profile model fit of J, H, K and L bands of NGC 7130. The axis and colors are the same as in the previous figures. In the M band, the galaxy looks almost pointlike so no fit is needed.

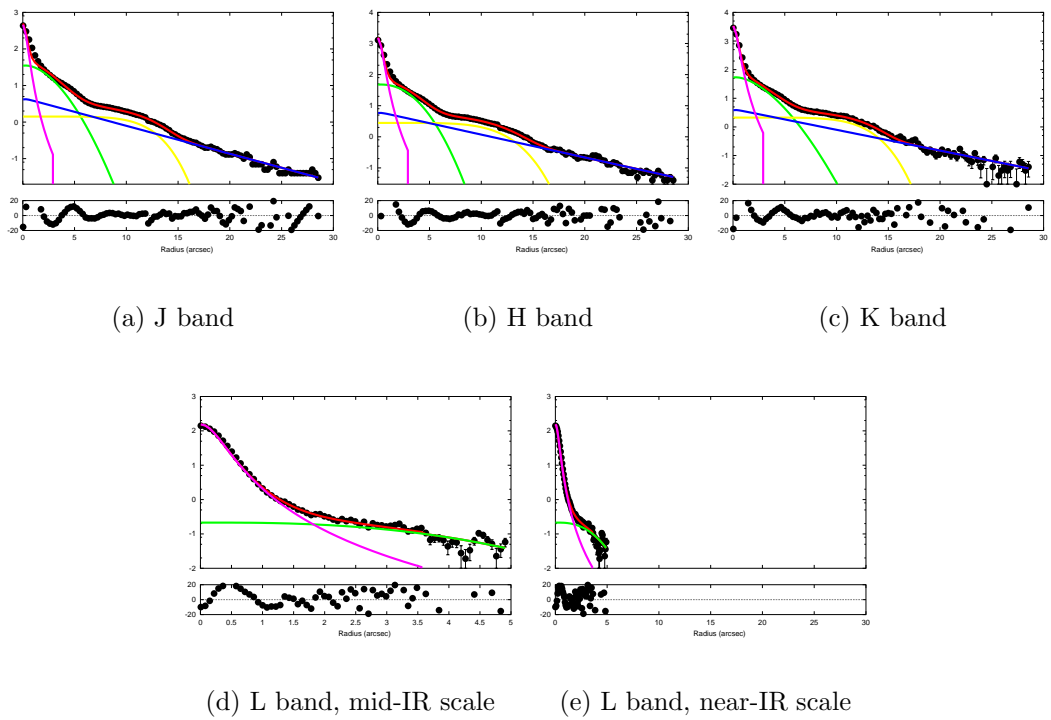
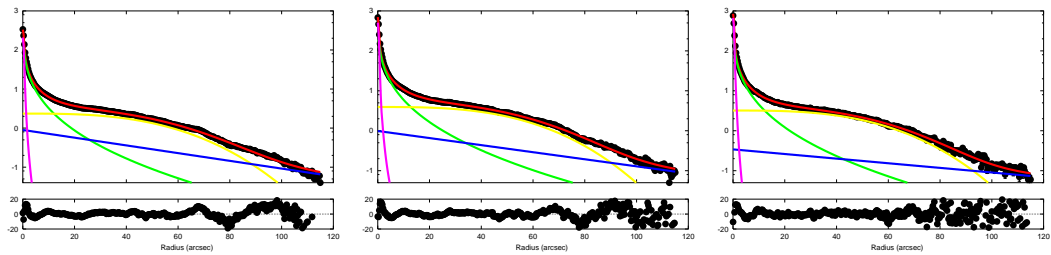


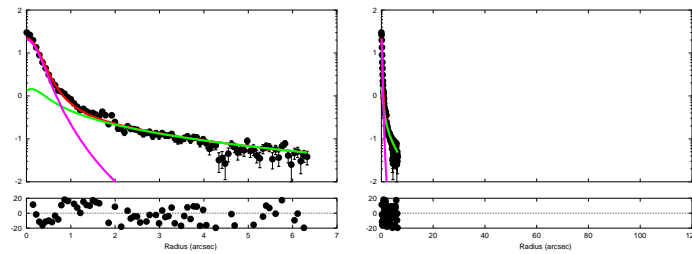
Figure 4.36: Radial surface brightness profile model fit of M and L bands of MCG -3-58-7. The axis and colors are the same as in the previous figures.



(a) J band

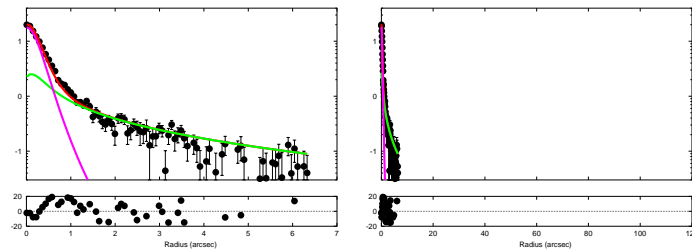
(b) H band

(c) K band



(d) L band, mid-IR scale

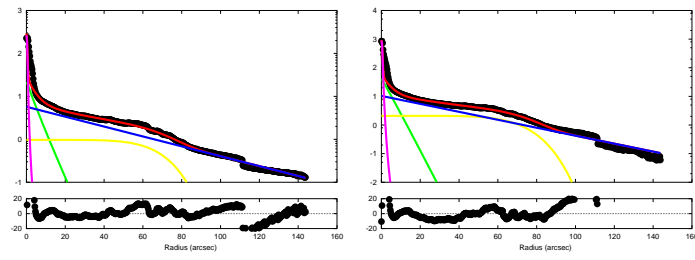
(e) L band, near-IR scale



(f) M band, mid-IR scale

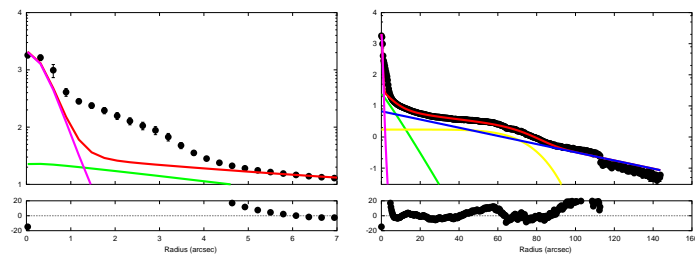
(g) M band, near-IR scale

Figure 4.37: Radial surface brightness profile model fit of J, H, K, L, and M bands of NGC 7496. The axis and colors are the same as in the previous figures. This galaxy has a very strong and big bar, as can be noted in the near-IR profiles.



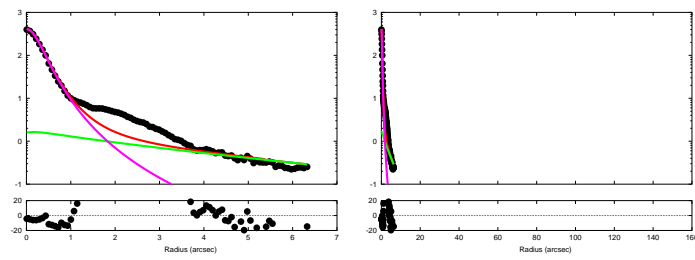
(a) J band

(b) H band



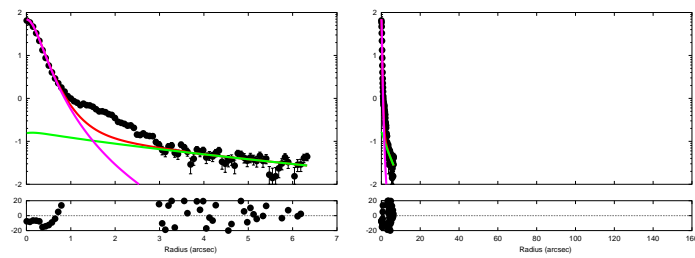
(c) K band, mid-IR scale

(d) K band, near-IR scale



(e) L band, mid-IR scale

(f) L band, near-IR scale



(g) M band, mid-IR scale

(h) M band, near-IR scale

Figure 4.38: Radial surface brightness profile model fit of J, H, K, L, and M bands of NGC 7582. The axis and colors are the same as in the previous figures. A strong star-forming region near $r \approx 2.5''$ (c) is excluded from the fits in all bands.

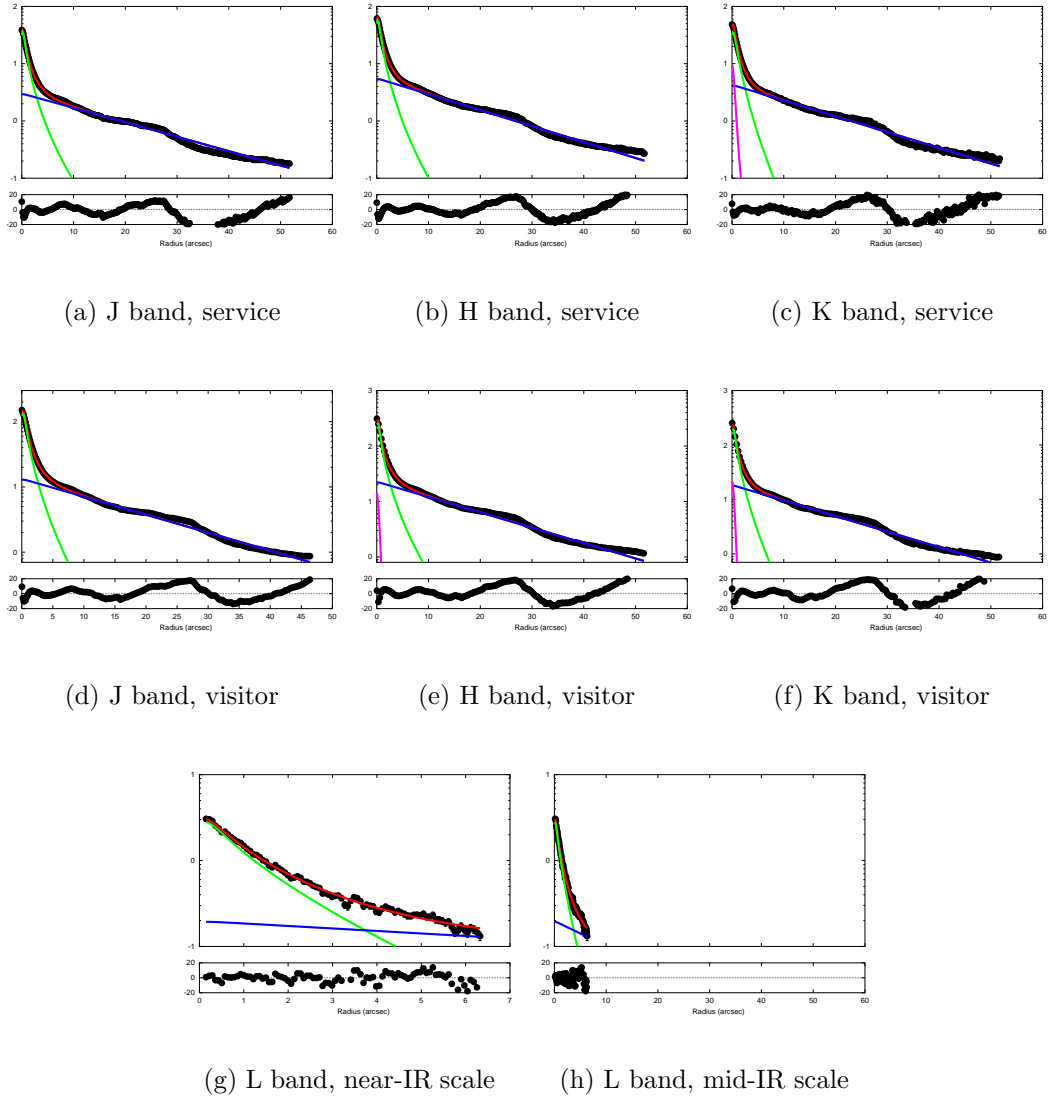


Figure 4.39: Radial surface brightness profile model fit of J, H, K, L and M bands of NGC 7590. The axis and colors are the same as in the previous figures. This galaxy was observed twice in the near-IR bands, in service and visitor modes with Sofi. In both cases, there is no detectable point source in the J band. And the 3 cases where it is detected, it contributes less than 0.3% to the total light. In the L band, no point source is detected either. See text for details.

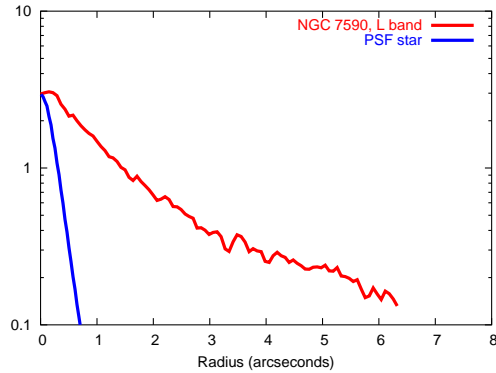


Figure 4.40: Comparison of PSF star and galaxy radial surface brightness profiles of L band of galaxy NGC 7590. It is evident that the galaxy is extended unless a strong variation in seeing conditions degraded the galaxy image at a level where no point source can be detected. Adding the fitting results in the near-IR and the resulting *Spitzer* spectra after star-formation subtraction, it seems this galaxy has at most a very weak AGN.

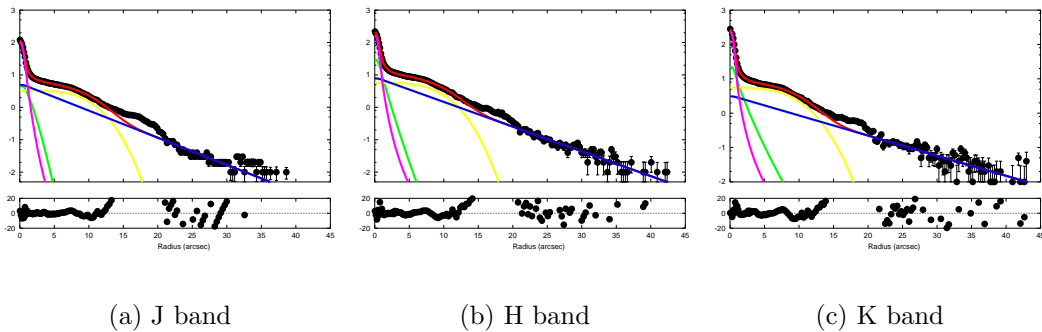


Figure 4.41: Radial surface brightness profile fitting of J, H, and K bands of galaxy CGCG 381-051. The axis and colors are the same as in the previous figures. The fit does not include the region between $r \approx 15$ and $r \approx 20$ arcseconds, which corresponds to the end of the galaxy's arms.

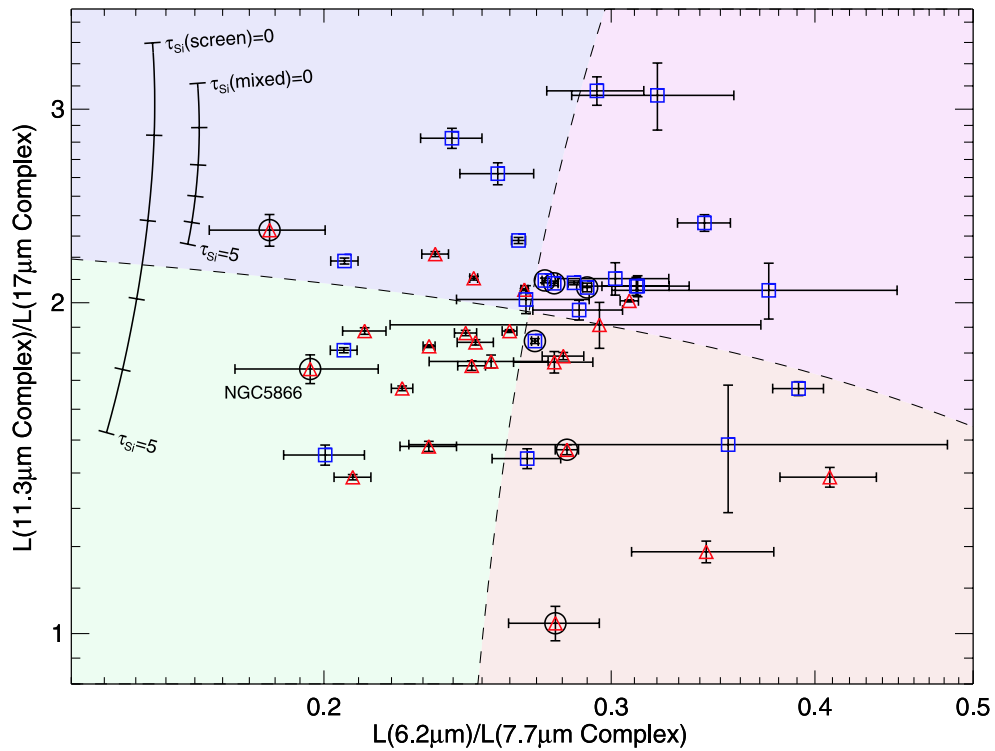


Figure 4.42: Interband strength ratios of the four main PAH bands at 6.2, 7.7, 11.3, and $17\mu\text{m}$ present in *Spitzer*-IRS of Smith *et al.* (2007). Red triangles indicate galaxies with AGN (Seyfert or LINER) types, whereas blue squares are galaxies with HII-dominated nuclei. Galaxies with measurable silicate absorption ($\tau_{Si} > 0.01$) are circled. The highlighted regions indicate zones used for the construction of template spectra shown in Fig. 4.43. Fig. from Smith *et al.* (2007).

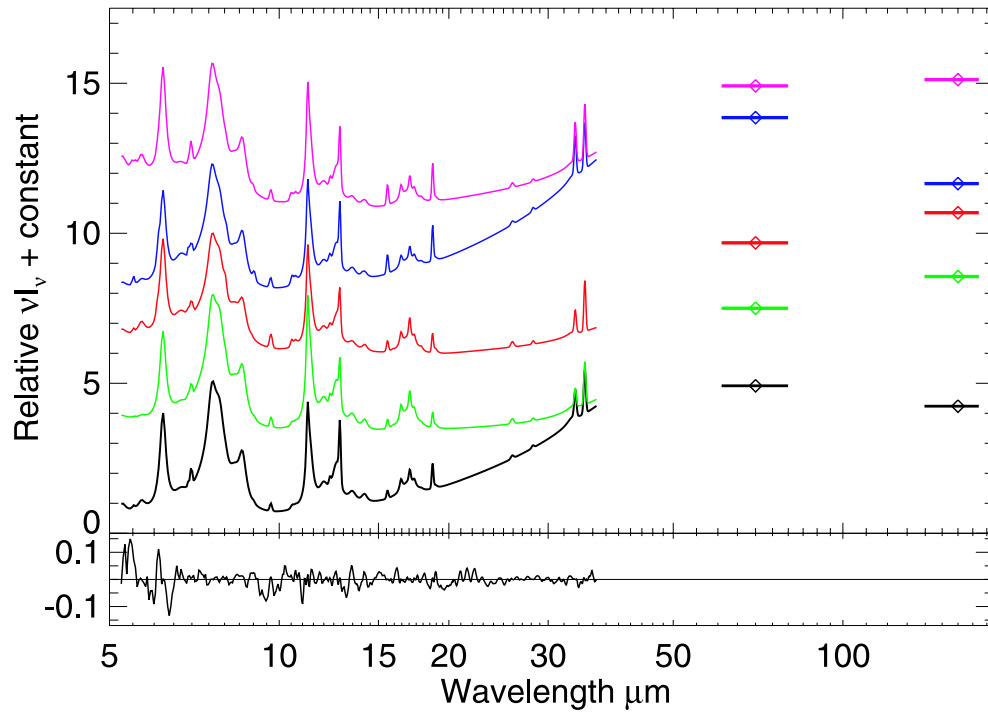
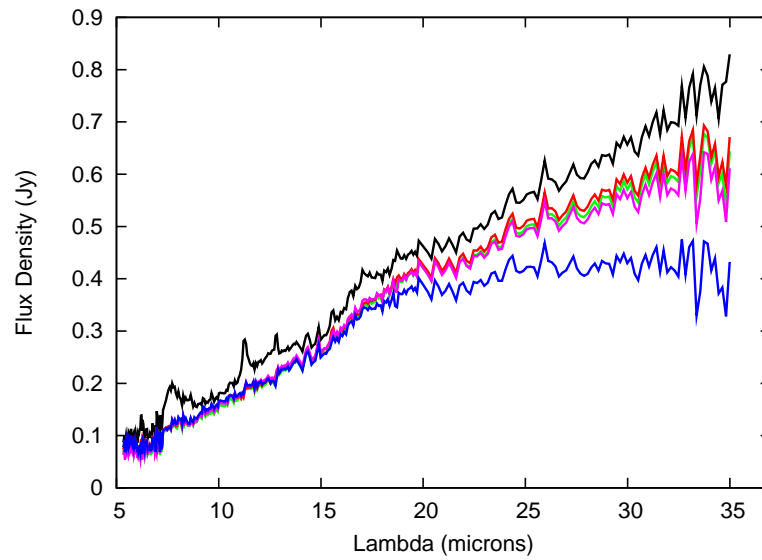
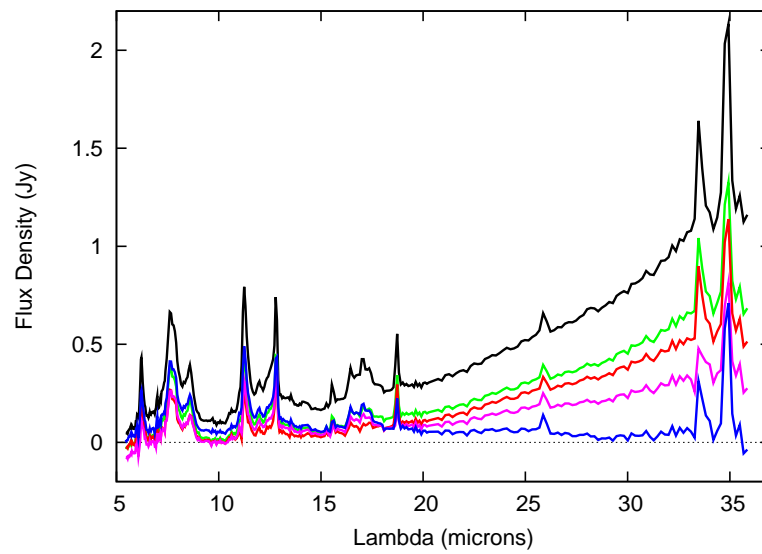


Figure 4.43: Noise-free mid-IR templates, produced by a total IR luminosity-weighted average of all spectra (black) and from subsample means for each region in Fig. 4.42 (colors). The units are arbitrary I_ν , with a constant offset of 2.5 units between each spectra. Mean matched 70 and 160 μm intensities are also shown. The bottom panel contains the normalized residuals (model spectrum)/model, averaged over the sample, with 20% trimmed from the extremes of the distribution. Fig. from Smith *et al.* (2007).



(a) MCG-3-58-7



(b) NGC 5953

Figure 4.44: Examples of extreme subtracted spectra: observed spectra (black) and the subtracted spectra using the four templates of Smith *et al.* (2007) (magenta, blue, red, and green). The top panel shows the subtraction of MCG-3-58-7, where the PAH features almost completely disappear, opposed to the subtracted spectra of NGC 595 (bottom panel), where the PAH residuals remain very strong. The main differences between the templates starting at $\lambda \approx 20 \mu\text{m}$ are evident.

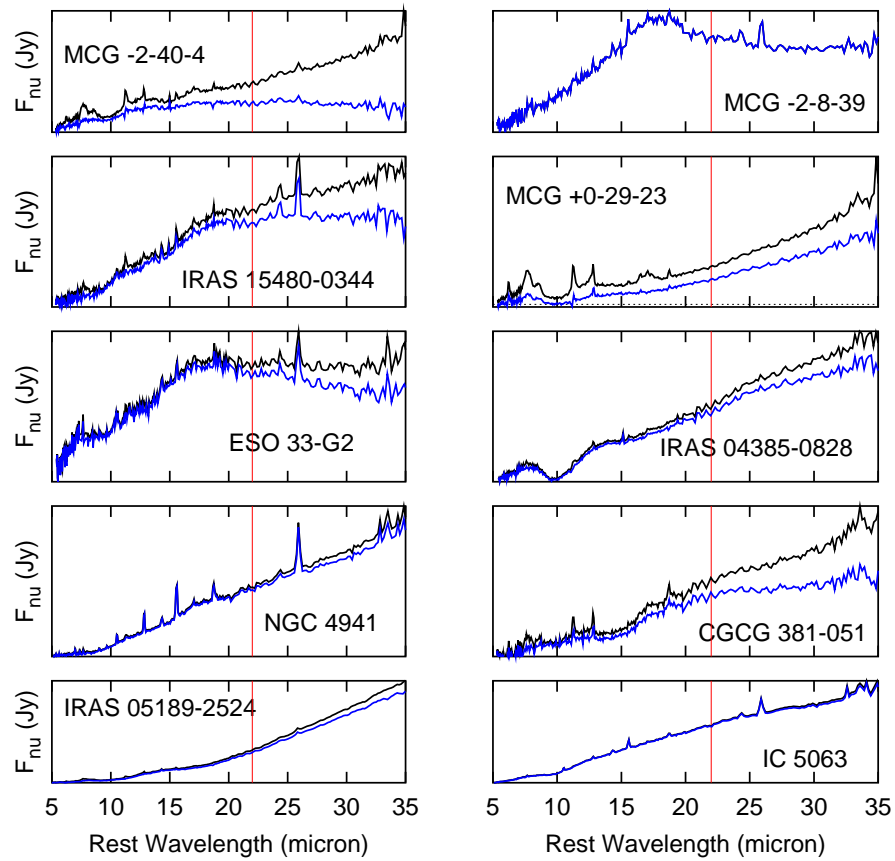


Figure 4.45: *Spitzer*-IRS spectra without star formation. The black line indicates the reduced spectra shown in Fig. 3.10, the blue line is the star formation subtracted spectra, and the red vertical line is the limited from where the star formation subtraction begins to be too much uncertain (see text for details).

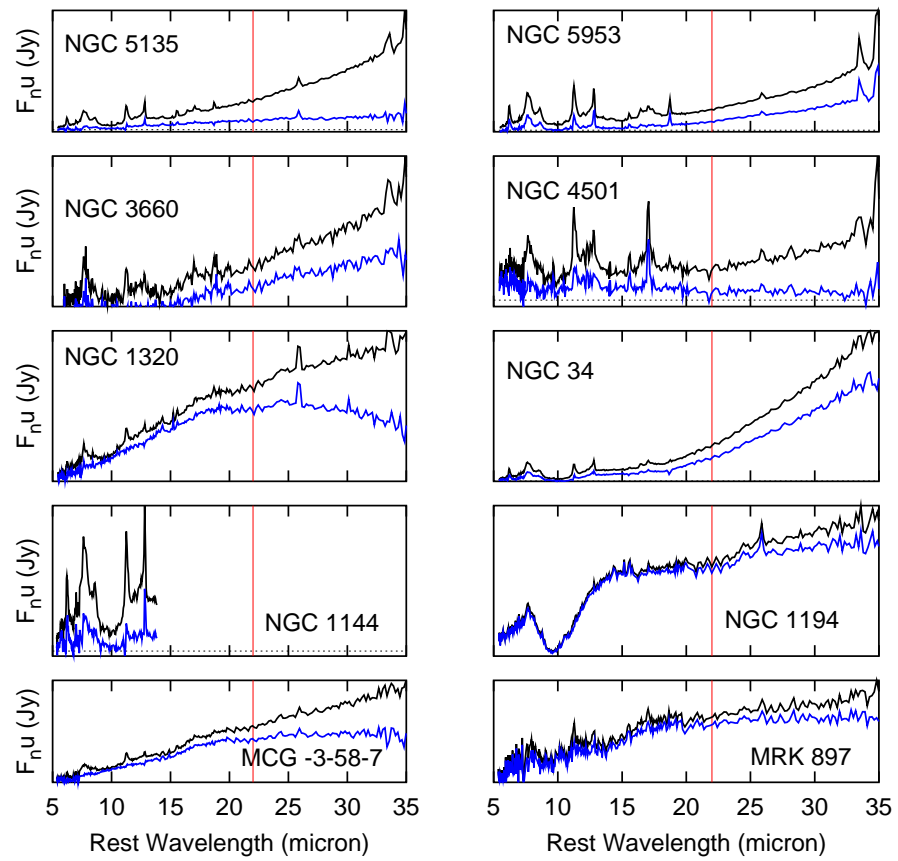


Figure 4.45: Continued

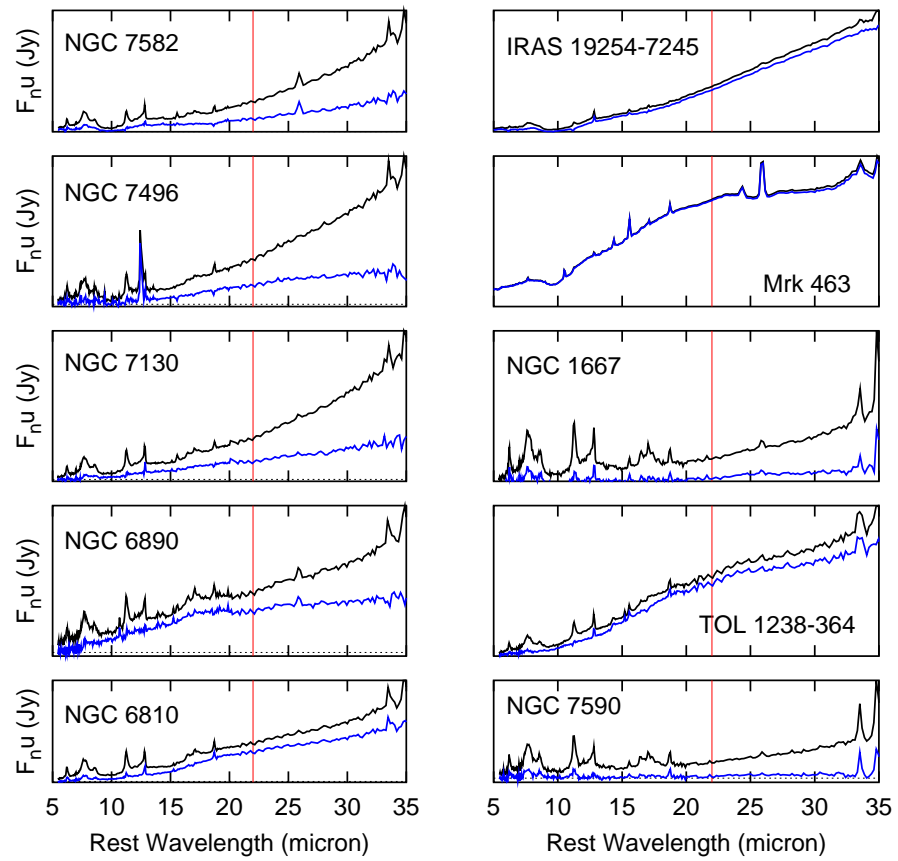


Figure 4.45: Continued

Chapter 5

Modeling the SEDs

Once we have separated the nuclear emission from the light coming from the galaxy, we can construct the nuclear infrared Spectral Energy Distribution (SED). Each point of the SED corresponds to the calibrated flux of the nuclear component obtained from the fitted galaxy's profiles, and the error bar is a combination of the flux calibration and the fitting process (explained in detail in Sec 4.2.3). The “star-formation cleaned” *Spitzer*-IRS spectra are included in the SEDs, scaled to the photometric point in the N band, when available.

There are some bands where the galaxy was not detected. In these cases an upper limit is calculated as 2 times the root mean square (RMS) of the background level in the raw images. These upper limits are introduced in the corresponding nuclear SED, and are represented as blue arrows. Also, there is one case where the emission is so weak that it was impossible to construct a brightness profile. In this case all the detected emission is included in the SED, but it is considered as an upper limit.

As the fitted stellar components in the surface brightness profiles are consistent from one band to another, we expect that the SEDs show the correct shape. Even if one structural component is slightly overestimated or underestimated, the SED will not be affected showing only a net shift. But, in bands where the galaxy looks point-like, or when a good representation of the PSF was not available, specially in the M and N bands, no profile fitting is performed and all the emission is assumed as nuclear. If this assumption is correct, and the stellar components of the shorter wavelengths are over- or underestimated, the shape of the SED will be distorted and the best torus emission models will yield inaccurate results.

We compare our observed SEDs with 2 of the last published torus emission models (described in detail in Chapter 2). The first is the model of Fritz *et al.* (2006), a flared, smooth disk of gas and dust, with proper treatment of sublimation temperature differences between the dust types (silicates and carbon). The second model is that proposed by Nenkova *et al.* (2008), where the torus is modeled as a clumpy distribution of gas and dust.

In order to include the spectra in the modeling, we give each point an error in such a way that all the spectral points included have a similar weight than the photometric points:

$$\frac{1}{\sum 1/\sigma_{\text{phot}}^2} = \frac{1}{\sum 1/\sigma_{\text{spec}}^2} \quad (5.1)$$

$$\Rightarrow \sigma_{\text{spec}} = \sqrt{\frac{N_{\text{spec}}}{\sum \sigma_{\text{phot}}^{-2}}}, \quad (5.2)$$

Where σ_{phot} are the photometric errors, σ_{spec} are the errors of each point of the spectra, and N_{spec} is the

number of points of the spectra included in the modeling.

5.1 Continuous Model

Fritz *et al.* (2006) investigated a rather small parameter space, as shown in Table 2.1, including not only more realistic distributions but also cases with dust density increasing with the radius.

We programmed a simple routine that calculates the scaling factor needed to move the model toward the SED points and then, calculates the χ^2 of each model. The 20 models with lowest χ^2 are included in the final analysis.

The scaling factor α is obtained from:

$$\chi^2 = \sum_{i=1}^N \frac{(y_i - \alpha \cdot y(x_i))^2}{\sigma_i^2}, \quad (5.3)$$

where y_i are the SED and spectral points, $y(x_i)$ are the model points, σ_i are the errors of the SED and the spectra, and N is the number of photometric points in the SED plus the number of points of the spectra included in the minimization (we do not include the spectra further of $\lambda \approx 20\mu\text{m}$ as mentioned in 4.5). To obtain α , we minimize:

$$\begin{aligned} \frac{d\chi^2}{d\alpha} &= 0 & (5.4) \\ 2 \cdot \sum_{i=1}^N \frac{y_i - \alpha y(x_i)}{\sigma_i^2} \cdot y(x_i) &= 0 \\ \Rightarrow \sum_{i=1}^N \frac{y_i \cdot y(x_i)}{\sigma_i} &= \alpha \cdot \sum_{i=1}^N \frac{y^2(x_i)}{\sigma_i} \\ \Rightarrow \alpha &= \frac{\sum y_i \cdot y(x_i) / \sigma_i}{\sum y^2(x_i) / \sigma_i} & (5.5) \end{aligned}$$

Once α is determined for each model, we calculate the χ^2 using Eqn. 5.3 and search for the 20 lowest χ^2 values. The value of χ^2 allows us to discriminate between models for each single galaxy, telling us that one model is better than others, but this value does not tell us much about the 'goodness' of the fit because we do not know the true errors associated with the spectra. We selected only 20 models in order to avoid overcrowding the plots: as can be seen, the first 20 best models do not represent a good fit to the data.

In order to compare all the fitted SEDs, they are plotted together in Fig. 5.1, where the lines in magenta represent the best 5 models, the next 5 are represented by color blue, then green and, finally, the red lines represent the last 15-20 acceptable models. In order to visualize the results, we construct a histogram for each parameter and each galaxy including the results of the best 20 models (Figs. 5.3-5.41). We do not show the histogram of the β parameter, the exponent of the angular distribution of dust, because it has only 2 possible values: 0 or 6, and the preferred value is reported in the corresponding caption. Also we construct a histogram including the mode and the median (Fig. 5.2, mode in red and median in blue) of each parameter for all the galaxies.

5.1.1 Results

We found that the modeling results are rather poor. Looking at the fitted SEDs, the sources showing a $10\mu\text{m}$ absorption feature (and no strong PAH emission), in general are represented quite well, but in those SEDs where no absorption is observed, the models tend to predict a strong $10\mu\text{m}$ absorption (or even moderate emission)

feature in order to attain the large width of the overall torus emission. In the cases, like NGC 6810 (Fig. 5.30) or NGC 7130 (Fig. 5.34) and others, where no $10\ \mu\text{m}$ absorption is observed and the strong emission from PAH could not be accounted for (Section 4.5) the modeling is very poor. When looking at the 'global' histograms (Fig. 5.2), the preferred column densities are quite small, with $N_H \sim 10^{22}$ and a very sharp distribution of values, contrary to what has been observed (Maiolino, 2001). It is very interesting that the models have a dust distribution concentrated in the center ($\beta = -0.5$ is by far the preferred value), and the angle of aperture of the torus is rather small (20° being the preferred value). The models predict an almost edge-on presentation of the torus, being more common values between 0 and 40° from the equatorial plane of the torus. The size of the torus is the least constrained parameter, but it tends to be large: the outer radius being 100-300 times the inner radius.

The column density at the equator is an output of the model, and in order to obtain the column density in the line of sight, we use:

$$N_H = N_H^{eq} \cdot \exp\{-\gamma|\cos(\theta)|\}, \quad (5.6)$$

where N_H^{eq} , as already said, is an output of the model, γ is the exponent of the angular part of the dust distribution, and θ is the aperture angle of the torus measured from the torus equator.

5.2 Clumpy Model

Nenkova *et al.* (2008) constructed a database including all the parameters values that they consider better describe the observed AGN SEDs. The ranges are listed in Table 2.2. The fitting method is the same used for the smooth models and the resulting 50 better models are shown in Fig. 5.42, and the histograms for each galaxy are shown in Figs. 5.44-5.82. In this case, the best 10 models are represented by lines in cyan color, the second best group of 10 models is in magenta, then blue, green and the last 10 models are in red. The mode and median preferred values are also shown (Fig. 5.43, mode in red and median in blue). Note that the number of clouds presented in the histograms is the number of clouds intercepting the line of sight, not an equatorial ray as the model parameter \mathcal{N}_0 . This value is calculated as $\mathcal{N}(\beta) = \mathcal{N}_0 \cdot \exp(-\beta^2/\sigma^2)$, where β start in the torus equator.

5.2.1 Results

In order to compare the opacities found in both models (smooth model using $\tau_{9.7\mu}$, and clumpy model using τ_V), we can use the relation found by Roche and Aitken (1984), $A_V/\tau_{9.7\mu} = 18.5$ for the solar neighborhood, or the relation for the Galactic center $A_V/\tau_{9.7\mu} \approx 9$ found by Roche and Aitken (1985). High densities are expected in the structure we are studying, so the relation found for molecular clouds could be more adequate. However, Roche *et al.* (2007) found that galaxies with very deep silicate absorption bands have profiles similar to the diffuse ISM (represented by the μ Cep emissivity curve) while those with shallower silicate absorption are better matched by the molecular cloud (Trapezium) curve. This suggests that molecular cloud material does not produce most of the absorption, and that we might expect the grains with Trapezium-like emissivities (larger grains) to be found closest to the AGN, where small grain destruction by the AGN is expected or, alternatively, coagulation of grains located inside dense, colder clumps could explain the absence of small grains.

As both models predict a wide range in $10\ \mu\text{m}$ absorption for our sample, we transform the visual depths using both extreme values: $A_V/\tau_{9.7\mu} = 18.5$ (9), where we show the value found in molecular clouds in parenthesis. As $A_V = 1.1\tau_V$, $\tau_V = 16.8$ (8.2) $\tau_{9.7\mu}$, so the typical value of τ_V found in the smooth model is

$\tau_V \sim 100$ (~ 50), in complete agreement with the values found in clumpy models but with almost no spread, which is intriguing.

To derive the observed column density of each model we have to assume a gas-to-dust ratio (GDR). Using the standard Galactic value, $GDR = N_H/A_V = 1.79 \cdot 10^{21} \text{ cm}^{-2}$ (Predehl and Schmitt, 1995), we found for the clumpy models:

$$N_H = GDR \cdot 1.1 \cdot \tau_V \cdot \mathcal{N}_0 \cdot \exp \left[\frac{-(90 - i)^2}{\sigma^2} \right], \quad (5.7)$$

where τ_V is the optical depth of each cloud at visual wavelengths, \mathcal{N}_0 is the number of torus clouds intercepted by an equatorial line of sight, i is the angle between the torus symmetry axis and the line of sight (i.e., the viewing angle), and σ is the angular width of the cloud distribution (i.e., the aperture of the torus). Note that the parameters of the model involved in this expression are \mathcal{N}_0 , τ_V , i , and σ . The preferred column density found for the sample is $10^{22-23} \text{ cm}^{-2}$, in good agreement with that found by the smooth model, although in this case the distribution is wider. The individual cloud optical depth in the visual range between 100 and 150, preferentially.

The number of clouds found in the lines of sight are rather small, ranging from 2 to 6 clouds, as found by Nenkova *et al.* (2008). The other parameters are less constrained: moderate to large torus sizes ($Y \sim 30-100$ times the inner radius), large torus apertures ($\sigma \sim 60^\circ - 75^\circ$), and not sharply centrally concentrated clouds ($q \sim 0 - 1$). A wide range of the inclinations of the systems respect to us is observed.

In general, the clumpy models are more successful at fitting the observed SEDs: although the χ_m^2 in is not an indication of the ‘goodness’ of the fit, it is possible to compare both models for the same galaxy, and as the uncertainties are the same, a lower χ_m^2 in effectively indicates a better fit. The χ_m^2 in for each galaxy and both models are shown in Table 5.3. We tabulate the mode, median and standard deviation (1σ) of the fitted clumpy parameters for each galaxy in Table 5.2. We do not include the corresponding table for the smooth model because those results are considerably worse. Only in cases where the star formation emission could not be completely subtracted the models try to account for the PAH features and poorly predict the near-IR emission corresponding to the torus contribution (NGC 34, Fig. 5.44; NGC 1143, Fig 5.51; for example). In general, although the spectra are included only until $\lambda = 20\mu\text{m}$, all the emission is properly modeled. It is worth highlighting that the models are capable of reproducing all the range of $10 \mu\text{m}$ absorption, from the flat featureless continuum of NGC 1320 (Fig. 5.54) to the marked absorption in NGC 1194 (Fig. 5.53), although it does not successfully reproduce the extremely deep absorption found in NGC 7172 (Fig. 5.76). We find that there is a wide variation in the model ability to restrict the parameters: from very narrow distribution of values in IRAS 05189-2524 (Fig. 5.57) for example, to very spread distributions in, for example, NGC 5506 (Fig. 5.67).

Table 5.1: Mode (Mo), median (Me) and standard deviation (σ) values for each of the parameters for each of the galaxies modeled with the continuous torus emission model.

Galaxy (1)	β			Aperture Angle θ			Optical Depth τ			Torus Size $R_{\text{out}}/R_{\text{in}}$			Viewing Angle i		
	Mo (2)	Me (3)	σ (4)	Mo (5)	Me (6)	σ (7)	Mo (8)	Me (9)	σ (10)	Mo (11)	Me (12)	σ (13)	Mo (14)	Me (15)	σ (16)
IRAS 05189-2524	-0.50	-0.50	0.34	20	20	4.47	6	6	2.05	300	100	135.77	0	30	23.50
ESO 33-G2	-0.50	-0.50	0.28	20	20	0	1	2	2.61	300	300	98.91	60	40	23.26
IRAS 04385-0828	-0.50	-0.50	0.44	20	20	0	6	6	2.04	30	30	125.55	60	40	21.83
NGC 1320	-0.50	-0.50	0.26	20	20	0	1	1	3.83	300	300	110.81	0	30	22.54
NGC 1194	-1	-0.50	0.45	20	20	0	6	6	1.84	30	30	132.13	60	40	24.82
MCG -2-8-39	-0.50	-0.50	0.34	20	20	4.47	6	6	2.05	300	100	135.77	0	30	23.50
NGC 1143	-0.50	-0.50	0.45	20	20	4.47	6	6	2.04	30	30	132.13	0	30	22.38
IRAS 15480-0344	-0.50	-0.50	0.34	20	20	4.47	6	6	2.05	300	100	135.77	0	30	23.50
IRAS 01475-0740	-0.50	-0.50	0.24	20	20	9.40	0.30	0.30	2.17	100	100	0	0	20	20.10
ESO 541-IG12	0	0	0.44	20	20	19.33	0.60	0.60	0.58	100	100	91.51	20	20	16.82
IRAS 00521-7054	-0.50	-0.50	0.11	20	20	8.89	0.60	0.60	0.15	300	300	105.99	0	30	20.49
IRAS 00198-7926 North	-0.50	-0.50	0.24	20	20	7.33	0.30	0.30	4.03	100	100	51.10	0	20	23.26
IRAS 00198-7926 South	-0.50	-0.50	0.24	20	20	11.74	1	1	0.22	100	100	73.27	0	20	17.31
NGC 34	-0.50	-0.50	0.34	20	20	4.47	6	6	2.05	300	100	135.77	0	30	23.50
CGCG 381-051	-0.50	-0.50	0.34	20	20	4.47	10	6	3.49	300	100	135.77	0	40	24.12
NGC 7590	-0.50	-0.50	0	20	20	10.21	2	2	0.50	300	300	82.08	0	20	17.25
NGC 7582	-0.50	-0.50	0.43	20	20	4.47	6	6	2.05	30	30	130.41	60	40	22.82
NGC 7496	-0.50	-0.50	0.38	20	20	4.47	6	6	2.05	300	100	135.77	0	30	22.54
MCG -3-58-7	-0.50	-0.50	0.43	20	20	4.47	6	6	2.05	30	30	130.41	60	40	22.82
NGC 7130	-0.50	-0.50	0.34	20	20	4.47	6	6	2.05	300	100	135.77	0	30	23.50
MRK 897	-0.50	-0.50	0.41	20	20	4.47	6	6	2.05	30	30	133.66	0	40	22.31
IC 5063	-0.50	-0.50	0.34	20	20	4.47	6	6	2.05	300	100	135.77	0	30	23.50

Continued on Next Page. . .

Table 5.1 – Continued

(1)	(2)	(3)	(4)	(5)	(6)	(7)	(8)	(9)	(10)	(11)	(12)	(13)	(14)	(15)	(16)
NGC 6890	-0.50	-0.50	0.34	20	20	4.47	10	6	3.11	300	100	135.77	60	40	23.05
NGC 6810	-0.50	-0.50	0.37	20	20	4.47	6	6	2.05	300	100	135.77	0	30	22.54
MCG +0-29-23	-0.50	-0.50	0.34	20	20	4.47	6	6	2.05	300	100	135.77	0	30	23.50
NGC 3660	-0.50	-0.50	0	20	20	9.40	0.30	0.30	1.26	300	300	0	20	20	19.22
NGC 4501	-1	-1	0.50	40	40	10.21	3	3	1.88	30	30	98.64	40	30	24.52
TOL 1238-364	-0.50	-0.50	0.34	20	20	4.47	6	6	2.05	300	100	135.77	0	30	23.50
NGC 4941	-0.50	-0.50	0.34	20	20	4.47	6	6	2.05	300	100	135.77	0	30	23.50
MCG -3-34-64	-0.50	-0.50	0	20	20	8.89	1	1	0.40	300	300	0	40	30	19.44
NGC 5135	-0.50	-0.50	0.34	20	20	4.47	6	6	2.05	300	100	135.77	0	30	23.50
NGC 5953	-0.50	-0.50	0.31	20	20	0	0.10	0.10	0.10	300	300	0	0	40	29.47
MCG -2-40-4	-0.50	-0.50	0.32	20	20	4.47	0.30	6	4.18	300	300	137.81	0	40	22.31
NGC 1068	-0.50	-0.50	0.37	20	20	11.96	2	2	3.33	100	100	115.28	60	30	23.05
NGC 4388	-0.50	-0.50	0.34	20	20	4.47	6	6	2.05	300	100	135.77	0	30	23.50
NGC 4968	-0.50	-0.50	0.34	20	20	4.47	6	6	2.05	300	100	135.77	0	30	23.50
NGC 5506	-1	-0.50	0.43	20	20	6.16	6	6	1.88	30	30	138.51	60	30	26.61
NGC 7172	-1	-1	0.44	20	20	6.16	6	6	1.70	30	30	135.71	0	10	25.65
NGC 7674	-0.50	-0.50	0.38	20	20	4.47	6	6	2.05	300	100	135.77	0	30	22.54

Table 5.2: Mode (Mo), median (Me) and standard deviation (σ) values for each of the parameters for each of the galaxies modeled with the clumpy torus emission model.

Galaxy (1)	q			\mathcal{N}_0^{eq}			Aperture Angle σ			Optical Depth τ			Viewing Angle i			Y = R _{out} /R _{in}		
	Mo (2)	Me (3)	σ (4)	Mo (5)	Me (6)	σ (7)	Mo (8)	Me (9)	σ (10)	Mo (11)	Me (12)	σ (13)	Mo (14)	Me (15)	σ (16)	Mo (17)	Me (18)	σ (19)
NGC 34	0	0	0	13	12	4.63	75	75	7.27	30	30	11.12	90	70	34.95	30	30	0
IRAS 00198-7926 N	0	0	0.40	1	3	4.92	60	45	18.04	300	60	129.35	80	80	9.82	200	200	82.98
IRAS 00198-7926 S	1	1	0.90	3	3	2.51	75	60	19.50	10	150	170.42	90	80	10.78	5	5	61.69
IRAS 00521-7054	1	1	0.27	6	6	0.90	75	75	10.15	100	100	31.30	30	30	15.51	100	100	70.23
ESO 541-IG012	2	2	0.42	1	1	0	15	15	0	500	500	135.83	0	30	21.98	5	10	68.73
IRAS 01475-0740	1	1	0.51	7	6	1.62	75	75	7.15	100	100	35.23	0	20	15.51	100	100	66.92
NGC 1068	0	1	1.13	13	15	4.14	30	30	11.52	10	10	229.66	90	90	15.24	5	5	4.95
NGC 1144	0	0	0.49	14	15	1.19	75	75	6.94	10	10	4.54	90	80	14.67	30	30	34.32
NGC 1194	1	1	1.01	2	2	1.11	60	60	6.28	60	60	31.67	0	10	11.58	30	30	77.87
NGC 1320	0	0	1.19	3	3	2.17	30	30	18.04	20	20	158.31	70	70	17.87	200	200	50.78
IRAS 04385-0828	3	3	1.41	6	6	1.74	45	60	15.34	150	150	161.90	60	50	19.40	100	100	50.35
ESO 33-G2	0	0	0.97	3	3	2.53	15	15	11.82	20	20	144.82	70	70	13.40	100	100	34.32
IRAS 05189-2524	1	1	0.30	6	6	4.47	45	45	15.92	100	100	15.87	50	50	24.74	30	30	61.71
NGC 4388	0	0	0.66	11	10	4.12	45	45	10.45	80	80	21.41	50	70	16.64	30	30	0
NGC 4501	3	3	0	1	1	0	15	15	0	100	100	72.64	0	20	21.08	5	5	57.22
TOL 1238-364	1	1	1	10	7	4.36	75	75	9.68	100	100	39.81	70	50	24.62	30	30	0
NGC 4941	1	1	0.62	2	3	1.34	60	60	10.03	150	150	45.44	10	20	14.24	30	30	49.26
NGC 4968	0	0	0.91	6	6	3.79	15	30	22.69	100	60	38.97	90	80	26.96	200	200	68.74
MCG -3-34-64	1	1	0.49	11	12	4.38	60	60	10.74	300	200	103.98	90	80	11.07	30	30	69.55
NGC 5135	0	0	0	6	7	4.91	15	15	6.97	20	20	12.16	90	90	3.70	200	200	14.14
NGC 5506	1	1	1.09	7	7	4.09	30	30	22	150	20	65.38	80	70	25.95	200	200	65.16
NGC 5953	0	0	0.44	14	15	1.87	75	75	6.94	150	150	95.13	70	70	14.75	200	200	32.83

Continued on Next Page...

Table 5.2 – Continued

(1)	(2)	(3)	(4)	(5)	(6)	(7)	(8)	(9)	(10)	(11)	(12)	(13)	(14)	(15)	(16)	(17)	(18)	(19)
MCG -2-40-4	2	2	0	2	2	2.25	60	60	7.48	80	80	9.26	0	20	27.03	100	100	68.72
IRAS 15480-0344	2	2	0.73	4	6	6.48	30	30	18.24	150	150	53.12	90	80	27.23	30	30	73.89
NGC 6810	1	1	0.43	7	7	4.38	75	75	12.95	200	200	36.55	30	30	29.99	100	100	56.84
NGC 6890	2	2	0.96	11	10	4.08	45	45	12.49	150	150	65.22	90	80	13.70	200	200	71.34
IC 5063	0	0	0	4	4	1.52	15	30	17.78	30	30	11.72	90	90	6.13	200	200	0
MRK 897	3	3	0	1	1	0	15	15	2.97	100	150	72.21	0	20	22.41	5	5	62.79
NGC 7130	2	2	0.48	14	14	1.33	75	75	14.87	150	150	29.95	60	70	16	200	200	50.14
MCG -3-58-7	1	1	0.88	3	3	1.60	60	45	20.23	150	100	99.30	30	30	24.40	30	30	69.55
NGC 7496	0	0	0	2	2	1.05	60	60	6.94	200	200	55.66	0	10	7.17	30	30	29.29
NGC 7582	0	0	0.33	5	6	3.48	75	75	5.55	40	40	13.89	0	20	30.77	30	30	55.80
NGC 7590	3	3	0	12	12	1.85	75	75	7.27	10	10	4.18	80	70	16.10	5	5	0
NGC 7674	1	1	0.67	2	3	1.87	60	60	12.84	150	150	45.84	20	20	23.73	30	30	40.78
CGC 381-051	1	1	0	5	4	0.88	75	60	10.45	300	300	41.85	20	20	12.82	100	100	58.18
MCG +0-29-23	0	0	0	6	6	5.27	75	75	7.48	60	40	15.47	10	20	34.13	30	30	0

Table 5.3: Comparison between the χ_{min}^2 obtained with the clumpy and smooth modeling. The clumpy models are better than the smooth models in describing the torus emission. The median χ^2 for the clumpy models is 6.19, and for the smooth models is 76.3

Galaxy	Clumpy χ_{min}^2 †	Smooth χ_{min}^2 §
IRAS 05189-2524	0.15	2.78
ESO 33-G2	16.96	138.98
IRAS 04385-0828	24.8	76.30
NGC 1320	1.49	21.42
NGC 1194	1.60	626.86
MCG -2-8-39	802.94	7411.11
NGC 1143	155.84	2579.88
IRAS 15480-0344	5.99	66.16
IRAS 01475-0740	0.37	2.86
ESO 541-IG12	0.44	0.31
IRAS 00521-7054	0.93	3.18
IRAS 00198-7926 N	11.96	32.25
IRAS 00198-7926 S	6.62	5.70
NGC 34	123313.41	189373.15
CGCG 381-051	3.48	18.78
NGC 7590	1.72e16	1.75e16
NGC 7582	46.39	158.52
NGC 7496	4.57	23224.74
MCG -3-58-7	0.39	3.97
NGC 7130	98.29	372.07
MRK 897	12.68	8.28
IC 5063	6.08	227.97
NGC 6890	6.19	50.38
NGC 6810	24.62	152.57
MCG +0-29-23	629.12	958.53
NGC 3660	176.43	0.68
NGC 4501	1.95	30.68
TOL 1238-364	3.08	1.70e15
NGC 4941	2.31e15	190.83
MCG -3-34-64	0.41	57.49
NGC 5135	292.89	607.69
NGC 5953	4.86e6	553601.73

Continued on Next Page...

Table 5.3 – Continued

Galaxy	Clumpy χ_{min}^2 †	Smooth χ_{min}^2 §
MCG -2-40-4	1.22	5.74
NGC 1068	0.34	0.44
NGC 4388	3522.48	12096.90
NGC 4968	5.37	1308.53
NGC 5506	0.74	0.34
NGC 7172	1166.35	1910.76
NGC 7674	0.58	7.64

†Clumpy models with 7 degrees of freedom.

§Smooth models with 6 degrees of freedom.

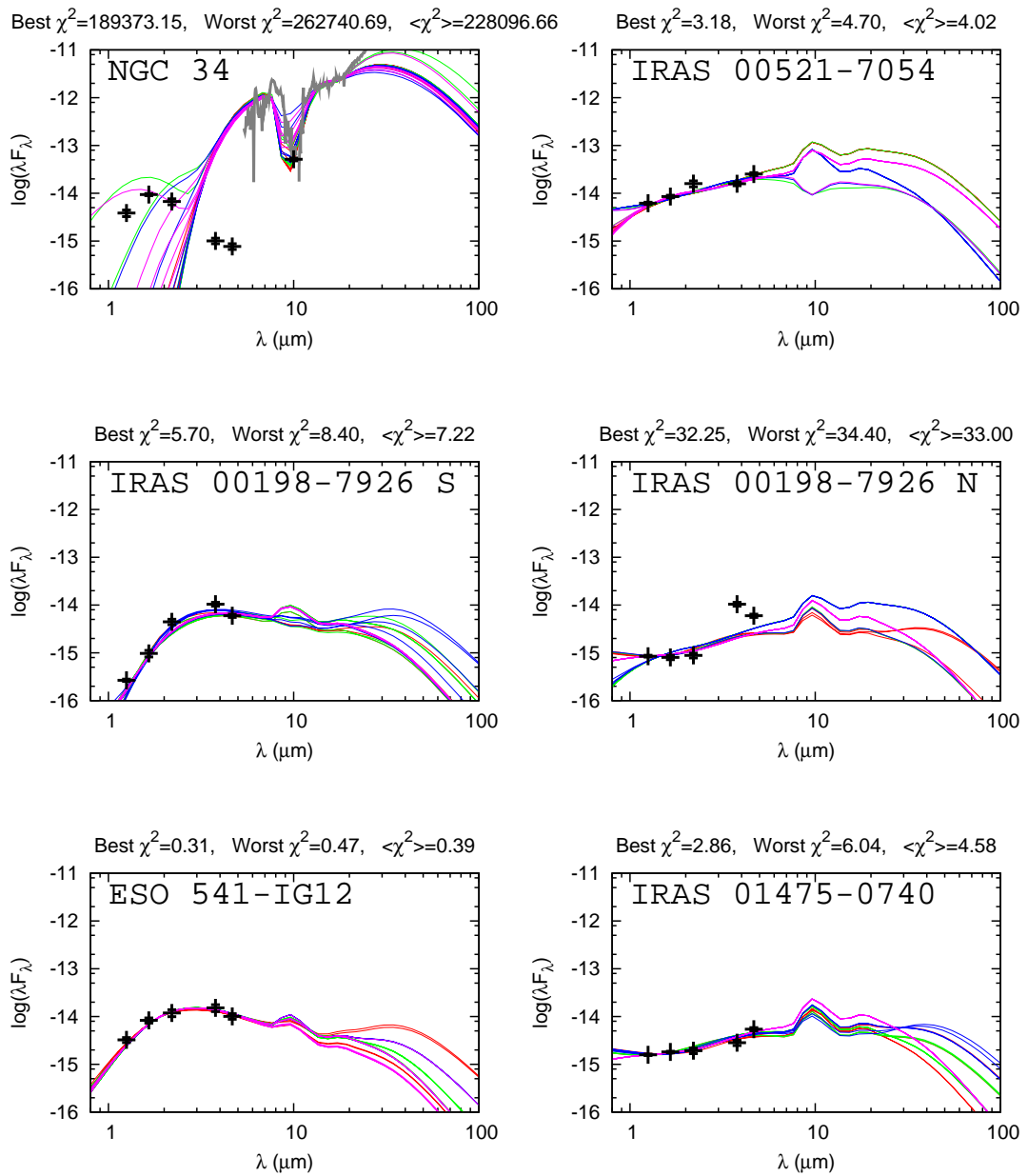


Figure 5.1: Nuclear IR SEDs with the 20 better fitted smooth models. Lines in magenta represent the best 5 models, the next 5 better models are represented by color blue, then green and, finally, the red lines represent the last 15-20 better models. Arrows in blue are upper limits for the non-detections. The photometric points are plotted in black, and the *Spitzer* spectra are plotted in gray. The minimum χ^2 , the maximum χ^2 included in the best 20 models, and the mean χ^2 are shown in the title of each SED.

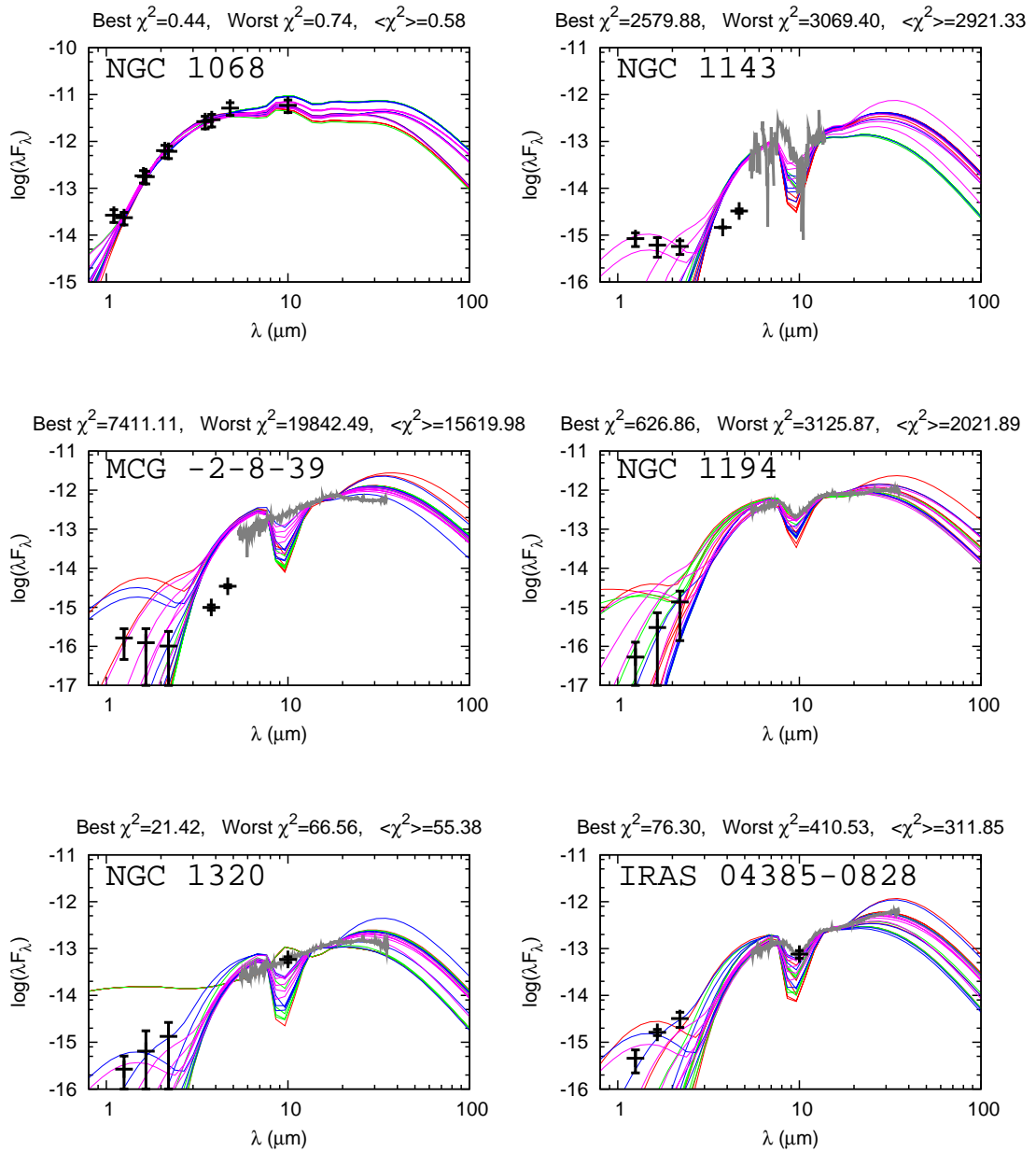


Figure 5.1: Continued.

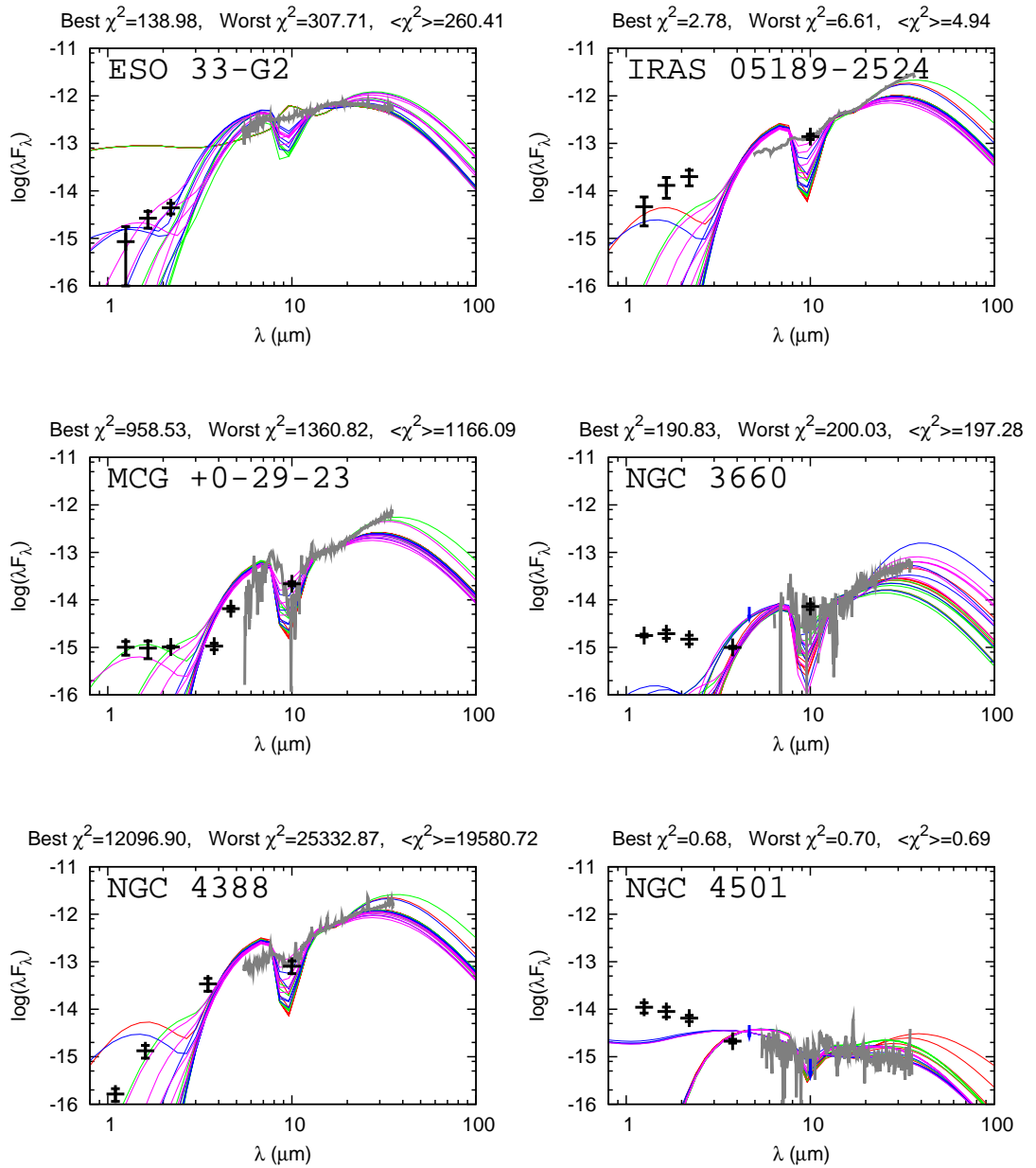


Figure 5.1: Continued.

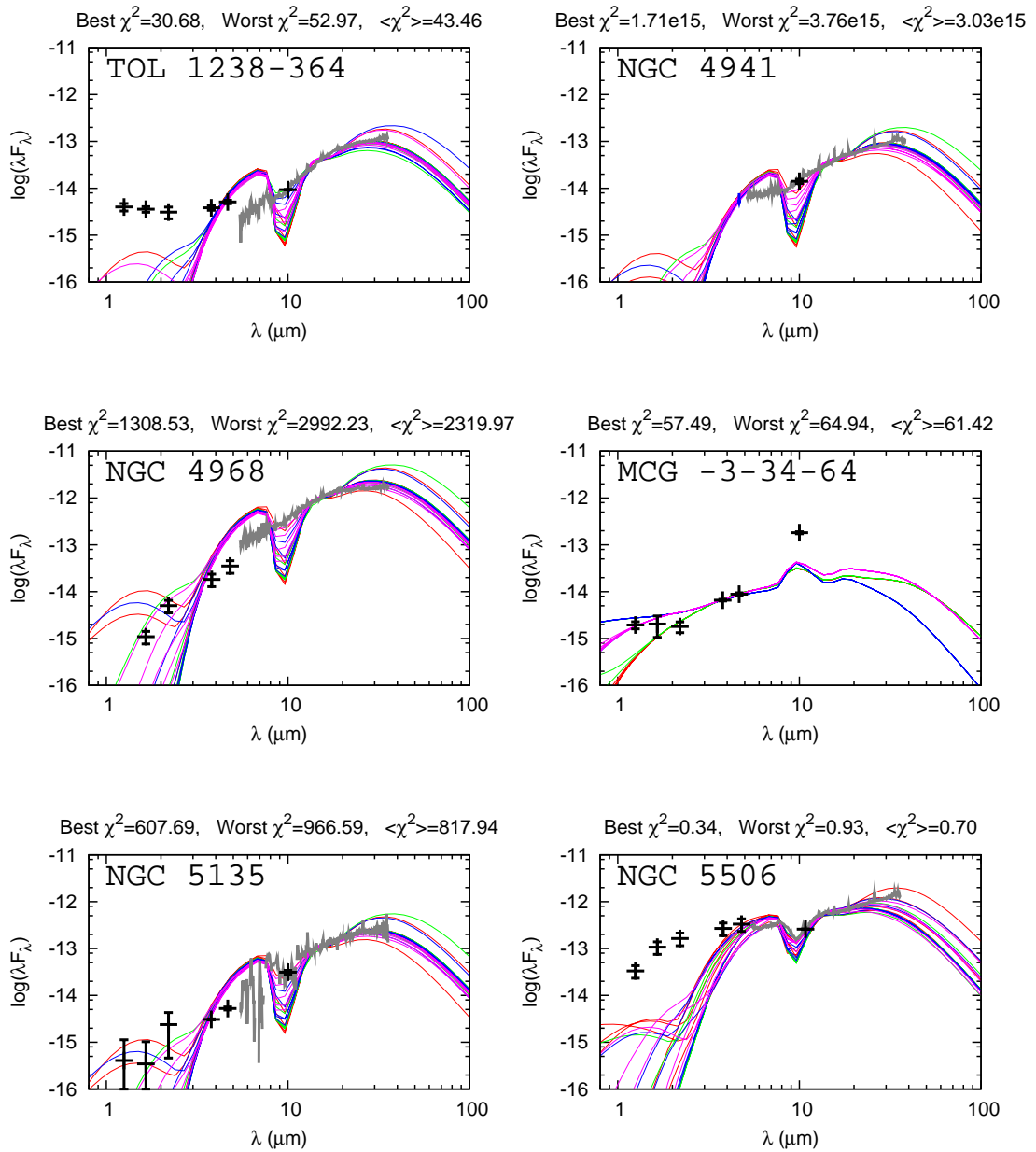


Figure 5.1: Continued.

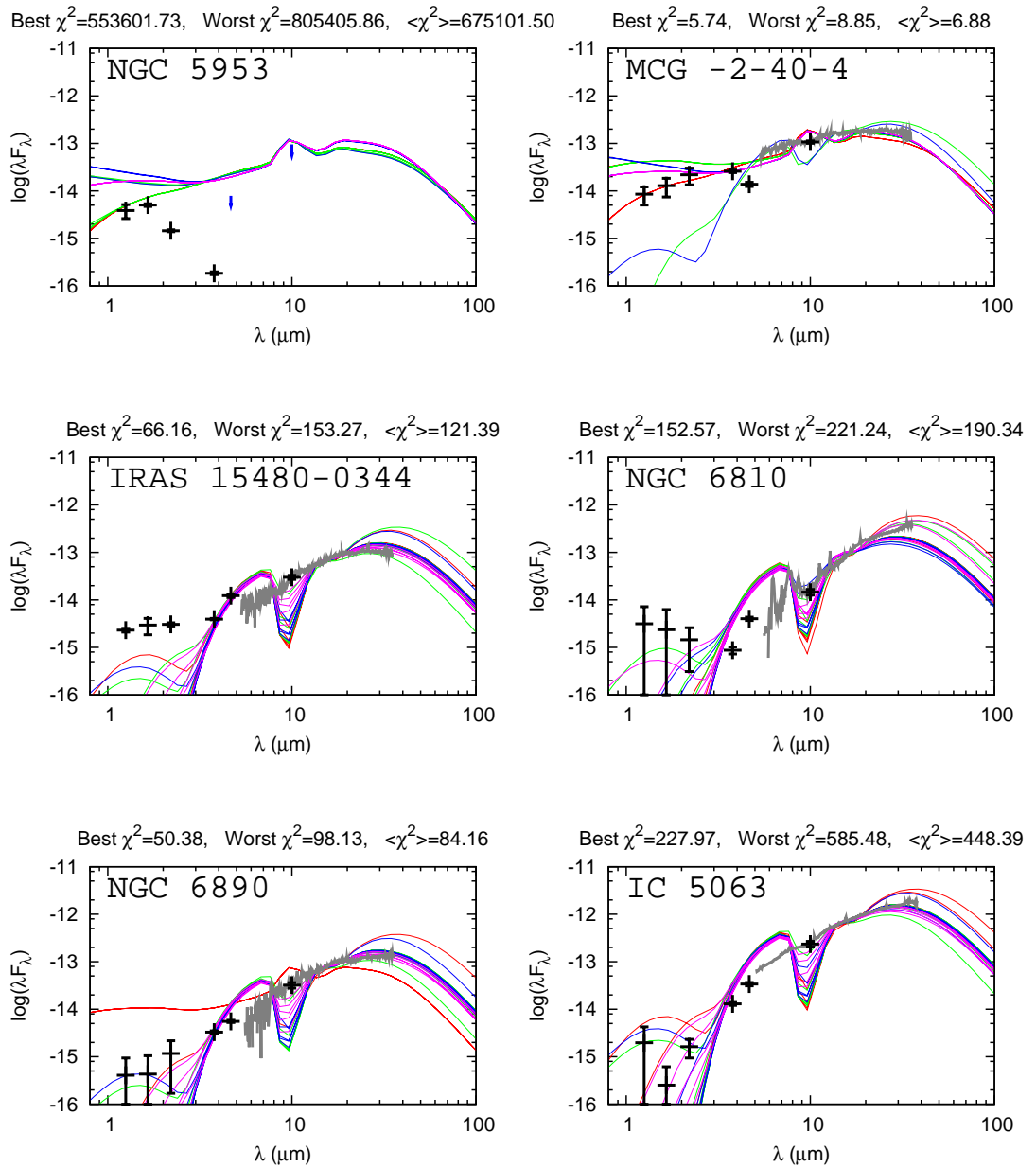


Figure 5.1: Continued

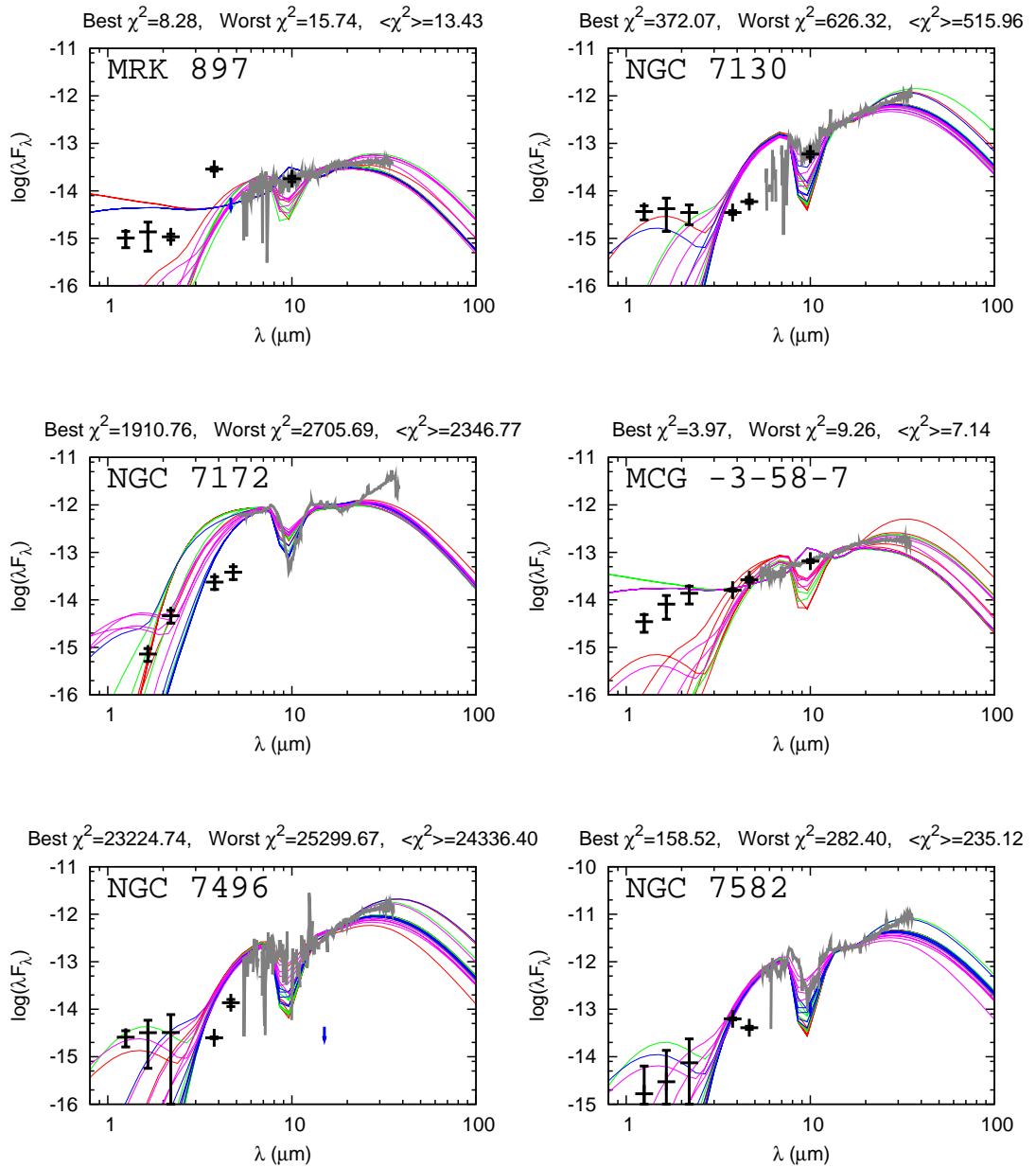


Figure 5.1: Continued

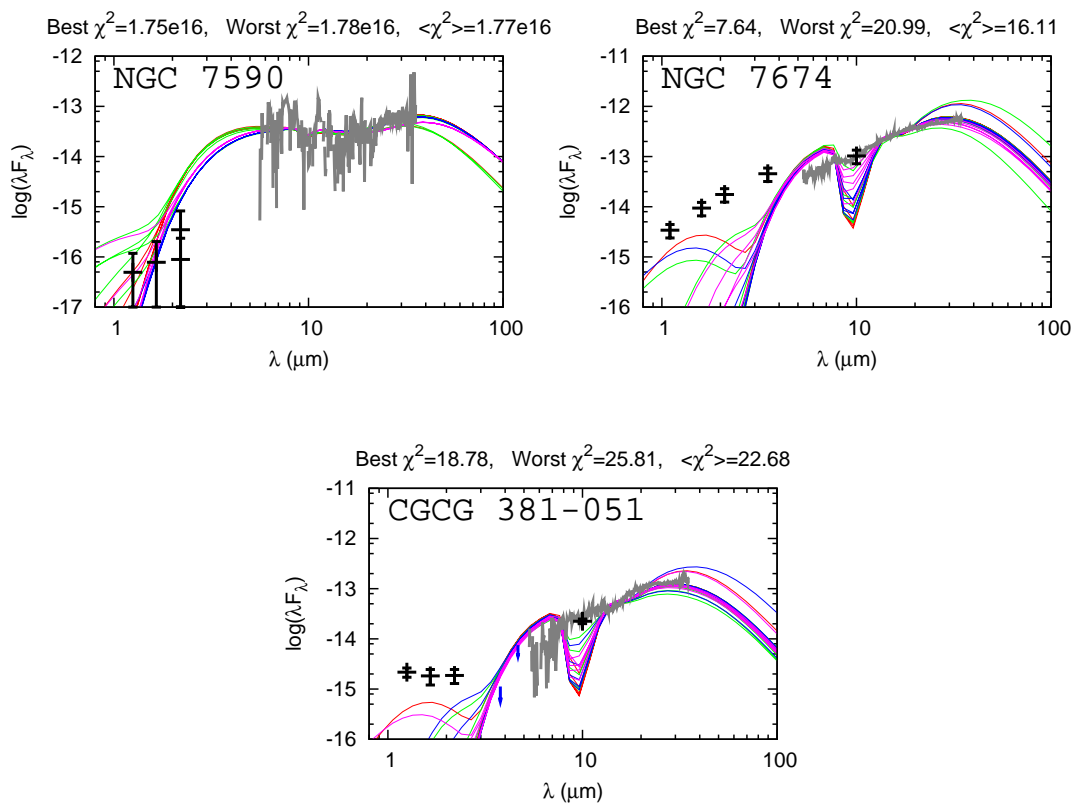


Figure 5.1: Continued

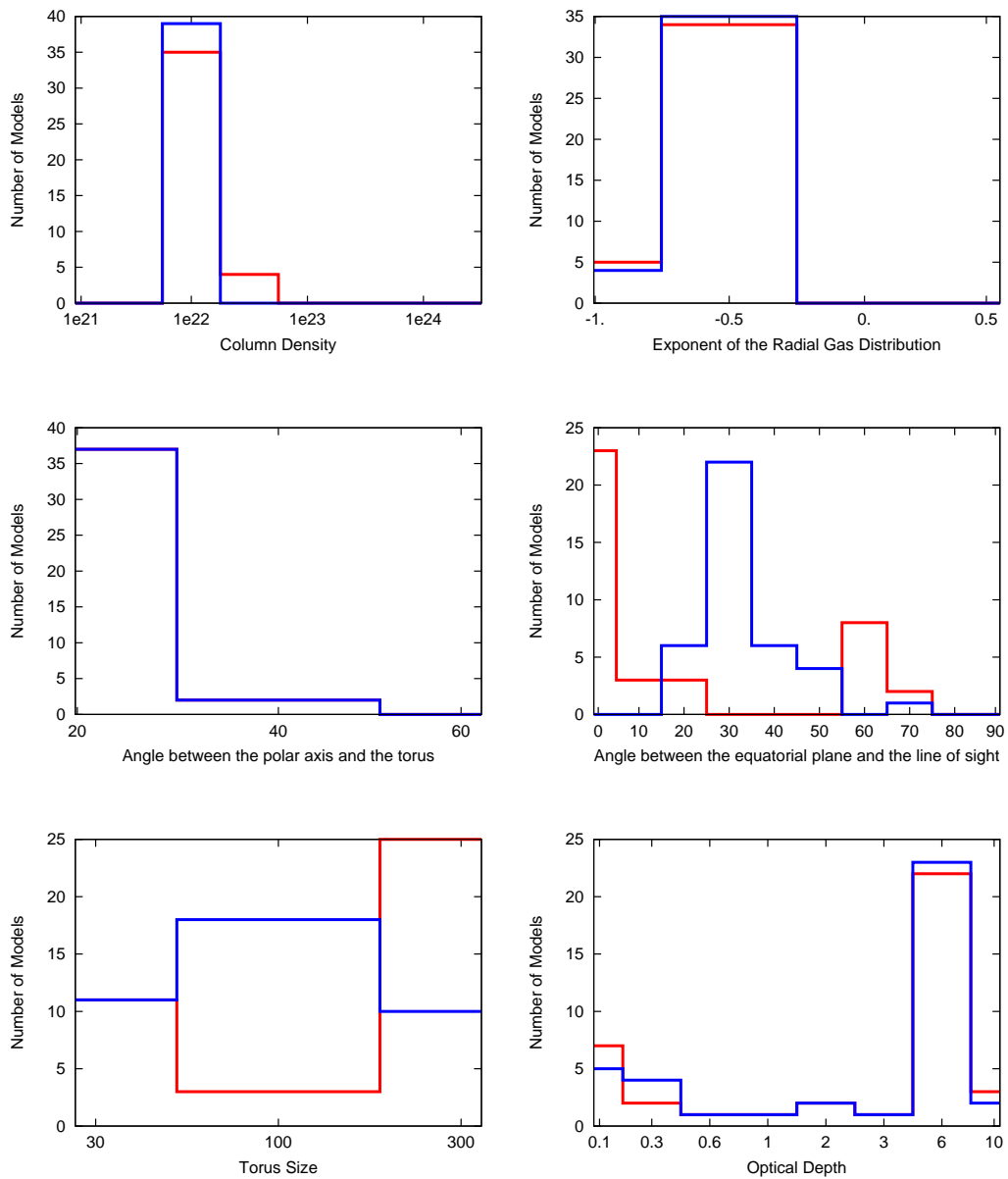


Figure 5.2: Preferred values for all the parameters of the smooth torus emission models. The mode values are plotted in red and the median values are plotted in blue. In the upper left panel the column density is plotted. In the upper right panel we plot the exponent of the radial distribution of dust. The middle panels, in the left the aperture angle of the torus is shown, and in the right the viewing angle of the system is shown. The torus size and the optical depth are shown in bottom left panel and bottom right panel, respectively.

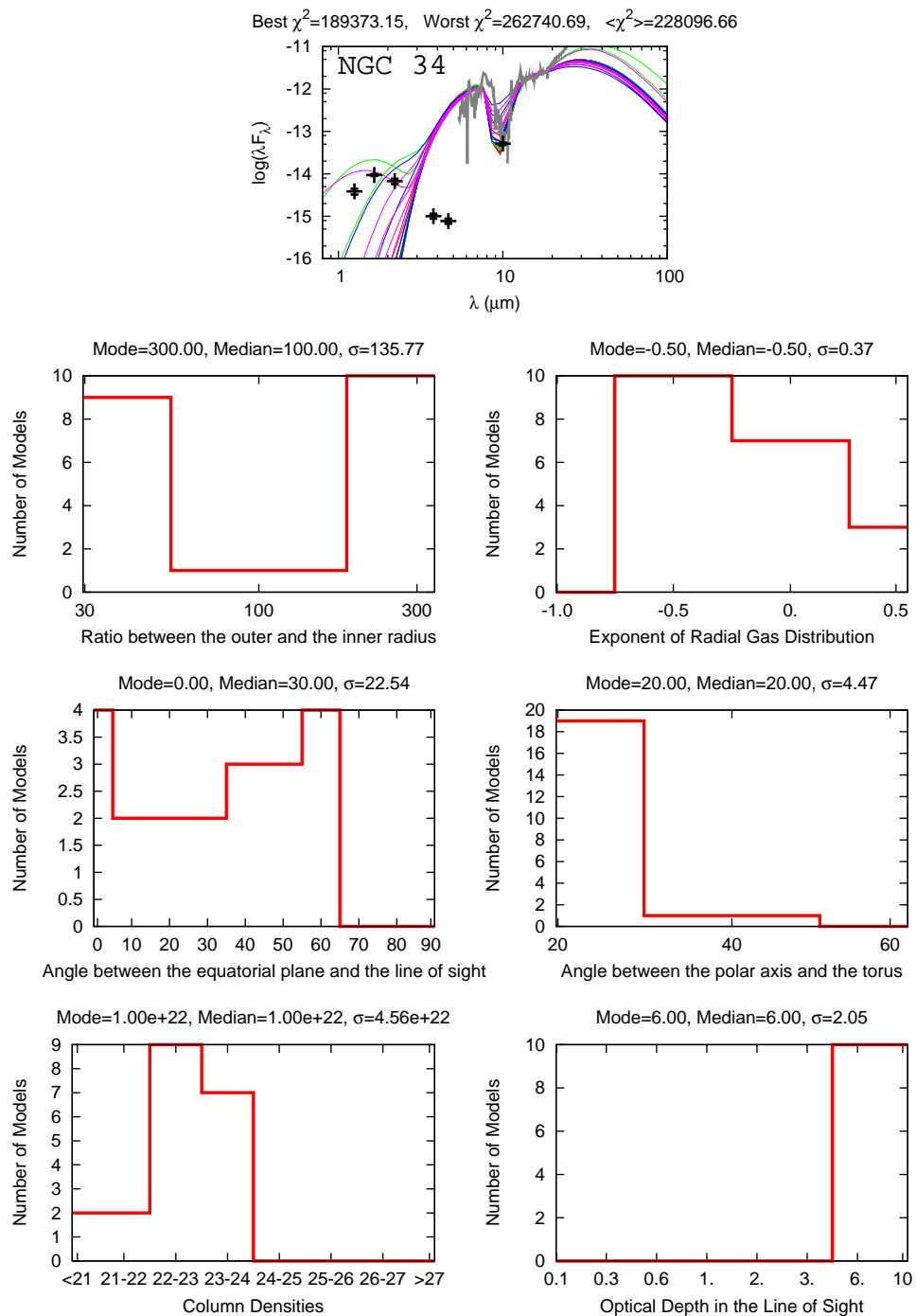


Figure 5.3: Best 20 smooth models fitted to NGC 34, with specific parameters histograms shown. The preferred value for γ , the exponent of the angular distribution of dust, is 0. Although some cases with $\gamma = 6$ are included. The top image is the modeled SED. In the upper left panel we show the size of the torus, while in the right panel we plot the exponent of the radial distribution of dust. The middle panels, in the left the inclination of the system is shown, and in the right the aperture angle of the torus is shown. The column density and the optical depth are shown in bottom left and bottom right panels, respectively.

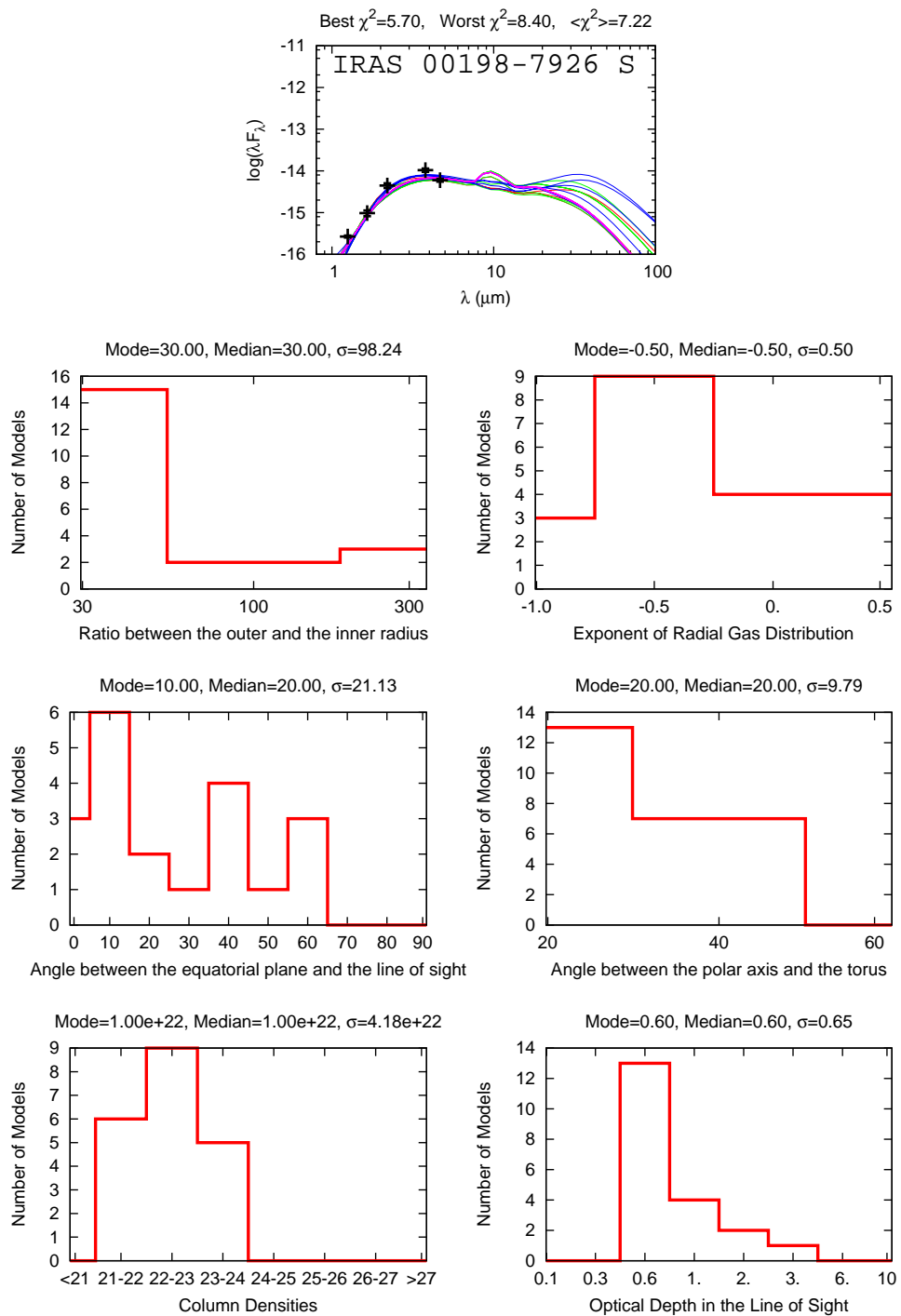


Figure 5.4: Best 20 smooth models fitted to IRAS 00198-7926 South, with specific parameters histograms shown. The preferred value for γ , the exponent of the angular distribution of dust, is 0. Although it includes some cases with $\gamma = 6$. The order of the panels is the same as in Fig. 5.3 and will be the same for all the smooth models.

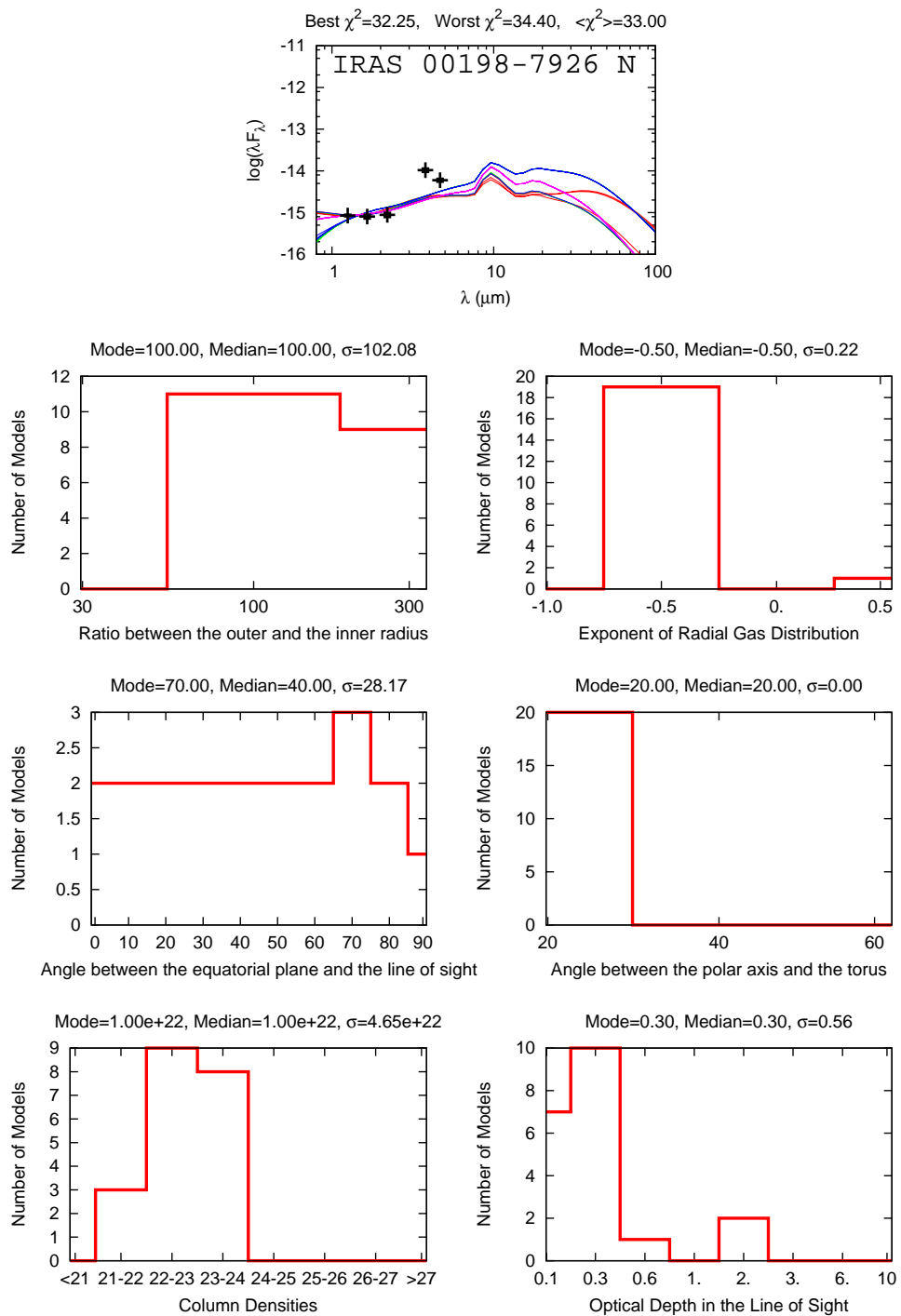


Figure 5.5: Best 20 smooth models fitted to IRAS 00198-7926 North, with specific parameters histograms shown. The preferred value for γ , the exponent of the angular distribution of dust, is 0. Although some cases with $\gamma = 6$ are accepted.

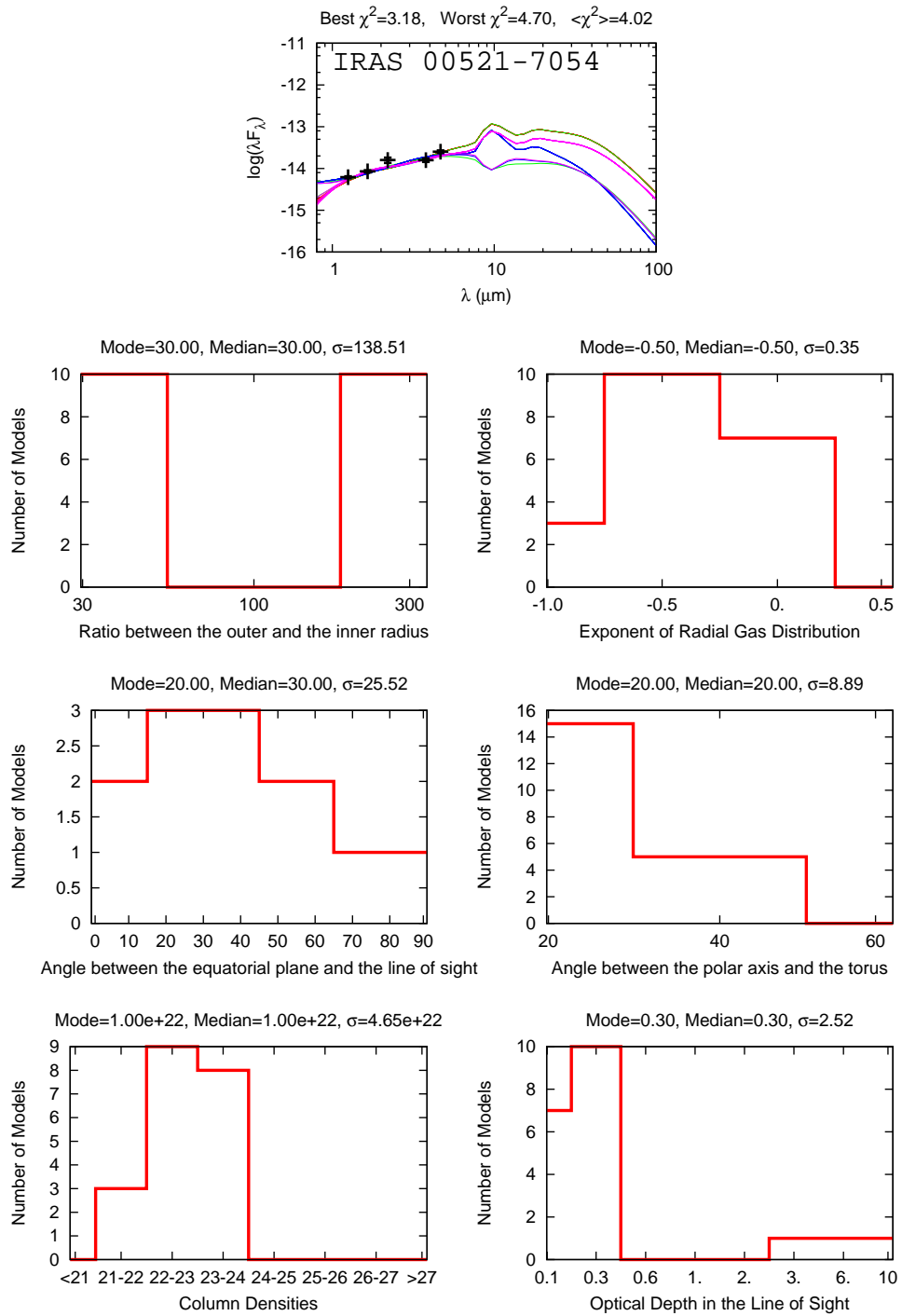


Figure 5.6: Best 20 smooth models fitted to IRAS 00521-7054, with specific parameters histograms shown. Only cases with $\gamma = 0$ are preferred.

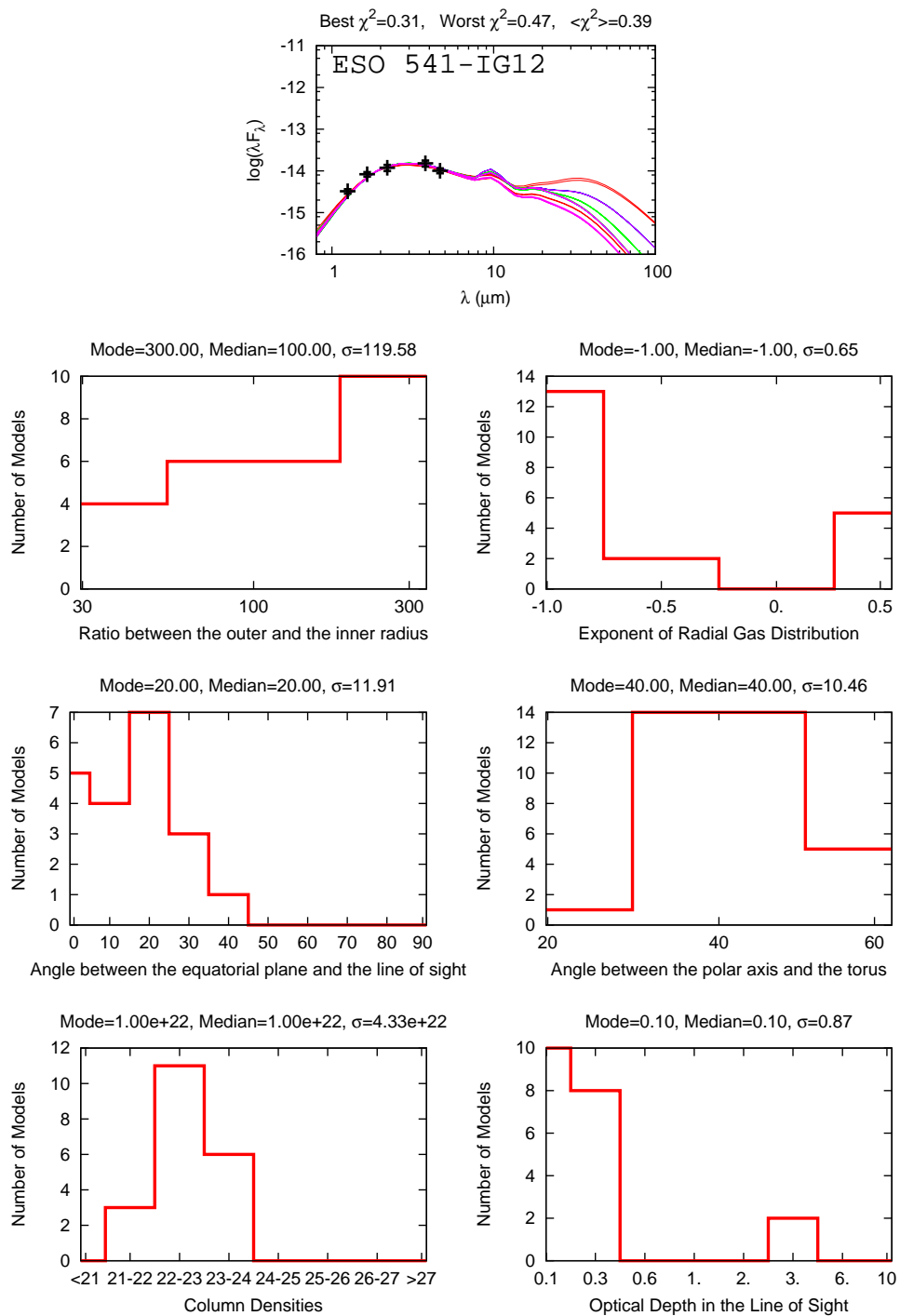


Figure 5.7: Best 20 smooth models fitted to ESO 541-IG12, with specific parameters histograms shown. The preferred value for γ , the exponent of the angular distribution of dust, is 0. Although some cases with $\gamma = 6$.

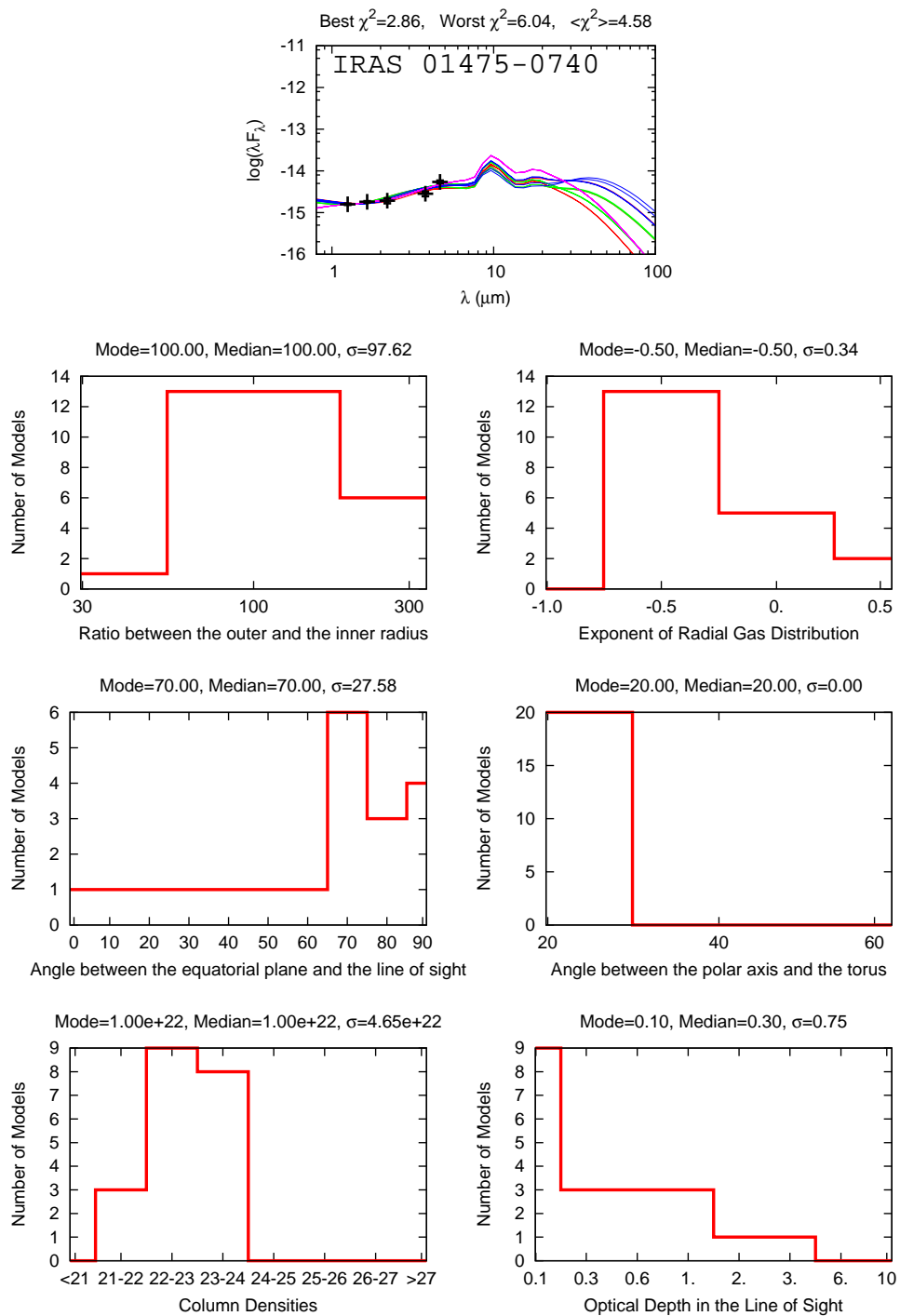


Figure 5.8: Best 20 smooth models fitted to IRAS 01475-0740, with specific parameters histograms shown. The preferred value for γ , the exponent of the angular distribution of dust, is 0. Although some cases with $\gamma = 6$.

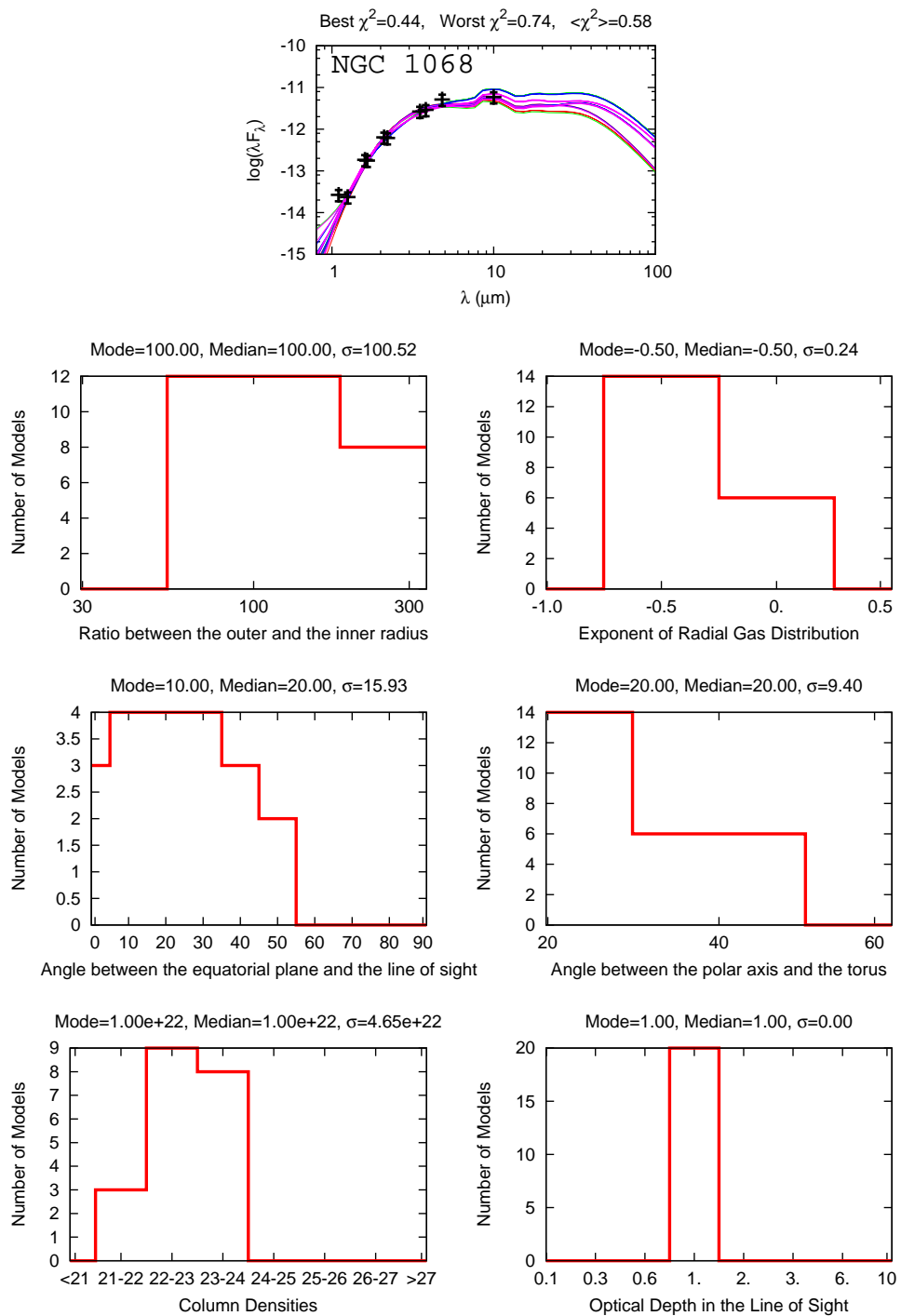


Figure 5.9: Best 20 smooth models fitted to NGC 1068, with specific parameters histograms shown. The preferred value for γ , the exponent of the angular distribution of dust, is 0. Although some cases with $\gamma = 6$.

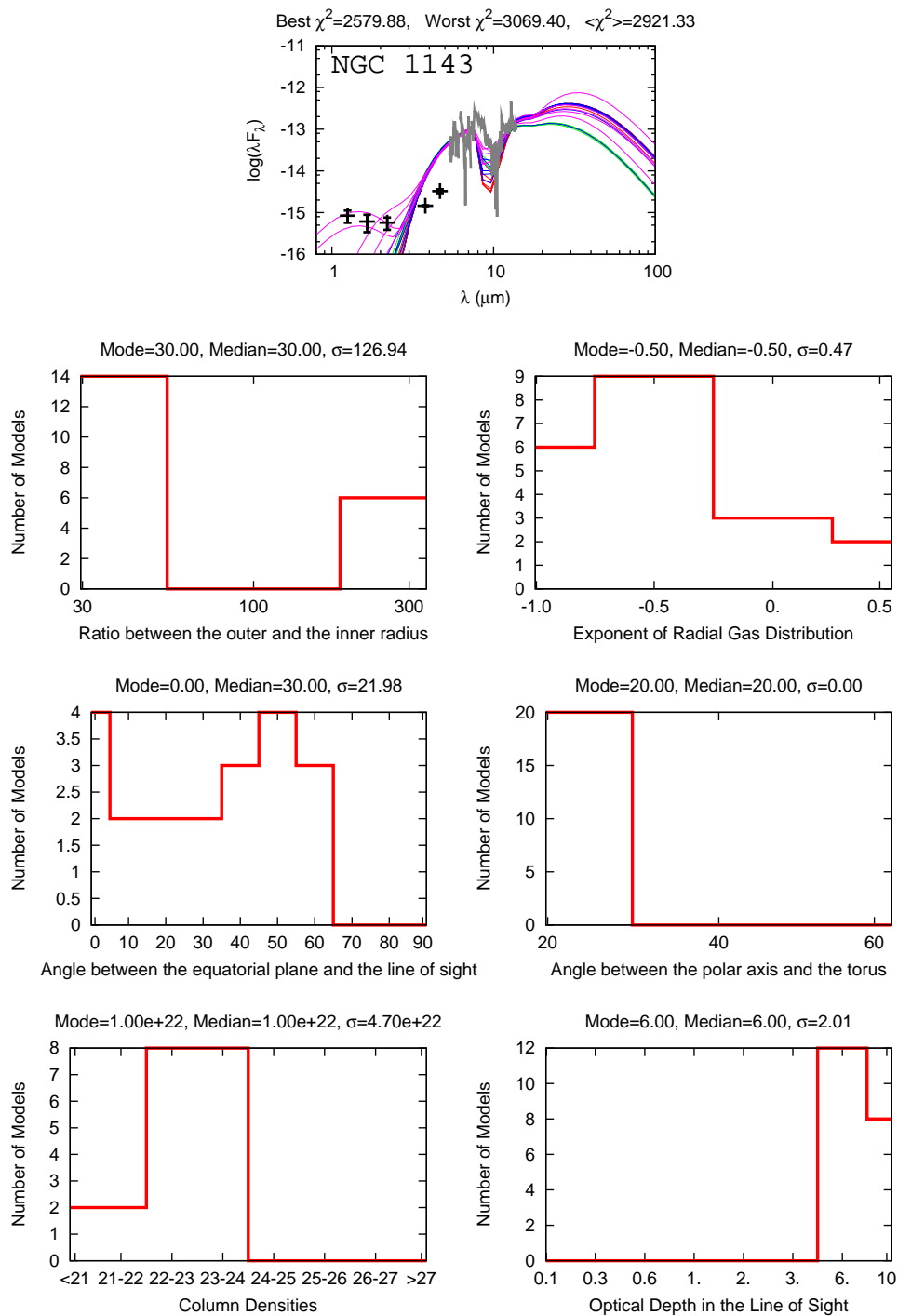


Figure 5.10: Best 20 smooth models fitted to NGC 1143, with specific parameters histograms shown. The preferred value for γ , the exponent of the angular distribution of dust, is 0. Although some cases with $\gamma = 6$.

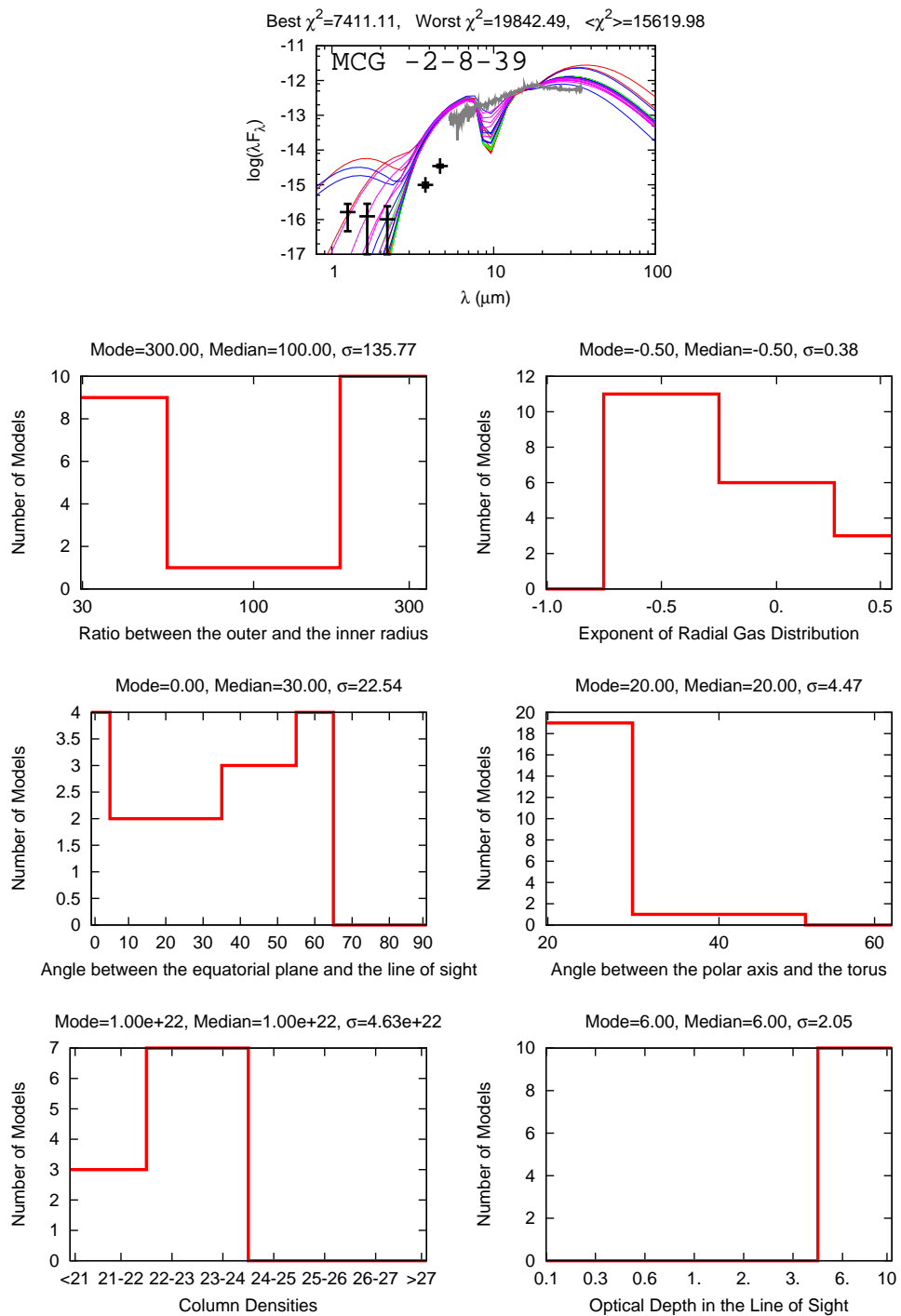


Figure 5.11: Best 20 smooth models fitted to MCG -2-8-39, with specific parameters histograms shown. The preferred value for γ , the exponent of the angular distribution of dust, is 0. Although some cases with $\gamma = 6$.

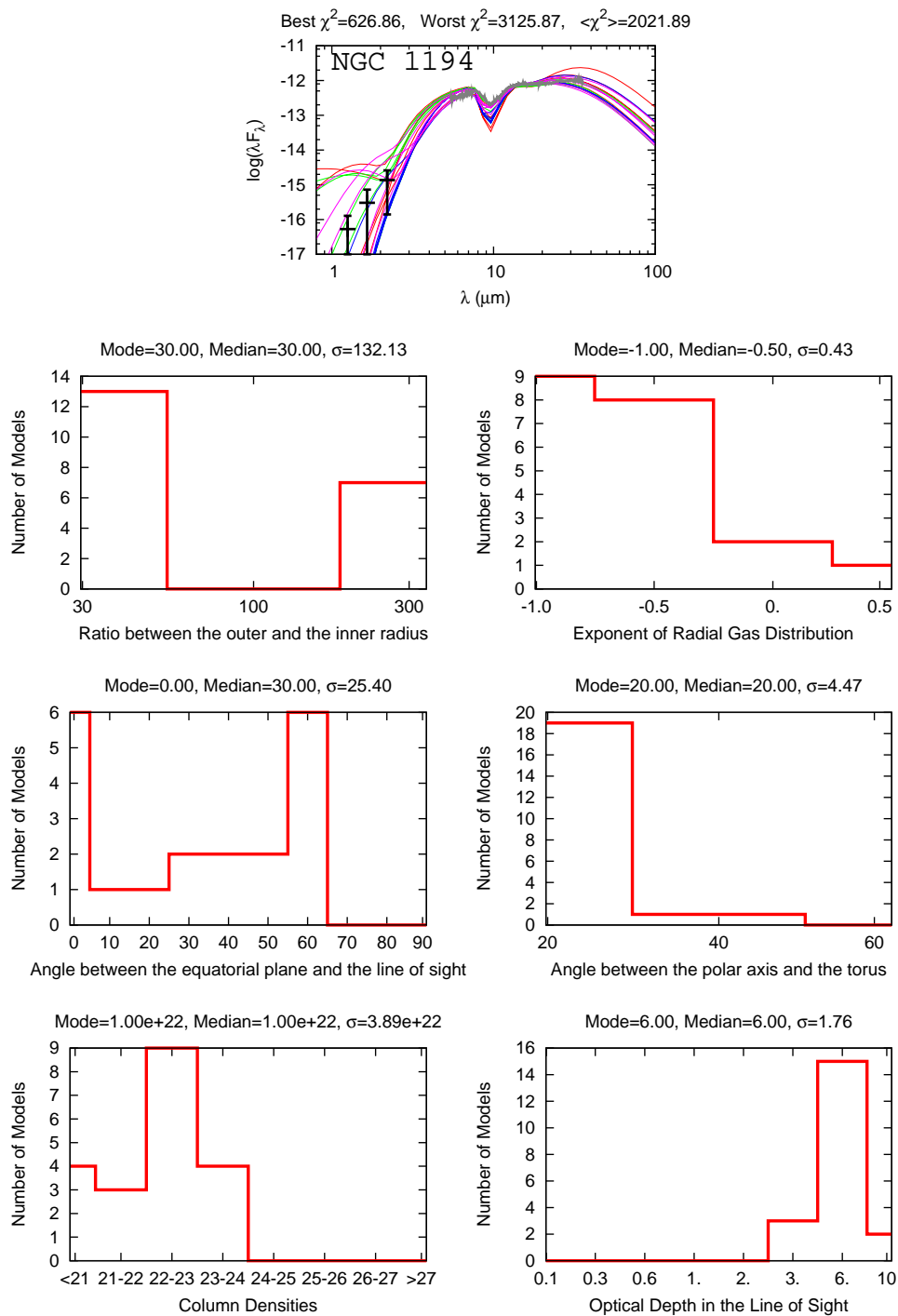


Figure 5.12: Best 20 smooth models fitted to NGC 1194, with specific parameters histograms shown. The preferred value for γ , the exponent of the angular distribution of dust, is 0. Although some cases with $\gamma = 6$.

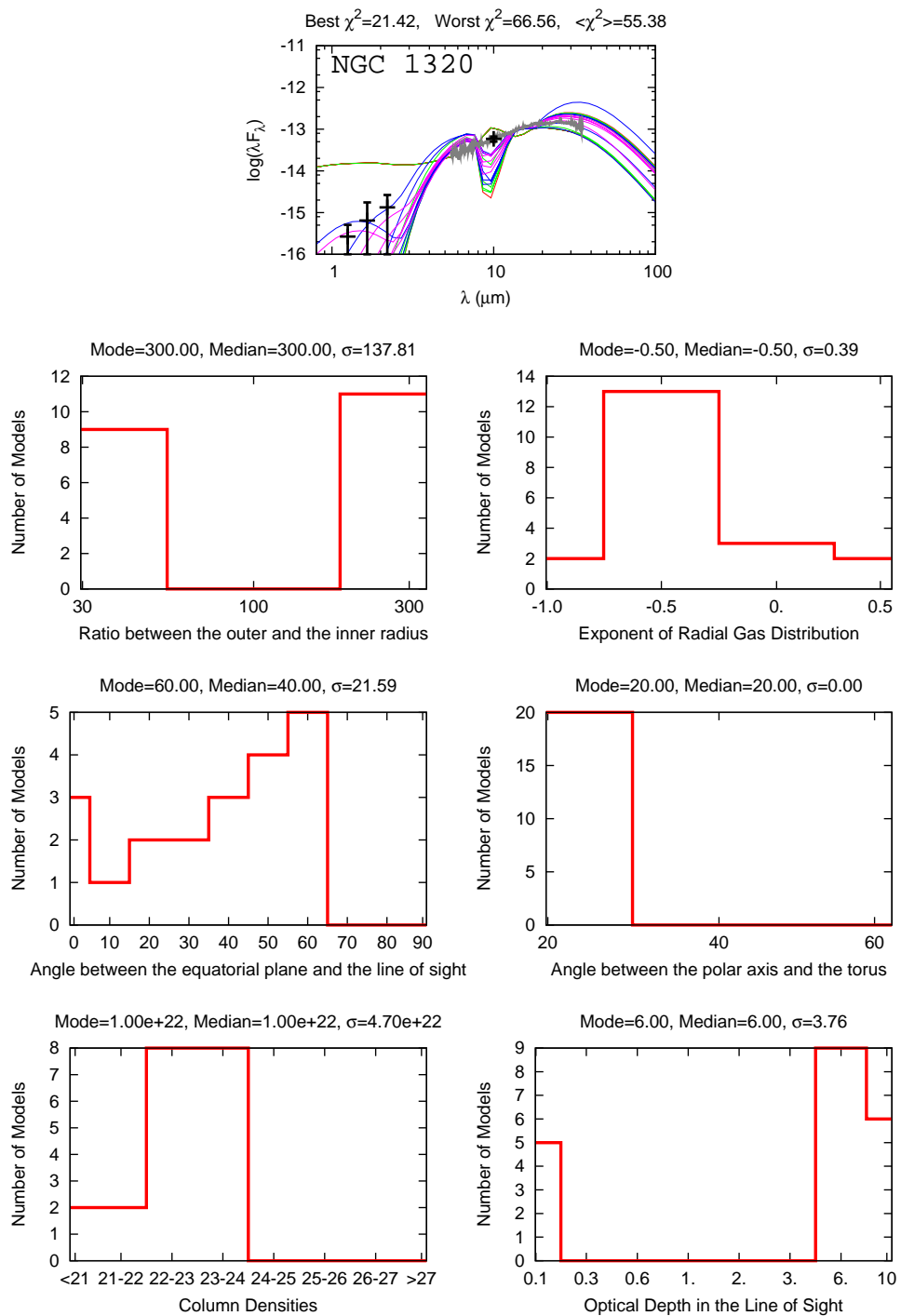


Figure 5.13: Best 20 smooth models fitted to NGC 1320, with specific parameters histograms shown. The preferred value for γ , the exponent of the angular distribution of dust, is 0. Although some cases with $\gamma = 6$.

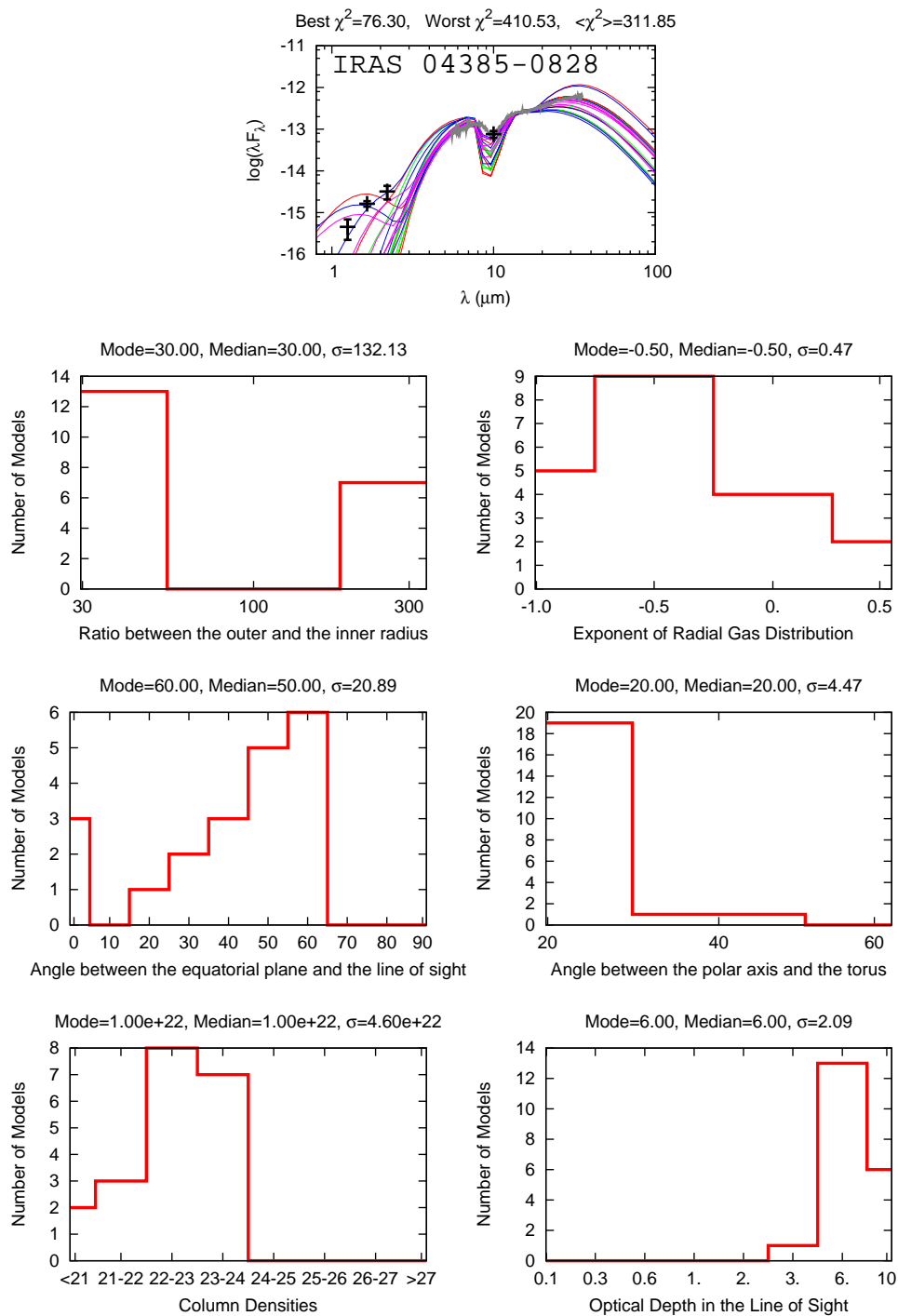


Figure 5.14: Best 20 smooth models fitted to IRAS 04385-0828, with specific parameters histograms shown. The preferred value for γ , the exponent of the angular distribution of dust, is 0. Although some cases with $\gamma = 6$.

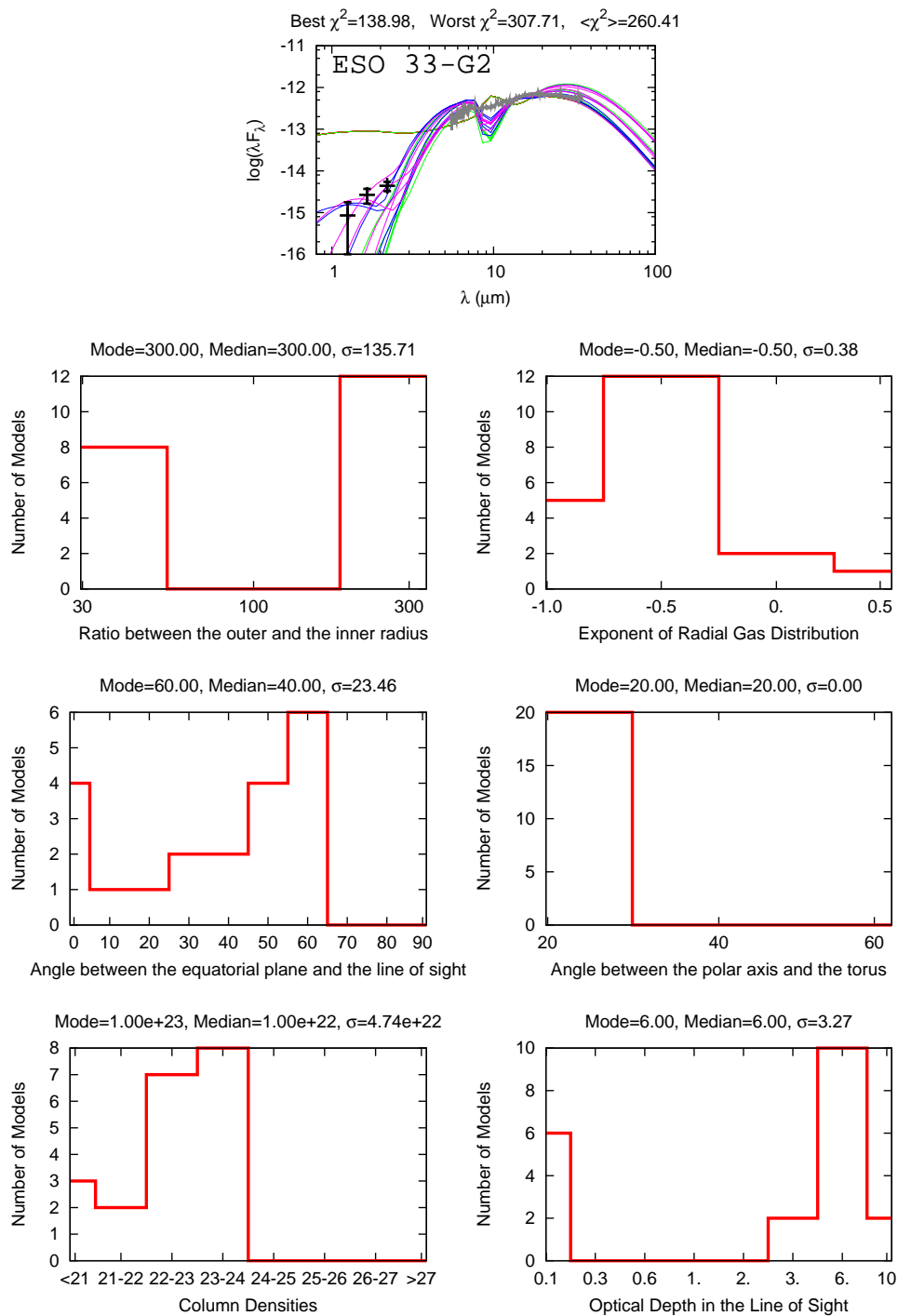


Figure 5.15: Best 20 smooth models fitted to ESO 33-G2, with specific parameters histograms shown. The preferred value for γ , the exponent of the angular distribution of dust, is 0. Although some cases with $\gamma = 6$.

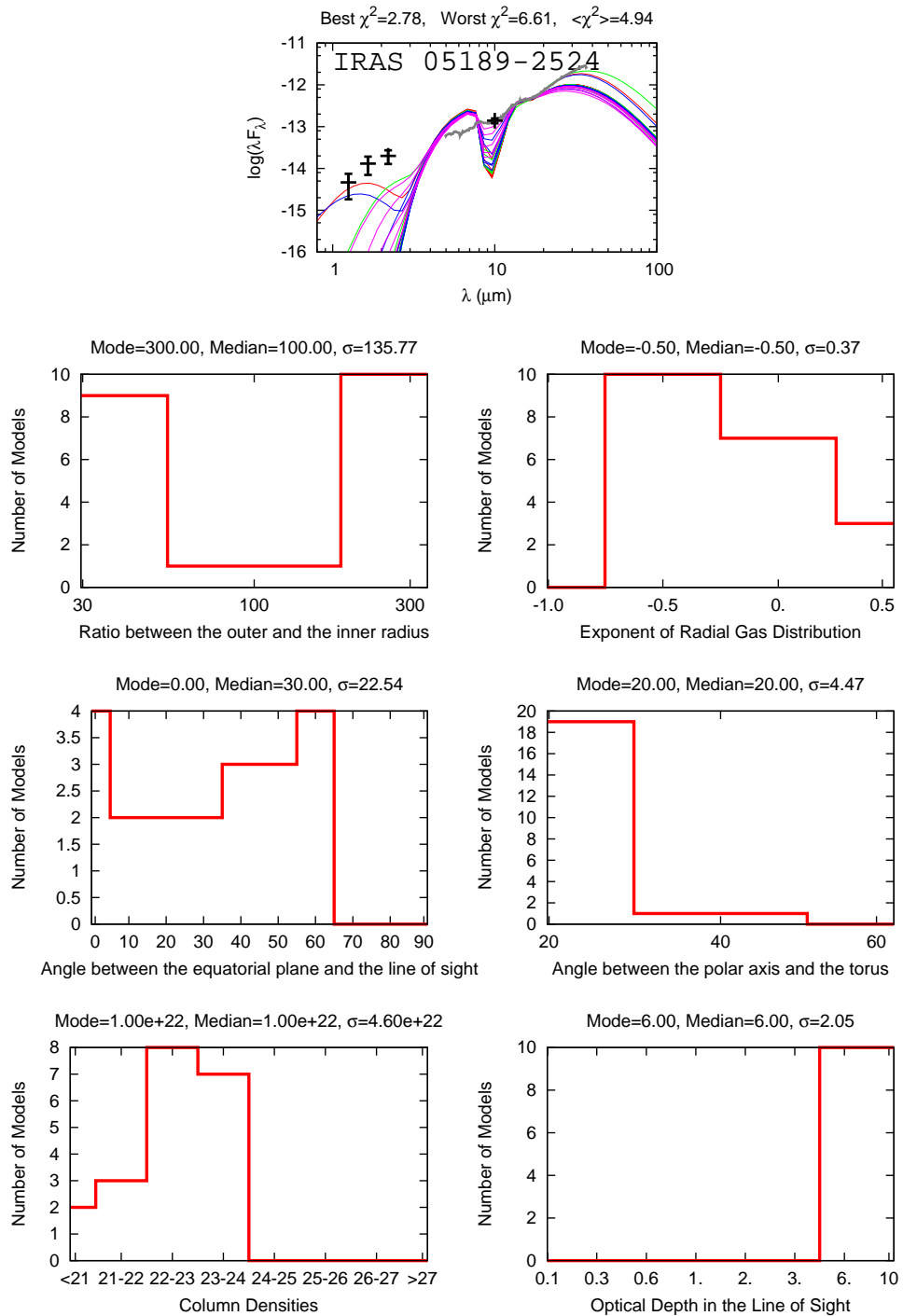


Figure 5.16: Best 20 smooth models fitted to IRAS 05189-2524, with specific parameters histograms shown. The preferred value for γ , the exponent of the angular distribution of dust, is 0. Although some cases with $\gamma = 6$.

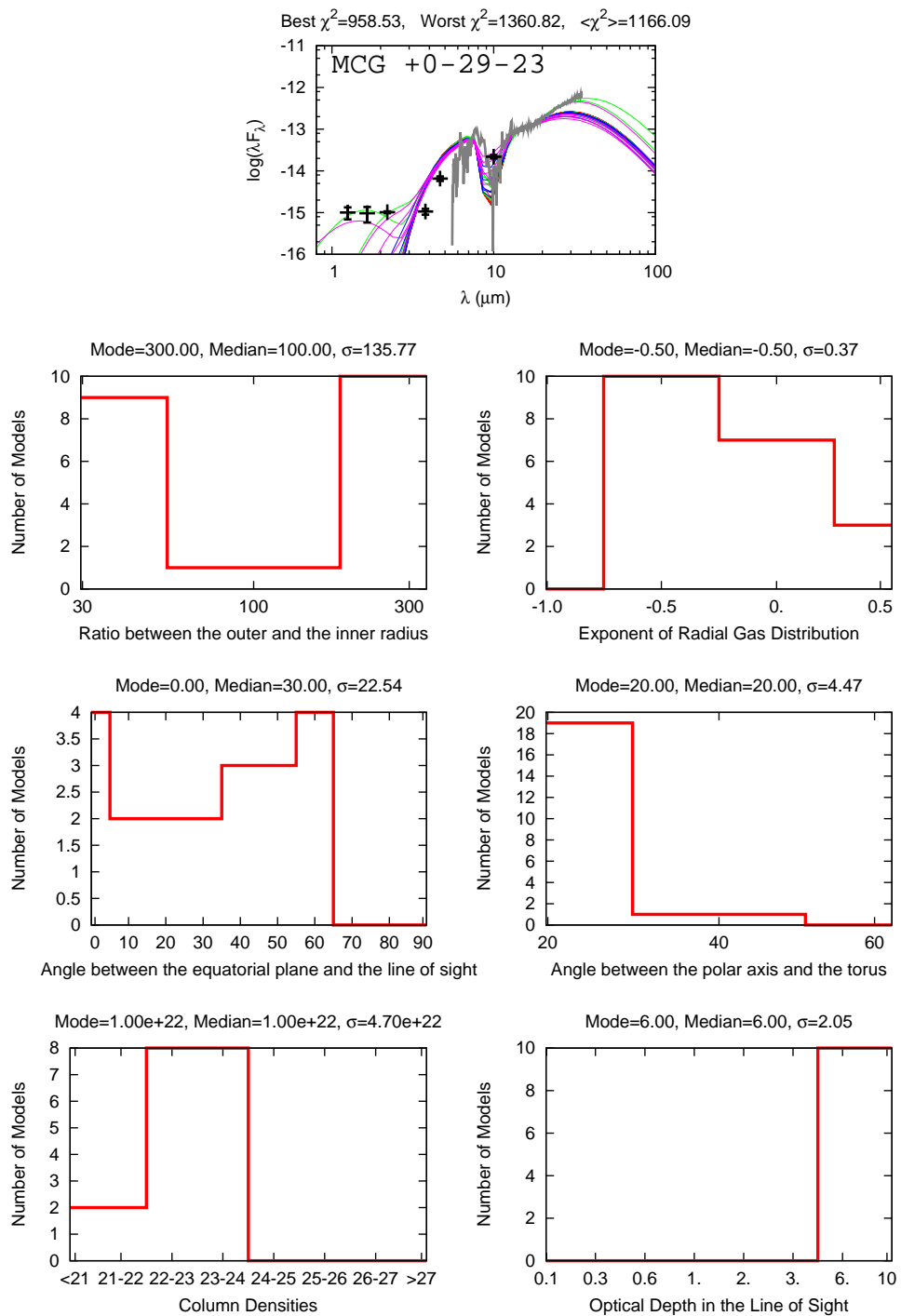


Figure 5.17: Best 20 smooth models fitted to MCG +0-29-23, with specific parameters histograms shown. The preferred value for γ , the exponent of the angular distribution of dust, is 0. Although some cases with $\gamma = 6$.

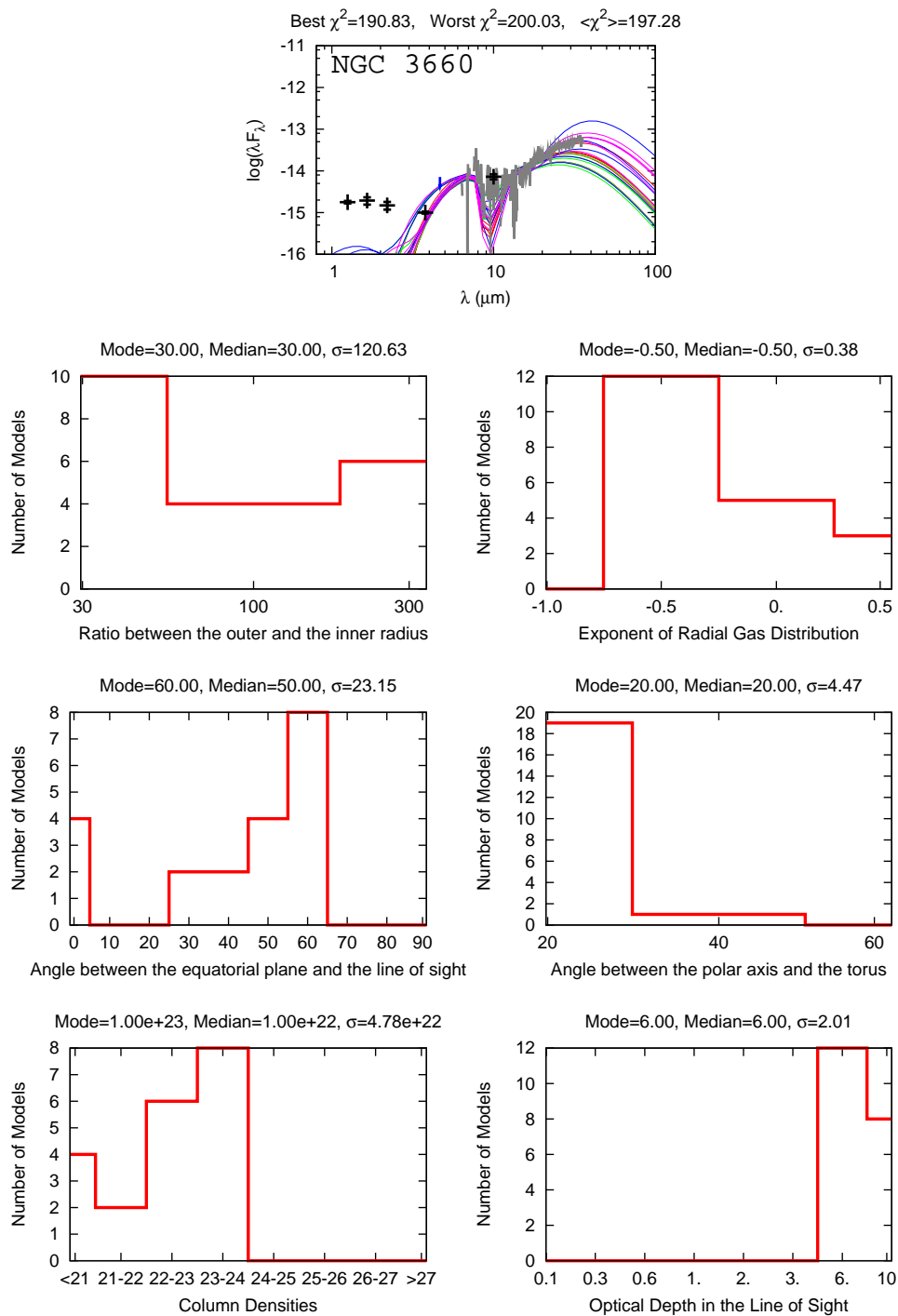


Figure 5.18: Best 20 smooth models fitted to NGC 3660, with specific parameters histograms shown. The preferred value for γ , the exponent of the angular distribution of dust, is 0. Although some cases with $\gamma = 6$.

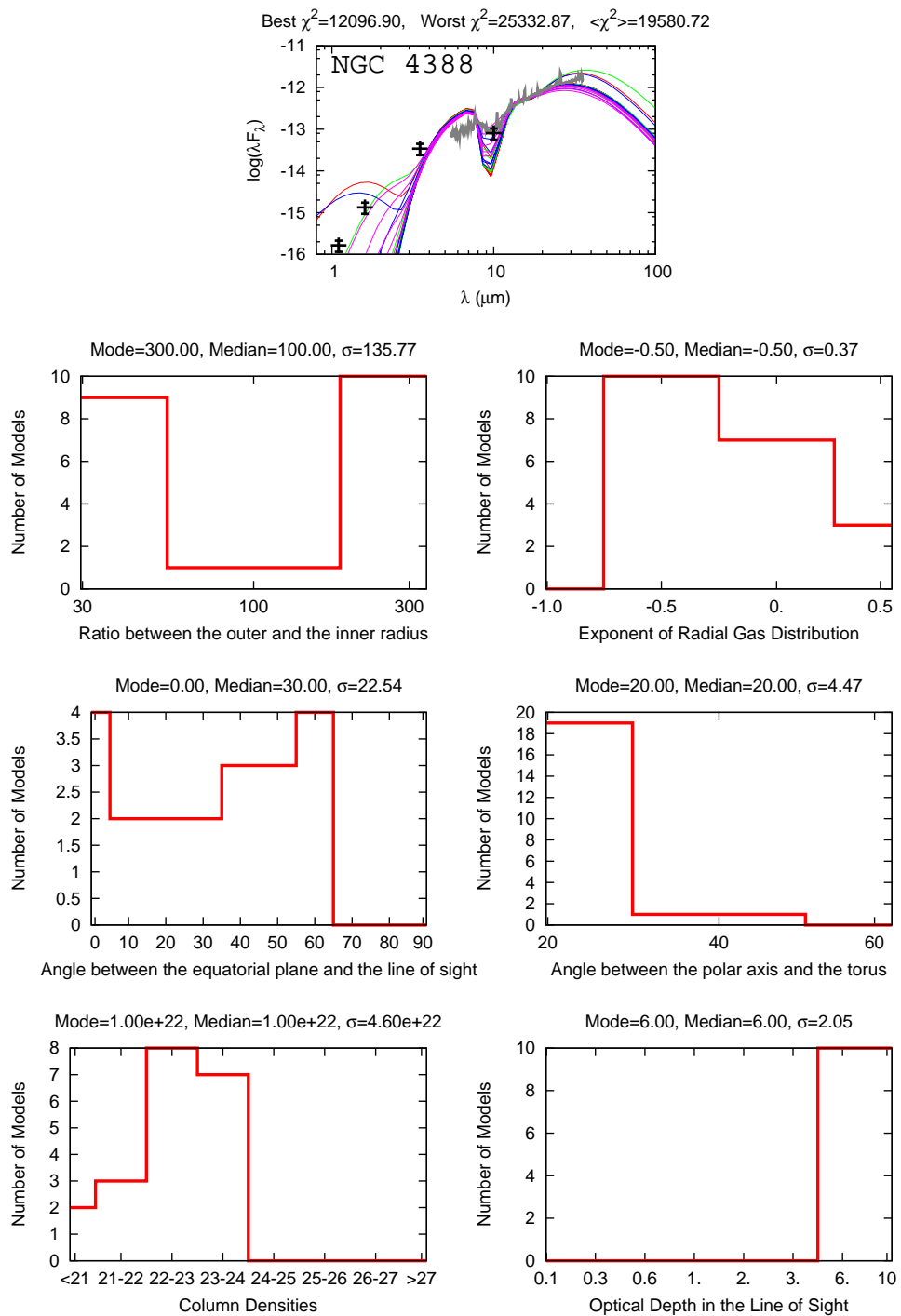


Figure 5.19: Best 20 smooth models fitted to NGC 4388, with specific parameters histograms shown. The preferred value for γ , the exponent of the angular distribution of dust, is 0. Although some cases with $\gamma = 6$.

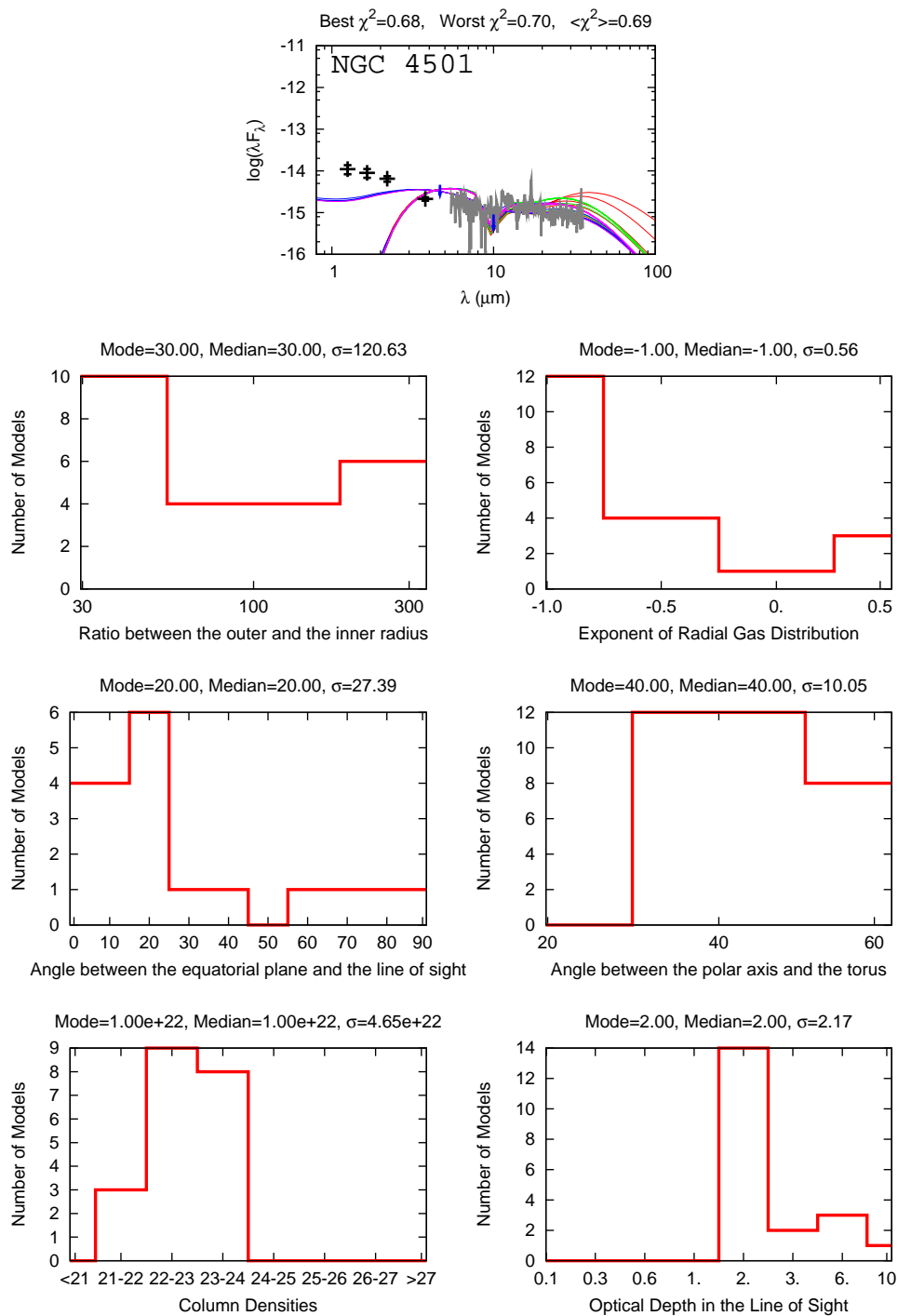


Figure 5.20: Best 20 smooth models fitted to NGC 4501, with specific parameters histograms shown. The preferred value for γ , the exponent of the angular distribution of dust, is 0. Although some cases with $\gamma = 6$.

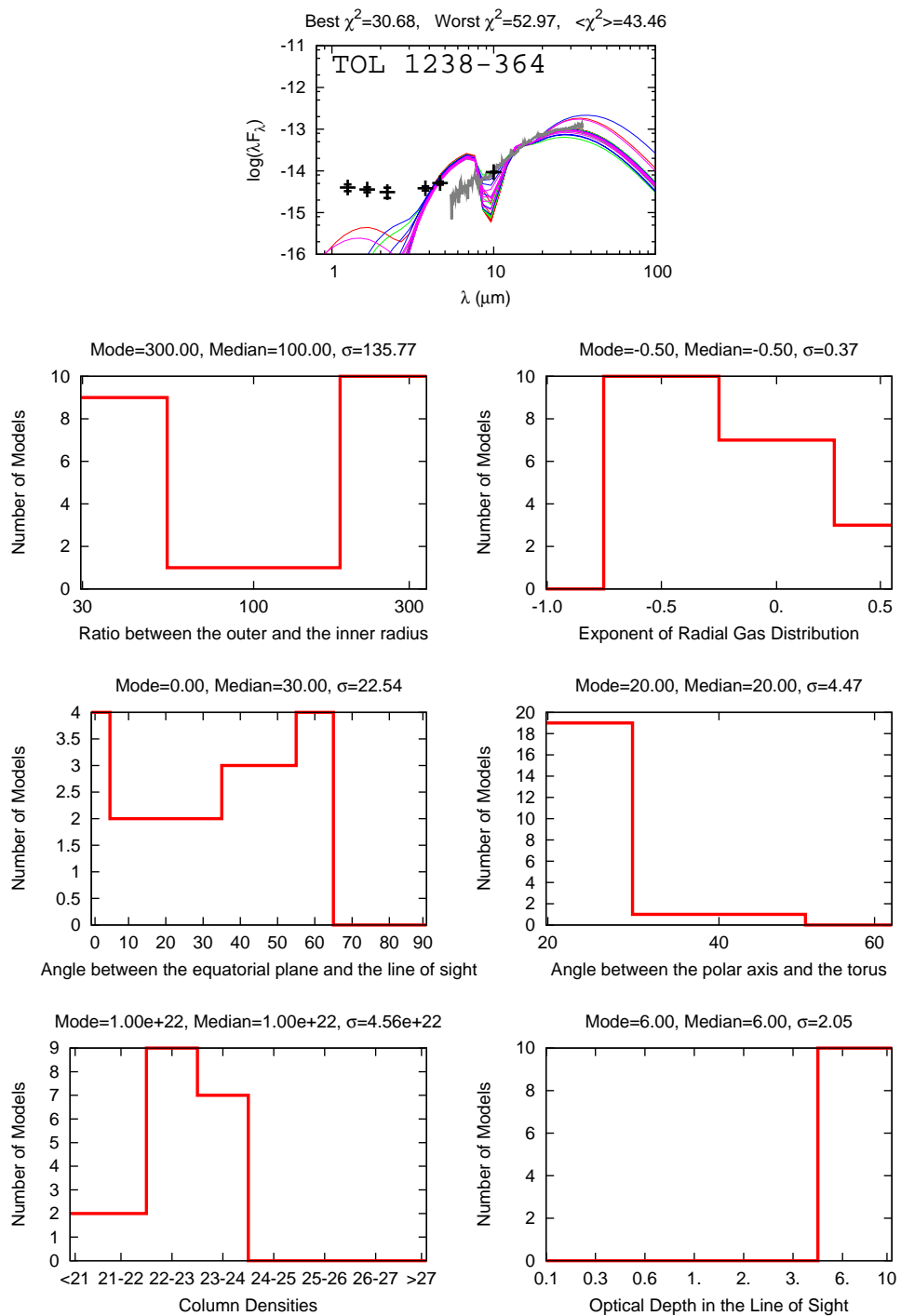


Figure 5.21: Best 20 smooth models fitted to TOL 1238-364, with specific parameters histograms shown. The preferred value for γ , the exponent of the angular distribution of dust, is 0. Although some cases with $\gamma = 6$.

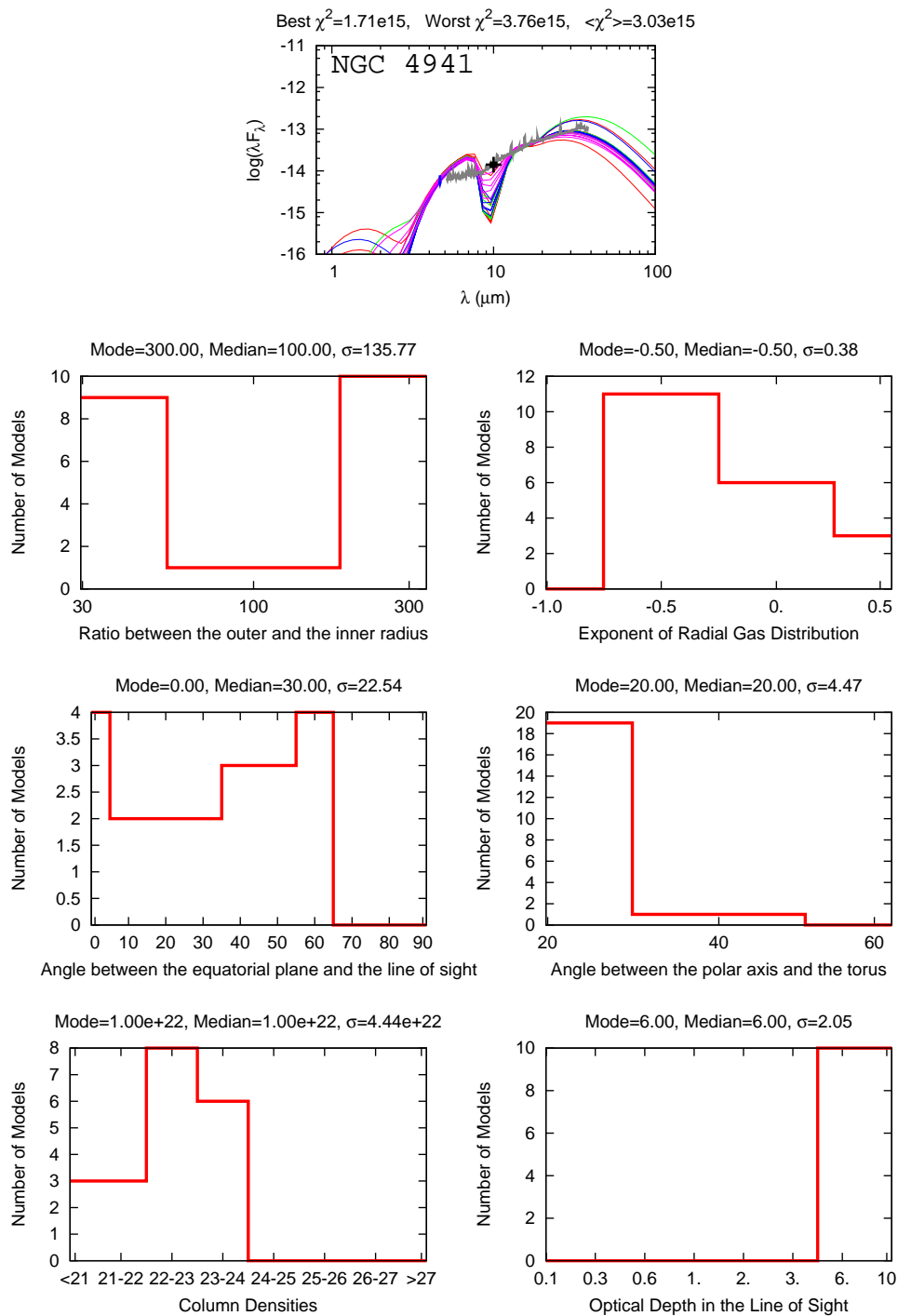


Figure 5.22: Best 20 smooth models fitted to NGC 4941, with specific parameters histograms shown. The preferred value for γ , the exponent of the angular distribution of dust, is 0. Although some cases with $\gamma = 6$.

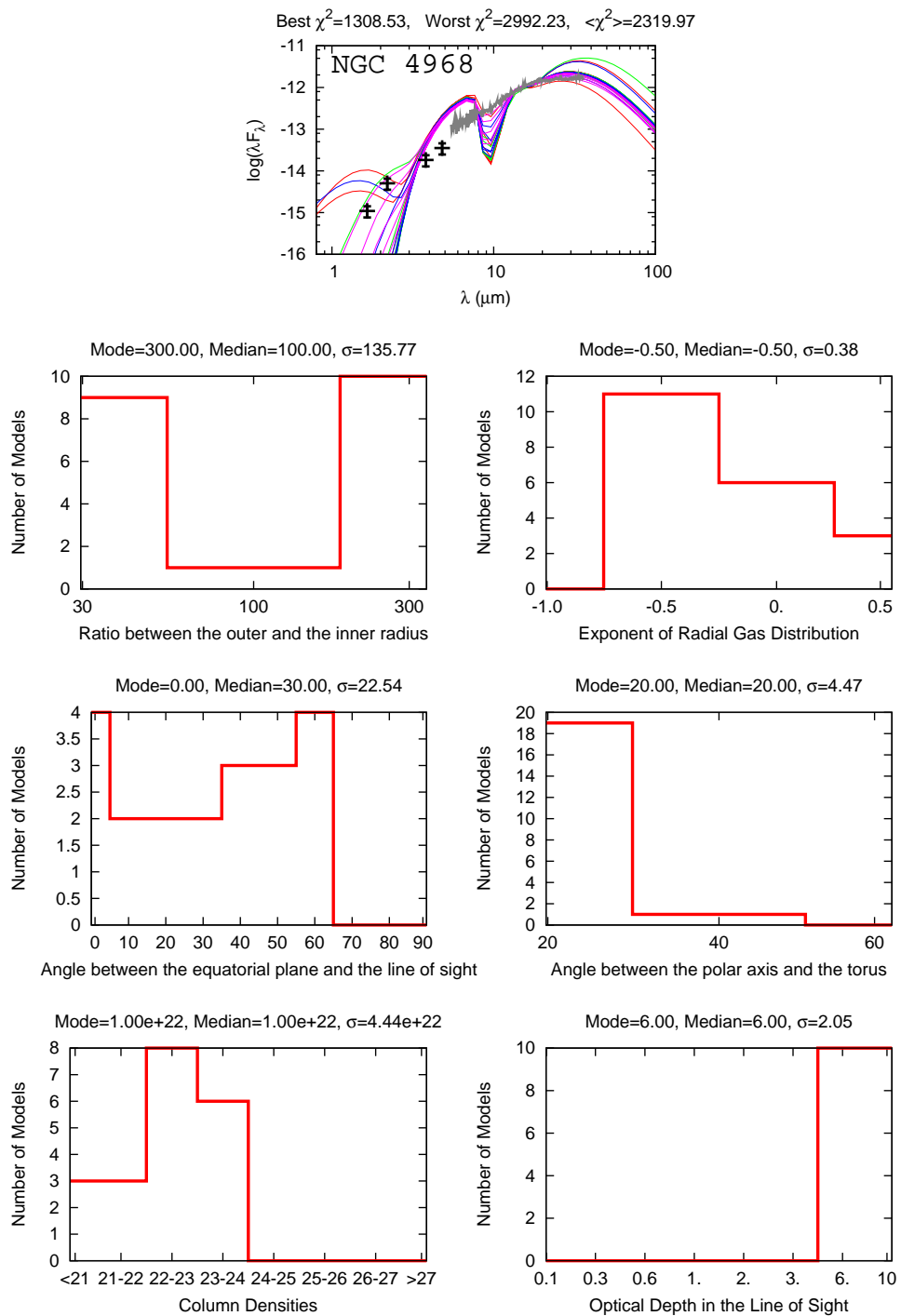


Figure 5.23: Best 20 smooth models fitted to NGC 4968, with specific parameters histograms shown. The preferred value for γ , the exponent of the angular distribution of dust, is 0. Although some cases with $\gamma = 6$.

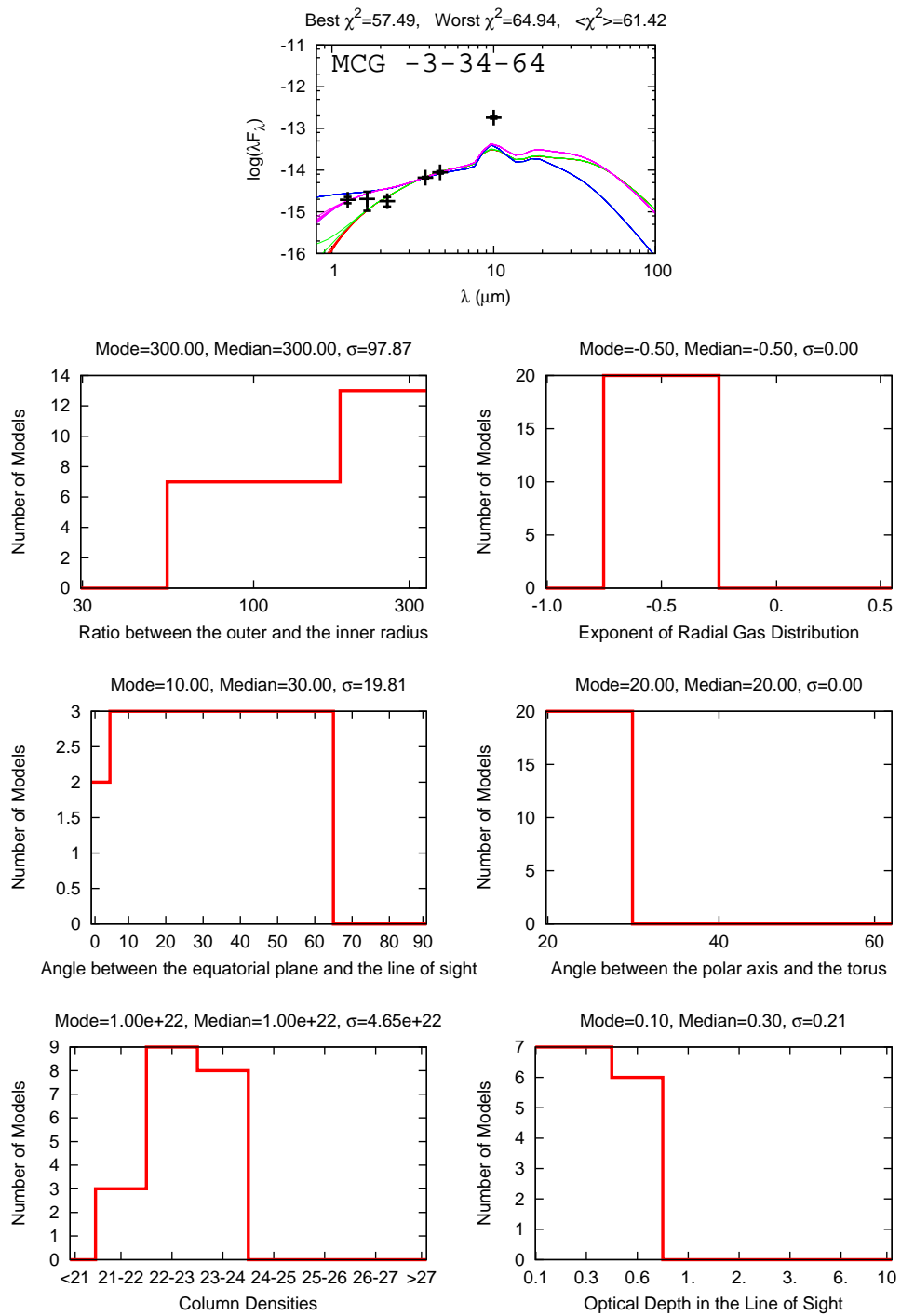


Figure 5.24: Best 20 smooth models fitted to MCG -3-34-64, with specific parameters histograms shown. Only cases with $\gamma = 0$ are preferred.

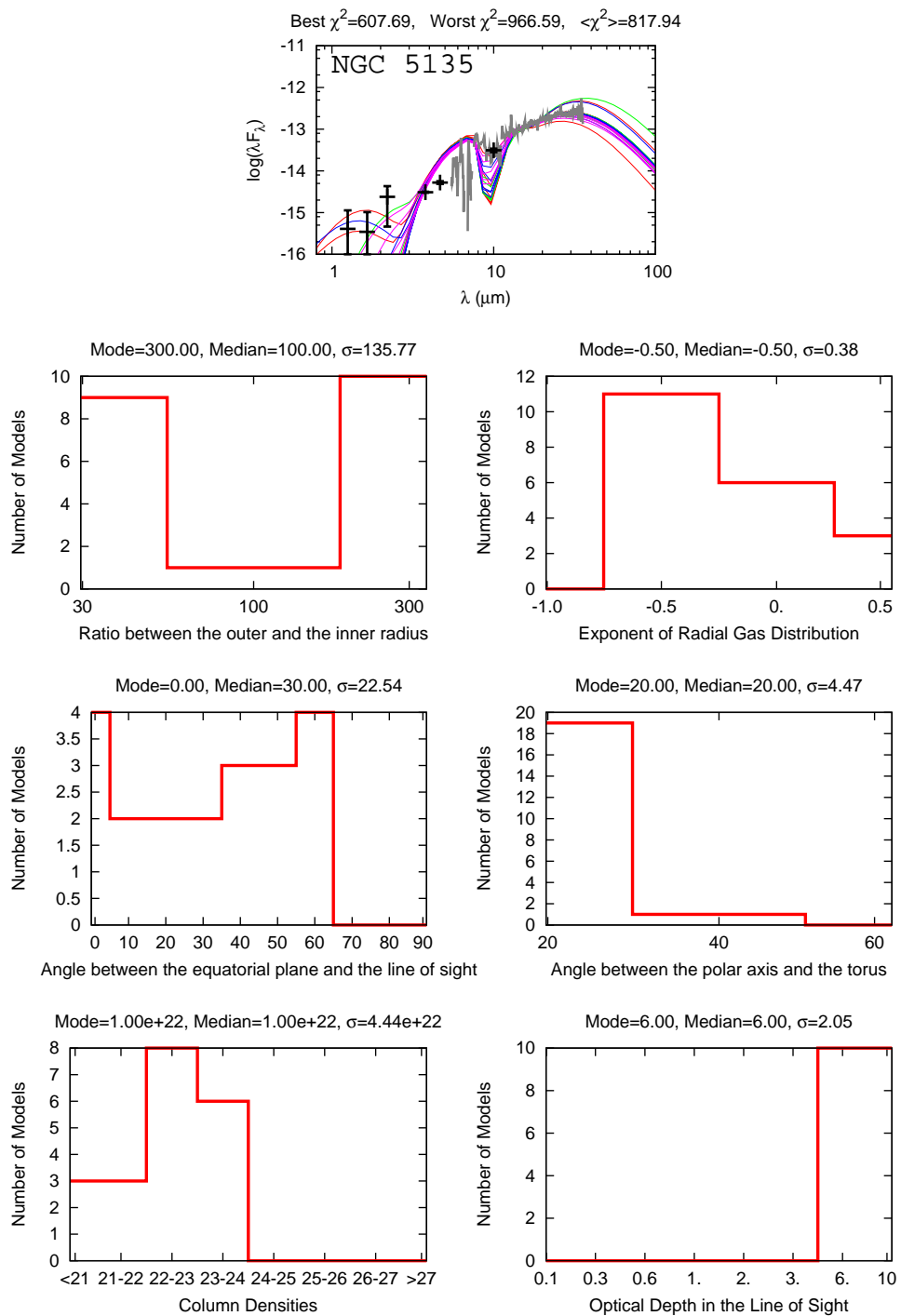


Figure 5.25: Best 20 smooth models fitted to NGC 5135, with specific parameters histograms shown. The preferred value for γ , the exponent of the angular distribution of dust, is 0. Although some cases with $\gamma = 6$.

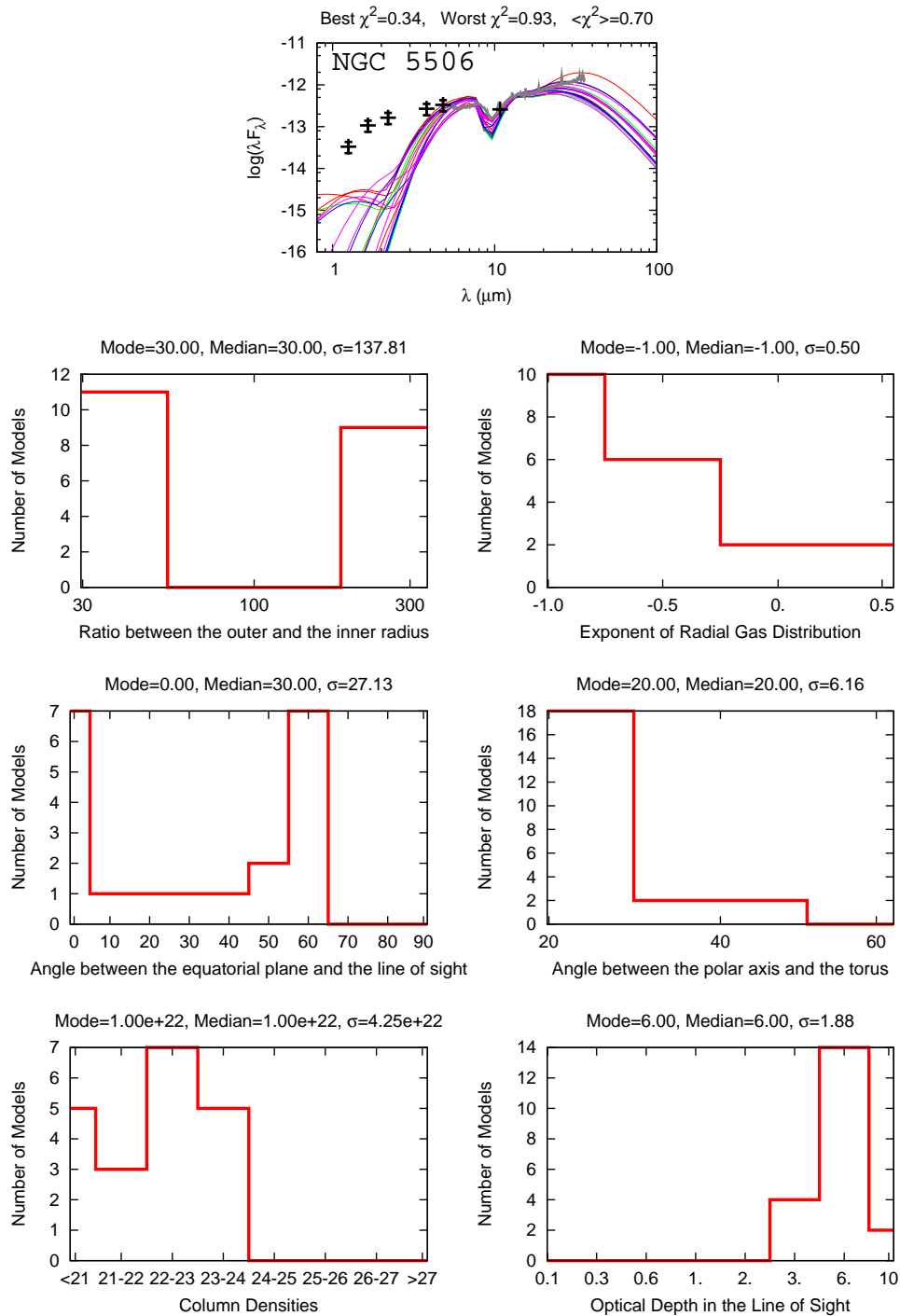


Figure 5.26: Best 20 smooth models fitted to NGC 5506, with specific parameters histograms shown. The preferred value for γ , the exponent of the angular distribution of dust, is 0. Although some cases with $\gamma = 6$.

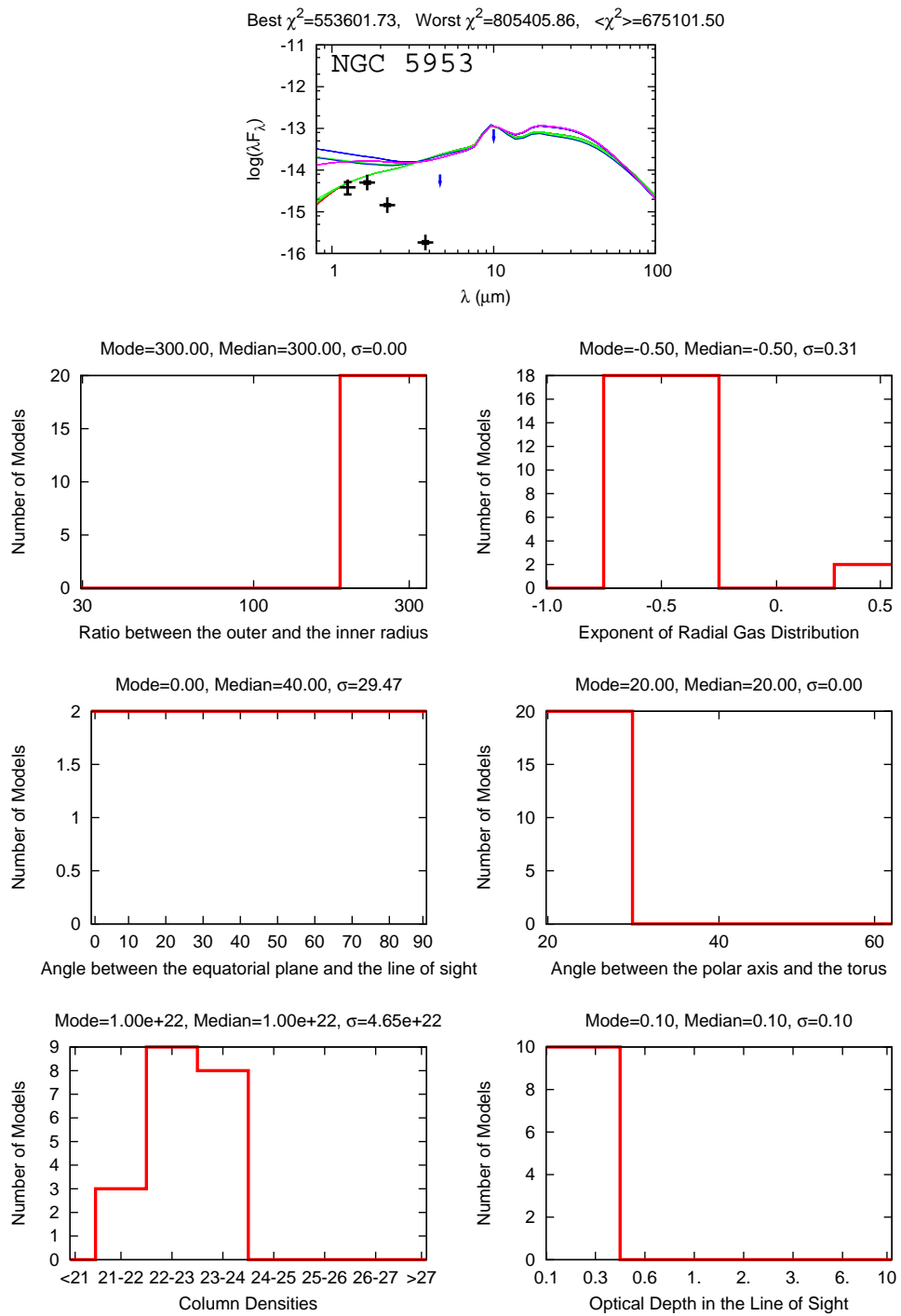


Figure 5.27: Best 20 smooth models fitted to NGC 5953, with specific parameters histograms shown. Only cases with $\gamma = 0$ are preferred.

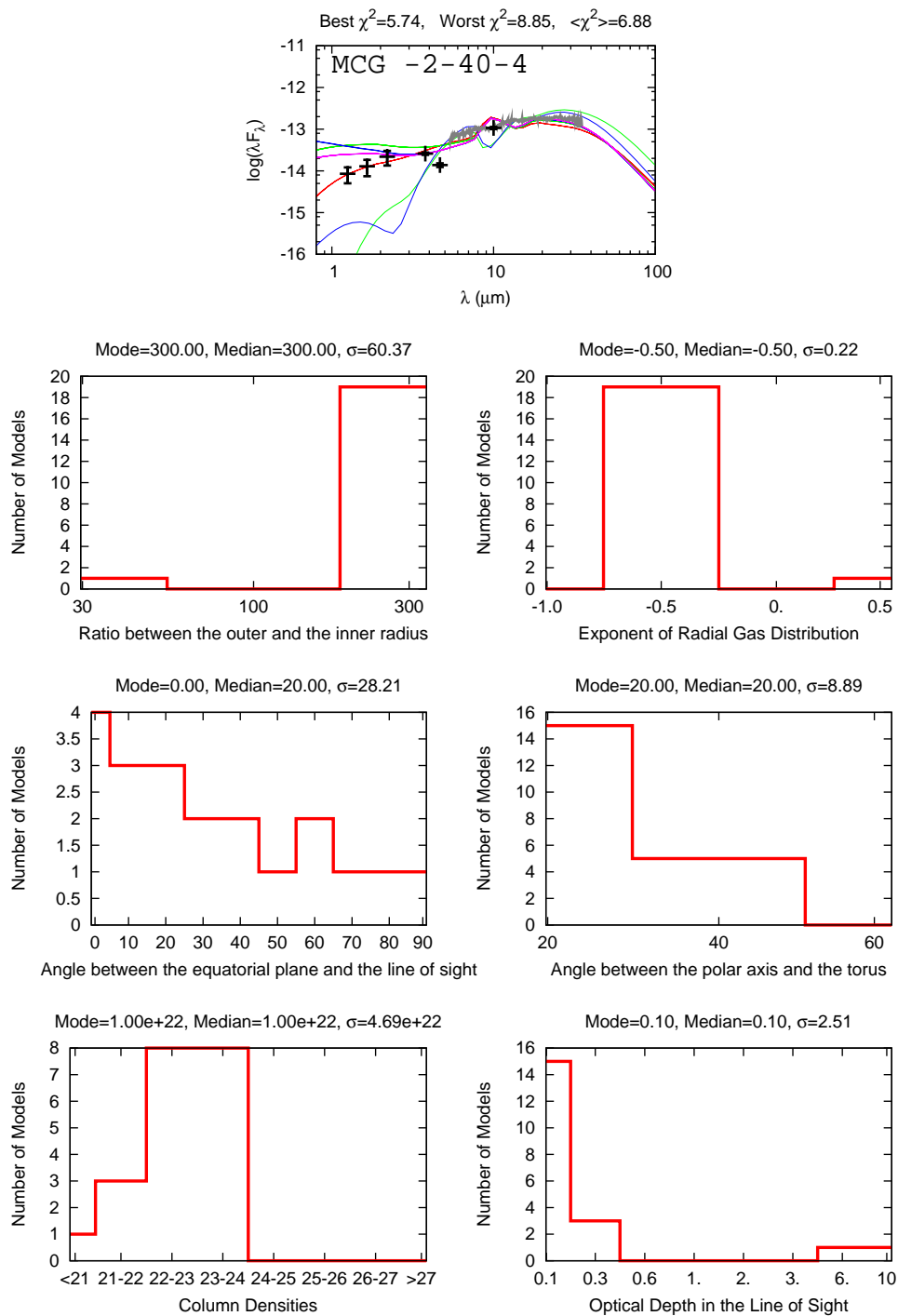


Figure 5.28: Best 20 smooth models fitted to MCG -2-40-4, with specific parameters histograms shown. The preferred value for γ , the exponent of the angular distribution of dust, is 0. Although some cases with $\gamma = 6$.

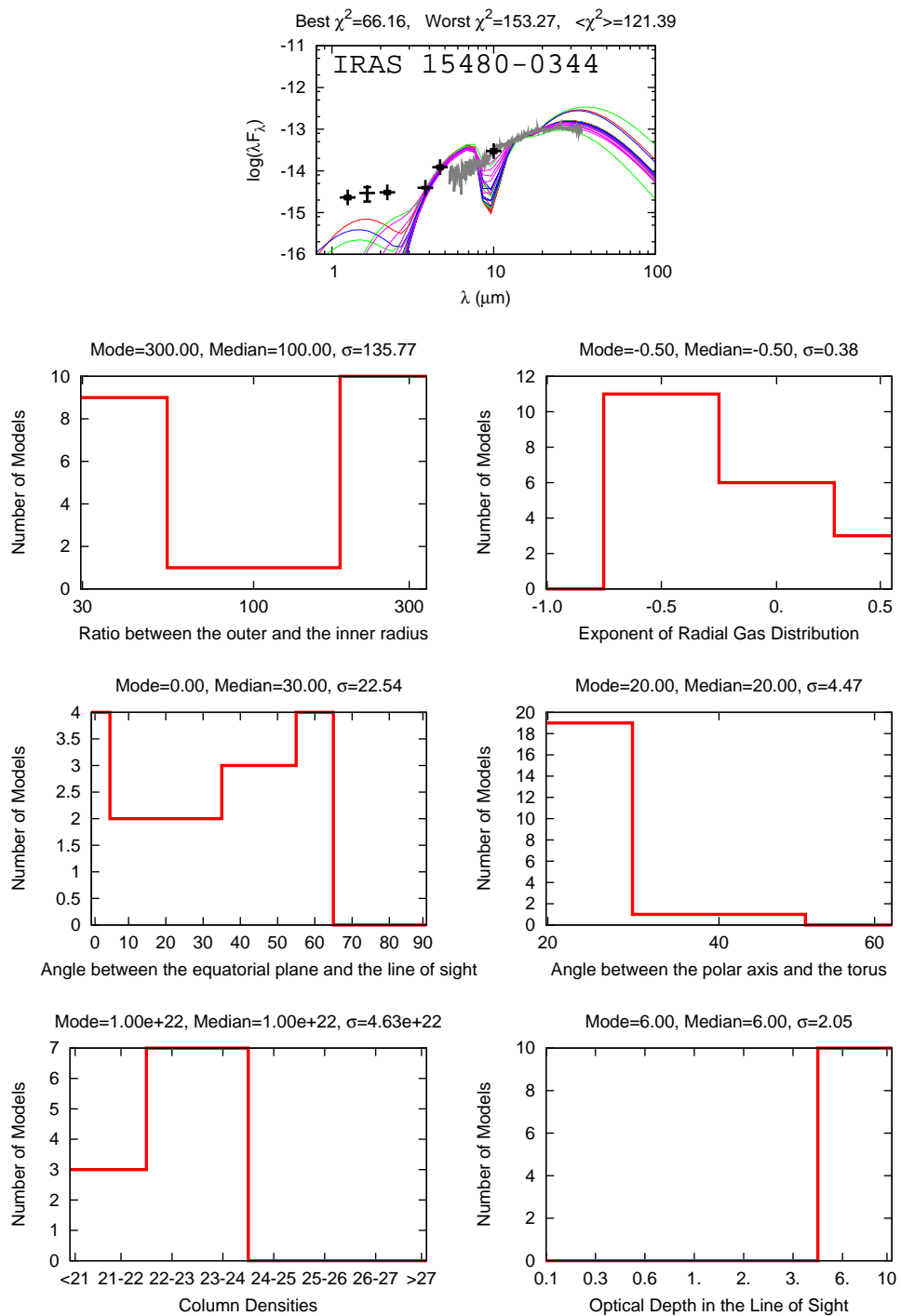


Figure 5.29: Best 20 smooth models fitted to IRAS 15480-0344, with specific parameters histograms shown. The preferred value for γ , the exponent of the angular distribution of dust, is 0. Although some cases with $\gamma = 6$.

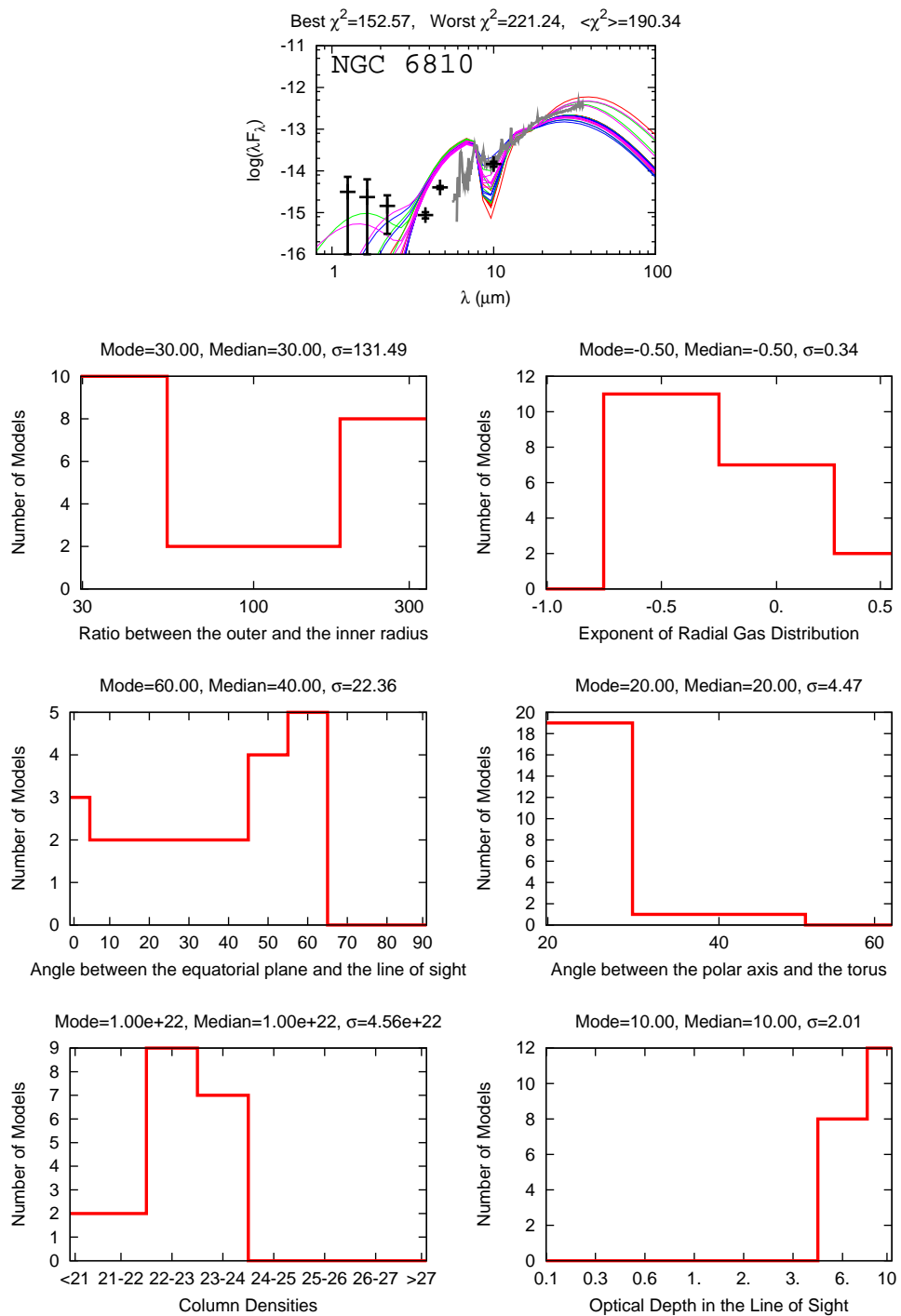


Figure 5.30: Best 20 smooth models fitted to NGC 6810, with specific parameters histograms shown. The preferred value for γ , the exponent of the angular distribution of dust, is 0. Although some cases with $\gamma = 6$.

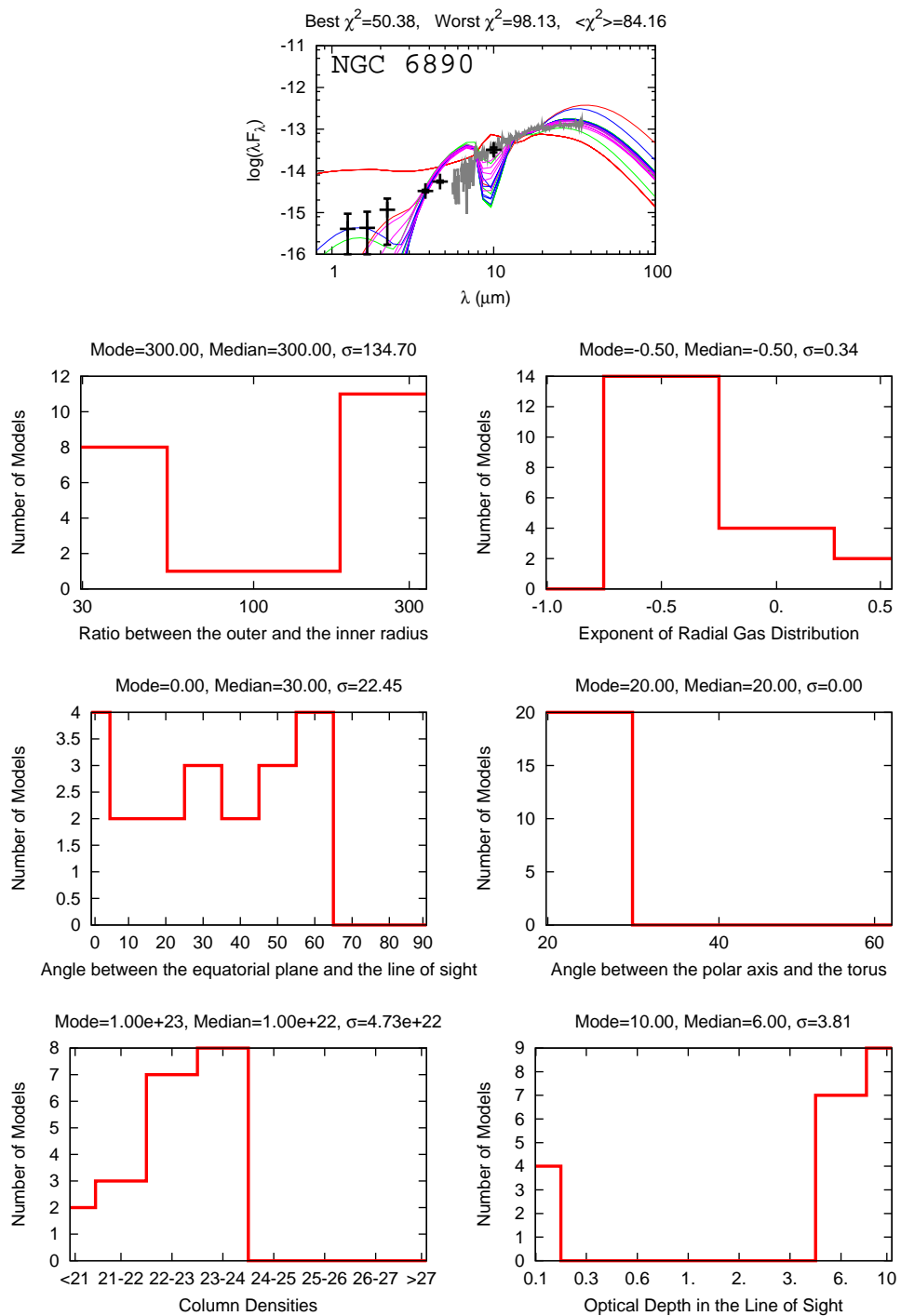


Figure 5.31: Best 20 smooth models fitted to NGC 6890, with specific parameters histograms shown. The preferred value for γ , the exponent of the angular distribution of dust, is 0. Although some cases with $\gamma = 6$.

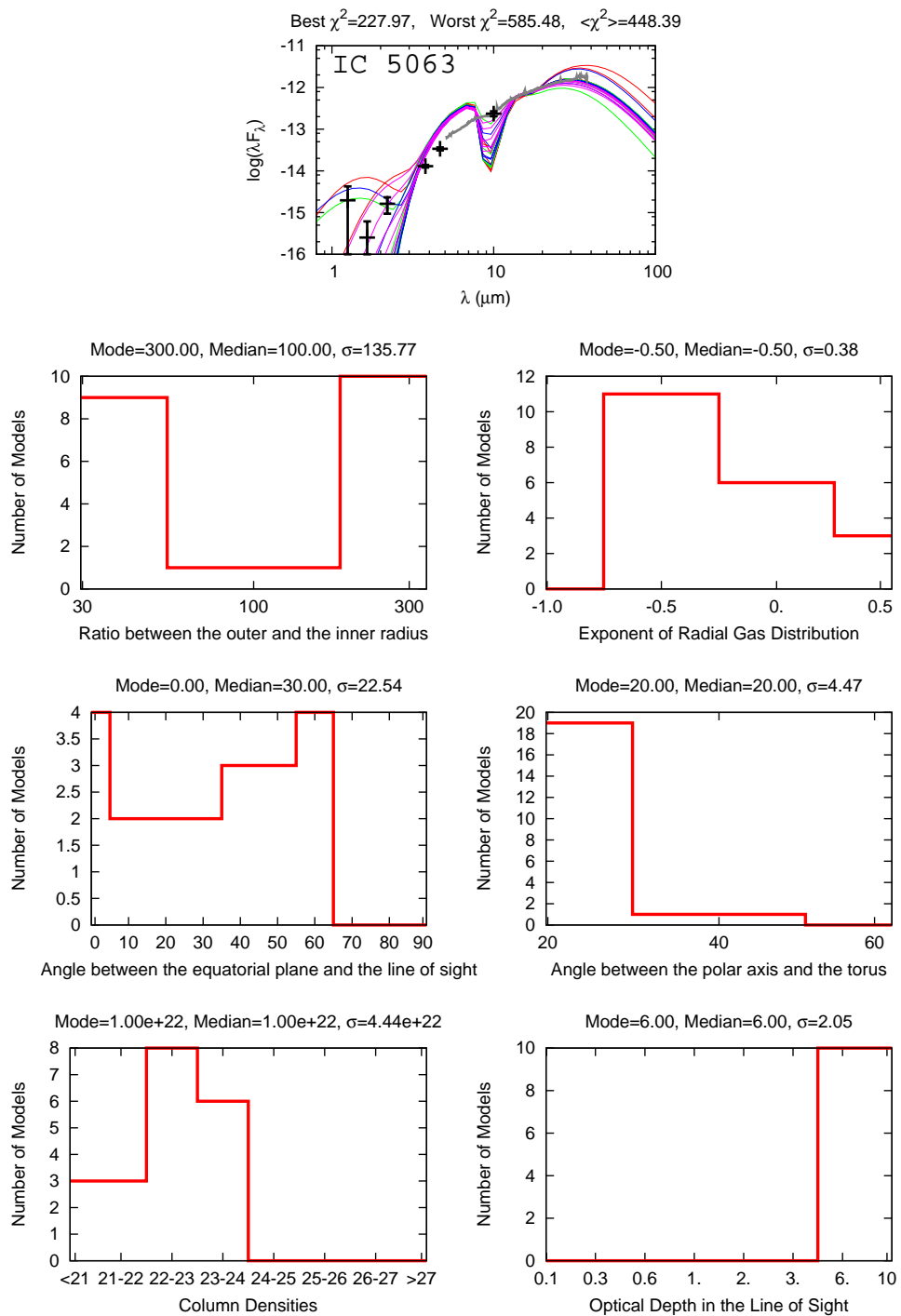


Figure 5.32: Best 20 smooth models fitted to IC 5063, with specific parameters histograms shown. The preferred value for γ , the exponent of the angular distribution of dust, is 0. Although some cases with $\gamma = 6$.

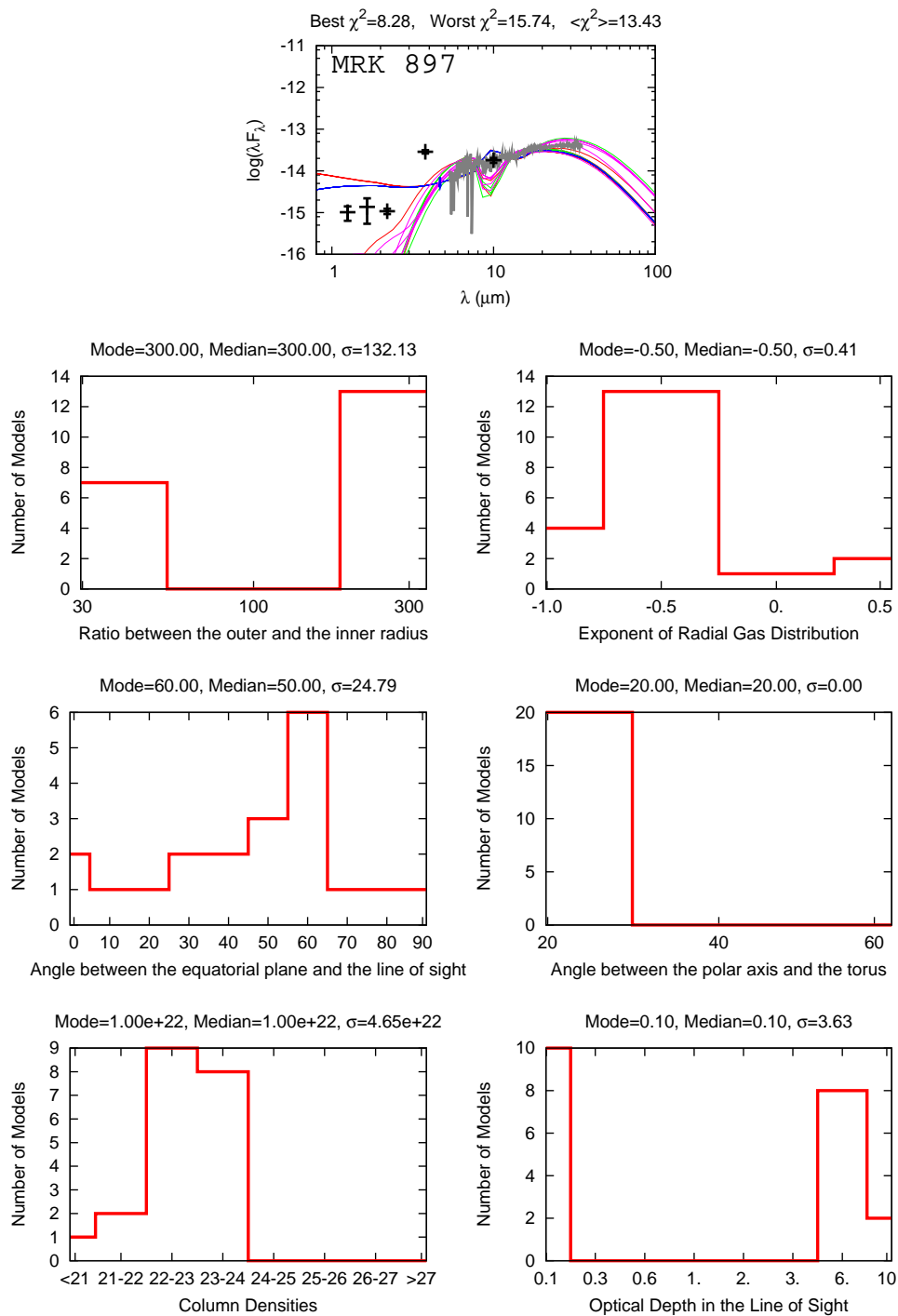


Figure 5.33: Best 20 smooth models fitted to MRK 897, with specific parameters histograms shown. The preferred value for γ , the exponent of the angular distribution of dust, is 0. Although some cases with $\gamma = 6$.

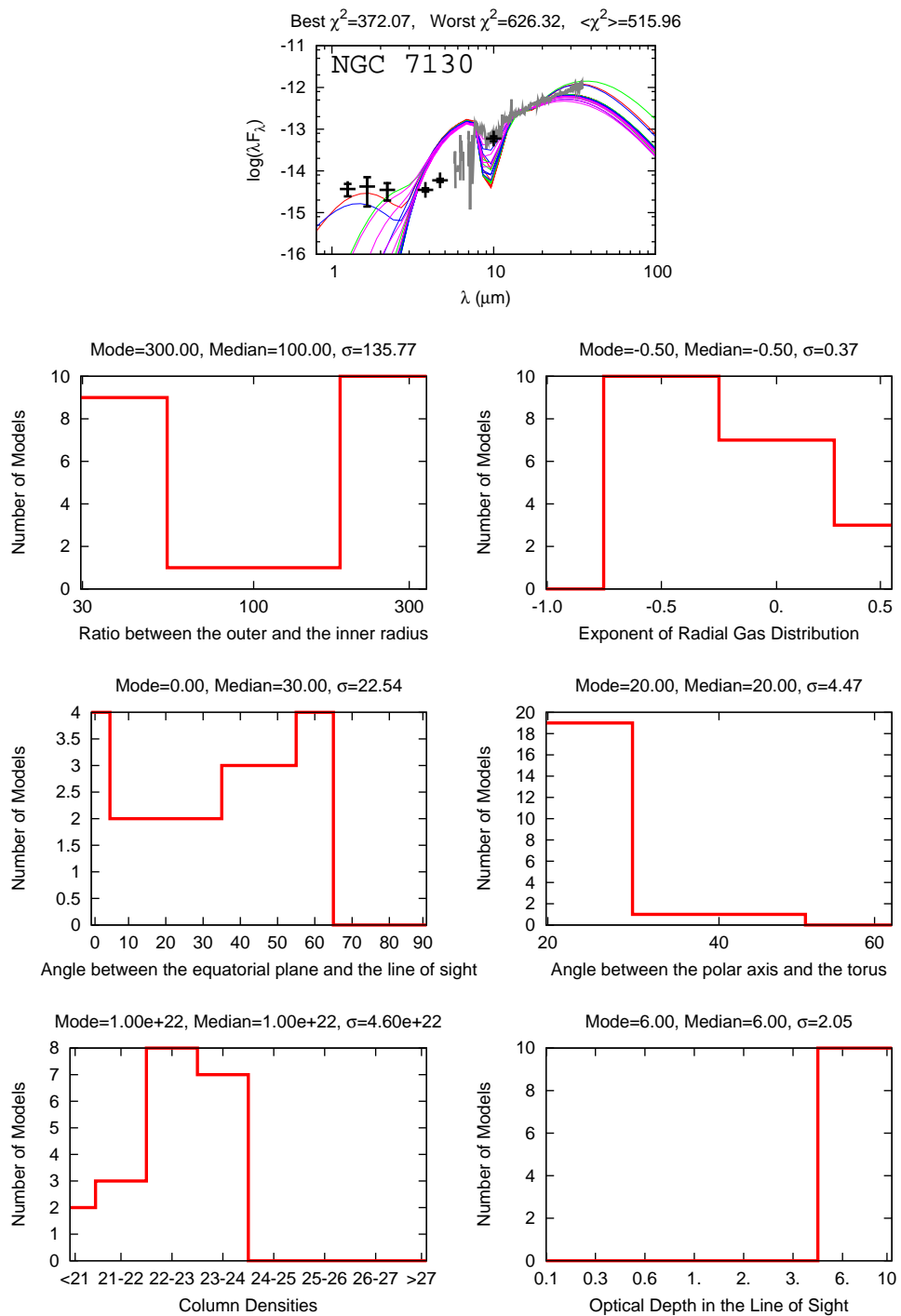


Figure 5.34: Best 20 smooth models fitted to NGC 7130, with specific parameters histograms shown. The preferred value for γ , the exponent of the angular distribution of dust, is 0. Although some cases with $\gamma = 6$.

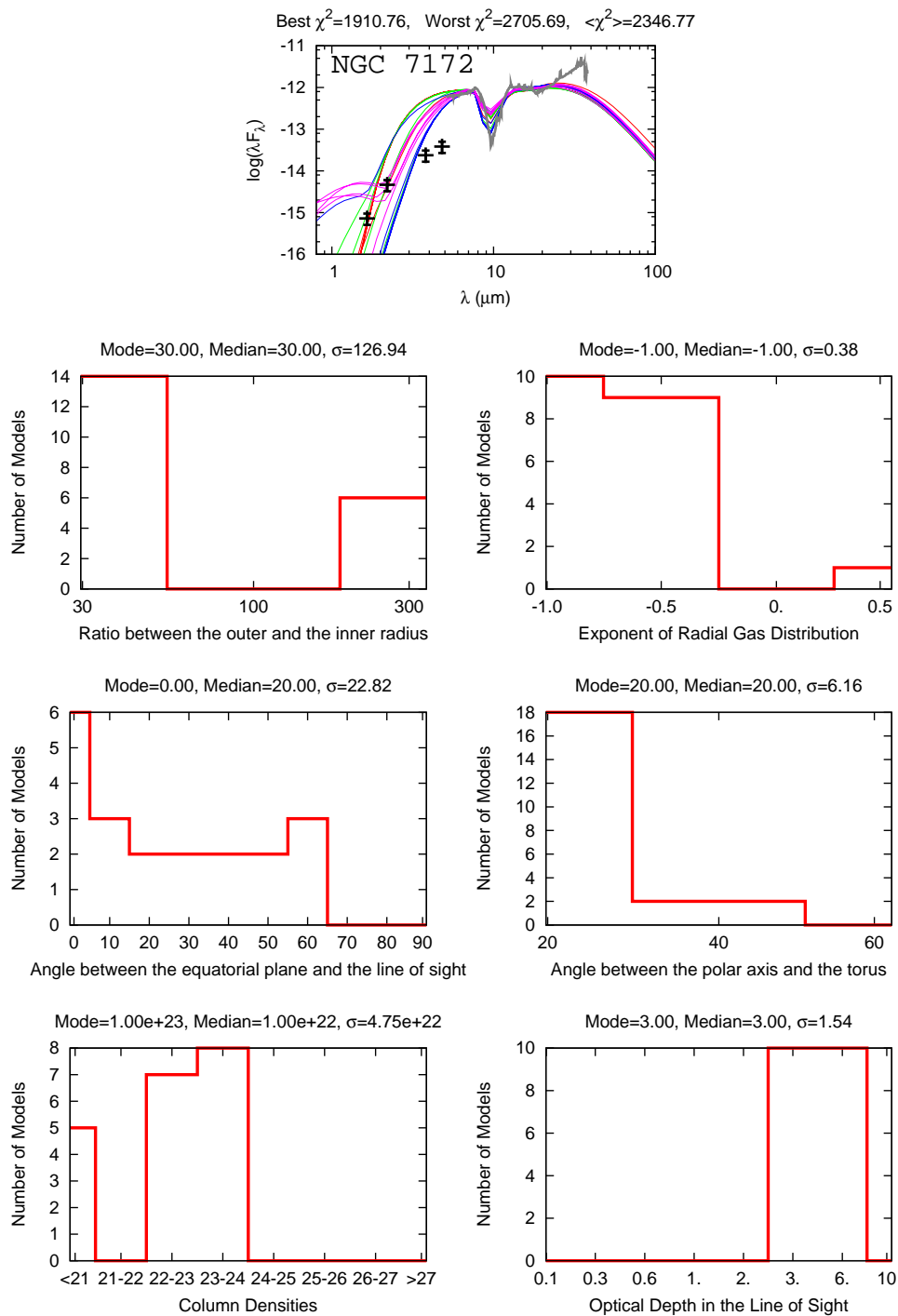


Figure 5.35: Best 20 smooth models fitted to NGC 7172, with specific parameters histograms shown. The preferred value for γ , the exponent of the angular distribution of dust, is 0. Although some cases with $\gamma = 6$.

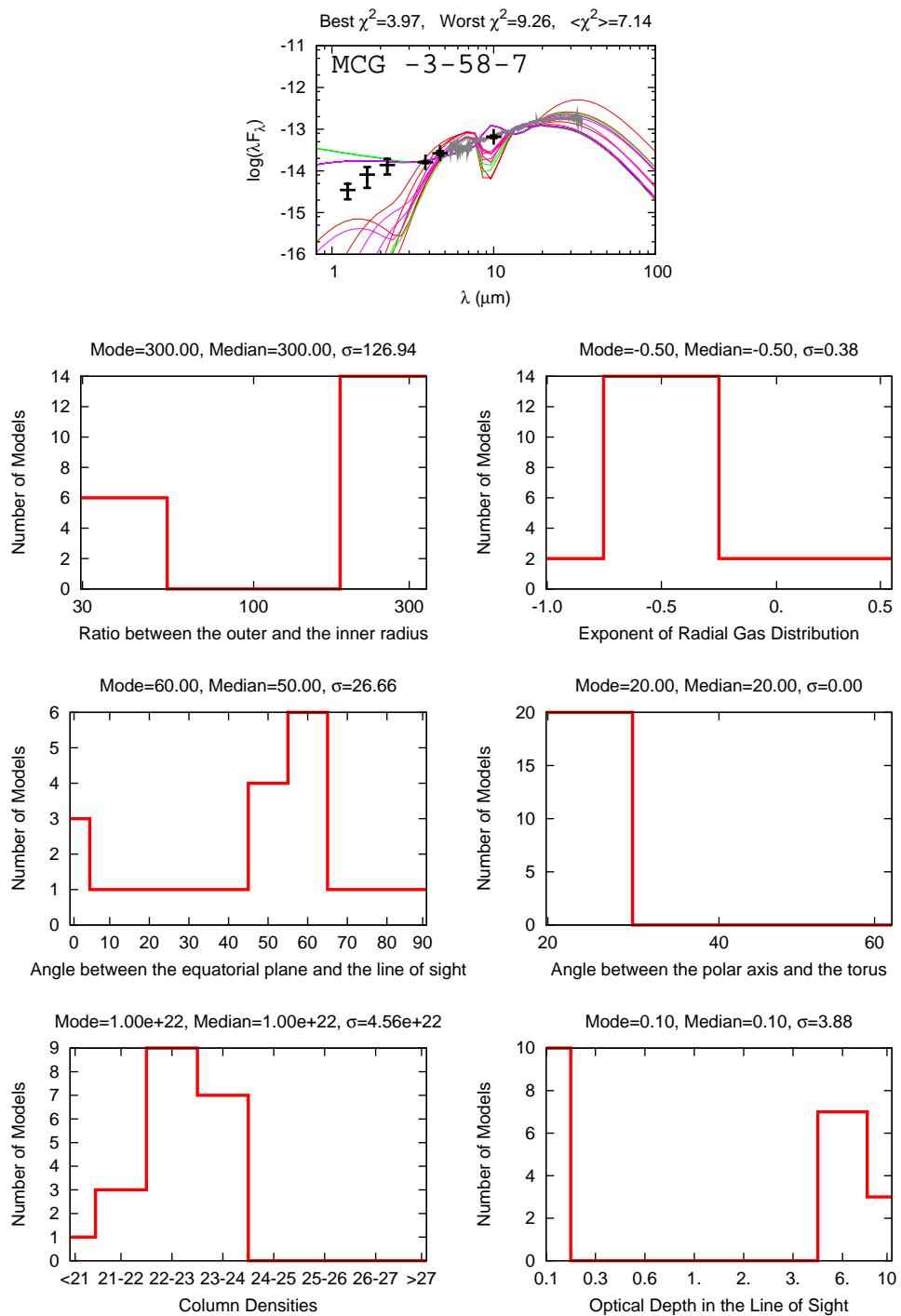


Figure 5.36: Best 20 smooth models fitted to MCG -3-58-7, with specific parameters histograms shown. The preferred value for γ , the exponent of the angular distribution of dust, is 0. Although some cases with $\gamma = 6$.

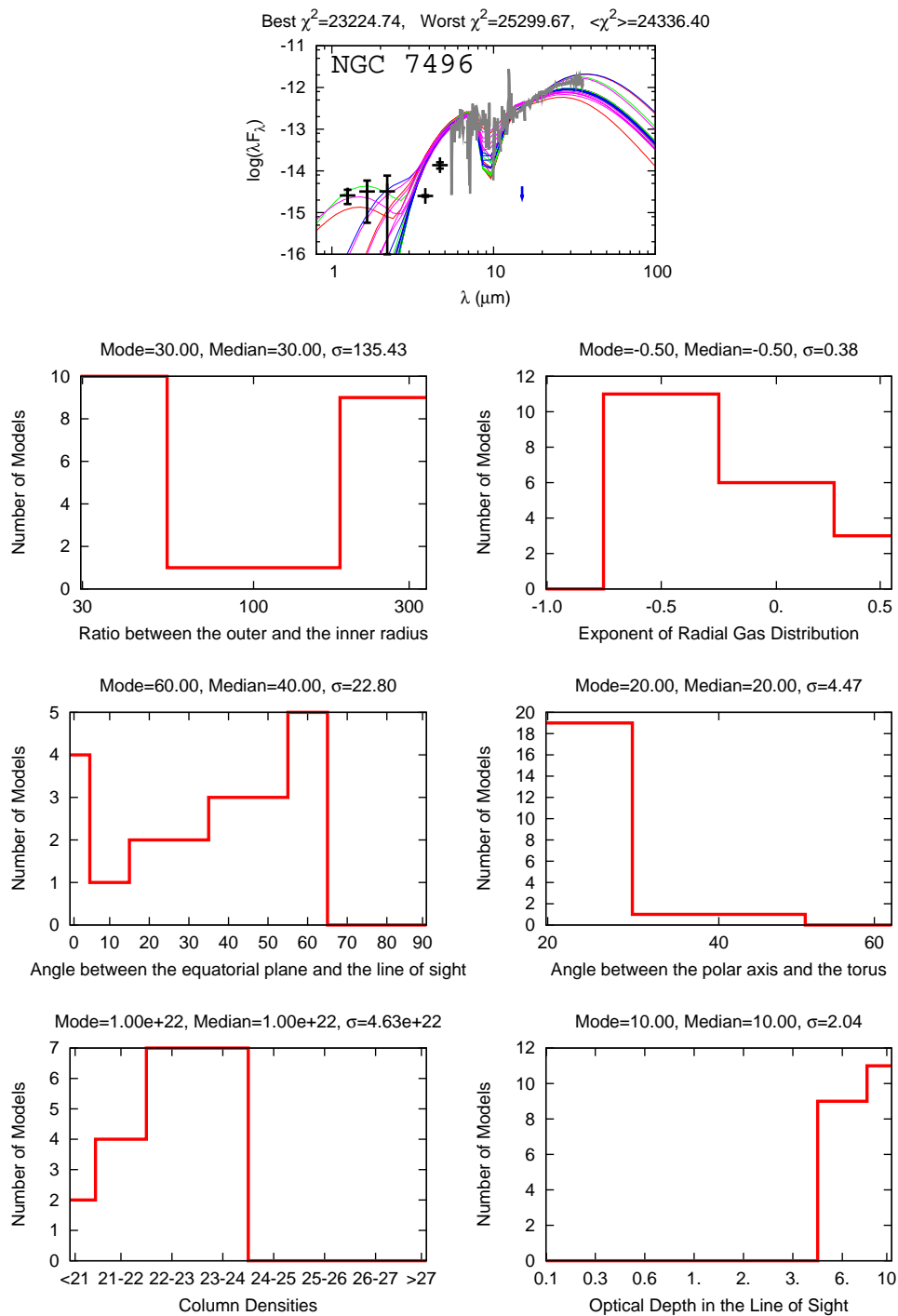


Figure 5.37: Best 20 smooth models fitted to NGC 7496, with specific parameters histograms shown. The preferred value for γ , the exponent of the angular distribution of dust, is 0. Although some cases with $\gamma = 6$.

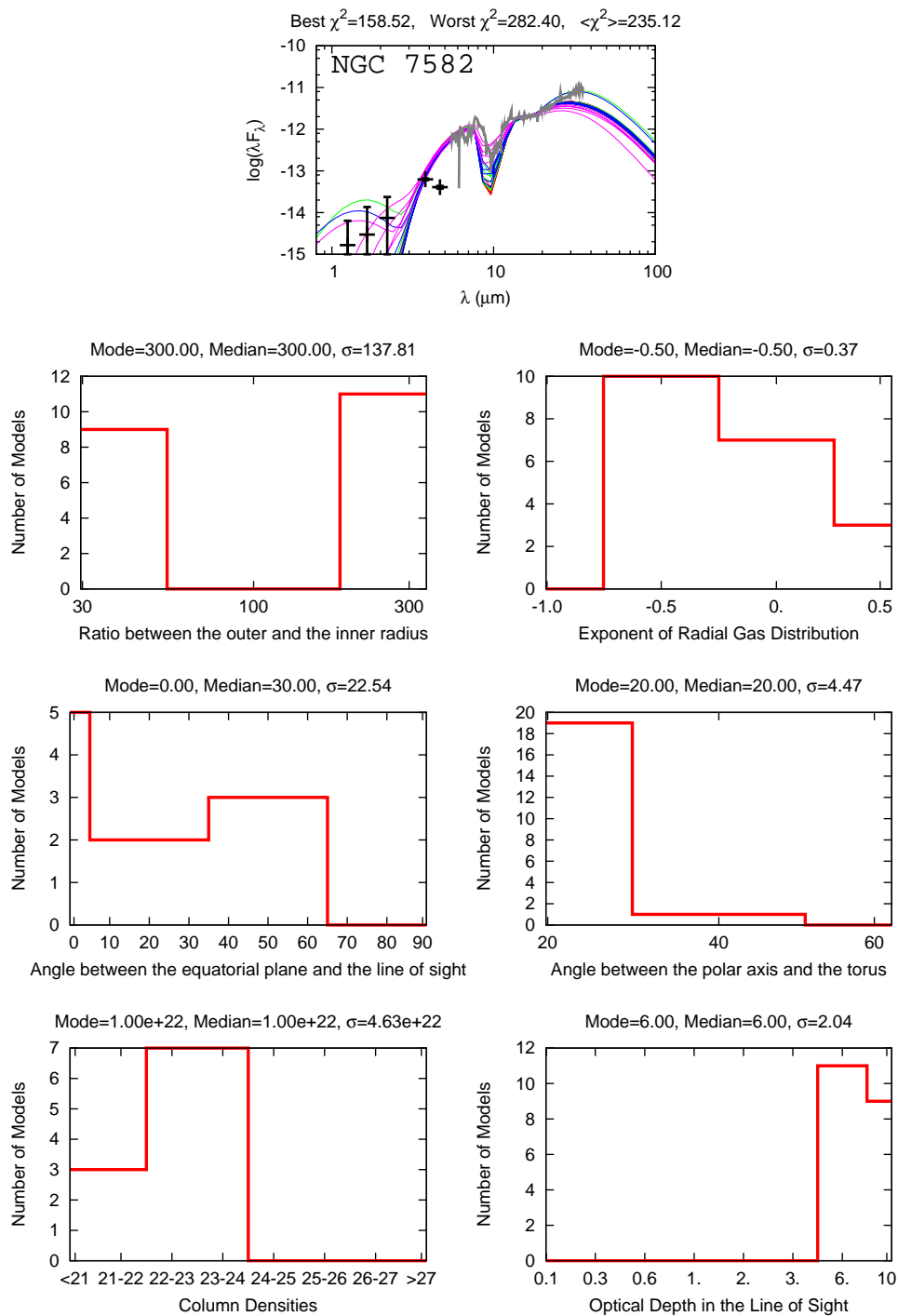


Figure 5.38: Best 20 smooth models fitted to NGC 7582, with specific parameters histograms shown. The preferred value for γ , the exponent of the angular distribution of dust, is 0. Although some cases with $\gamma = 6$.

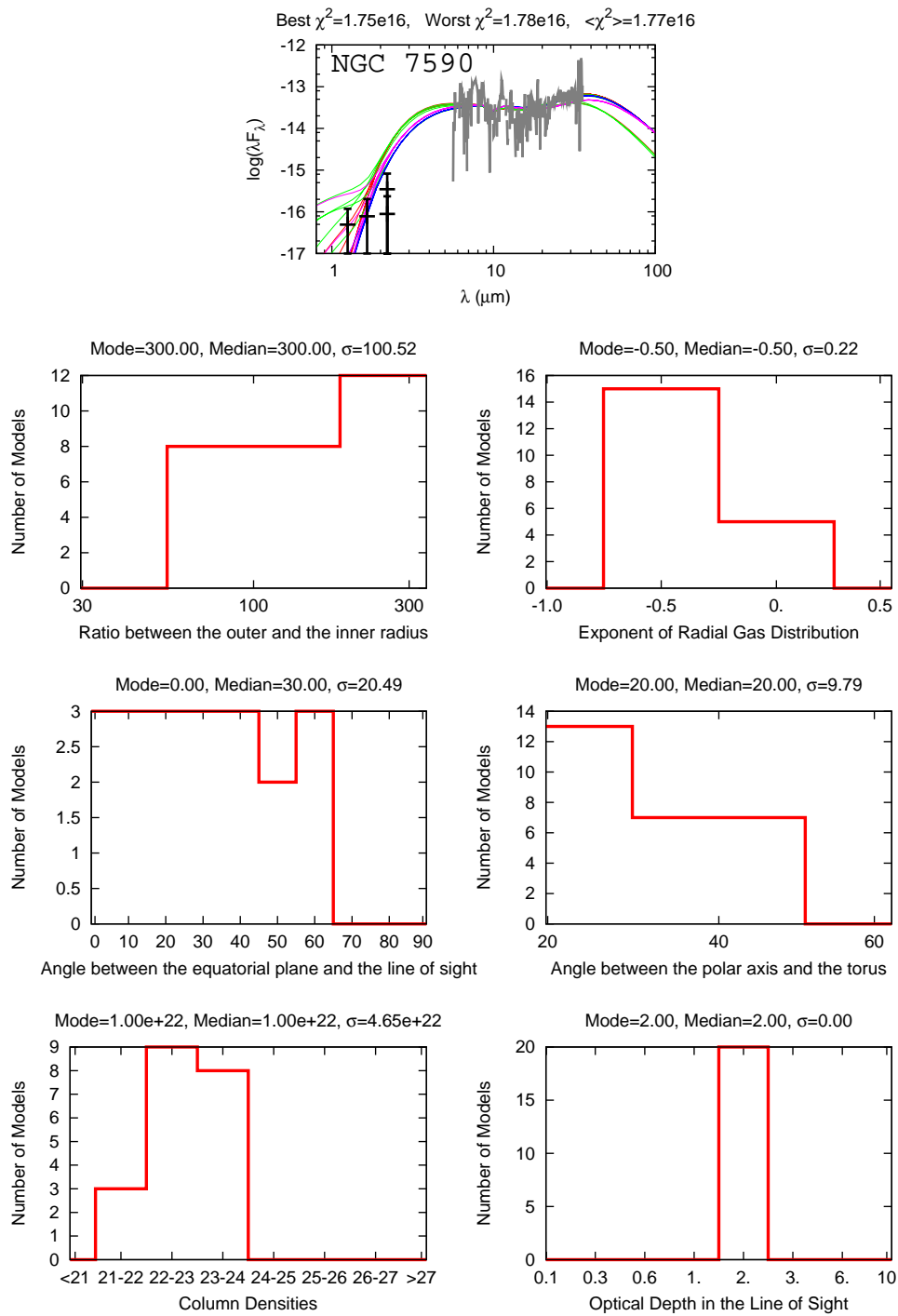


Figure 5.39: Best 20 smooth models fitted to NGC 7590, with specific parameters histograms shown. Only cases with $\gamma = 0$ are preferred.

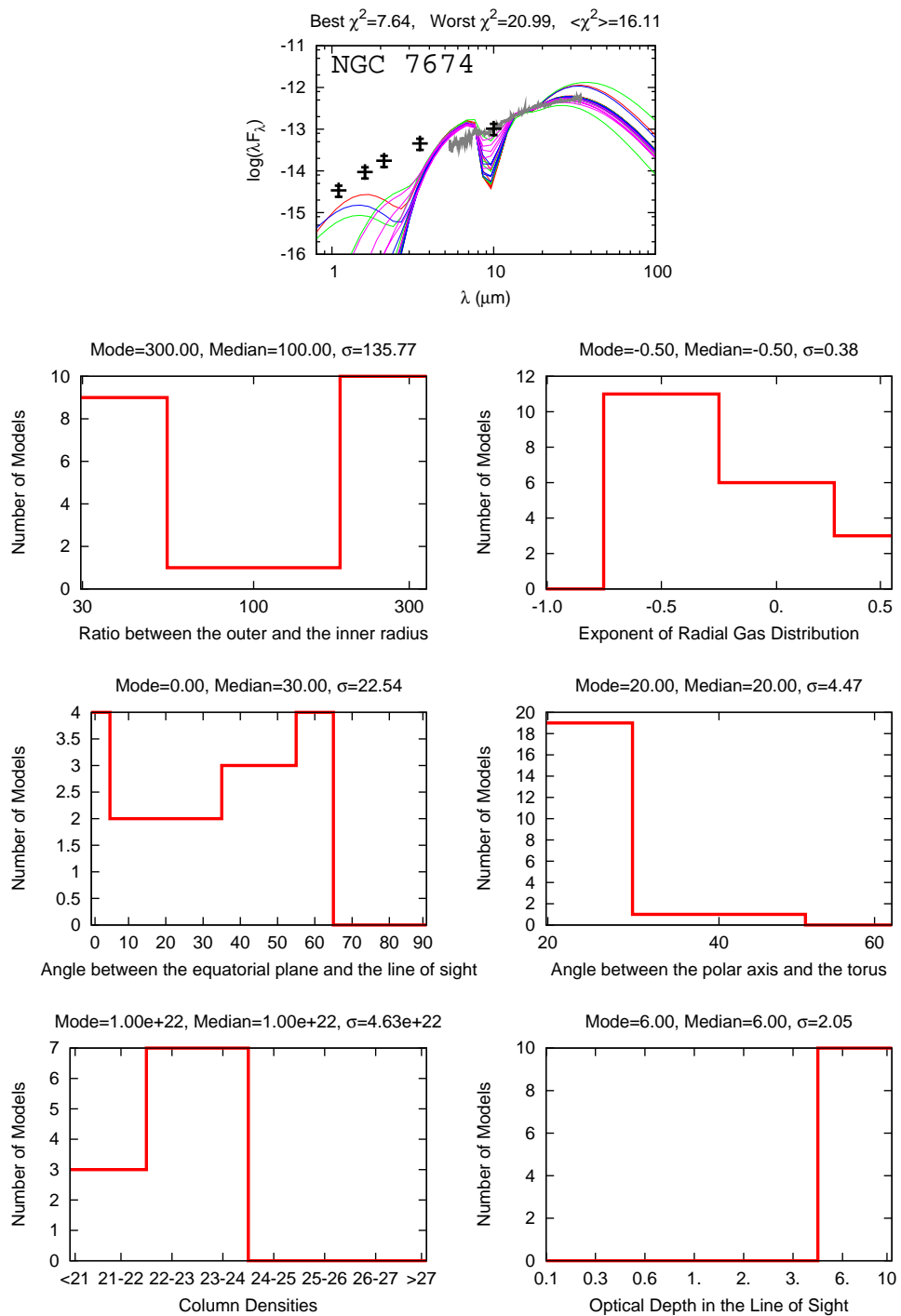


Figure 5.40: Best 20 smooth models fitted to NGC 7674, with specific parameters histograms shown. The preferred value for γ , the exponent of the angular distribution of dust, is 0. Although some cases with $\gamma = 6$.

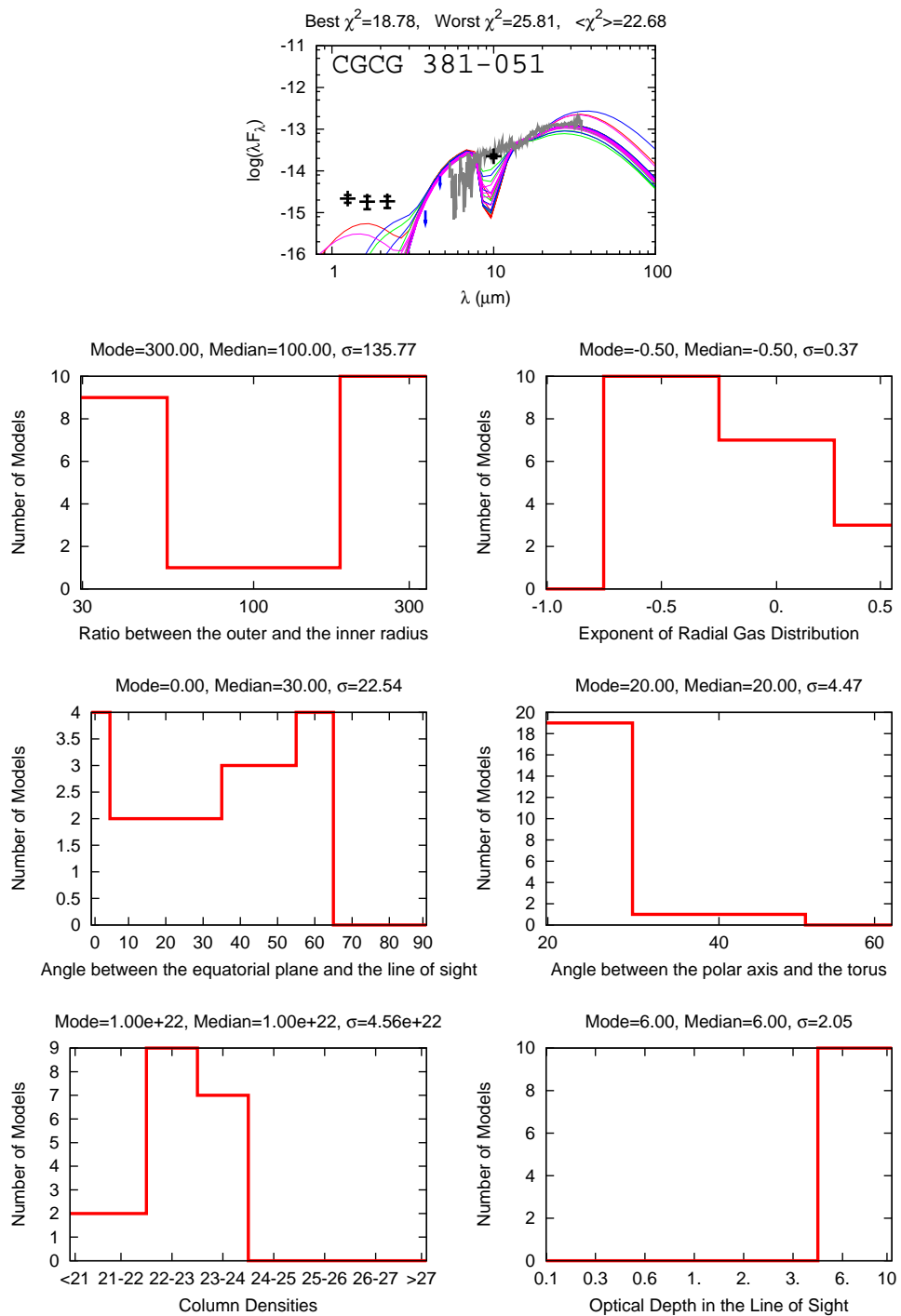


Figure 5.41: Best 20 smooth models fitted to CGCG 381-051, with specific parameters histograms shown. The preferred value for γ , the exponent of the angular distribution of dust, is 0. Although some cases with $\gamma = 6$.

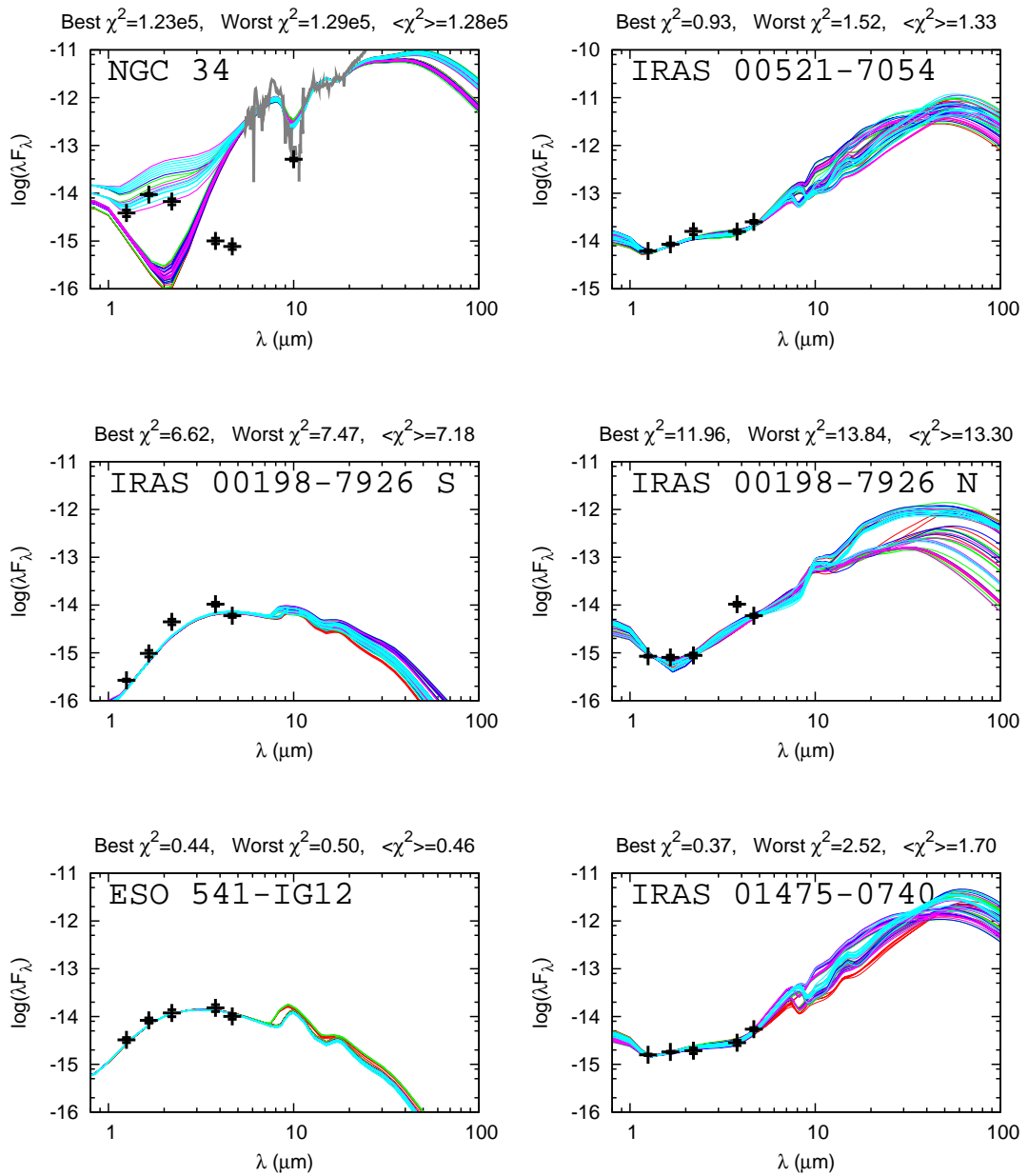


Figure 5.42: Nuclear IR SEDs with the 50 better fitted clumpy models. Lines in cyan represent the best 10 models, the next 5 better models are represented by color magenta, then blue, green, and, finally, the red lines represent the last 40-50 better models. Arrows in blue are upper limits for the non-detections. The photometric points are plotted in black, and the *Spitzer* spectra are plotted in gray. The minimum χ^2 , the maximum χ^2 included in the best 50 models, and the mean χ^2 are shown in the title of each SED.

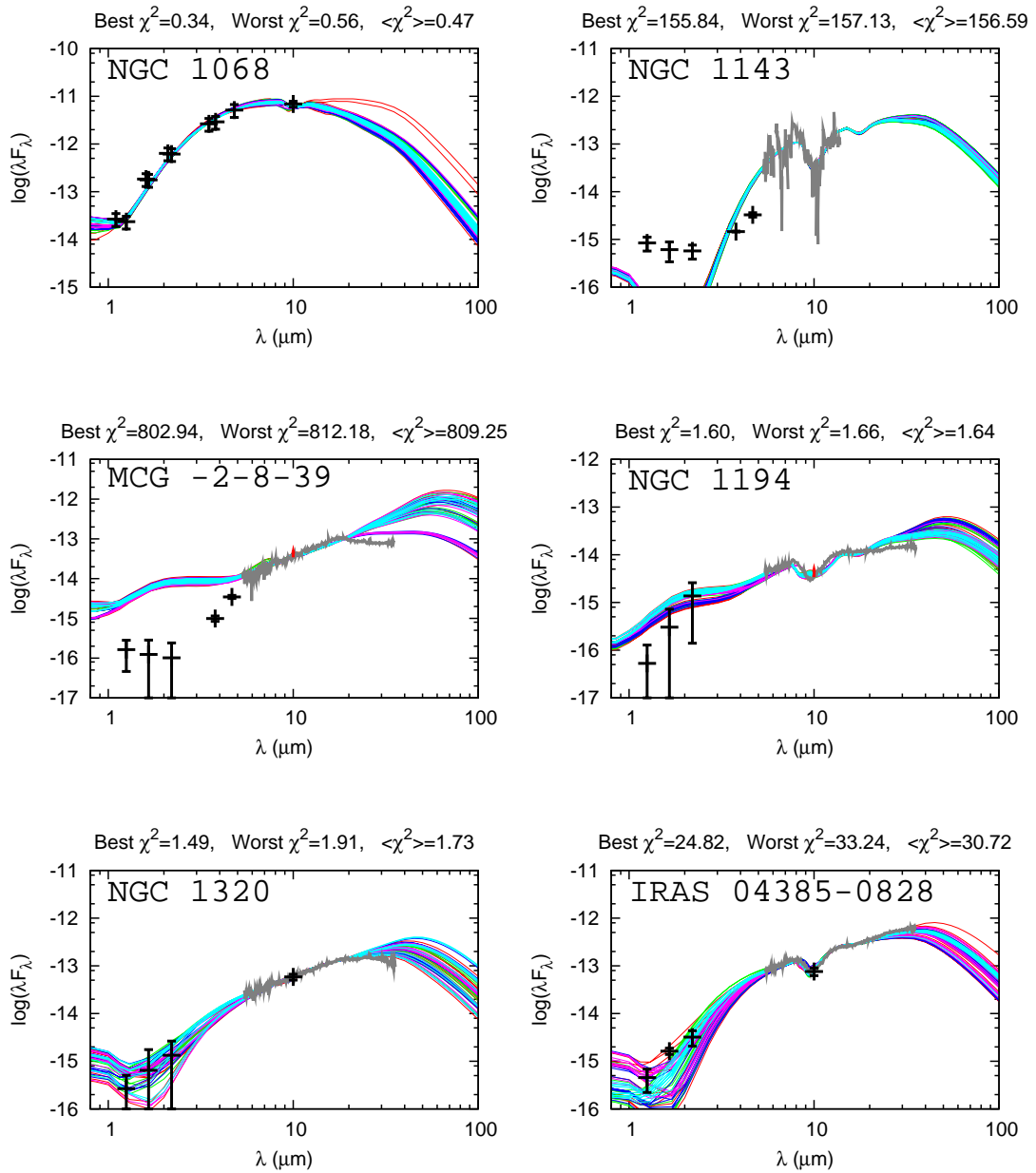


Figure 5.42: Continued.

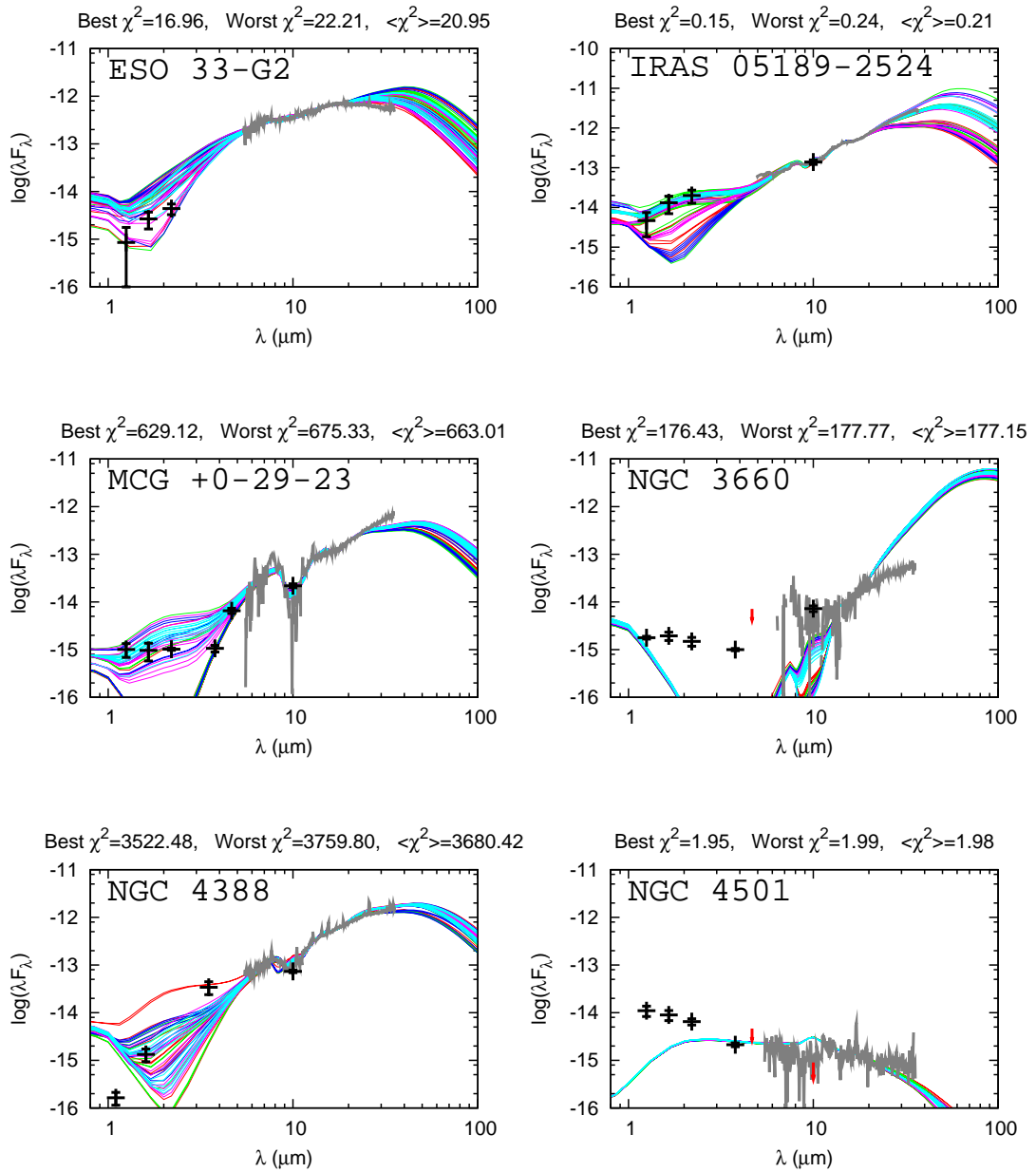


Figure 5.42: Continued.

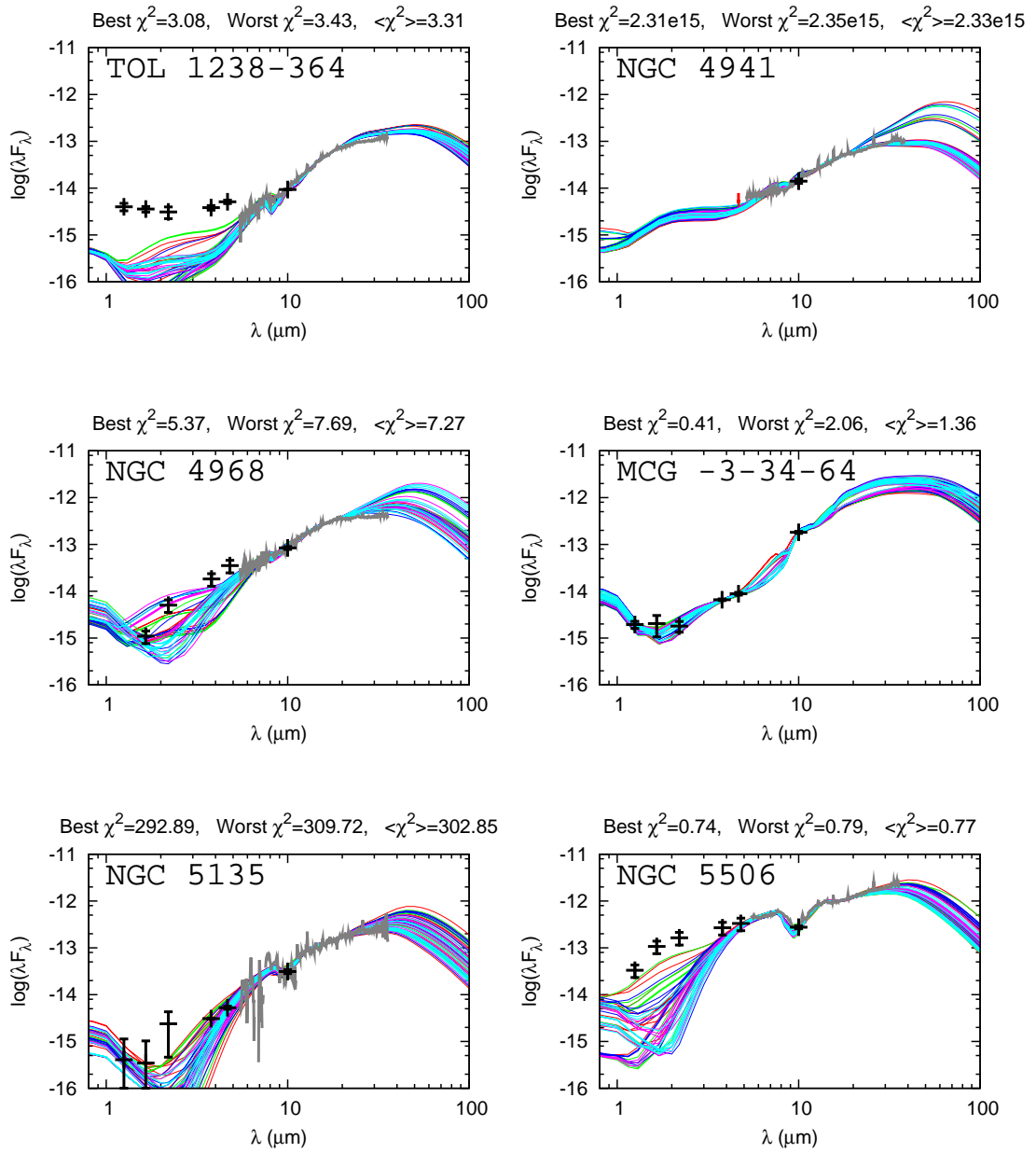


Figure 5.42: Continued.

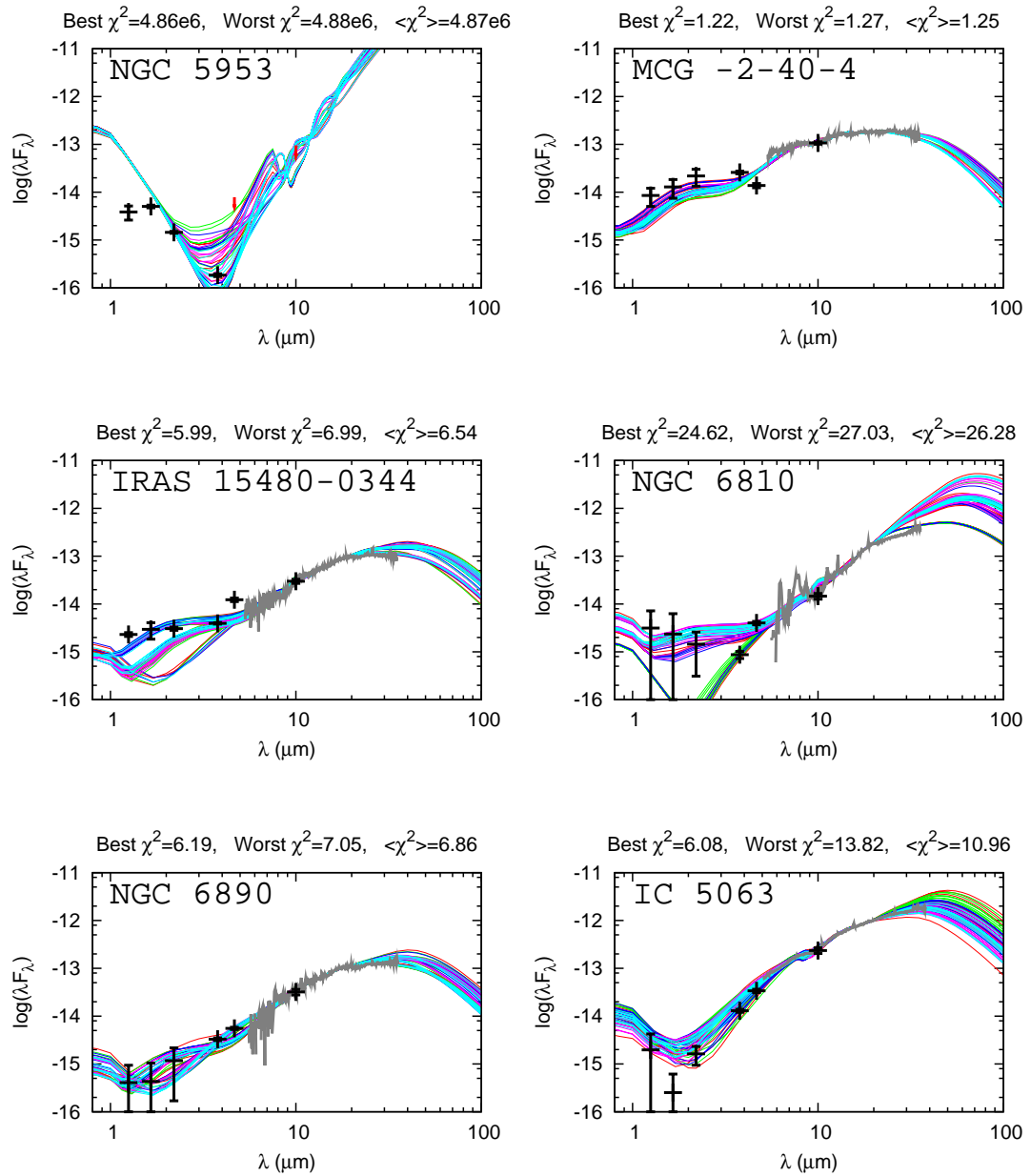


Figure 5.42: Continued

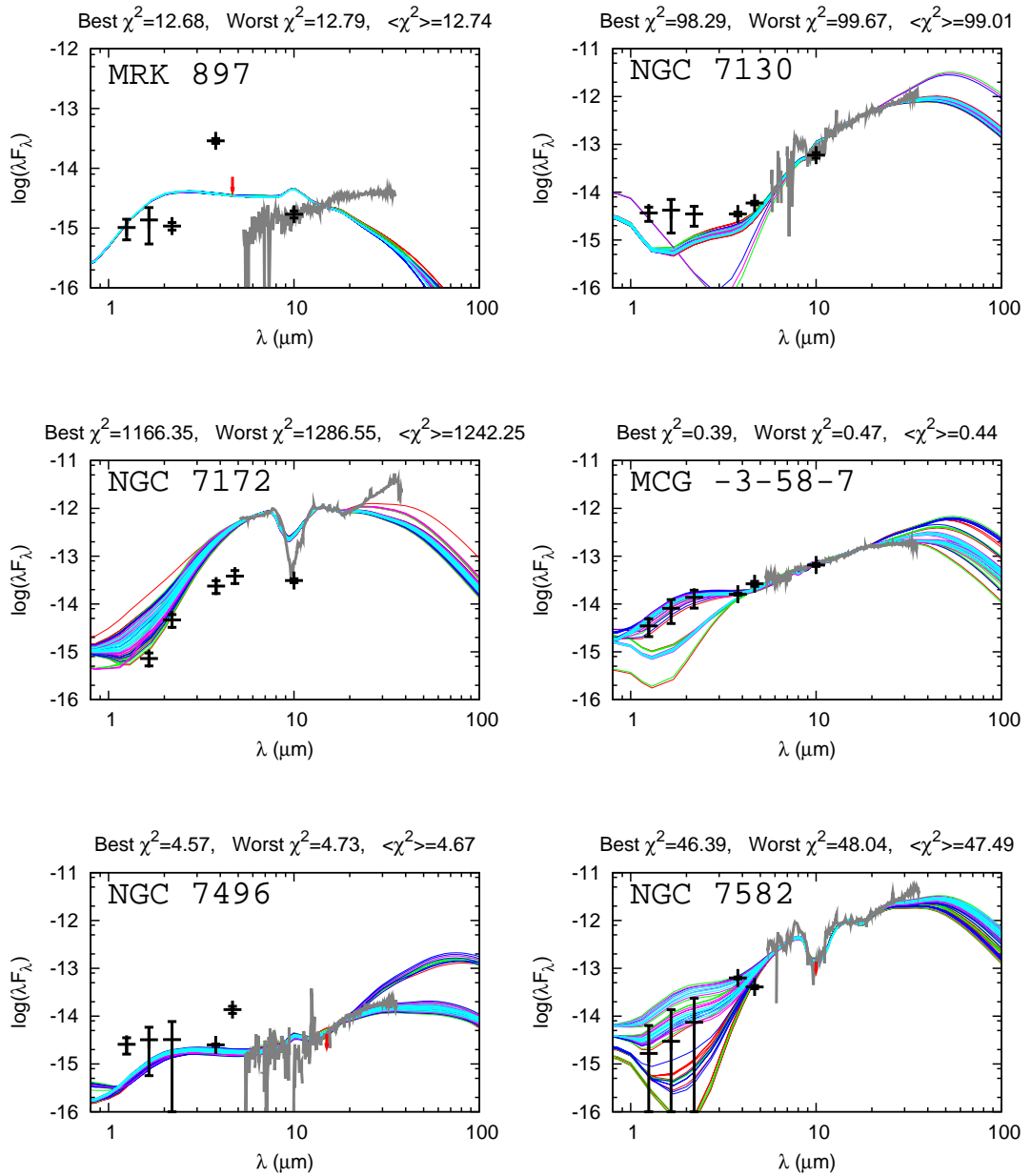


Figure 5.42: Continued

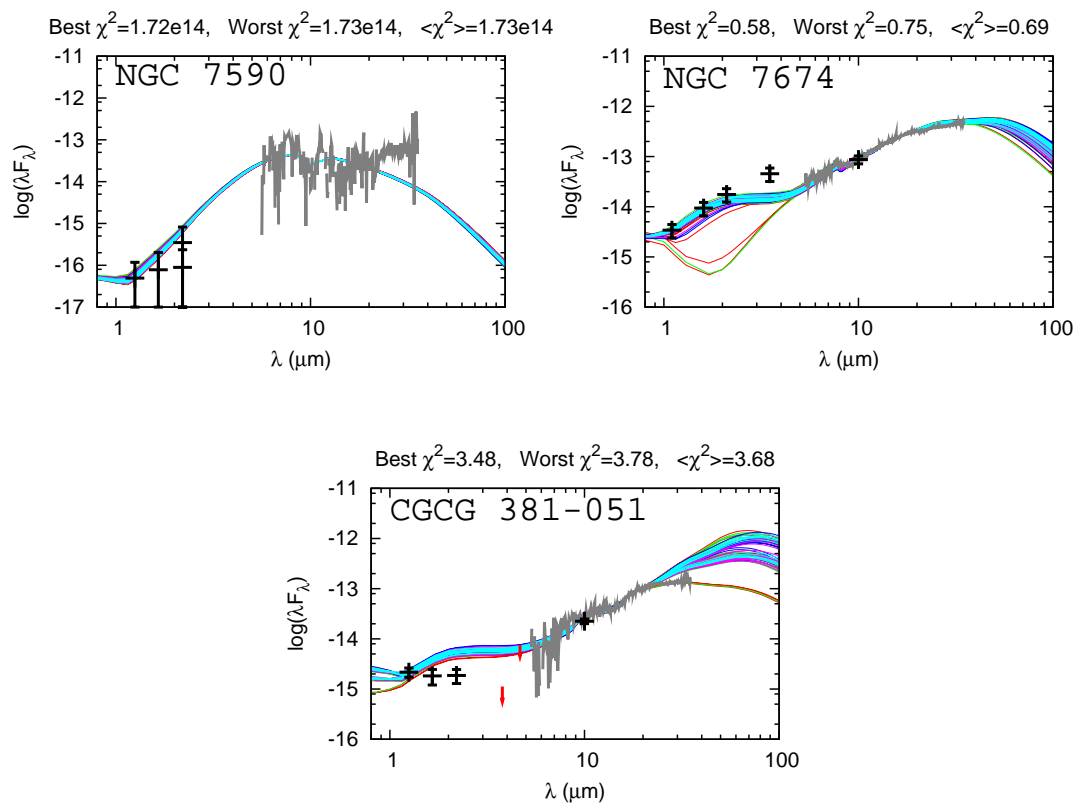


Figure 5.42: Continued

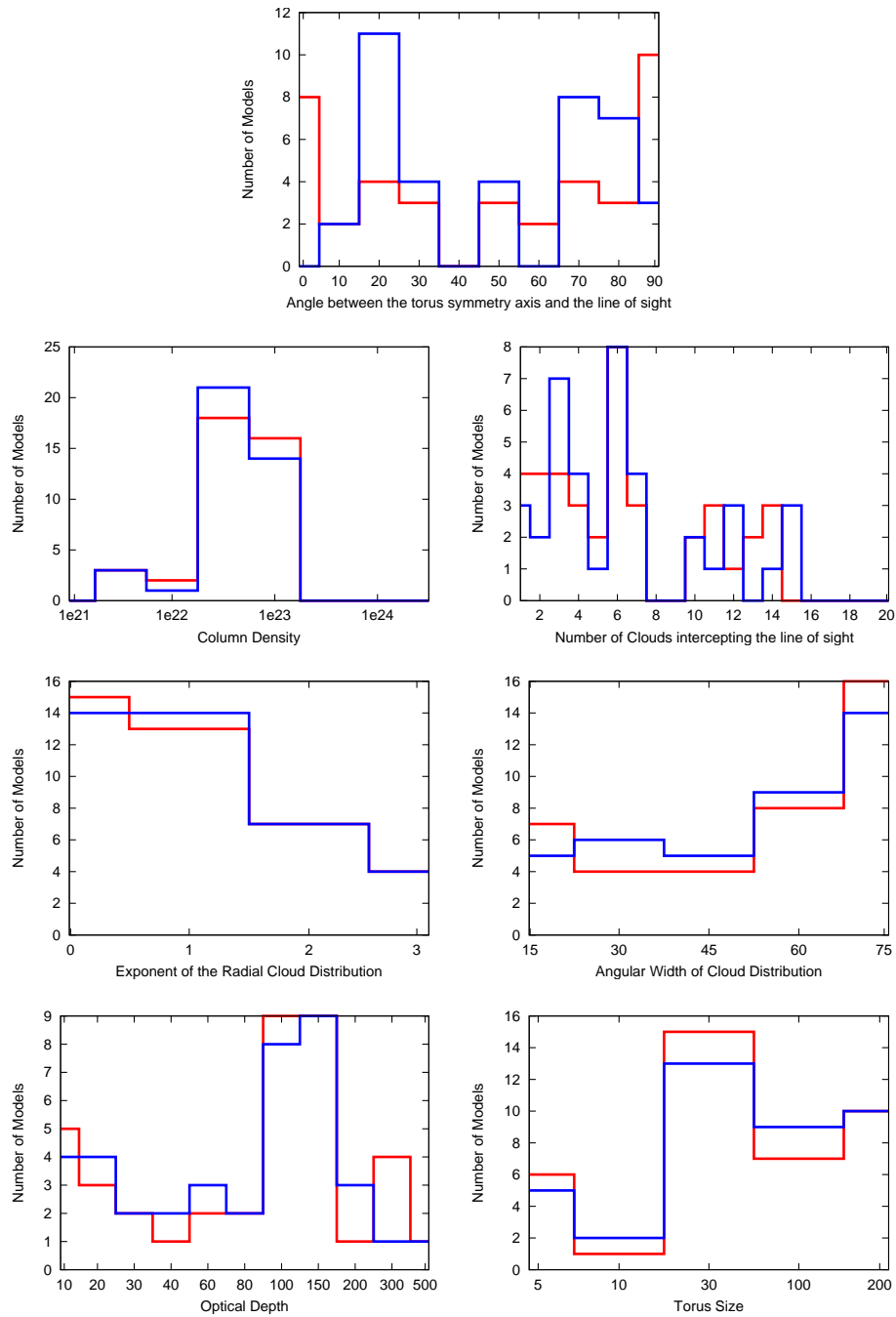


Figure 5.43: Preferred values for all the parameters of the clumpy torus emission models. The mode values are plotted in red and the median values are plotted in blue. In the top panel we show the viewing angle of the systems. The upper panels show the column density in the left and the number of clouds in the line of sight in the right. The exponent of the radial cloud distribution is shown in middle left panel, and the angular width of the distribution of clouds (i.e., the aperture of the torus) is plotted in the middle right panel. In the bottom panels the optical depth of each cloud at left and the torus size are shown at right, are shown.

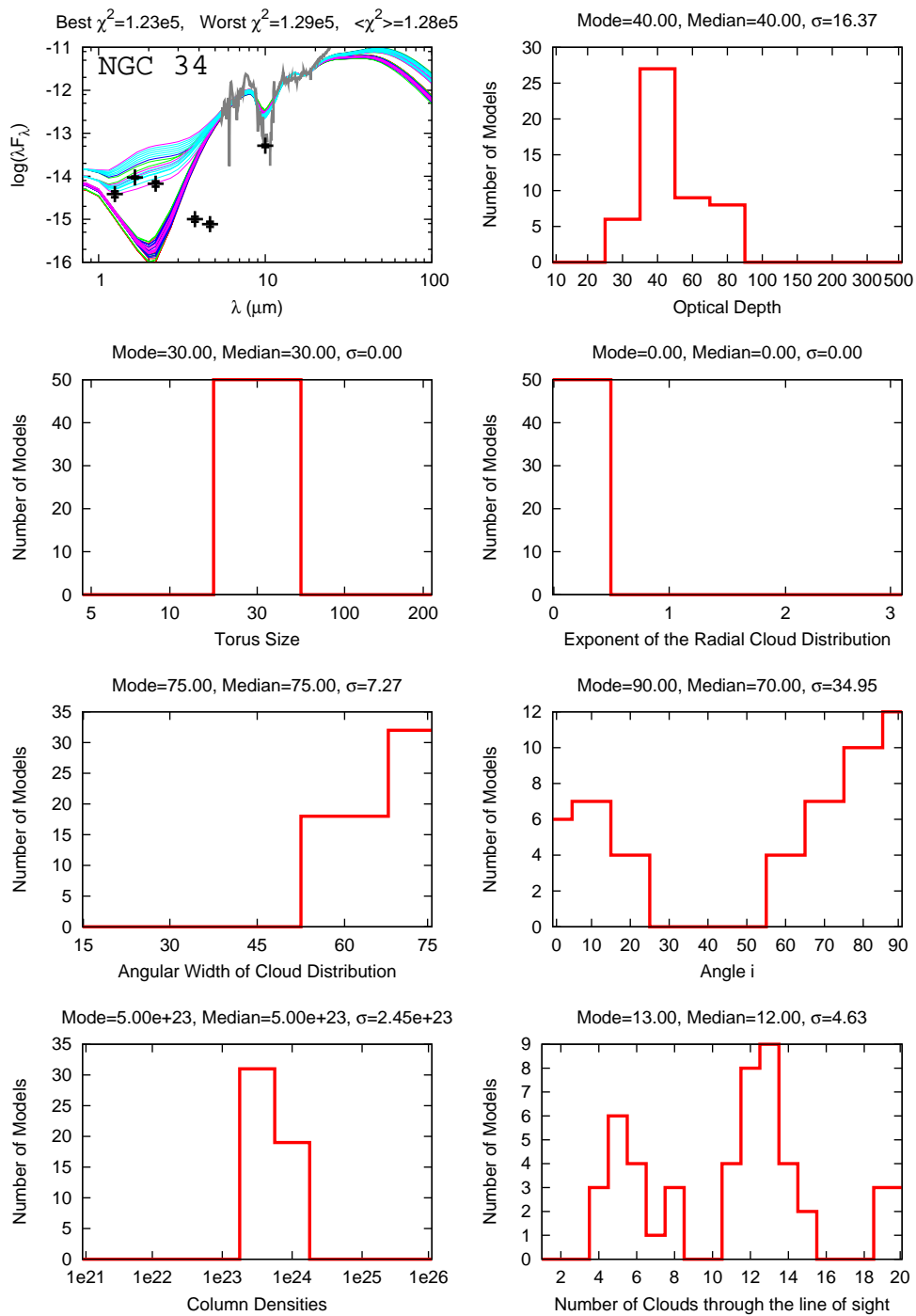


Figure 5.44: Best 50 clumpy models fitted to NGC 34, with specific parameters histograms shown. The histogram describing the type of dust grains preferred is not shown. The silicate description of Ossenkopf *et al.* (1992) is preferred in this case. The upper panels show the modeled SED in the left and the optical depth at right. Then the torus size (left) and the exponent of the radial cloud distribution are shown (right). Next plots show the angular width of the distribution of clouds is plotted (left) and the viewing angle (right). In the bottom panels the column density at left and the number of clouds in the line of sight at right, are shown.

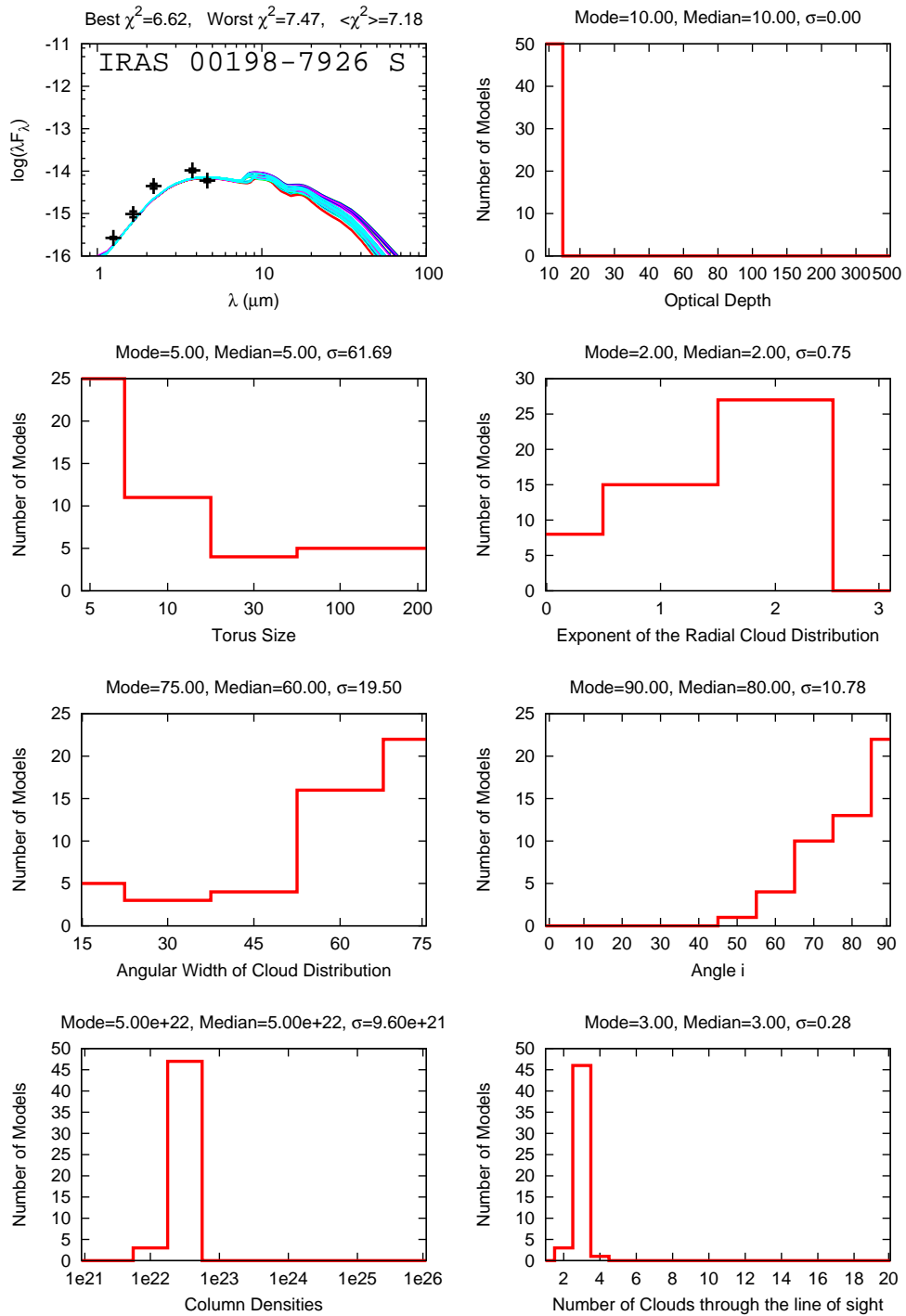


Figure 5.45: Best 50 clumpy models fitted to IRAS 00198-7926 North, with specific parameters histograms shown. The preferred silicate description is that of Draine (2003), although the description of Ossenkopf *et al.* (1992) is also accepted in some cases. The order of the panels is the same as in Fig. 5.44 and will be the same for all the clumpy models.

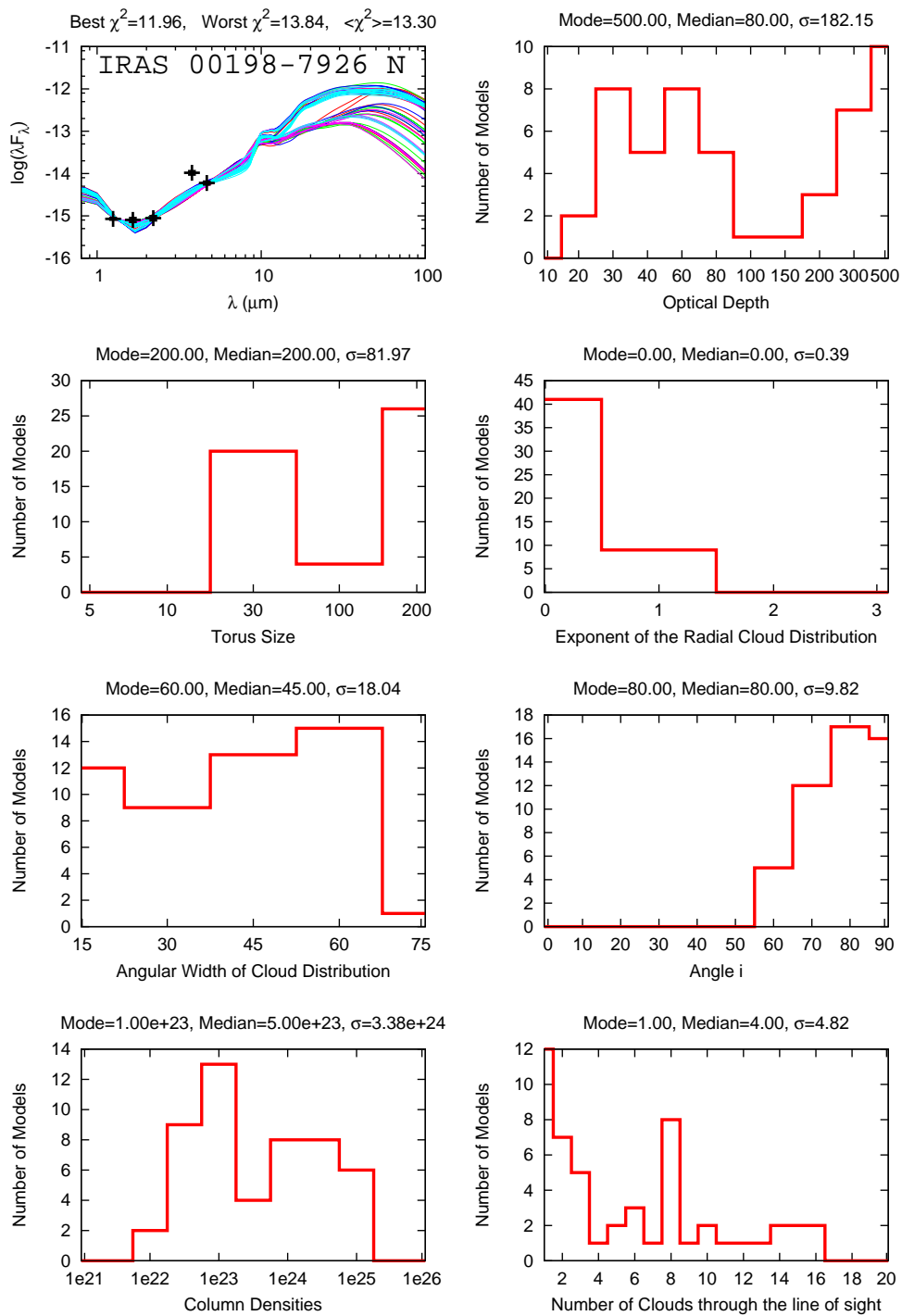


Figure 5.46: Best 50 clumpy models fitted to IRAS 00198-7926 South, with specific parameters histograms shown. This is the only case where half of the 50 better models prefer a Ossenkopf *et al.* (1992) description for the silicates, and the other half prefer the description of Draine (2003).

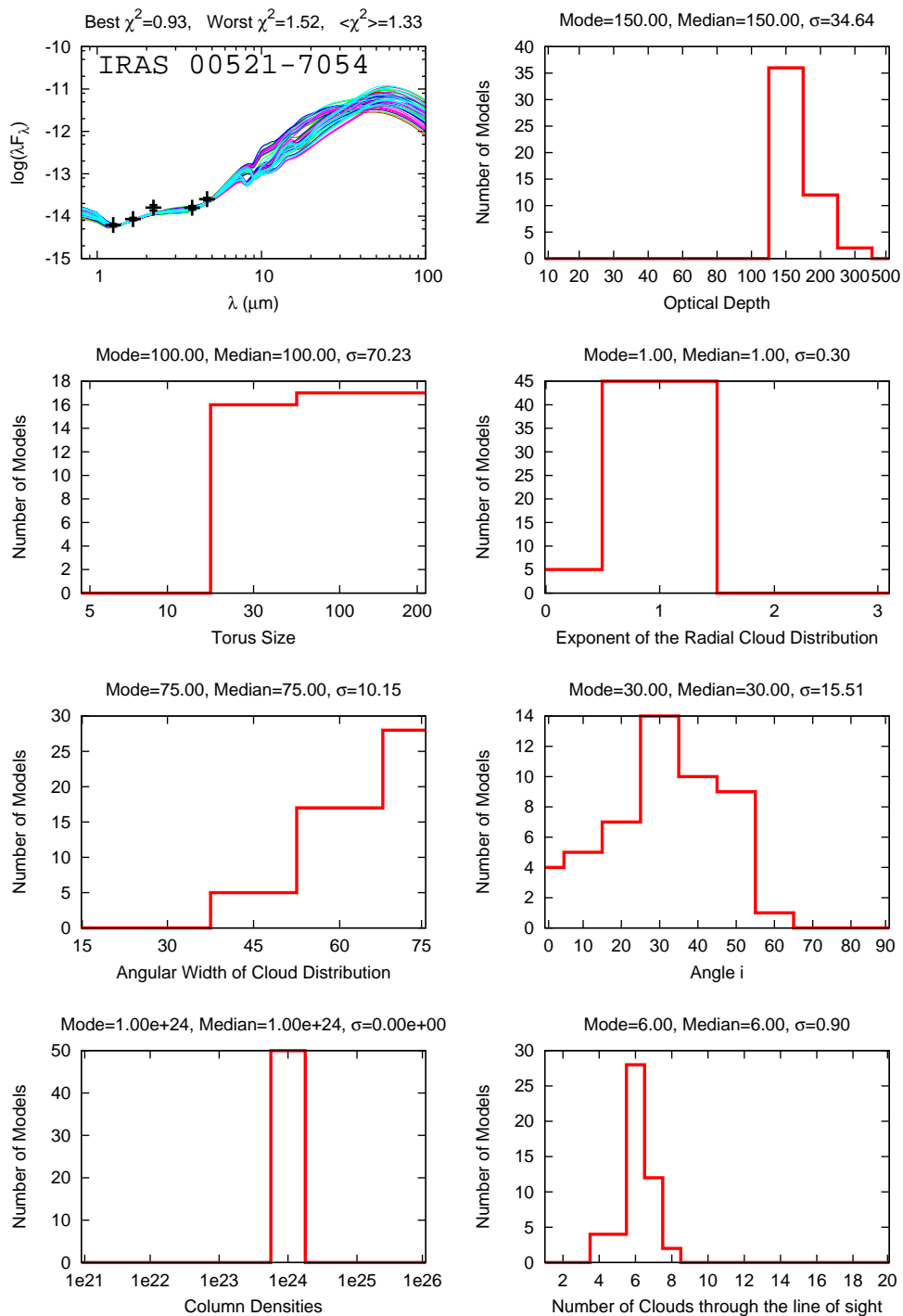


Figure 5.47: Best 50 clumpy models fitted to IRAS 00521-7054, with specific parameters histograms shown. The preferred description for the silicates is that of Ossenkopf *et al.* (1992), but some cases described by Draine (2003) are included.

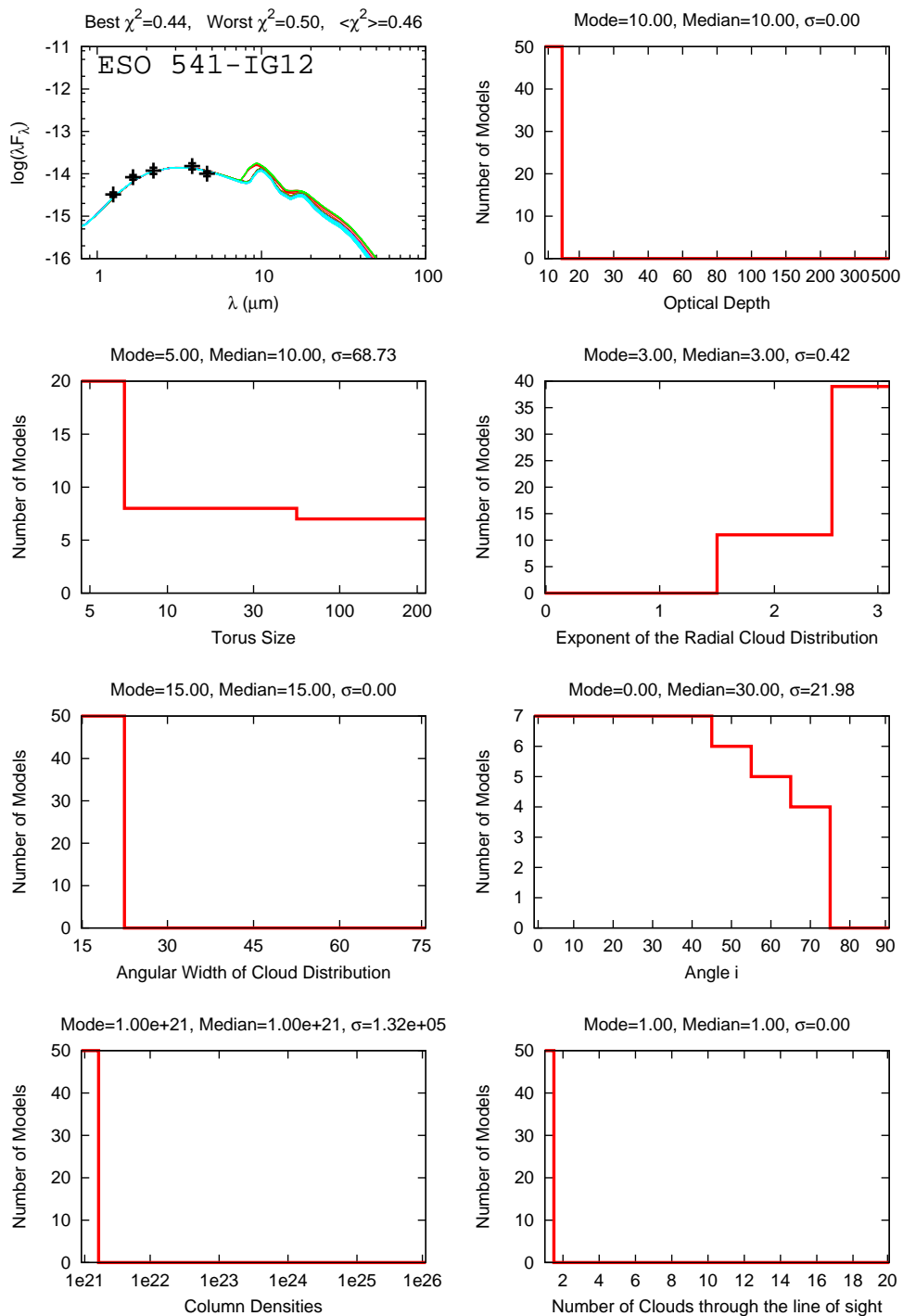


Figure 5.48: Best 50 clumpy models fitted to ESO 541-IG12, with specific parameters histograms shown. The preferred description for the silicates is that of Ossenkopf *et al.* (1992), but some cases described by Draine (2003) are included.

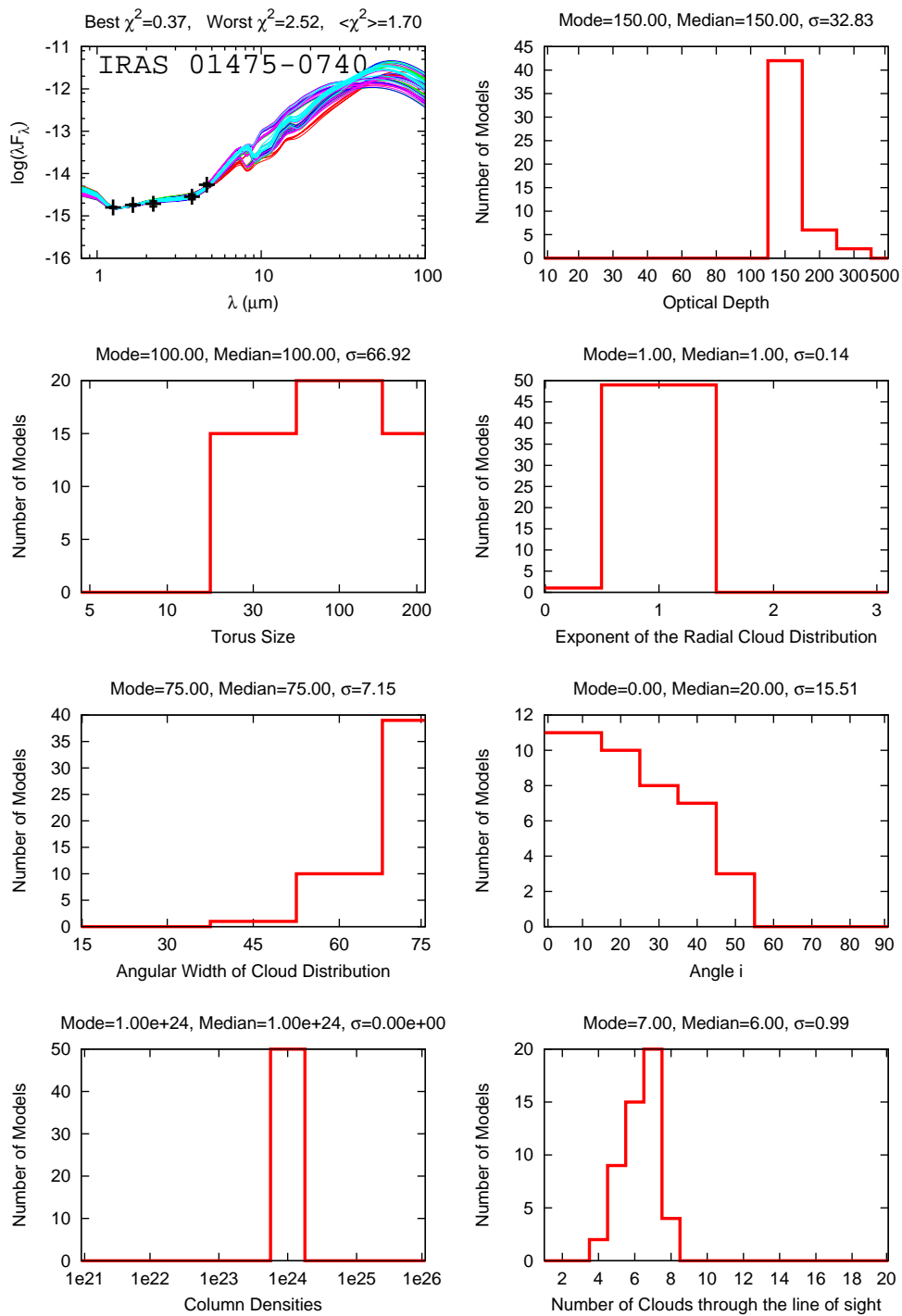


Figure 5.49: Best 50 clumpy models fitted to IRAS 01475-0740, with specific parameters histograms shown. The preferred description for the silicates is that of Ossenkopf *et al.* (1992), but some cases described by Draine (2003) are included.

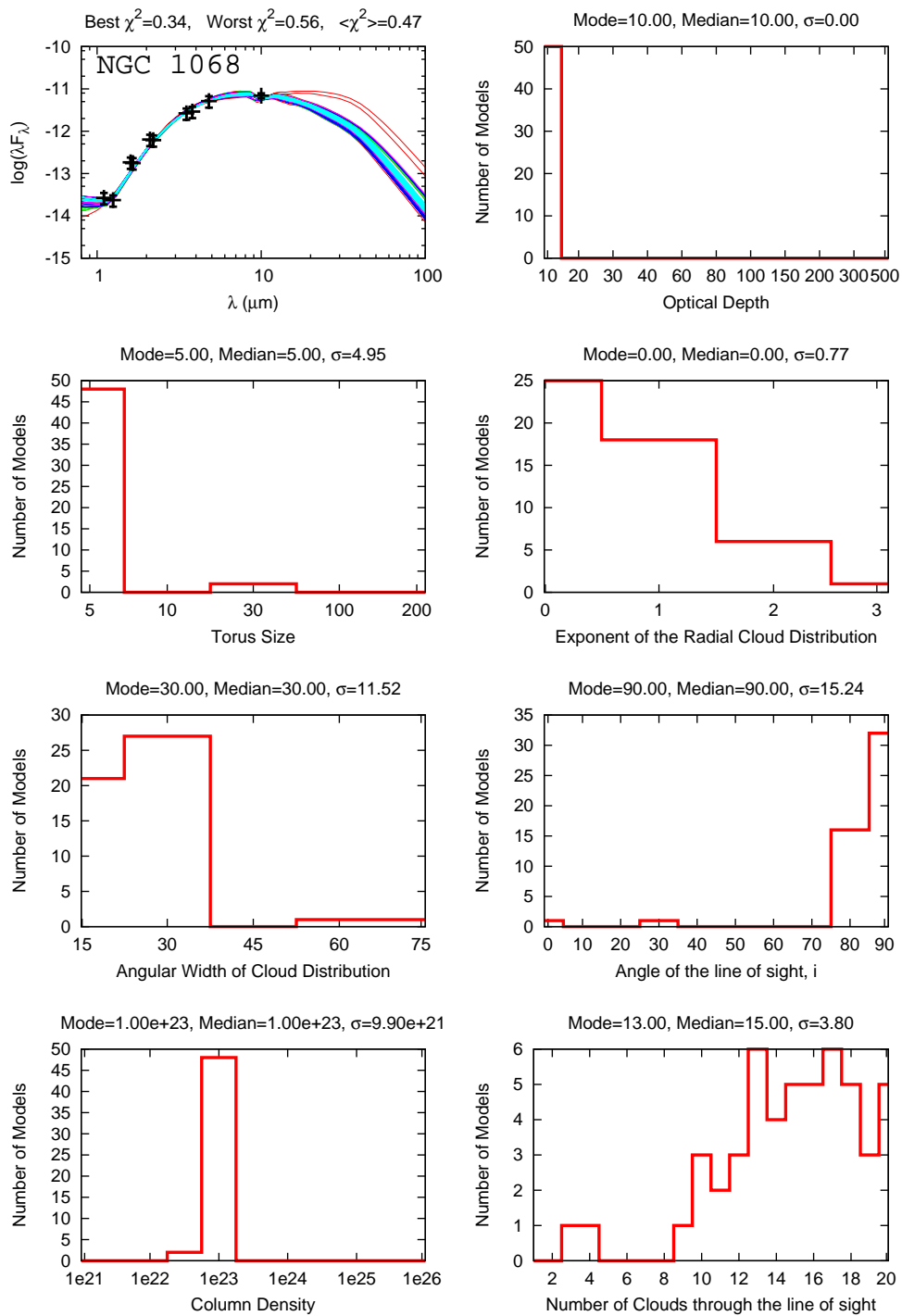


Figure 5.50: Best 50 clumpy models fitted to NGC 1068, with specific parameters histograms shown. The preferred description for the silicates is that of Ossenkopf *et al.* (1992), but some cases described by Draine (2003) are included.

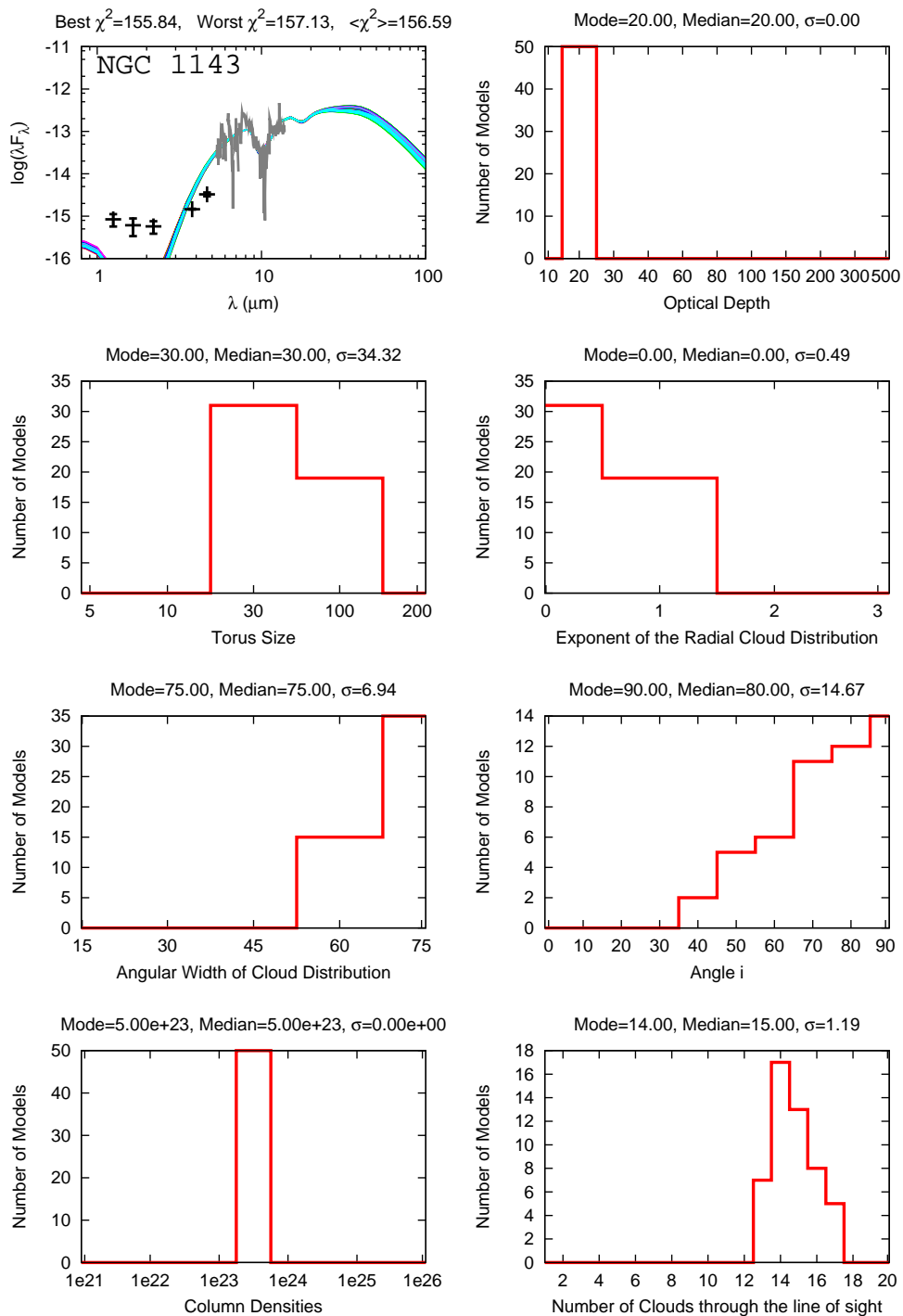


Figure 5.51: Best 50 clumpy models fitted to NGC 1143, with specific parameters histograms shown. The description of Ossenkopf *et al.* (1992) for the silicates is preferred.

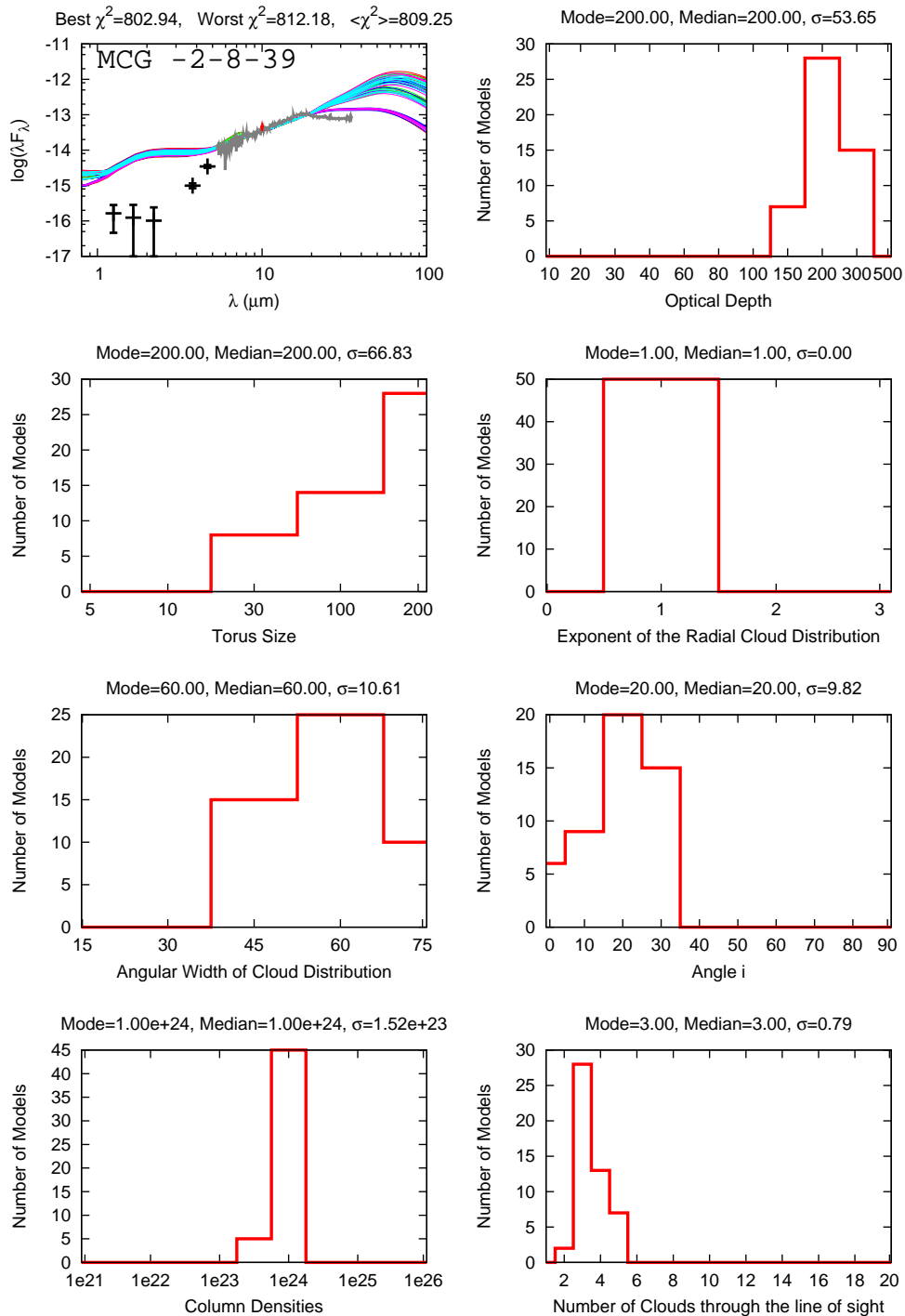


Figure 5.52: Best 50 clumpy models fitted to MCG -2-8-39, with specific parameters histograms shown. The description of Draine (2003) for the silicates is the preferred.

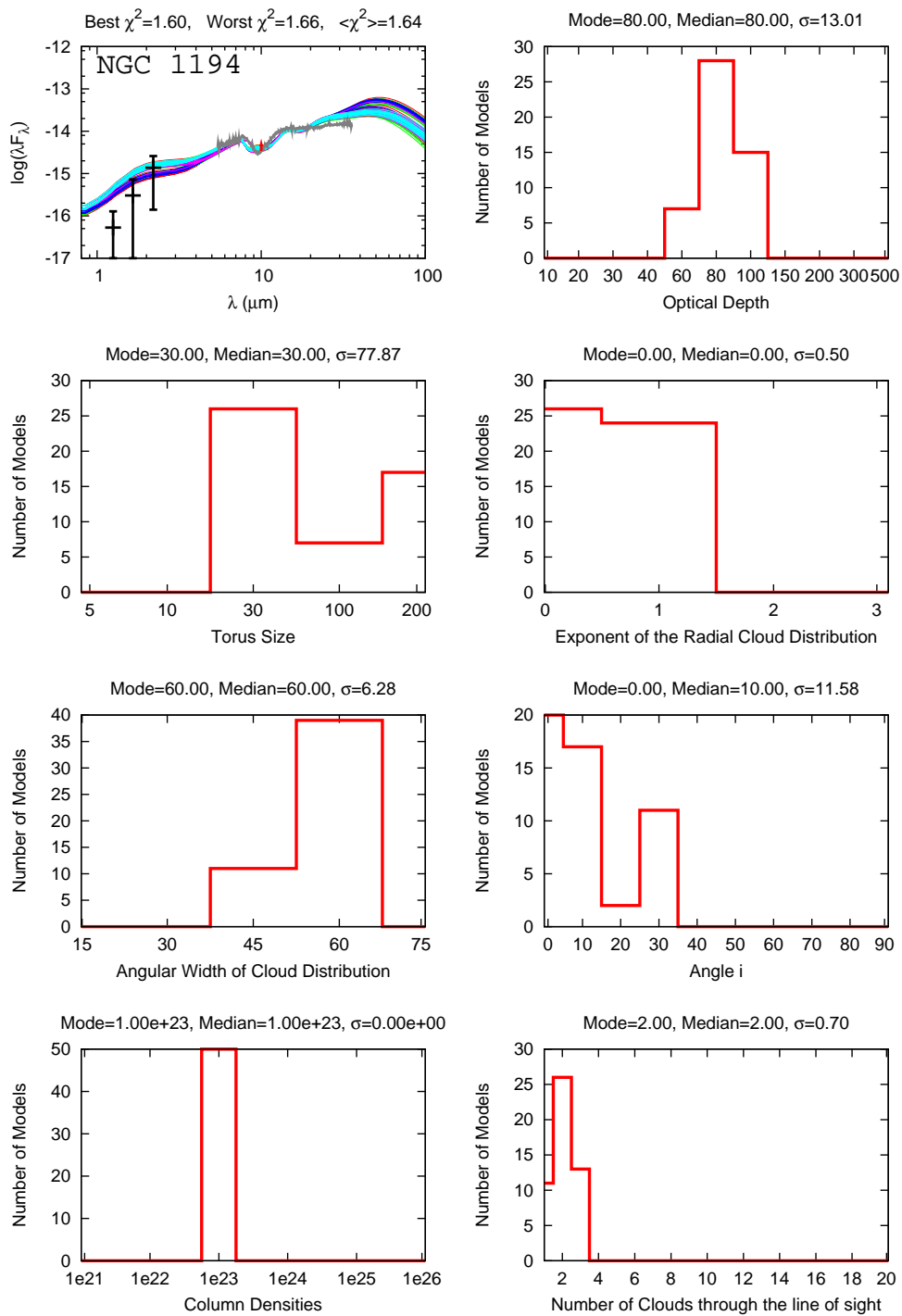


Figure 5.53: Best 50 clumpy models fitted to NGC 1194, with specific parameters histograms shown. The description of Draine (2003) for the silicates is the preferred.

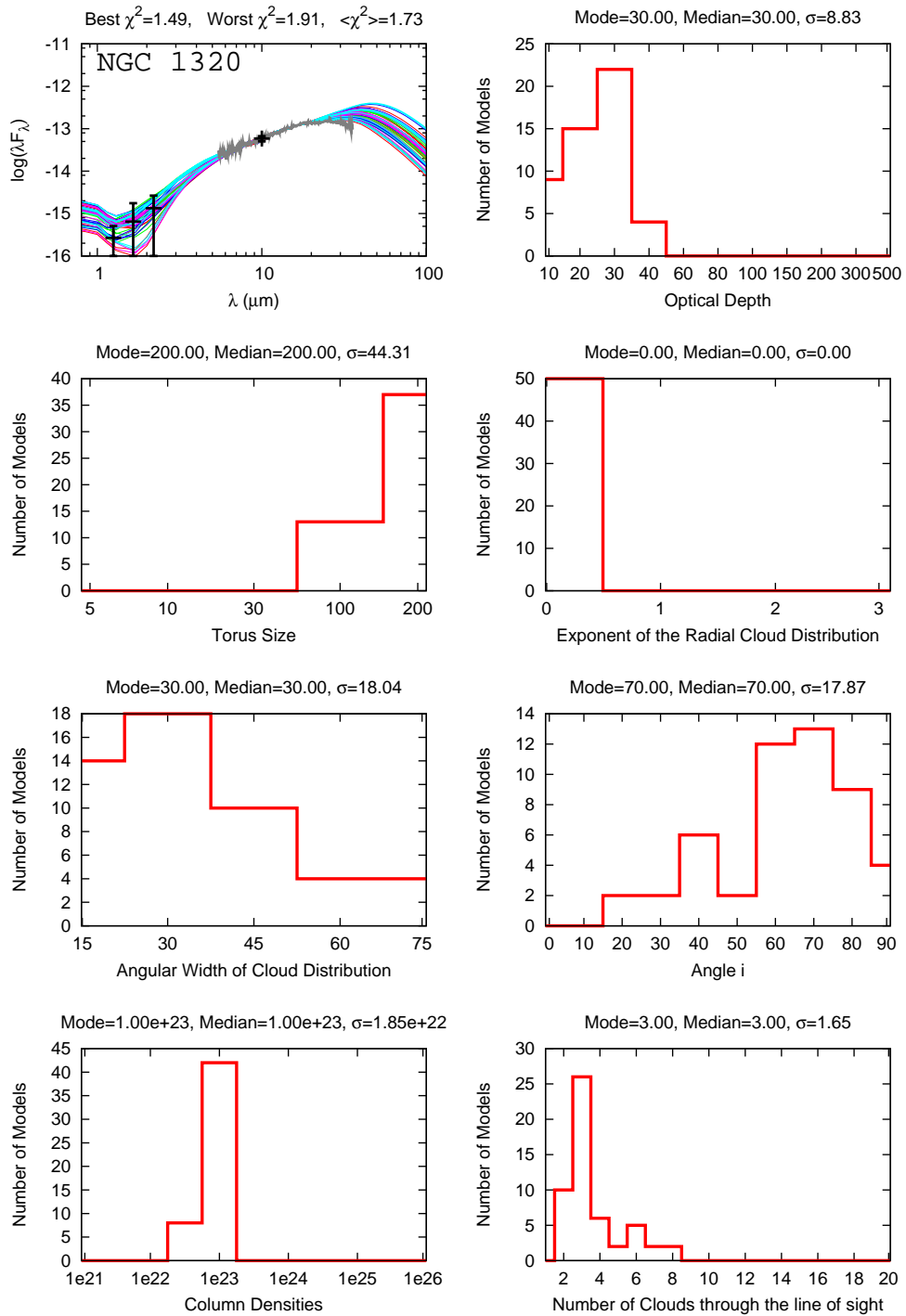


Figure 5.54: Best 50 clumpy models fitted to NGC 1320, with specific parameters histograms shown. The preferred description for the silicates is that of Ossenkopf *et al.* (1992), but some cases described by Draine (2003) are included.

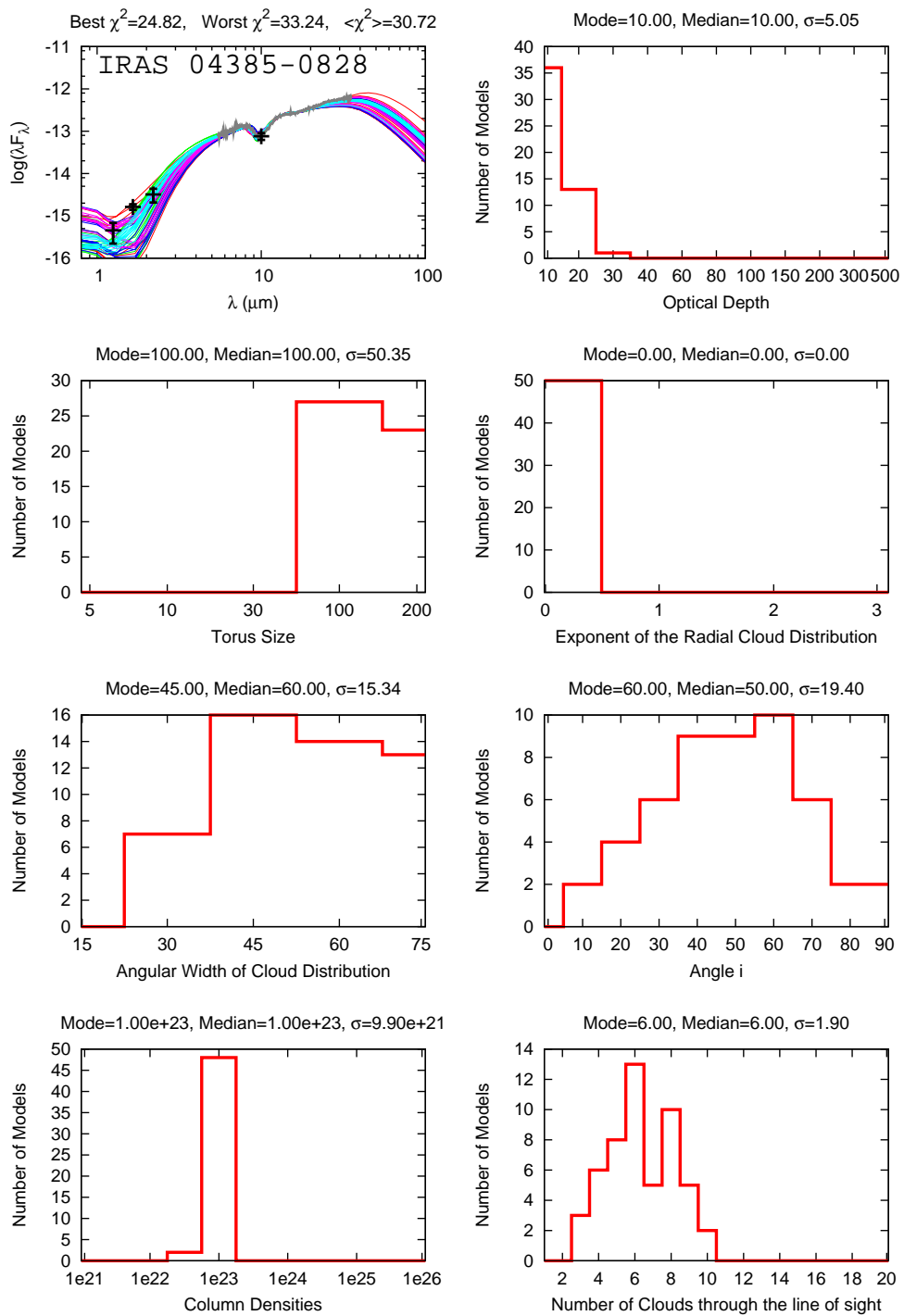


Figure 5.55: Best 50 clumpy models fitted to IRAS 04385-0828, with specific parameters histograms shown. The description of Draine (2003) for the silicates is the preferred.

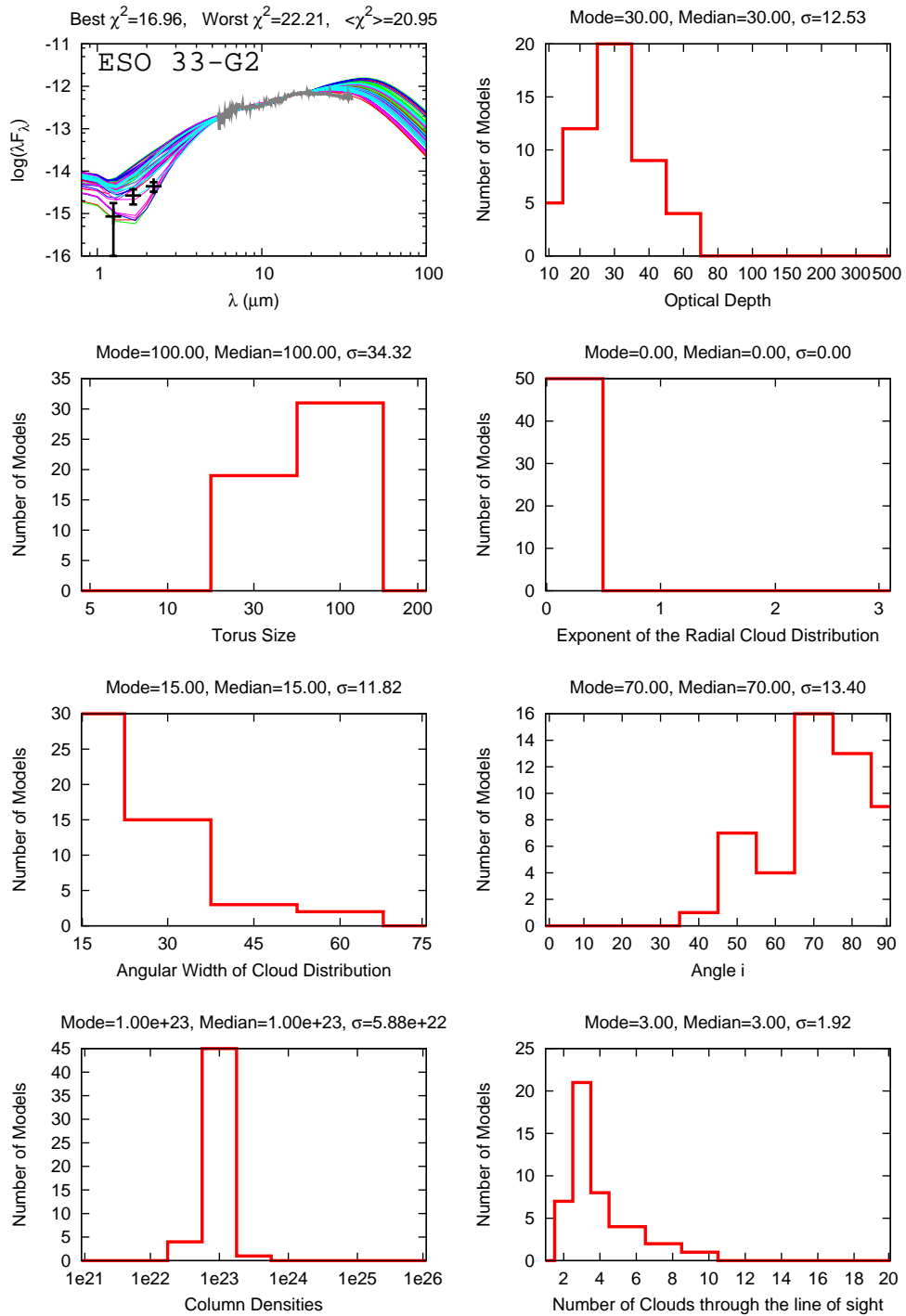


Figure 5.56: Best 50 clumpy models fitted to ESO 33-G2, with specific parameters histograms shown. The silicate description of Draine (2003) is preferred, but some cases with a Ossenkopf *et al.* (1992) description are also accepted.

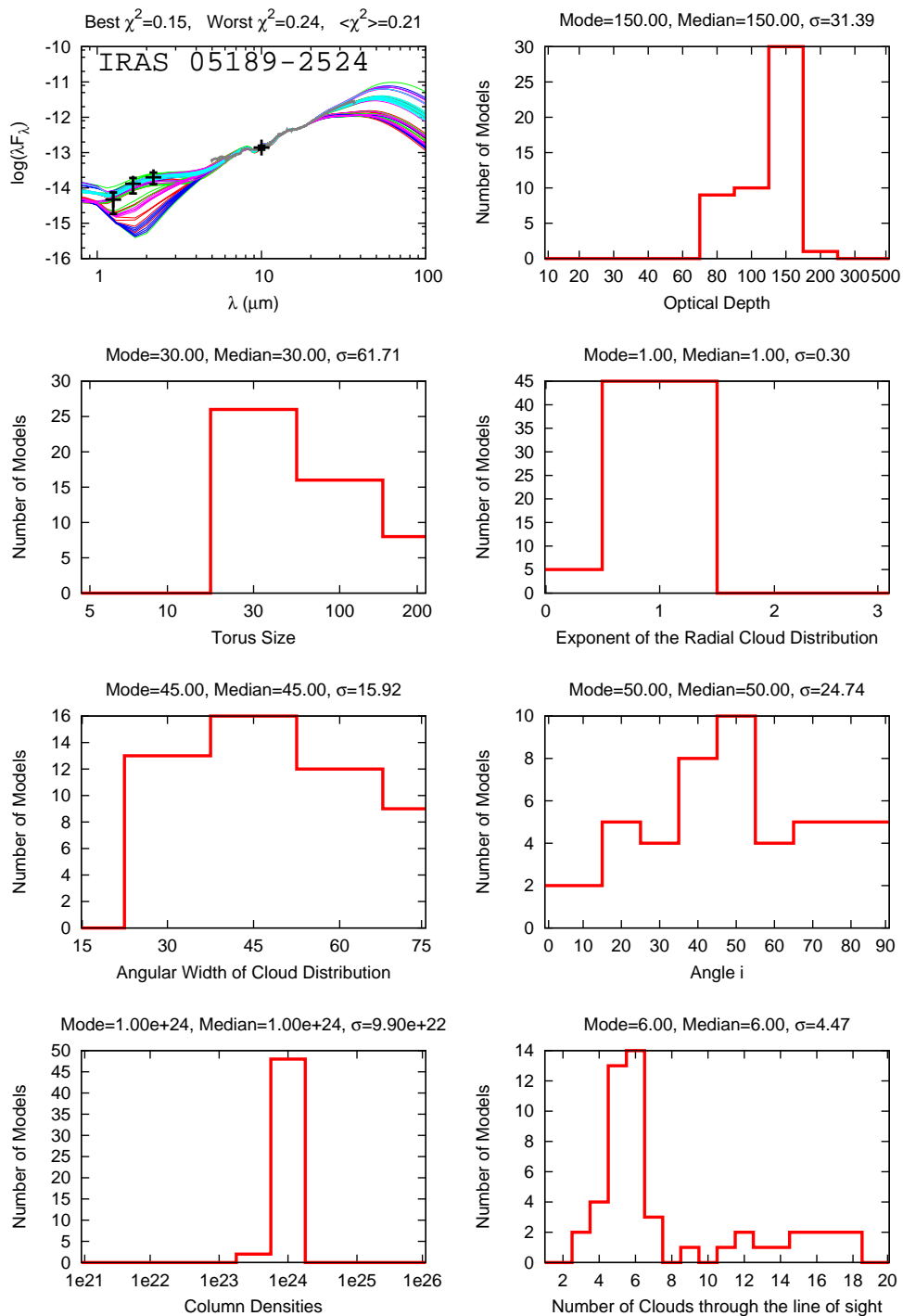


Figure 5.57: Best 50 clumpy models fitted to IRAS 05189-2524, with specific parameters histograms shown. The silicate description of Draine (2003) is preferred, but some cases with a Ossenkopf *et al.* (1992) description are also accepted.

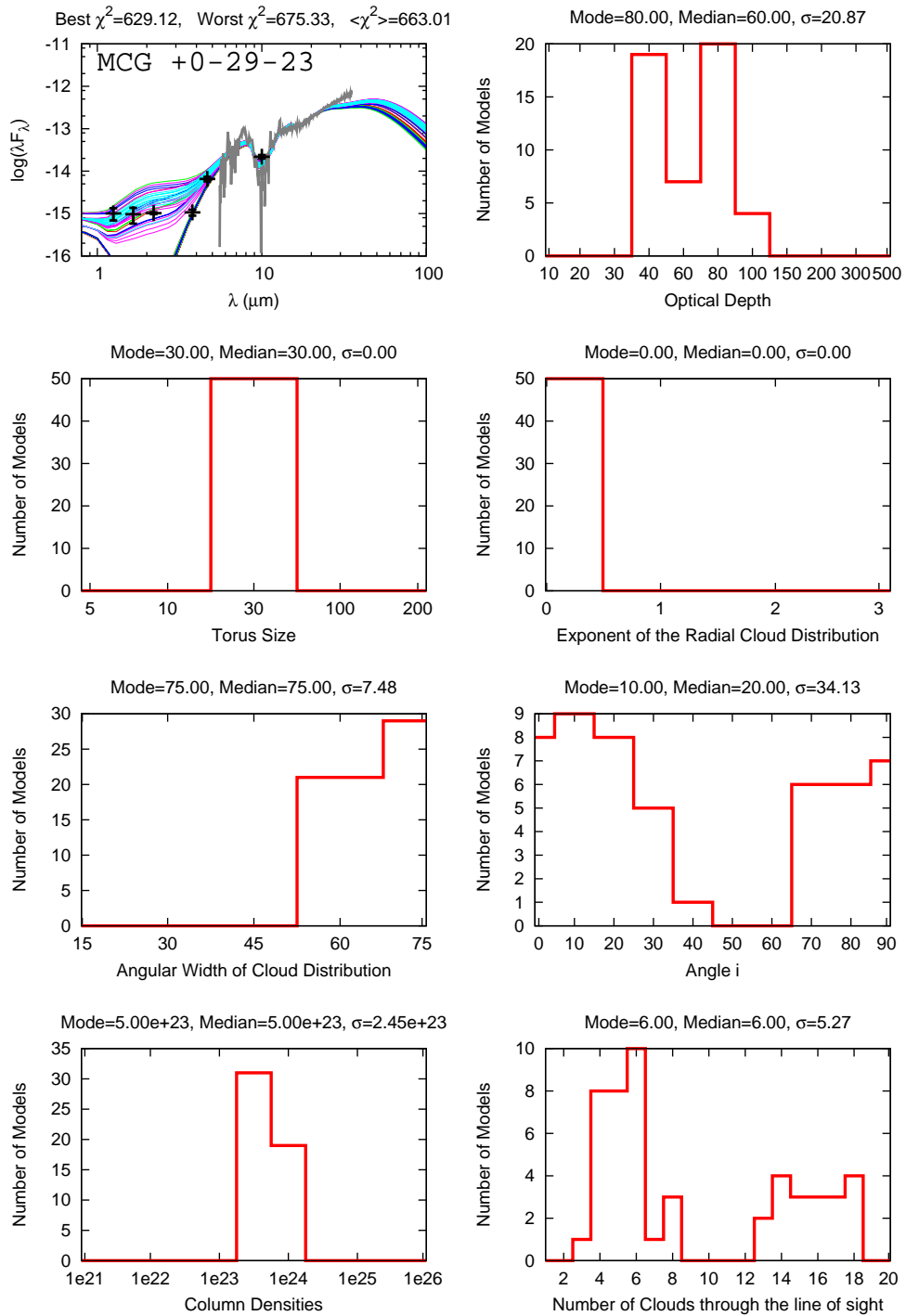


Figure 5.58: Best 50 clumpy models fitted to MCG +0-29-23, with specific parameters histograms shown. The description of Ossenkopf *et al.* (1992) for the silicates is preferred.

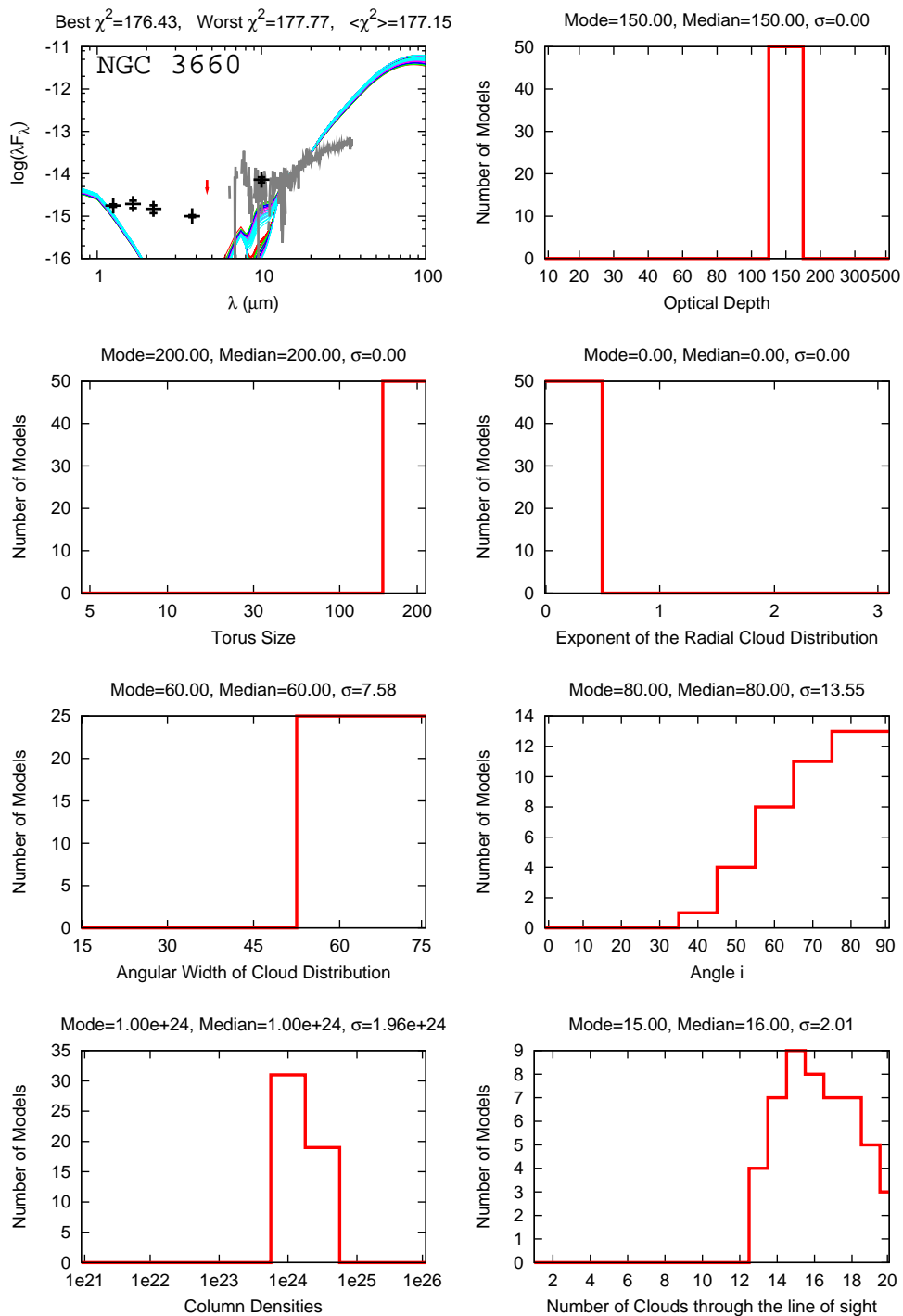


Figure 5.59: Best 50 clumpy models fitted to NGC 3660, with specific parameters histograms shown. The description of Draine (2003) for the silicates is the preferred.

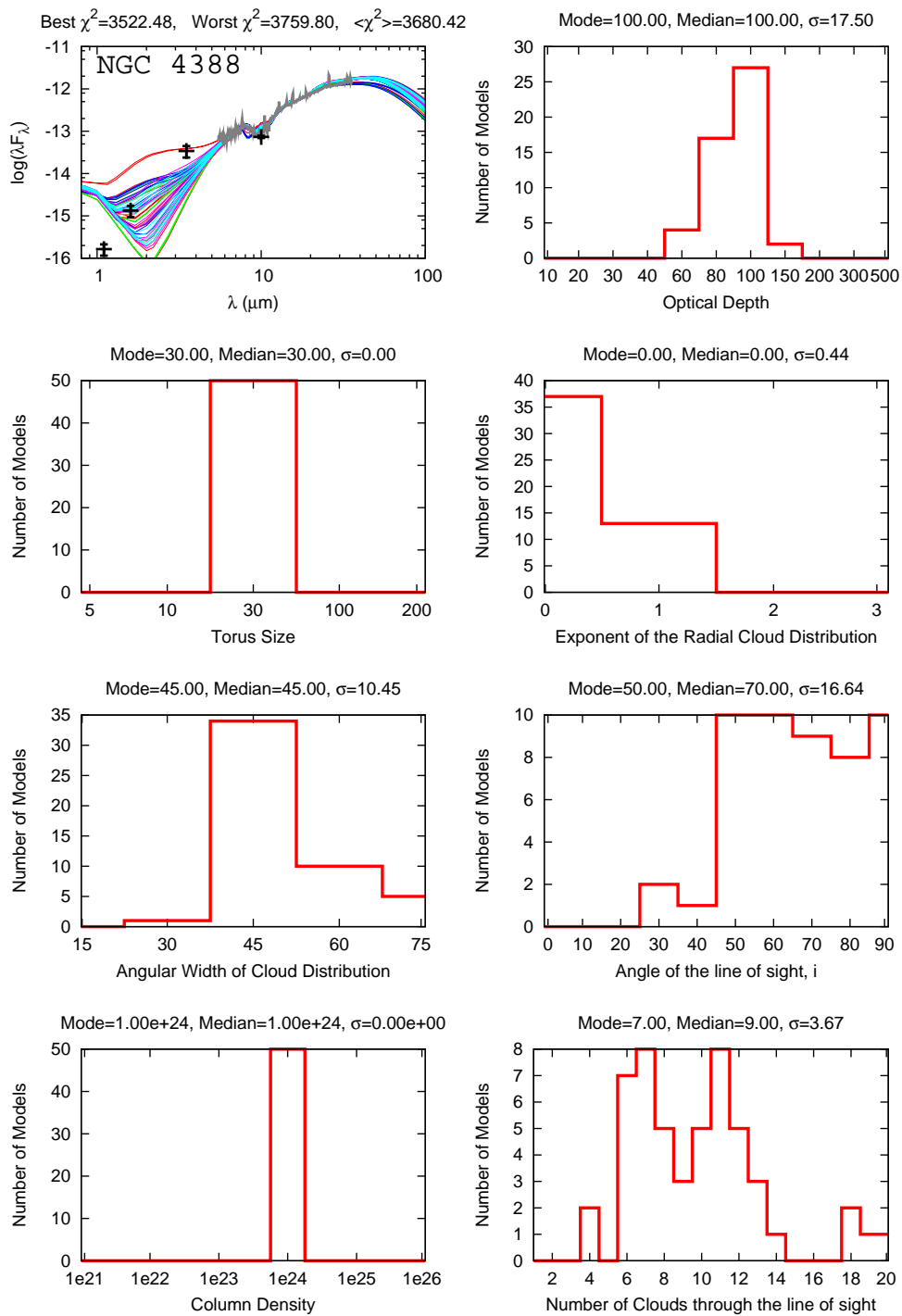


Figure 5.60: Best 50 clumpy models fitted to NGC 4388, with specific parameters histograms shown. The silicate description of Draine (2003) is preferred, but some cases with a Ossenkopf *et al.* (1992) description are also accepted.

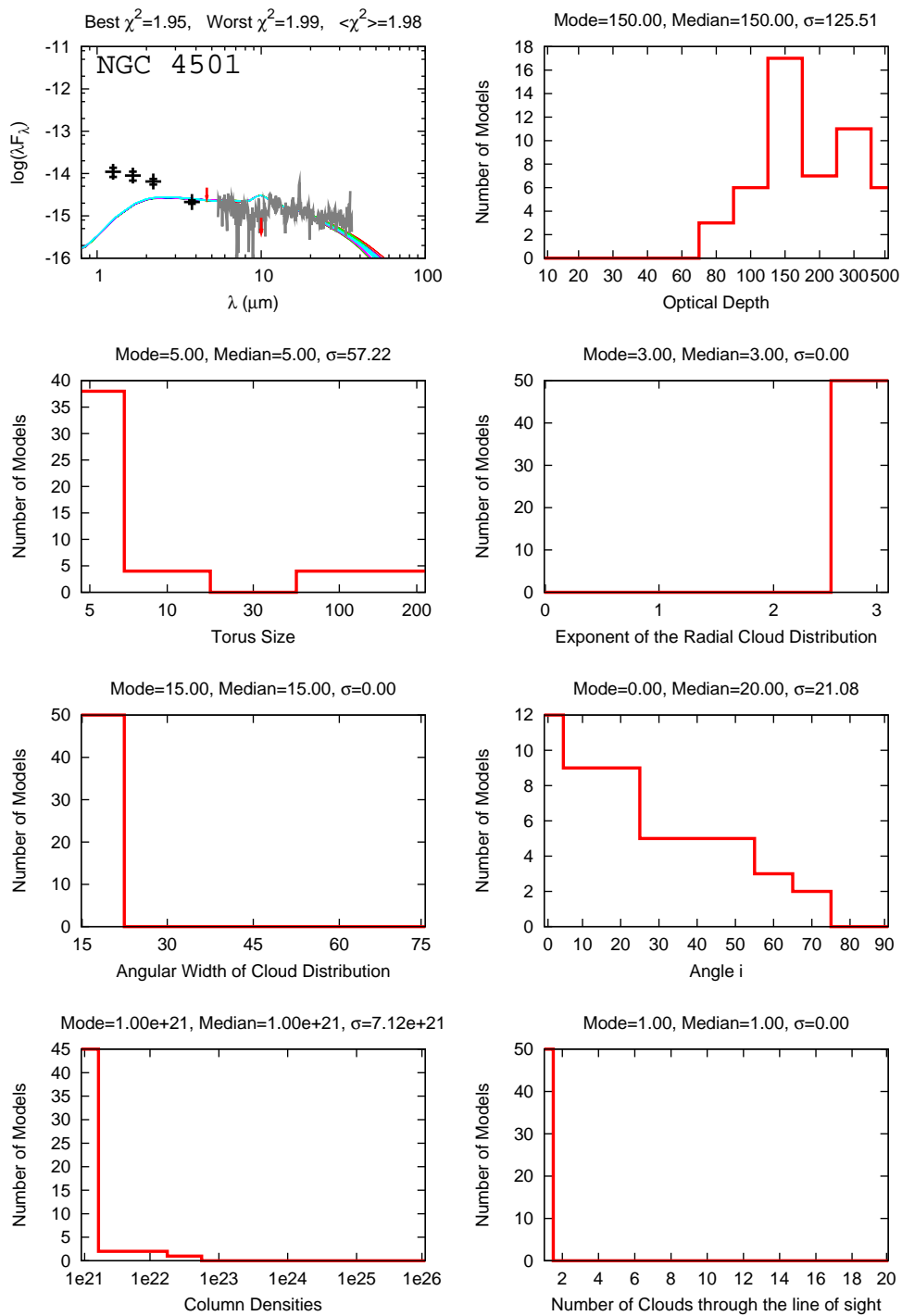


Figure 5.61: Best 50 clumpy models fitted to NGC 4501, with specific parameters histograms shown. The description of Ossenkopf *et al.* (1992) for the silicates is preferred.

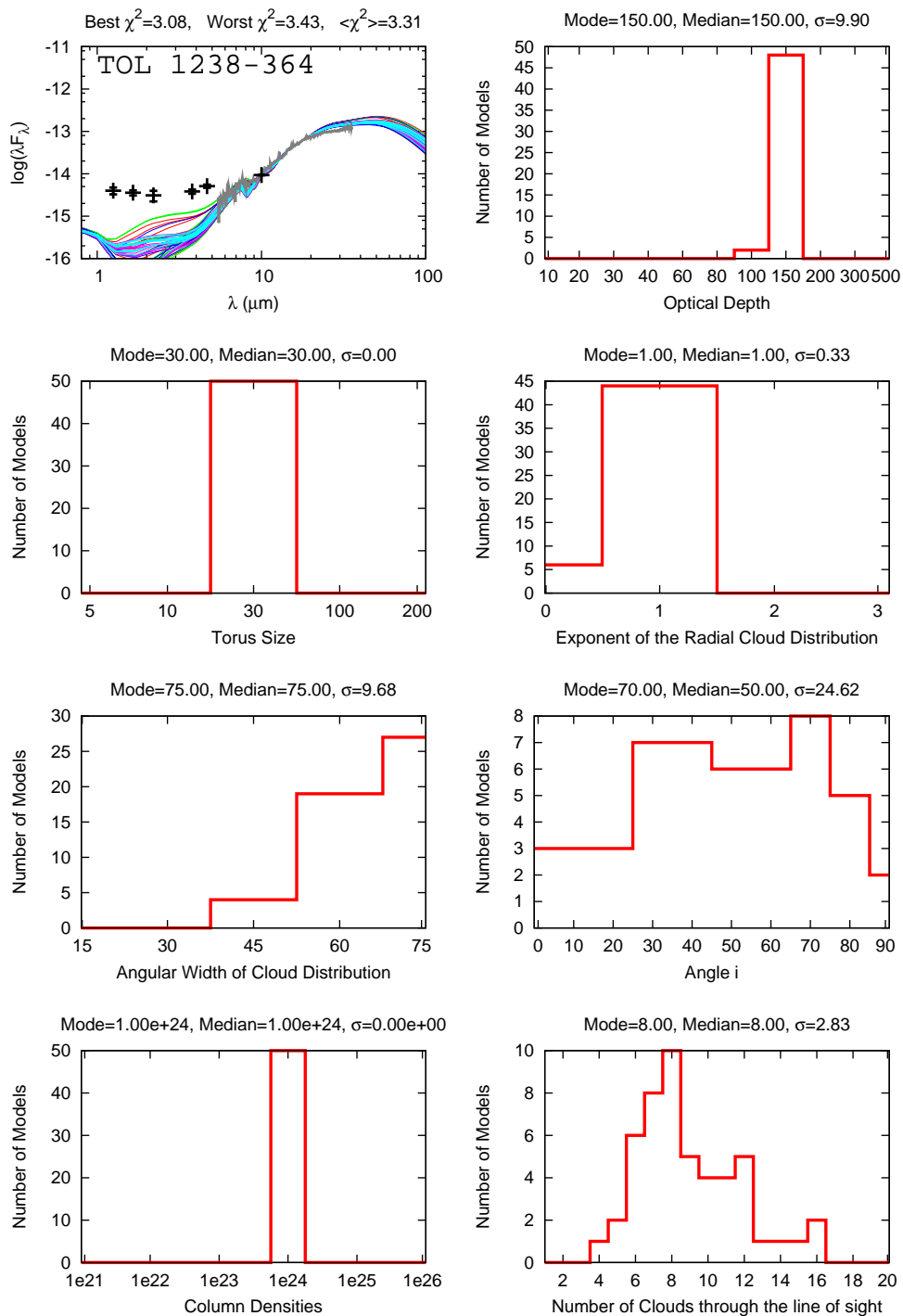


Figure 5.62: Best 50 clumpy models fitted to TOL 1238-364, with specific parameters histograms shown. The silicate description of Draine (2003) is preferred, but some cases with a Ossenkopf *et al.* (1992) description are also accepted.

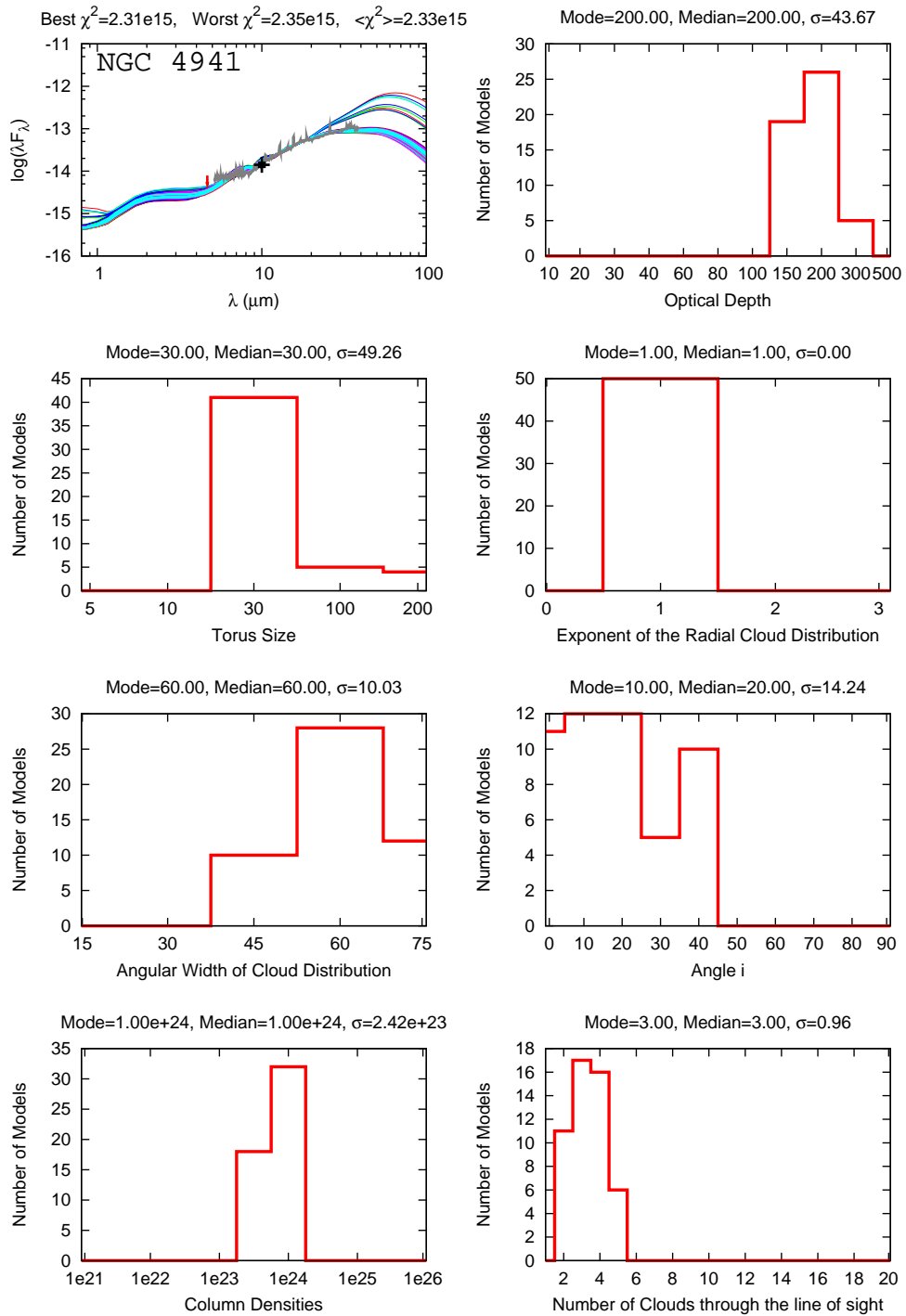


Figure 5.63: Best 50 clumpy models fitted to NGC 4941, with specific parameters histograms shown. The silicate description of Draine (2003) is the preferred.

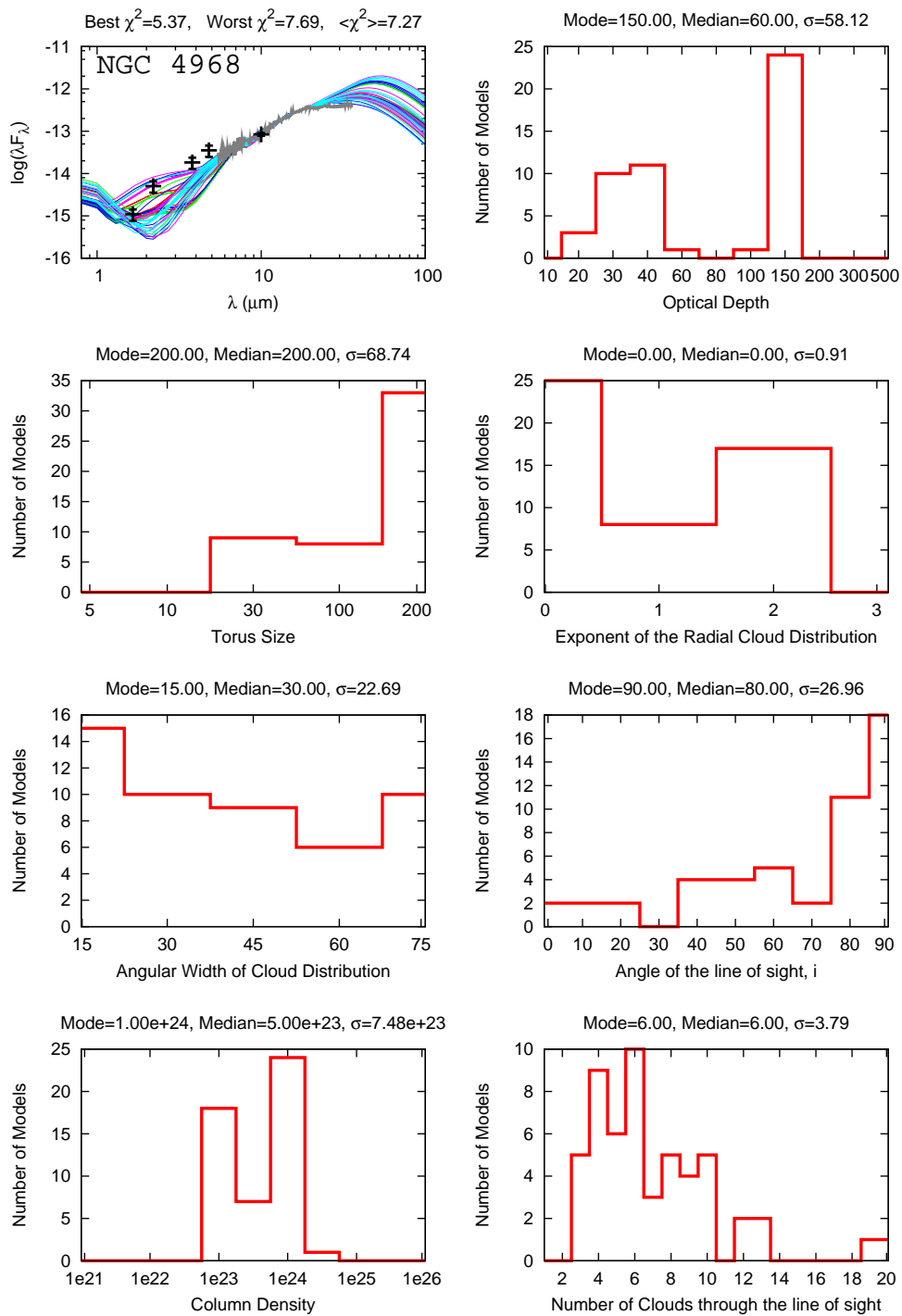


Figure 5.64: Best 50 clumpy models fitted to NGC 4968, with specific parameters histograms shown. The description of Draine (2003) for the silicates is the preferred.

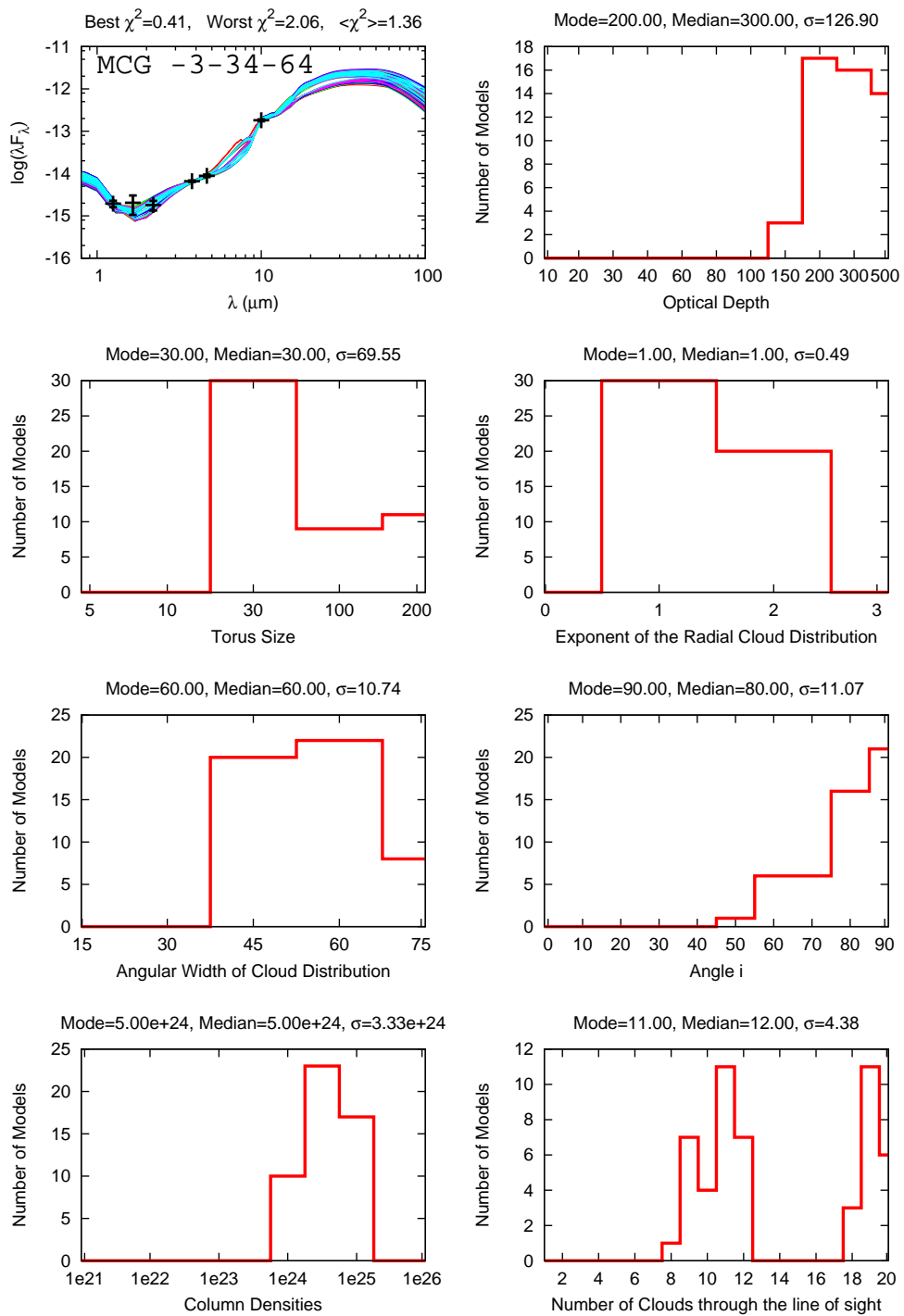


Figure 5.65: Best 50 clumpy models fitted to MCG -3-34-64, with specific parameters histograms shown. The preferred description for the silicates is that of Ossenkopf *et al.* (1992), but some cases described by Draine (2003) are included.

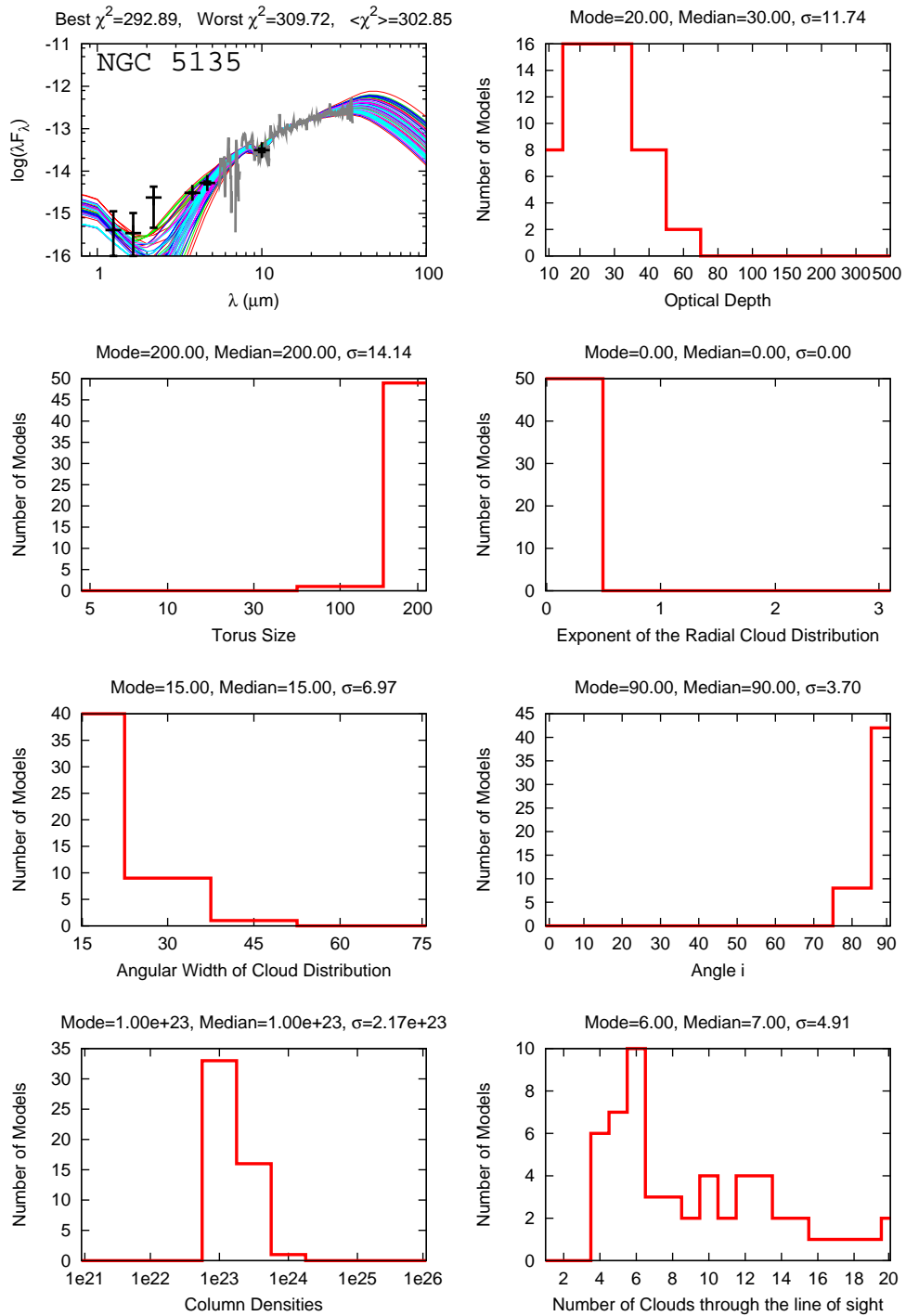


Figure 5.66: Best 50 clumpy models fitted to NGC 5135, with specific parameters histograms shown. The description of Ossenkopf *et al.* (1992) for the silicates is preferred.

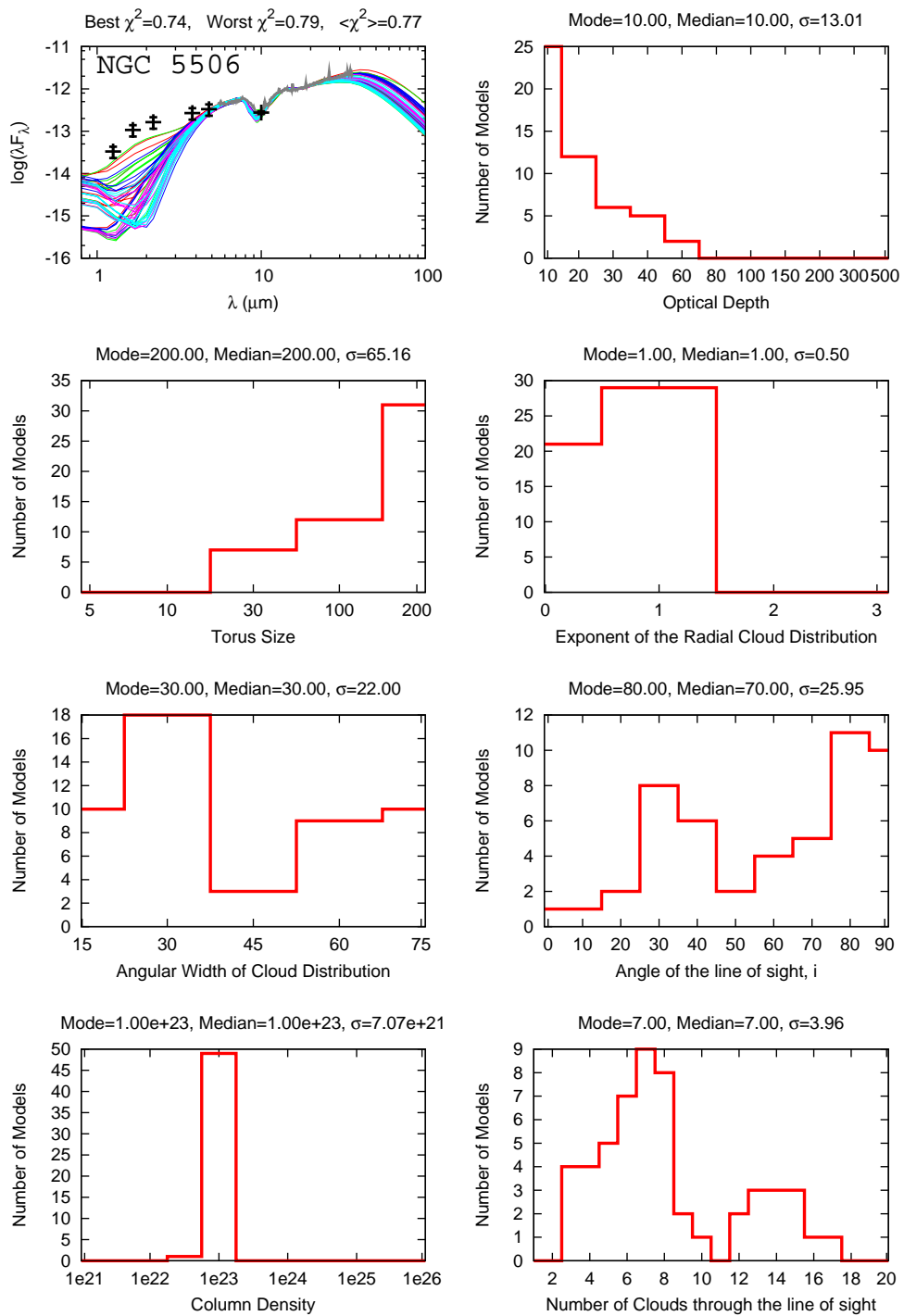


Figure 5.67: Best 50 clumpy models fitted to NGC 5506, with specific parameters histograms shown. The description of Draine (2003) for the silicates is the preferred.

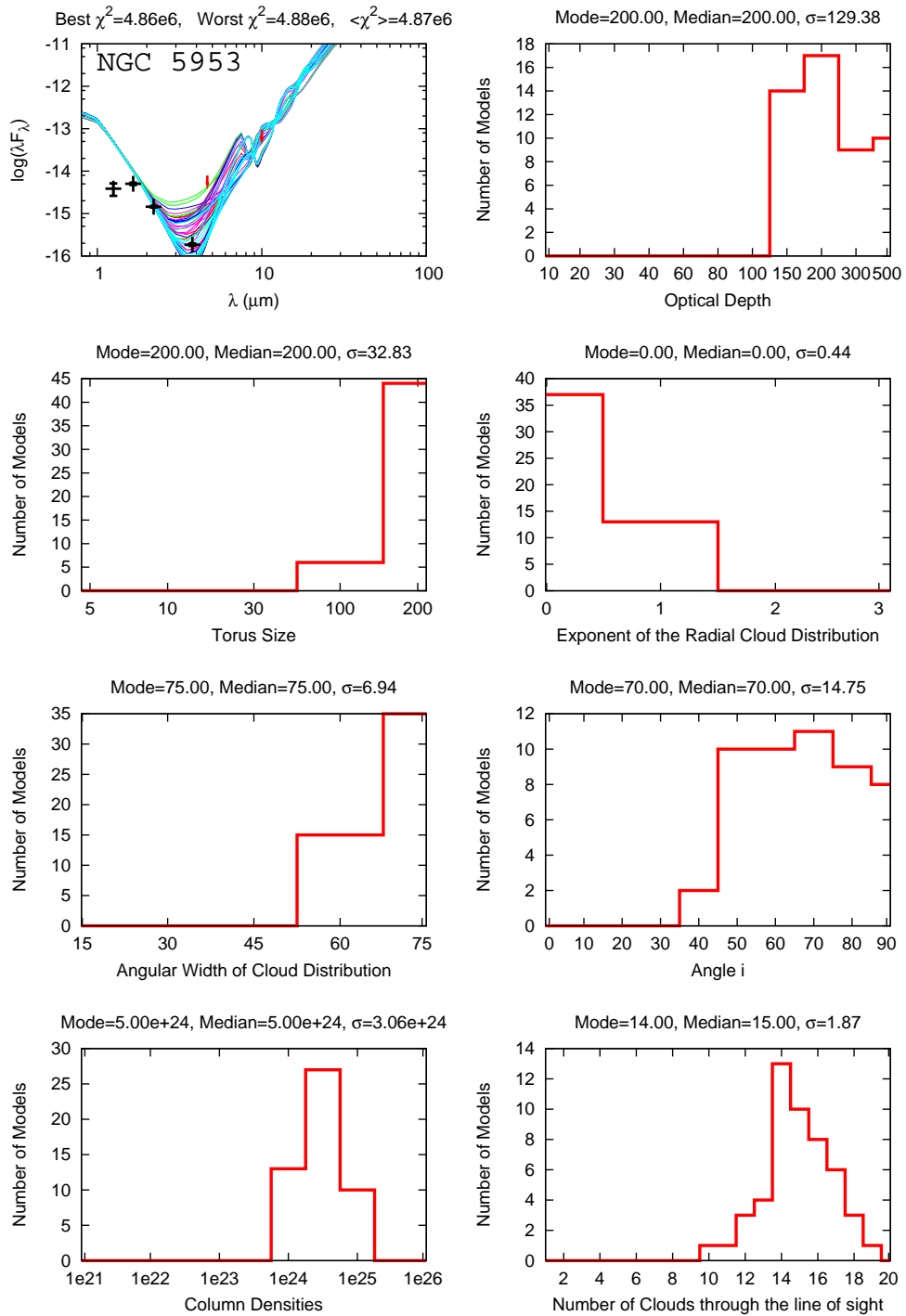


Figure 5.68: Best 50 clumpy models fitted to NGC 5953, with specific parameters histograms shown. The preferred description for the silicates is that of Ossenkopf *et al.* (1992), but some cases described by Draine (2003) are included.

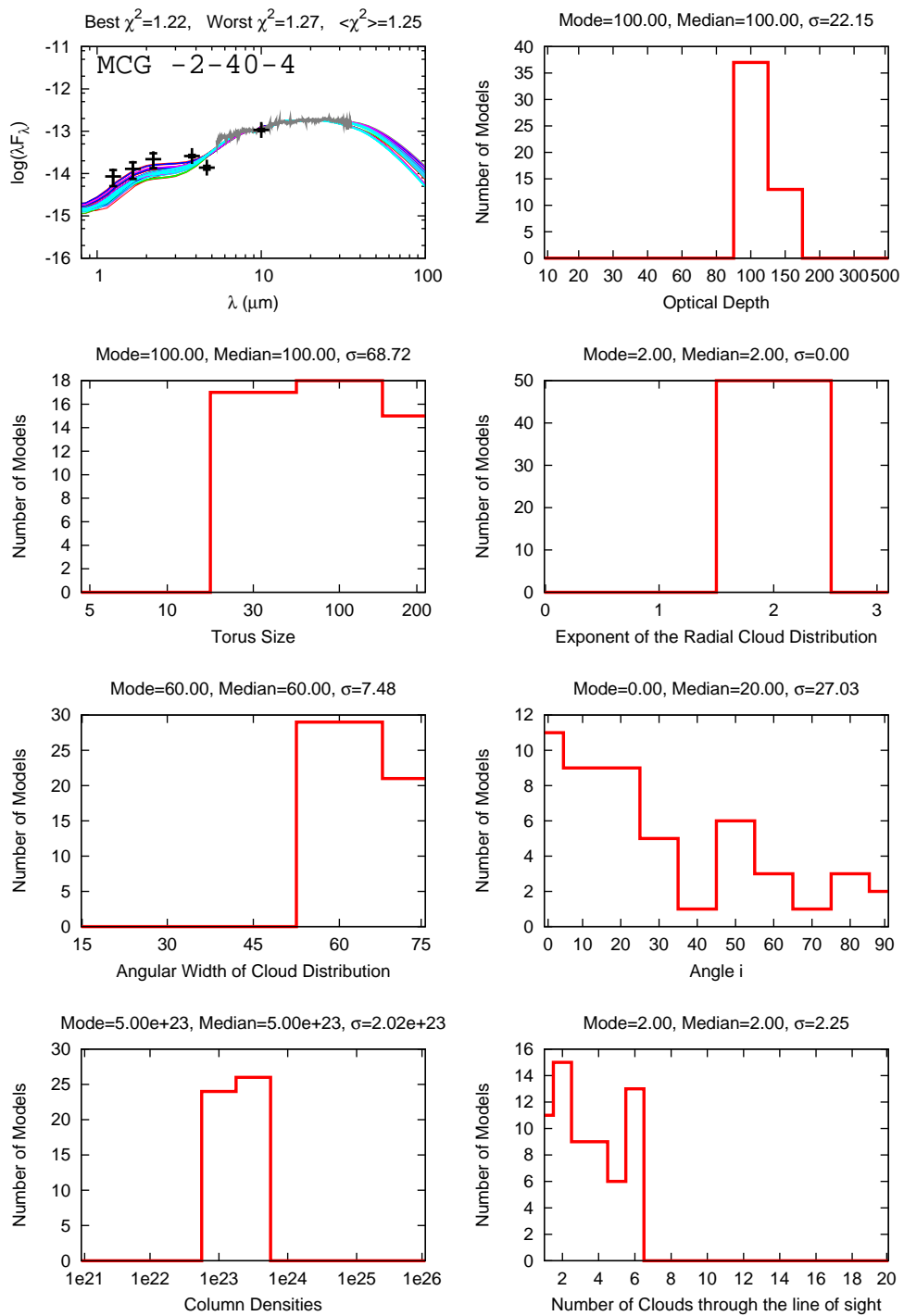


Figure 5.69: Best 50 clumpy models fitted to MCG -2-40-4, with specific parameters histograms shown. The description of Ossenkopf *et al.* (1992) for the silicates is preferred.

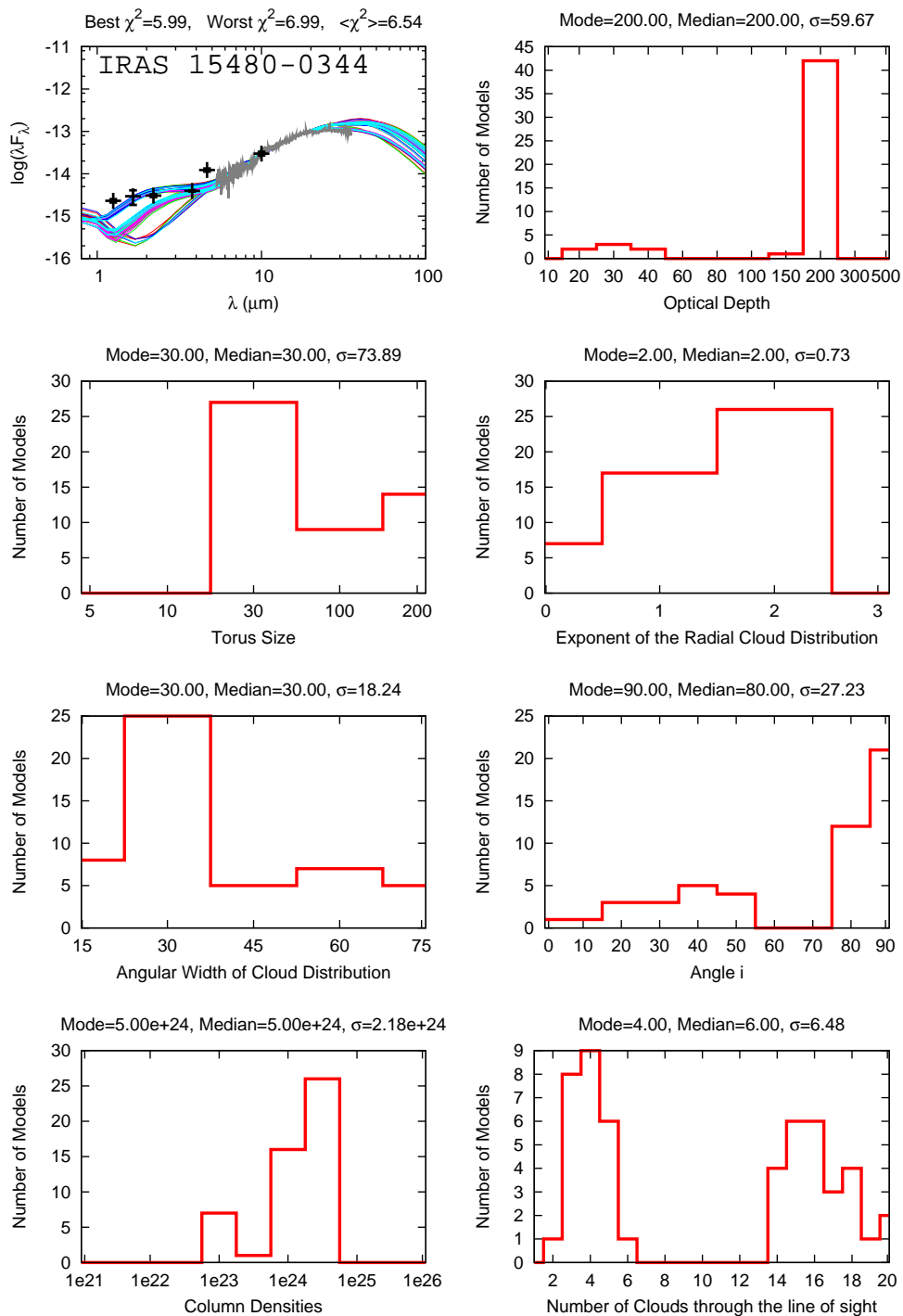


Figure 5.70: Best 50 clumpy models fitted to IRAS 15480-0344, with specific parameters histograms shown. The silicate description of Draine (2003) is preferred, but some cases with a Ossenkopf *et al.* (1992) description are also accepted.

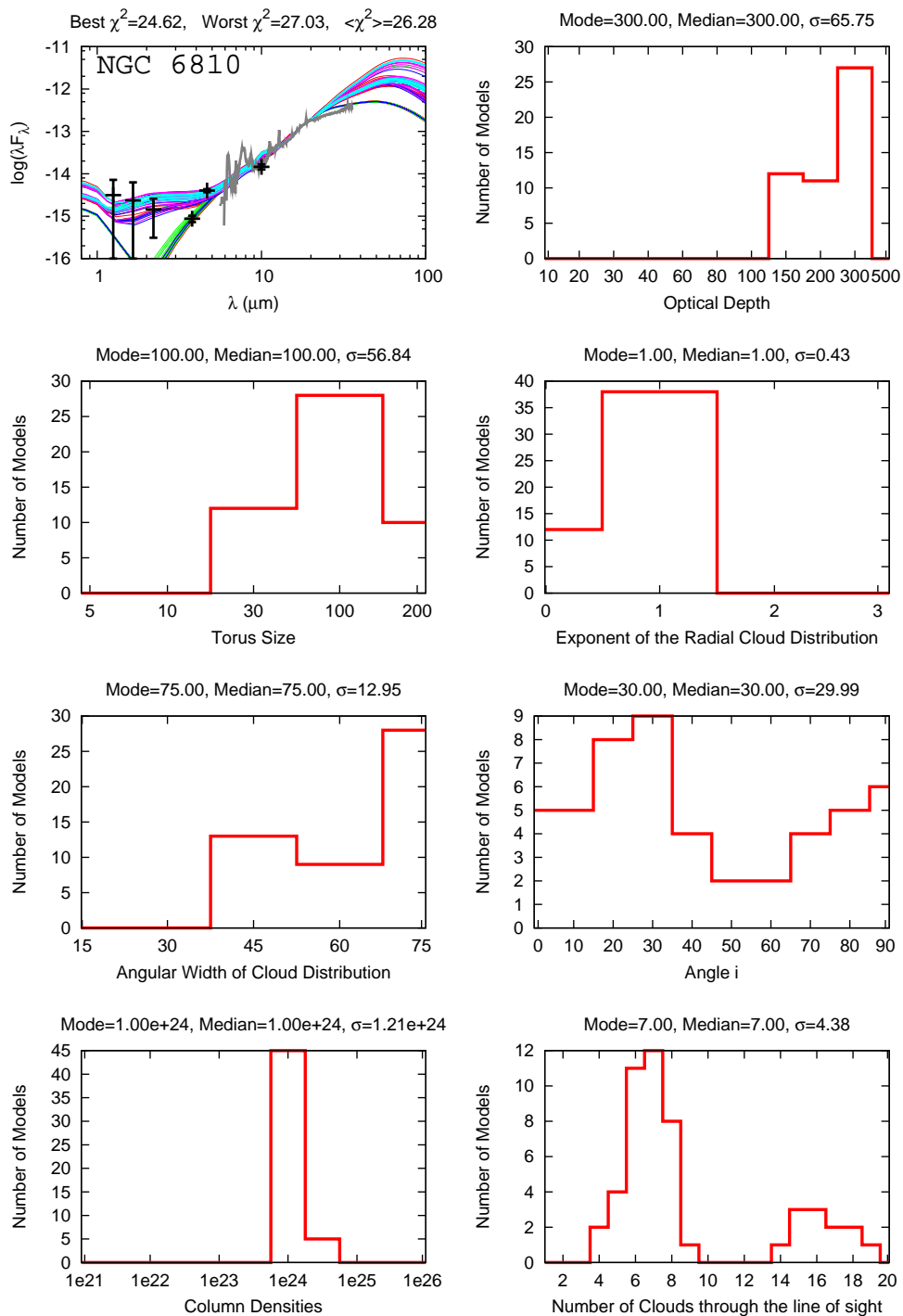


Figure 5.71: Best 50 clumpy models fitted to NGC 6810, with specific parameters histograms shown. The preferred description for the silicates is that of Ossenkopf *et al.* (1992), but some cases described by Draine (2003) are included.

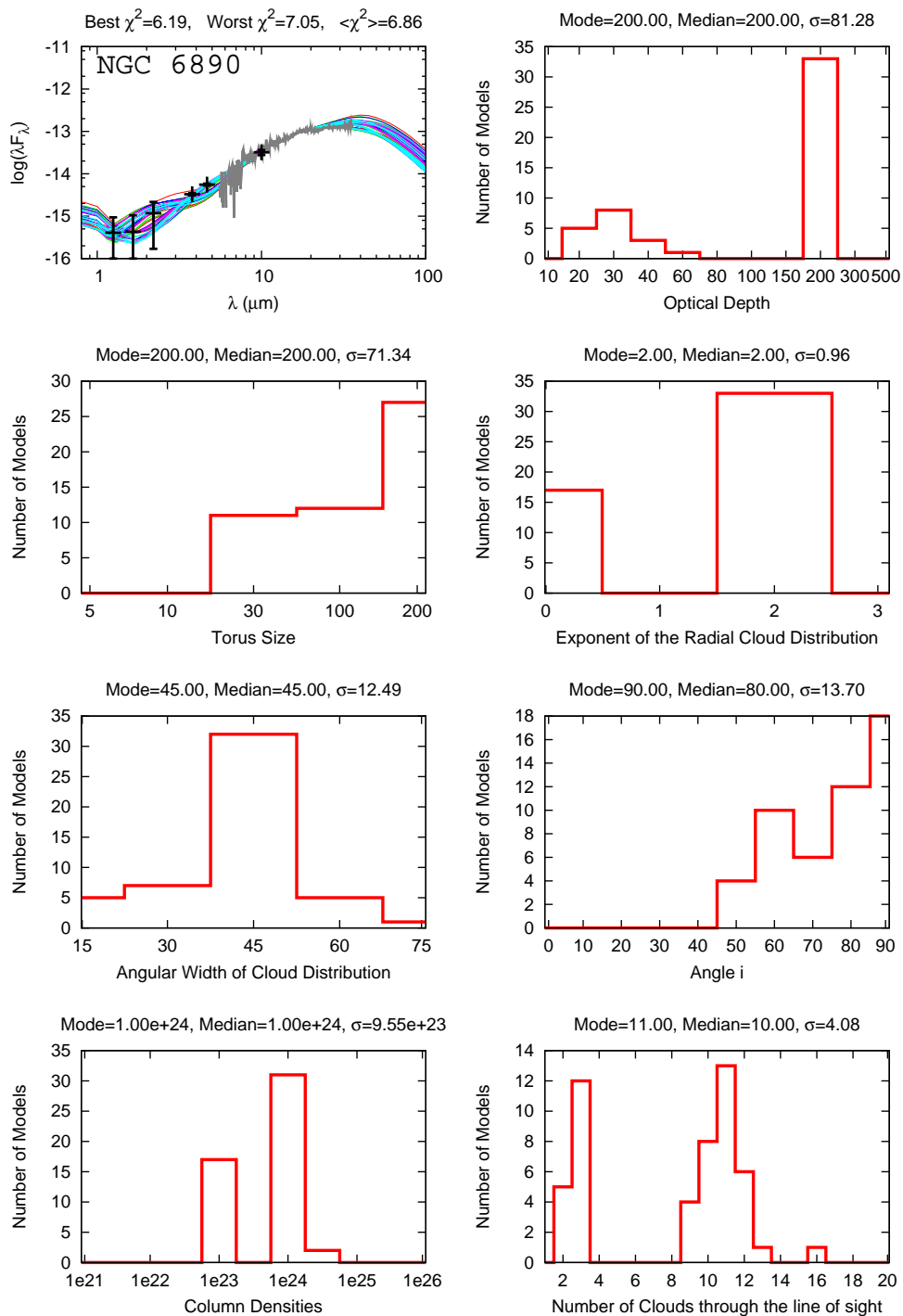


Figure 5.72: Best 50 clumpy models fitted to NGC 6890, with specific parameters histograms shown. The description of Ossenkopf *et al.* (1992) for the silicates is preferred.

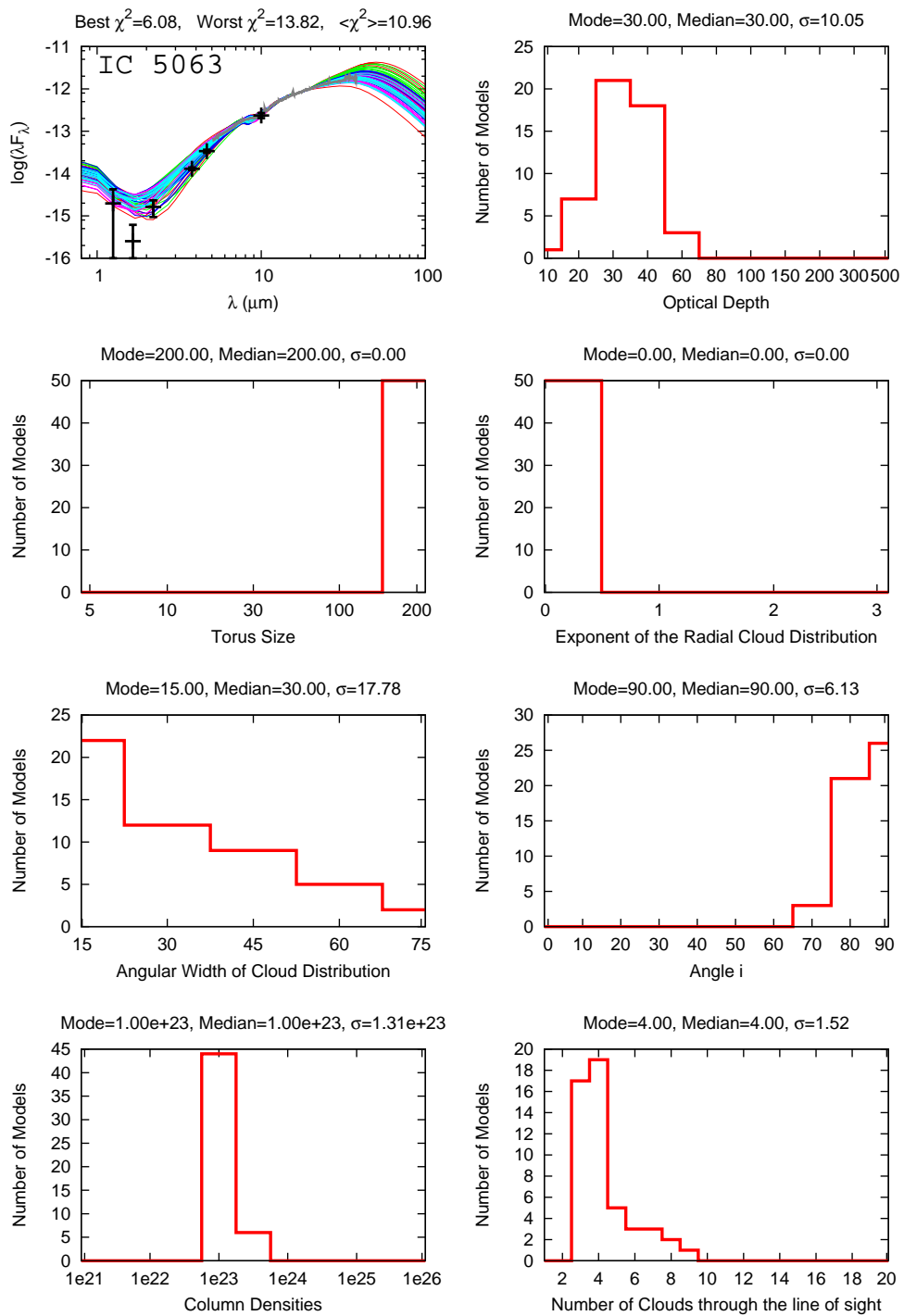


Figure 5.73: Best 50 clumpy models fitted to IC 5063, with specific parameters histograms shown. The description of Ossenkopf *et al.* (1992) for the silicates is preferred.

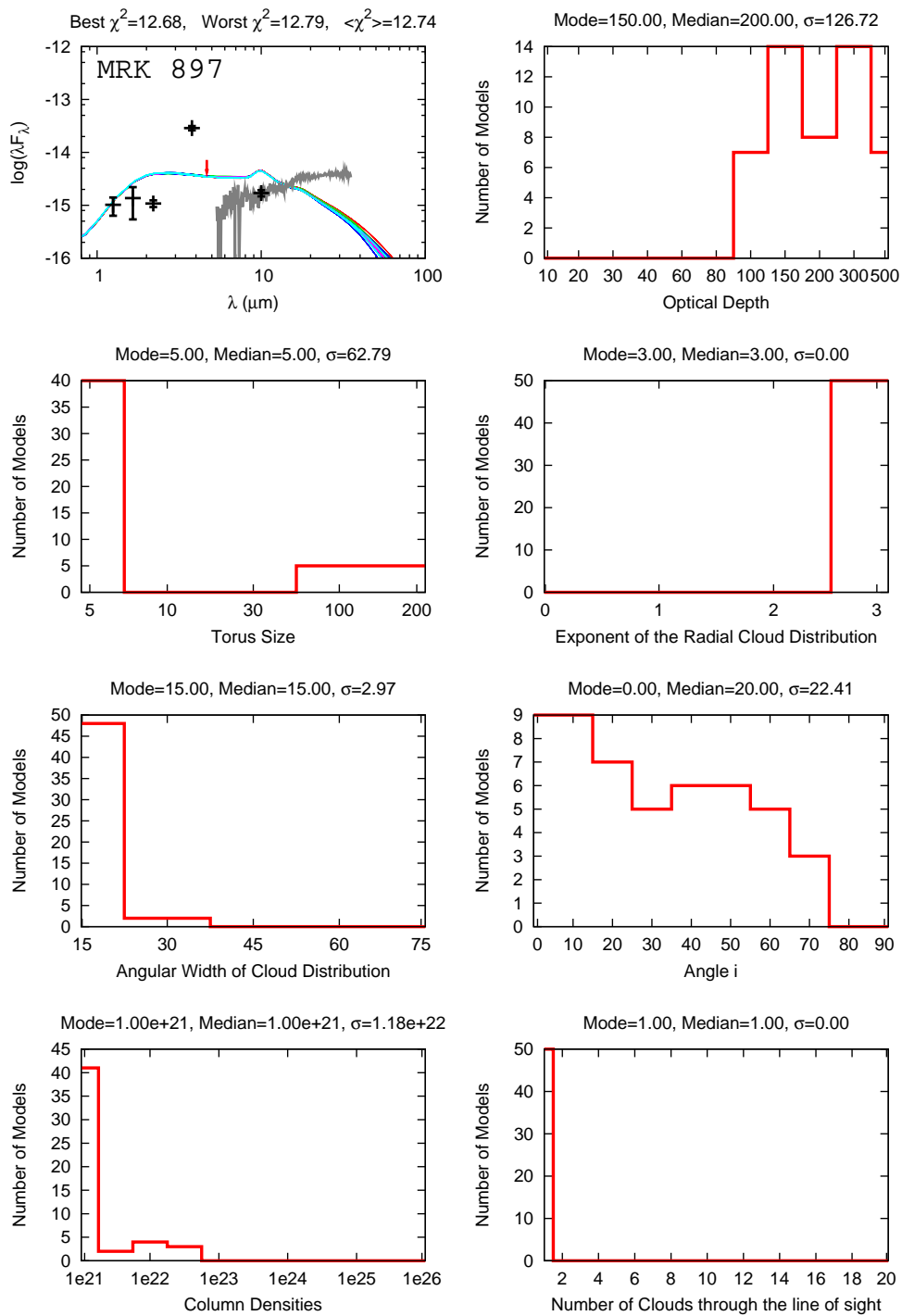


Figure 5.74: Best 50 clumpy models fitted to MRK 897, with specific parameters histograms shown. The description of Ossenkopf *et al.* (1992) for the silicates is preferred.

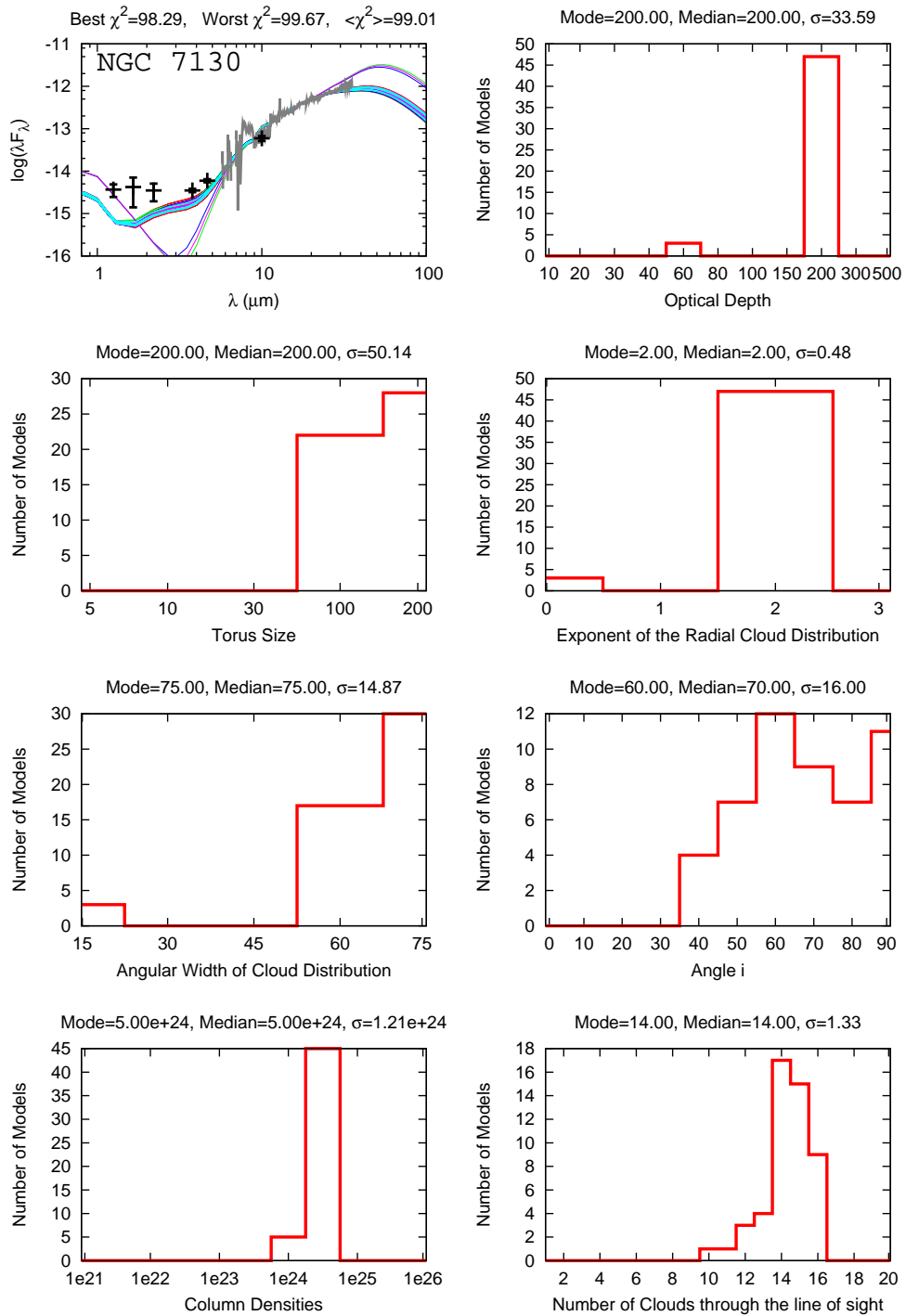


Figure 5.75: Best 50 clumpy models fitted to NGC 7130, with specific parameters histograms shown. The description of Ossenkopf *et al.* (1992) for the silicates is preferred.

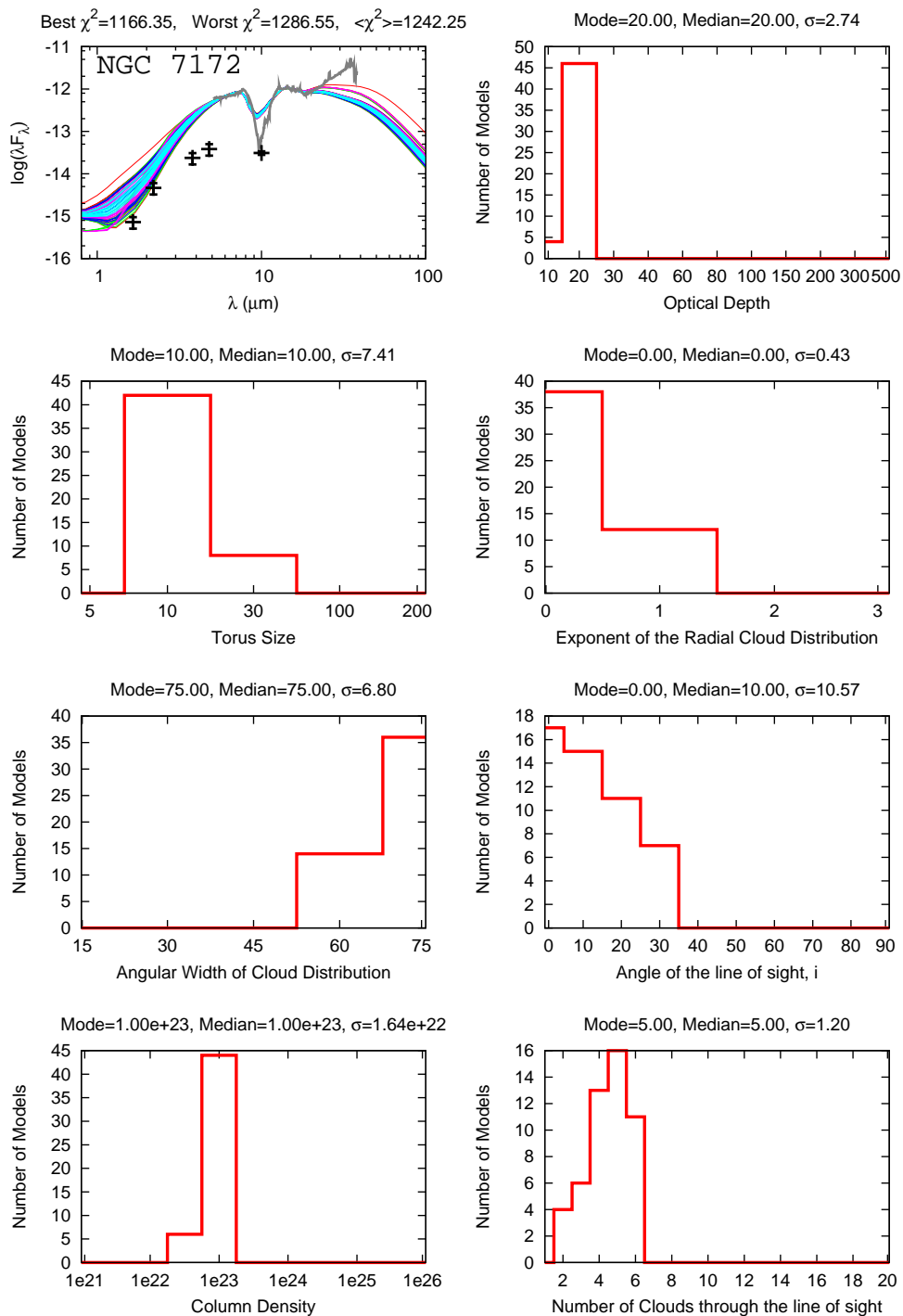


Figure 5.76: Best 50 clumpy models fitted to NGC 7172, with specific parameters histograms shown. The description of Draine (2003) for the silicates is the preferred.

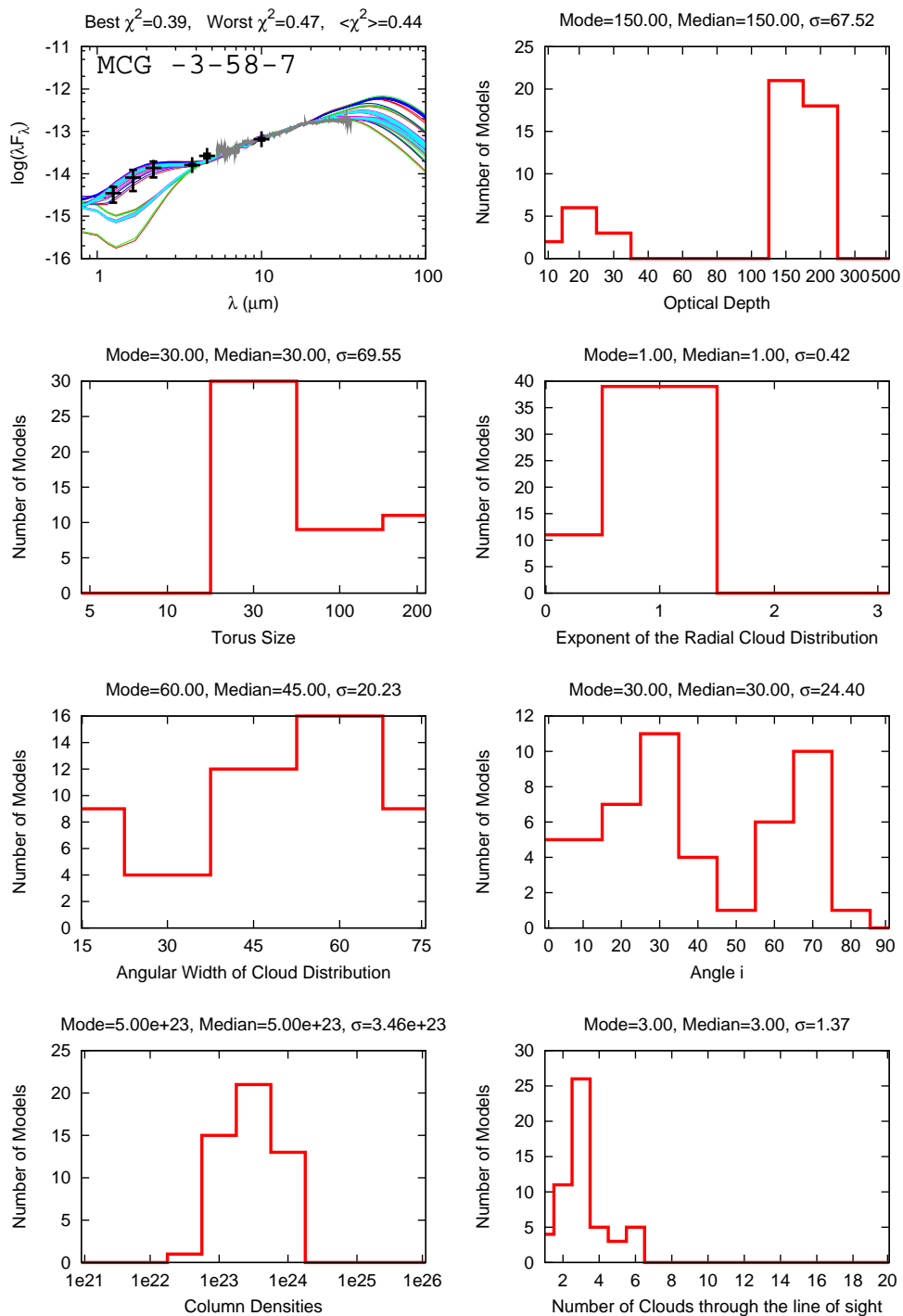


Figure 5.77: Best 50 clumpy models fitted to MCG -3-58-7, with specific parameters histograms shown. The preferred description for the silicates is that of Ossenkopf *et al.* (1992), but some cases described by Draine (2003) are included.

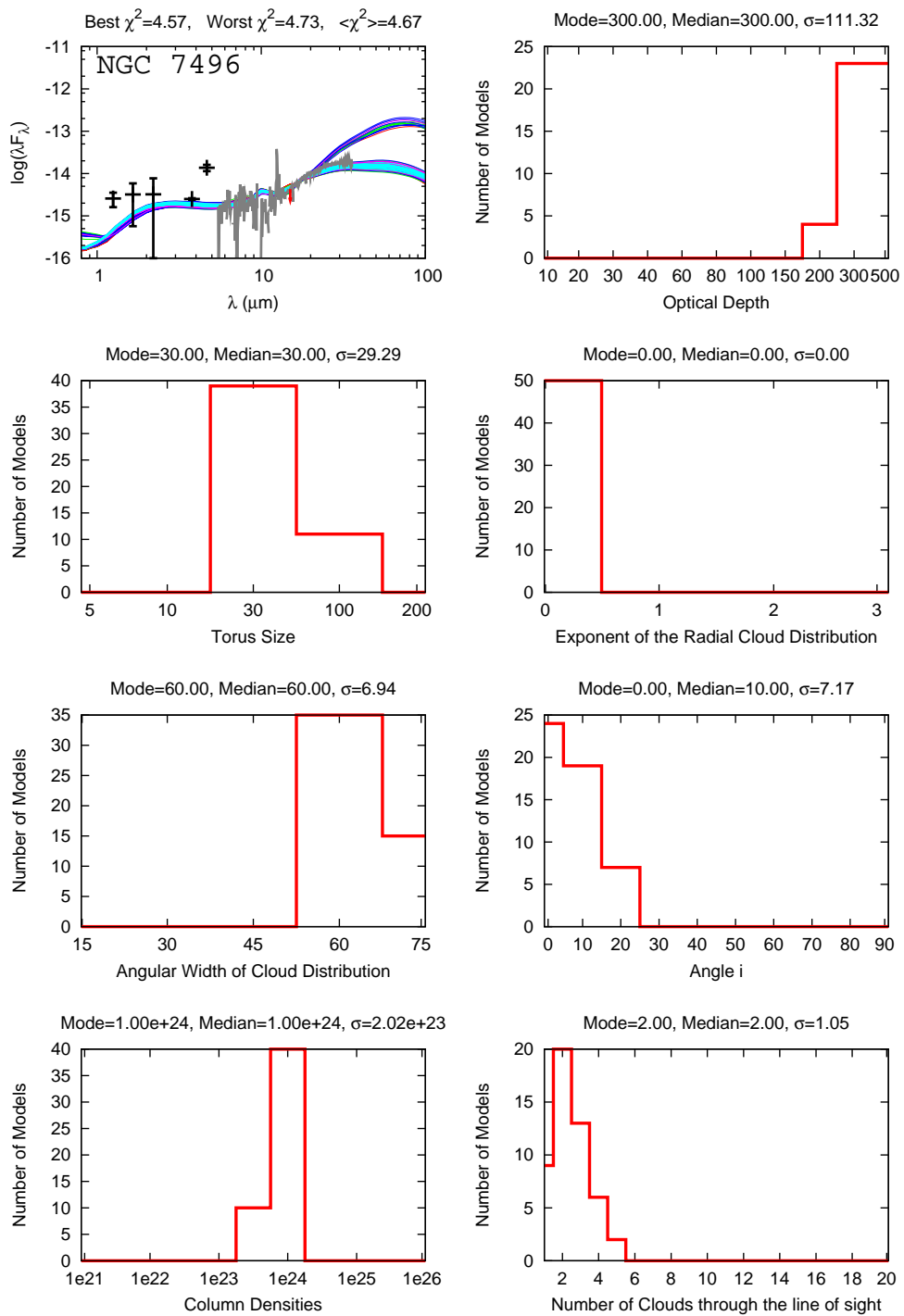


Figure 5.78: Best 50 clumpy models fitted to NGC 7496, with specific parameters histograms shown. The description of Draine (2003) for the silicates is the preferred.

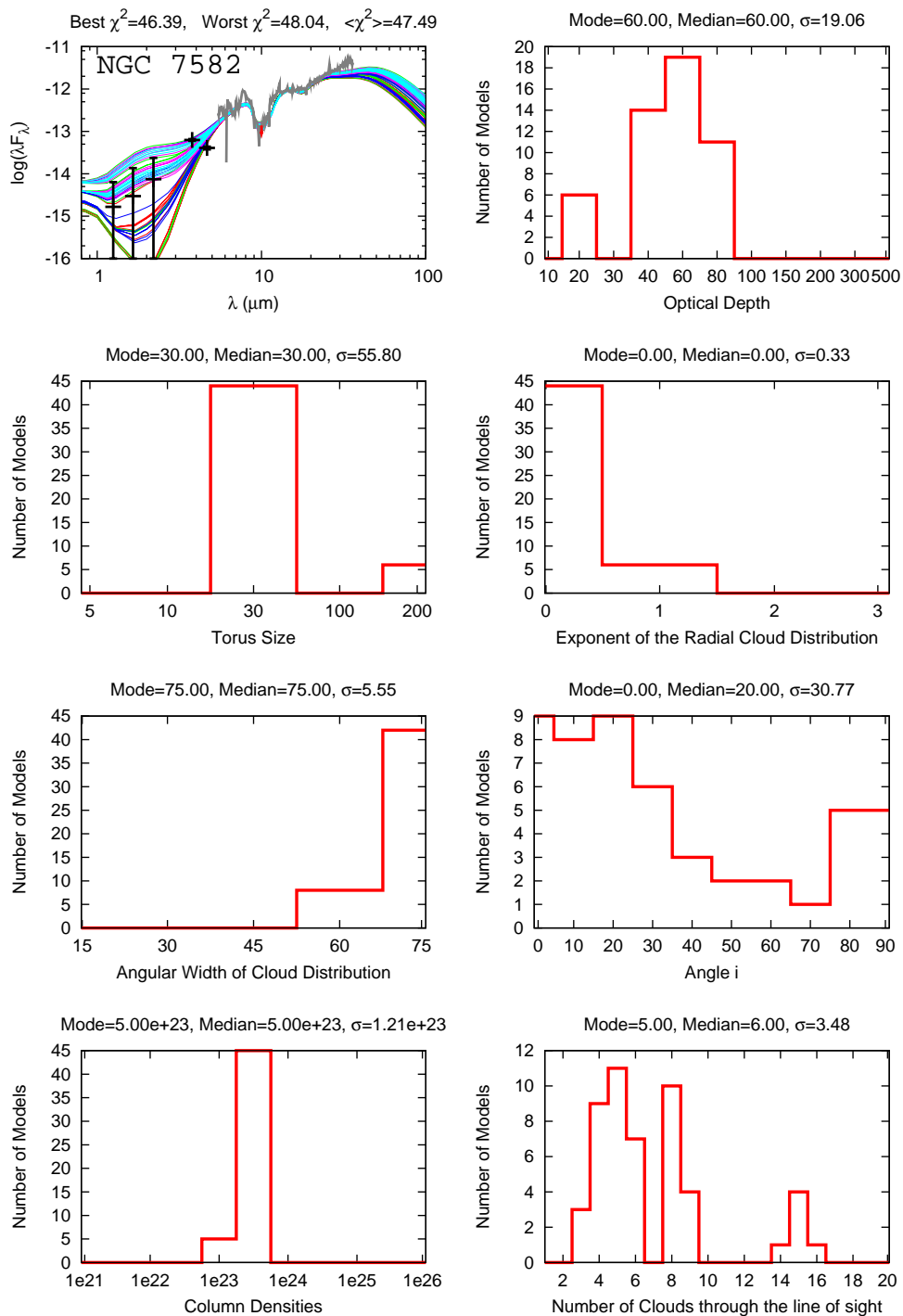


Figure 5.79: Best 50 clumpy models fitted to NGC 7582, with specific parameters histograms shown. The description of Ossenkopf *et al.* (1992) for the silicates is preferred.

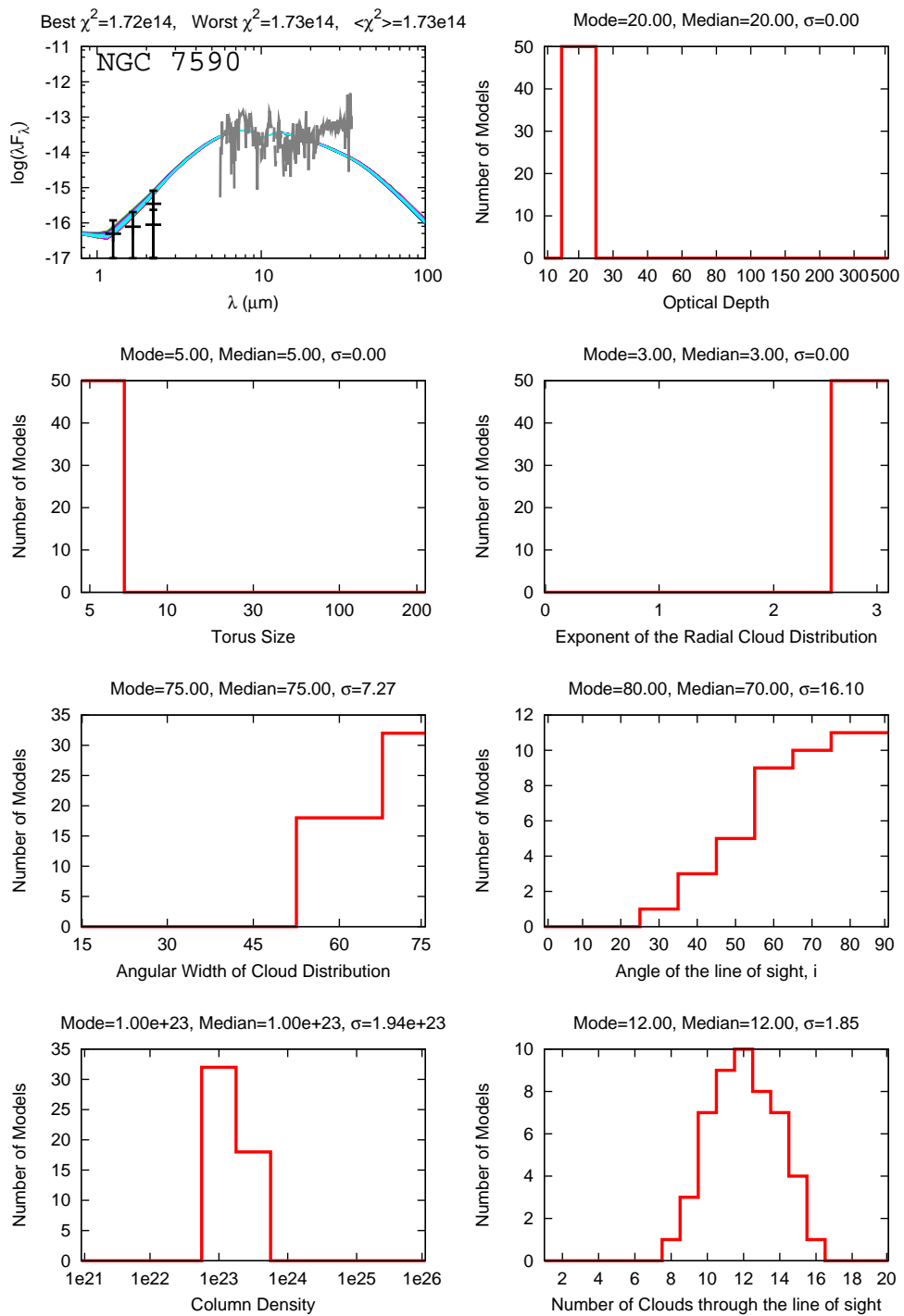


Figure 5.80: Best 50 clumpy models fitted to NGC 7590, with specific parameters histograms shown. The description of Ossenkopf *et al.* (1992) for the silicates is preferred.

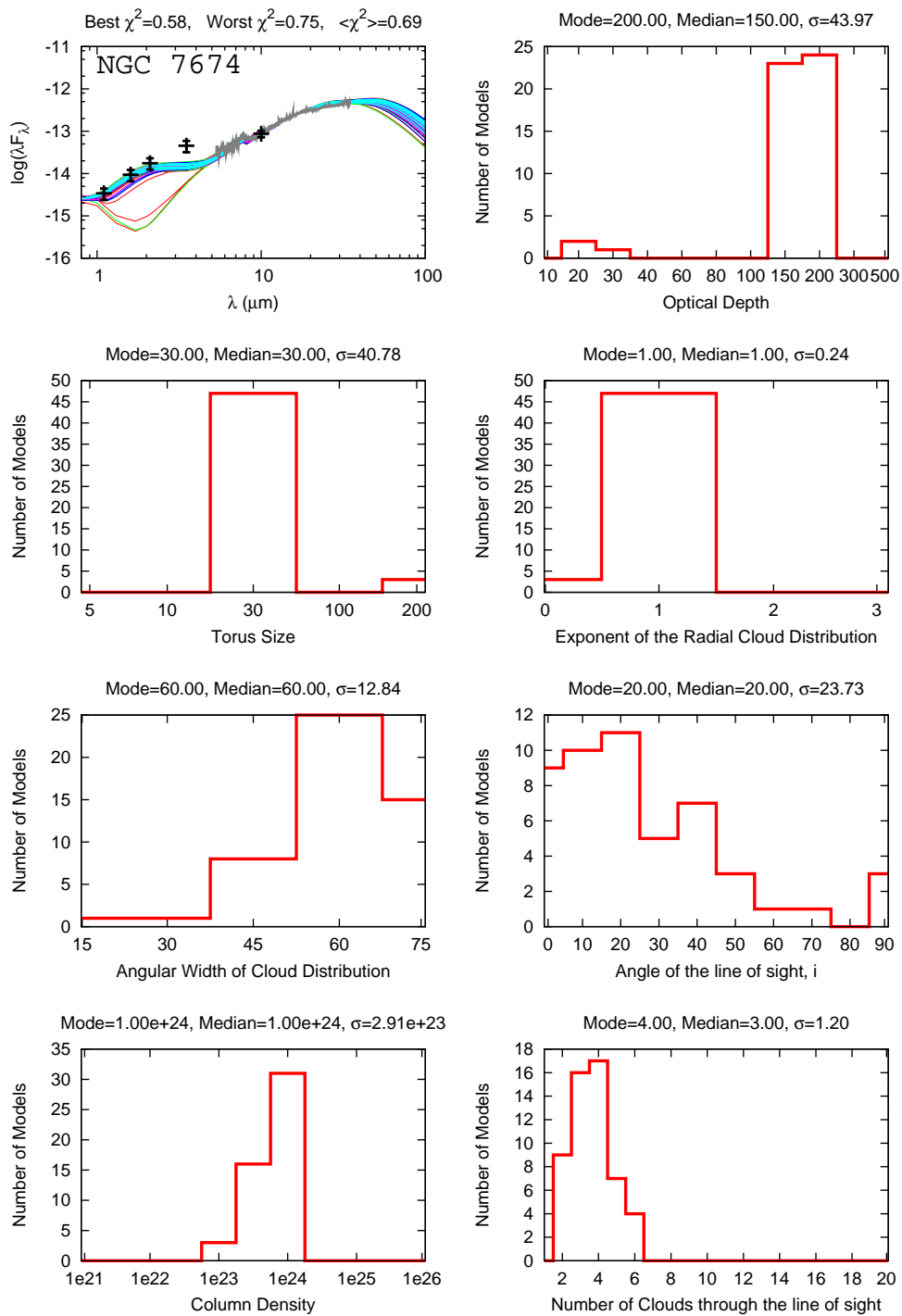


Figure 5.81: Best 50 clumpy models fitted to NGC 7674, with specific parameters histograms shown. The silicate description of Draine (2003) is preferred, but some cases with a Ossenkopf *et al.* (1992) description are also accepted.

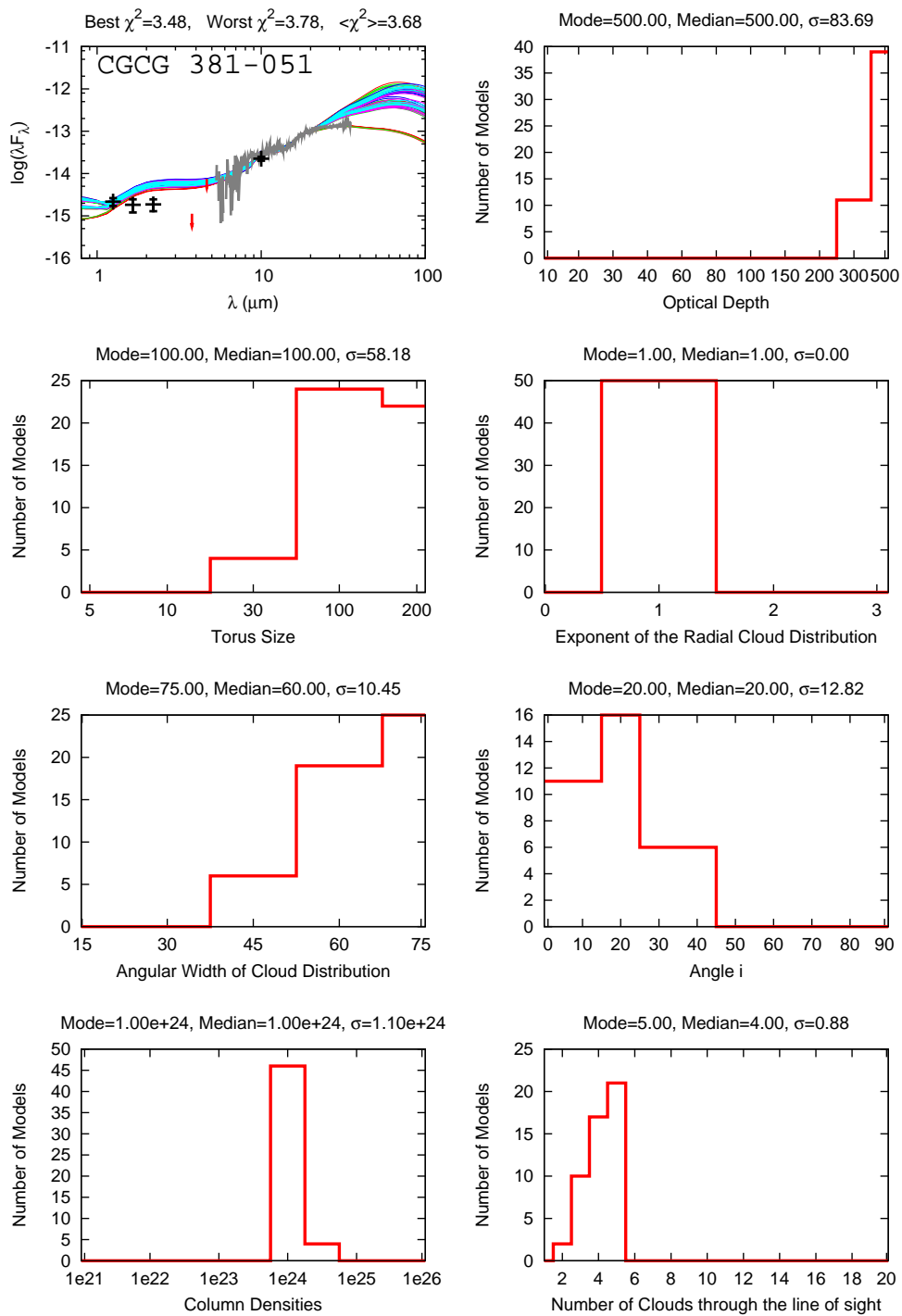


Figure 5.82: Best 50 clumpy models fitted to CGCG 381-051, with specific parameters histograms shown. The preferred description for the silicates is that of Ossenkopf *et al.* (1992), but some cases described by Draine (2003) are included.

Chapter 6

Results and Discussion

All the results we present in this chapter refer to the clumpy model of the torus emission, due to the poor performance of the smooth model. Galaxies MCG -2-8-39, NGC 3660, and NGC 7172 have been excluded from the analysis because the torus models poorly describe the observed SED. Probably, the L band observation of MRK 897 is deviated due to variability, and TOL 1238-364 is contaminated by stellar emission in the near-IR photometry, but the models correctly describe the observed spectra, so we include them in the following analysis together with the other 34 galaxies modeled. In Table 6.1 we list the IRAS fluxes and luminosities of the sample analyzed here, and in Table 6.2 we include all the other data obtained from the literature and used to obtain results from the torus emission modeling.

Here we briefly summarize our findings. The extinction derived for the central region of the galaxies in our sample is not due to dust in the galaxy, but to an excess of hot dust located very close to the center. Apparently, neither the column density, the size of the torus, nor the torus aperture angle are related to the luminosity of the objects, although the aperture angle is larger for the luminous quasars studied by Mor *et al.* (2009). The column densities derived through different methods are not correlated, indicating that they describe different properties of the same region or, simply, different regions. The $12\mu\text{m}/25\mu\text{m}$

color ratio of the nuclear torus are similar to those found with IRAS, which sample the entire galaxy, indicating that the AGN dominates the emission at these wavelengths. The bolometric luminosity of the AGNs derived through the torus emission modeling are $\gtrsim 2$ orders of magnitude lower than that obtained from the emission at $[\text{OIII}]\lambda 5007$ and this is not understood. The inner radii of the torus are $R_{in} \sim 0.1\text{-}3$ parsecs, while the outer radius of the torus ranges from 0.3 to 300 parsecs. The torus masses derived from the emission modeling are quite large, ranging from 100 to $\sim 10^9 M_{\odot}$. No segregation is found between HBLR and non-HBLR galaxies, although it seems that HBLR objects are more powerful than non-HBLR, as already suggested by Tran (2003).

6.1 AGN Contribution and Luminosity

Once we isolated the nuclear emission through the surface brightness profile fitting (Section 4.1.2) we can determine not only the flux radiated by the nucleus, but also its percentage contribution to the total galactic emission. Using the nuclear contribution in each band of our observations for every galaxy in our sample (Table 4.2 *), we find that the largest nuclear contribution in the near-IR occurs only for luminous sources (as given by the $[\text{OIII}]$ luminosities, an estimator of the bolometric AGN luminosity, $L_{[\text{OIII}]}$ values have been collected from Shu *et al.* (2007) and the NED database). But when moving to longer wavelengths this relation dilutes. In Fig. 6.2 we also show the nuclear contribution at $19\mu\text{m}$, as calculated by Tommasin *et al.* (2009). They defined the nuclear contribution and the extendedness ratio measuring and modeling spectral features, taking advantage of the different aperture size of the SH and LH slits (described briefly in Section 3.3) in *Spitzer*-IRS spectra.

We find that the galaxies where a hidden broad-line region (HBLR) has been

*The N band nuclear contribution is 100% in all galaxies, with the only exception of NGC 6810, where it is 39.4%

detected through spectropolarimetric observations, are more powerful than non-HBLR galaxies in the near-IR, as can be seen in Fig. 6.2, but at longer wavelengths, the segregation disappears (the distinction between HBLR and non-HBLR has been included in all the plots that might show a distinction between both classes, but no particular segregation has been found besides the one mentioned here).

As mentioned above, we estimated the bolometric luminosity of the AGN traced by the [OIII] luminosity, $L_{[\text{OIII}]}$. Heckman *et al.* (2004) used a sample of type 1 AGN to determine that $L_{[\text{OIII}],\text{bol}}/L_{\text{OIII}} \approx 3500$, but they used the [OIII] luminosity without including an extinction correction, due to the uncertain value of the NLR Balmer decrement measured in type 1 AGN. Using the extinction corrected L_{OIII} of a sample of type 2 Seyfert galaxies, Lamastra *et al.* (2009) found that $L_{[\text{OIII}]}^{\text{bol}}/L_{\text{OIII}}$ vary with luminosity: $L_{[\text{OIII}]}^{\text{bol}}/L_{\text{OIII}} \approx 87, 142, \text{ and } 454$ for $\log(L_{\text{OIII}}) = 38\text{-}40, 40\text{-}42, \text{ and } 42\text{-}44$ respectively. The bolometric luminosity of the AGN illuminating the modeled torus is estimated as $L_{\text{IR,bol}} = \alpha \times 4\pi d^2$, where d is the distance to the galaxy, and α is the scaling factor needed to shift the model to the observed SED points (Eqn. 5.3). We find that the luminosities determined from the torus emission modeling are ~ 2 orders of magnitude lower than the values derived from $L_{[\text{OIII}]}$, as shown in Fig. 6.3. Although the luminosities show a linear relation, as expected, we did not expect this discrepancy, which could be explained by the fraction of AGN bolometric luminosity observed, $L_{\text{bol}}^{\text{obs}}/L_{\text{bol}}$.

6.2 Column Densities

The column density towards the central regions of AGN may be derived by different methods, depending on the observations: in the X-rays the photoelectric cut-off indicates the column density needed to obscure the emitted power law spectra; the equivalent width of the 6.7 KeV Fe K α line has also been used as an estimator of the N_H ; in the optical, the H_α/H_β ratio of the narrow compo-

ment (emitted by the NLR) gives the reddening towards the NLR, while the ratio of the broad components gives a raw estimation of the obscuration towards the BLR. Also, using the torus emission models, the column density of the torus can be estimated.

It is known that these methods trace different regions of the central engine, but observational evidence has routinely shown that the X-ray determined column densities are of the order of or larger than the column densities of the torus as measured by $(H_\alpha/H_\beta)_{BLR}$. Based on the fast and strong variability of the X-ray emission (for example, NGC 1365 Risaliti *et al.* (2005)), the X-ray absorber would be localized closer to the AGN than the torus, which means that the column density of the torus could add to the “dust-free” column density of the X-ray absorber. On the other hand, the column density derived from the X-rays traces only the absorption in that particular line of sight, while the column density derived from the torus emission, collected from the entire emitting region, represents the luminosity weighted conditions of the torus. Also, it has been proposed that the obscuration observed in some AGN may be produced by dust in the host galaxy, which would translate into a correlation of the derived column density and the inclination of the galaxy (a more inclined galaxy would introduce more obscuration).

We investigate these issues with our modeling results. In Fig. 6.4 we compare the inclination of the galaxy with the column density determined from the torus emission modeling, the column density derived through X-ray observations, and the reddening of the NLR (directly related to the column density through the gas-to-dust ratio), obtained through the $(H_\alpha/H_\beta)_{NLR}$ ratio of the optical spectra we obtained in our observing runs of 2007 and 2008 (briefly described in Section 3.1.1). We find that the host galaxy is not the responsible of the excess of obscuration observed in type 2 Seyfert galaxies, because no correlation is found between any of these quantities.

We compare the different columns between themselves in Fig. 6.5. In the

upper left panel the column derived from the X-rays is compared to the column obtained from our torus modeling. It is evident that there is no correlation and that the N_H^{XR} are on average not larger than the N_H^{IR} , but quite the opposite (as foreseen by Nenkova *et al.* (2008)). No relation is found between the columns derived from the NLR observations and the N_H^{XR} or the N_H^{IR} columns (upper right and lower panels of Fig. 6.5, respectively) either. Additionally, it is found that the values of N_H^{NLR} are the lowest between the three columns, as expected since the BLR is the most external structure found in AGNs. These plots also confirm the finding of Tran (2003), that the detection or non-detection of broad components in spectropolarimetry is independent of the column density. In Fig. 6.6 we show the observed [OIII] luminosity versus the column densities determined through the torus emission modeling and from X-ray observations. Again, no correlation is found between these quantities, indicating that the more obscured objects in our sample do not lack a BLR and are not preferentially weaker.

6.3 Receding Torus?

Lawrence (1991) was the first in proposing the existence of a “receding torus” as the responsible for the obscuration observed in the central region of AGN. In this case, the torus aperture angle should increase with increasing AGN luminosity. We test this model with Fig. 6.7, where the aperture angle (σ parameter) is plotted against the observed luminosity in [OIII]. It is evident that no correlation exist between this parameter of the torus and the luminosity of the AGN in our sample. Mor *et al.* (2009) modeled the IR emission of 26 luminous quasars using clumpy models, and in the right panel of Fig. 6.7 we compare the distribution of the torus aperture that we find with that found by Mor *et al.* (2009). Remembering that the torus aperture parameter, σ , is defined to be zero at the equator and 90 at the symmetry axis of the torus, we find that the more luminous objects are modeled by larger angle aperture tori than our less luminous Seyferts, suggesting that the receding model could correctly describe the observations. The range in

luminosity and redshift covered by our sample is not large and all our galaxies are classified as Seyfert and are found nearby. That is probably why the relation between luminosity and angle aperture is not seen in the left panel of Fig. 6.7.

6.4 IRAS Colors

As the beam size of the IRAS satellite is large, the nuclear region can not be separated from the galaxy, and its radiation is diluted. We tested how diluted is the nuclear radiation comparing the $12\mu\text{m}/25\mu\text{m}$ color from IRAS observations with the colors found from the fitted torus models. In the upper-left panel of Fig. 6.8 we show this comparison, highlighting the differences found between the best fitted model (red triangles) and the model obtained with the median value of each parameter of the clumpy model (blue starred squares), joined by the black thin lines. We find a general identity between the colors of IRAS and the torus model, indicating that the dilution of the nuclear emission is not strong in all the objects at these wavelengths. A handful of tori are found to have hotter color than that observed in IRAS, and a couple of tori have cooler colors than the IRAS colors. The same comparison of colors is shown in the upper-right panel of Fig. 6.8, but the spectropolarimetric color coding is used in order to show that no particular trend is found between the objects of different classes. We find that the 6 galaxies with the hottest model colors in the upper panels of Fig. 6.8 are brighter than average, as they are located in the upper-left corner of the plot shown in the bottom-left panel of Fig. 6.8. It could be expected that the objects with the lowest color ratio would have the highest extendedness ratio (the IRAS color higher than the torus color means that the galaxy dominates), but as the extendedness ratio is measured only for 15 objects, we can not conclude about a possible correlation between these parameters (Fig. 6.8, bottom right panel).

6.5 Other Properties

6.5.1 Physical Sizes

The internal radius of the torus is set by the sublimation temperature of the dust and the luminosity of the AGN as has been confirmed by the dust reverberation results of Suganuma *et al.* (2006). Although each dust species, and each grain size, has a different sublimation temperature, it can be roughly estimated as $T_{sub} \approx 1500\text{K}$, and the inner radius obtained as (Nenkova *et al.*, 2008):

$$R_{in} = 0.4 \left\{ \frac{L_{bol}^{AGN}}{10^{45} [\text{erg/s}]} \right\}^{1/2} [\text{pc}], \quad (6.1)$$

where L_{bol}^{AGN} is the bolometric luminosity of the AGN. Once the inner radius of the torus is determined, the outer radius can be obtained through the $Y = R_{out}/R_{in}$ parameter of the clumpy models. We find that the inner radius ranges from 0.07 to 2.4 parsecs, with its distribution shown in the left panel of Fig. 6.9. The outer radius ranges from 0.3 to 305 parsecs, and the distribution is shown in the right panel of Fig. 6.9.

6.5.2 Torus Mass

The total mass of the torus can be estimated as (Nenkova *et al.*, 2008):

$$M_{\text{torus}} = m_H N_H^{(1)} \int N_C(r, \beta) dV, \quad (6.2)$$

where m_H is the nuclear mass of hydrogen, $N_H^{(1)}$ corresponds to the column density of one cloud, and $N_C(r, \beta)$ is the number of clouds along a particular path. This equation can be simplified and rewritten as:

$$M_{\text{torus}} = 4\pi m_H \sin(\sigma) N_{H, \text{torus}}^{eq} R_{in}^2 Y I_q(Y), \quad (6.3)$$

where $N_{H, \text{torus}}^{eq}$ is the equatorial column density of the torus, R_{in} is calculated as in Eqn. 6.1, σ and Y are parameters of the model, and I_q is 1 if $q = 2$ or 3, $Y/2 \ln Y$ if $q=1$, or $Y/3$ if $q = 0$. We find rather high torus masses, ranging from

~ 100 to $10^9 M_\odot$, as shown in Fig. 6.11. Siebenmorgen *et al.* (2005) reported the dust masses implied by a simple model of the dust emission in 2 quasars, being of the order of $10^{6-7} M_\odot$. Fritz *et al.* (2006) reported on the masses implied by the smooth modeling of the emission of type 1 and type 2 Seyferts, ranging from $\sim 70 - 10^7 M_\odot$.

6.6 Concluding Remarks and Future Work

In this thesis we have presented the nuclear $\sim 1-20\mu\text{m}$ spectral energy distribution (SED) for a large sample of nearby Seyfert 2 galaxies selected from the $12\mu\text{m}$ sample. From the results of clumpy torus models, we have found that neither the column density, the size of the torus, nor the torus aperture angle are related to the luminosity of the objects in our sample. This is possibly due to the rather narrow range in intrinsic luminosities of our sources. However the aperture angle seems to be larger for quasars, as found in the literature. The column densities derived through different methods are not correlated, in particular the column densities derived from the torus emission modeling are in average larger than the X-ray determined column densities, in strike contrast with previous results. The AGN dominates the emission in the mid-infrared wavelengths in the galaxies of our sample, as shown by the $12\mu\text{m}/25\mu\text{m}$ colors.

Observing in the infrared (IR) is a challenging task, but it allows to investigate the central, dusty regions of active galactic nuclei (AGN). The deconvolution of the nuclear emission from the contaminating stellar radiation is an affordable and effective way of obtaining a statistically large number of nuclear SEDs of AGNs. The clumpy models are clearly more successful than smooth models in describing the IR emission coming from the dusty torus surrounding the central engine of AGN, producing a wide range of emission and adequately strong features.

The recent development of near-IR interferometry allows to resolve the central engine of the nearest AGN. Other facilities being built at this very moment will

allow us to resolve the central regions of a larger number of AGN and probe the dynamics of these sources. Meanwhile, our SED library is by far the most carefully constructed and most comprehensive set of spectral energy distributions of type 2 Seyfert galaxies. Most likely this data set will be extensively used to test the new generation of 3-D hydrodynamical clumpy torus models, and more generally it represents a large and homogeneous set of high quality infrared imaging.

Table 6.1: IRAS fluxes and luminosities of the galaxies modeled by the clumpy torus emission model.

Galaxy	Flux (12 μ m)	Flux (25 μ m)	Flux (60 μ m)	Flux (100 μ m)	L $_{\nu}$ (12 μ m)	L $_{\nu}$ (25 μ m)	L $_{\nu}$ (60 μ m)	L $_{\nu}$ (100 μ m)
	Jy	Jy	Jy	Jy	L $_{\odot}$	L $_{\odot}$	L $_{\odot}$	L $_{\odot}$
(1)	(2)	(3)	(4)	(5)	(6)	(7)	(8)	(9)
NGC 34	0.40	2.51	16.84	17.61	1.69e+16	1.06e+17	7.13e+17	7.46e+17
IRAS 00198-7926 N	0.35	1.37	3.35	3.01	1.90e+17	7.43e+17	1.82e+18	1.63e+18
IRAS 00198-7926 S	0.35	1.37	3.35	3.01	1.90e+17	7.43e+17	1.82e+18	1.63e+18
IRAS 00521-7054	0.24	0.90	0.92	0.40	1.17e+17	4.39e+17	4.49e+17	1.95e+17
ESO 541-IG012	0.26	0.37	0.95	1.24	8.61e+16	1.22e+17	3.15e+17	4.11e+17
IRAS 01475-0740	0.32	0.84	1.10	1.05	1.09e+16	2.85e+16	3.73e+16	3.56e+16
NGC 1068	40.58	92.74	198.02	259.77	6.43e+16	1.47e+17	3.14e+17	4.12e+17
NGC 1144	0.26	0.62	5.35	11.60	2.31e+16	5.50e+16	4.75e+17	1.03e+18
NGC 1194	0.28	0.85	0.92	0.71	5.63e+15	1.71e+16	1.85e+16	1.43e+16
NGC 1320	0.31	1.32	2.21	2.82	2.99e+15	1.27e+16	2.13e+16	2.72e+16
IRAS 04385-0828	0.59	1.70	2.91	3.55	1.46e+16	4.21e+16	7.20e+16	8.79e+16
ESO 33-G2	0.24	0.47	0.82	1.84	8.98e+15	1.76e+16	3.07e+16	6.88e+16
IRAS 05189-2524	0.71	3.41	13.27	11.90	1.36e+17	6.53e+17	2.54e+18	2.28e+18
NGC 4388	1.03	3.72	10.46	18.10	7.94e+15	2.87e+16	8.07e+16	1.40e+17
NGC 4501	2.29	3.02	19.93	63.64	1.45e+16	1.91e+16	1.26e+17	4.02e+17
TOL 1238-364	0.66	2.63	9.08	14.03	8.55e+15	3.41e+16	1.18e+17	1.82e+17
NGC 4941	0.39	0.46	1.87	4.79	5.86e+14	6.92e+14	2.81e+15	7.20e+15
NGC 4968	0.62	1.16	2.48	3.39	6.58e+15	1.23e+16	2.63e+16	3.60e+16
MCG -3-34-64	0.95	2.88	6.22	6.37	2.80e+16	8.50e+16	1.84e+17	1.88e+17
NGC 5135	0.58	2.39	16.60	31.18	1.18e+16	4.88e+16	3.39e+17	6.36e+17
NGC 5506	1.25	4.24	8.44	9.24	5.26e+15	1.78e+16	3.55e+16	3.89e+16
NGC 5953	0.82	1.67	11.85	20.47	3.86e+15	7.85e+15	5.57e+16	9.63e+16
MCG -2-40-4	0.41	1.45	4.09	7.06	2.80e+16	9.89e+16	2.79e+17	4.82e+17

Continued on Next Page...

Table 6.1 – Continued

(1)	(2)	(3)	(4)	(5)	(6)	(7)	(8)	(9)
IRAS 15480-0344	0.24	0.72	1.09	4.05	2.31e+16	6.93e+16	1.05e+17	3.90e+17
NGC 6810	1.33	3.61	18.90	33.30	6.69e+15	1.82e+16	9.51e+16	1.68e+17
NGC 6890	0.36	0.80	4.01	8.26	2.58e+15	5.74e+15	2.88e+16	5.92e+16
IC 5063	1.15	3.95	5.79	3.66	1.63e+16	5.59e+16	8.20e+16	5.18e+16
MRK 897	0.37	0.86	2.97	5.59	2.77e+16	6.43e+16	2.22e+17	4.18e+17
NGC 7130	0.64	2.15	16.85	26.96	1.82e+16	6.12e+16	4.79e+17	7.67e+17
MCG -3-58-7	0.25	0.98	2.60	3.62	2.68e+16	1.05e+17	2.79e+17	3.88e+17
NGC 7496	0.62	2.00	10.21	16.59	1.70e+15	5.48e+15	2.80e+16	4.55e+16
NGC 7582	2.31	7.48	52.47	83.27	7.11e+15	2.30e+16	1.61e+17	2.56e+17
NGC 7590	0.69	0.94	7.81	21.05	2.12e+15	2.89e+15	2.40e+16	6.48e+16
NGC 7674	0.64	1.79	5.64	8.46	5.72e+16	1.60e+17	5.04e+17	7.56e+17
CGC 381-051	0.51	0.18	1.75	2.76	5.13e+16	1.81e+16	1.76e+17	2.77e+17
MCG +0-29-23	0.48	0.68	5.93	9.48	3.17e+16	4.50e+16	3.92e+17	6.27e+17

Table 6.2: Literature data compiled for the torus emission modeled galaxies.

Galaxy	PBL	Classification	$\log(L_{[OIII]})$ ergs/seg	$\log(N_H)$ cm^{-2}	AGN %	SB %	Error %	\mathcal{R}	Inclination	H_α/H_β
(1)	(2)*	(3) [‡]	(4)*	(5)*	(6) [†]	(7) [†]	(8) [†]	(9) [†]	(10)	(11) [§]
NGC 34	N	Sy2-HII	42.83	>24	52.9	47.1	±12.6	1.19	0.1377	15.3
IRAS 00198-7926 N	N	Sy2	42.67	>24	96.8	3.2	±0.8	...	0.3102	...
IRAS 00198-7926 S	N	Sy2	42.67	>24	96.8	3.2	±0.8	...	0.3102	...
IRAS 00521-7054	Y	Sy2	42.62	0.216	8.89
ESO 541-IG012	Y	Sy2	95.9	4.1	±1.9	...	0.2934	6.40
IRAS 01475-0740	Y	Sy2	41.76	21.59	93.8	6.2	±2.9	1.1	0.1692	7.47
NGC 1068	Y	Sy2	42.33	>25	0.07	7.0
NGC 1144	N	Sy2	41.87	20.699	0.0785	...
NGC 1194	non	Sy2	1.27	0.4642	6.89
NGC 1320	N	Sy2	41.05	...	95.4	4.6	±1.4	1.06	0.6851	3.77
IRAS 04385-0828	Y	Sy2	40.64	...	95.8	4.2	±2.3	1.11	0.5362	3.98
ESO 33-G2	N	Sy2	42.39	22.021	96.8	3.2	±1.9	...	0.344	5.15
IRAS 05189-2524	Y	Sy2	42.74	22.756	0.0571	...
NGC 4388	Y	Sy2-SB	41.85	23.43	91	9	±3.1	1.18	0.64	4.08
NGC 4501	N	Sy2	39.89	<21	70.2	29.8	±7.6	...	0.474	3.71
TOL 1238-364	Y	Sy2	41.89	>24	84.4	15.6	±3.7	...	0.1248	4.07
NGC 4941	N	Sy2	41.14	23.653	1.18	0.5017	4.68
NGC 4968	N	Sy2	42.38	20.92	90.1	9.9	±2	...	0.34	4.38
MCG -3-34-64	Y	Sy1.8	42.39	23.614	0.2533	4.17
NGC 5135	N	Sy2-HII	42.44	>24	0.01	5.83
NGC 5506	Y	Sy1.9	41.45	22.46	0.52	4.44
NGC 5953	non	LINER-Sy2	0.3674	4.21
MCG -2-40-4	Y	Sy2-HII	42.98	21.934	94.6	5.4	±0.8	1.2	0.1889	...
IRAS 15480-0344	Y	Sy2	43.02	>24	94.5	5.5	±0.5	1.09	0.112	4.64

Continued on Next Page...

Table 6.2 – Continued

(1)	(2)*	(3) [‡]	(4)*	(5)*	(6) [†]	(7) [†]	(8) [†]	(9) [†]	(10)	(11) [§]
NGC 6810	non	Sy2-HII	80.5	19.5	±8.8	1.26	0.4978	7.87
NGC 6890	N	Sy2	40.86	...	89.5	10.5	±1.3	...	0.1506	5.09
IC 5063	Y	Sy2	41.56	23.342	1.06	0.203	5.8
MRK 897	non	Sy2	53.8	46.2	±16.1	...	0.2127	4.34
NGC 7130	N	LINER	42.55	>24	77.2	22.8	±9.8	1.34	0.01	8.45
MCG -3-58-7	Y	Sy2	41.93	...	95.7	4.3	±1.7	1.04	0.1328	4.80
NGC 7496	N	Sy2-HII	40.22	22.699	81.2	18.8	±9.3	...	0.1096	5.23
NGC 7582	N	Sy2	41.36	23.95	68.8	31.2	±11.3	1.40	0.69	7.6
NGC 7590	N	Sy2-HII	40.02	<21	75.6	24.4	±10.3	...	0.6433	6.12
NGC 7674	Y	Sy1-HII	42.57	>24	0.04	4.8
CGCG 381-051	non	Sy2-HII	87.5	12.5	±14	1.02	0.0993	...
MCG +0-29-23	non	HII	0.07	8.61

*Data from Shu *et al.* (2007) and NED database. “non” in column (2) means the object has not been observed in spectropolarimetry.

[†]Data from Tommasin *et al.* (2009).

[‡]Data from unpublished data obtained by us, Tran (2003) and NED.

[§]Unpublished data obtained by us.

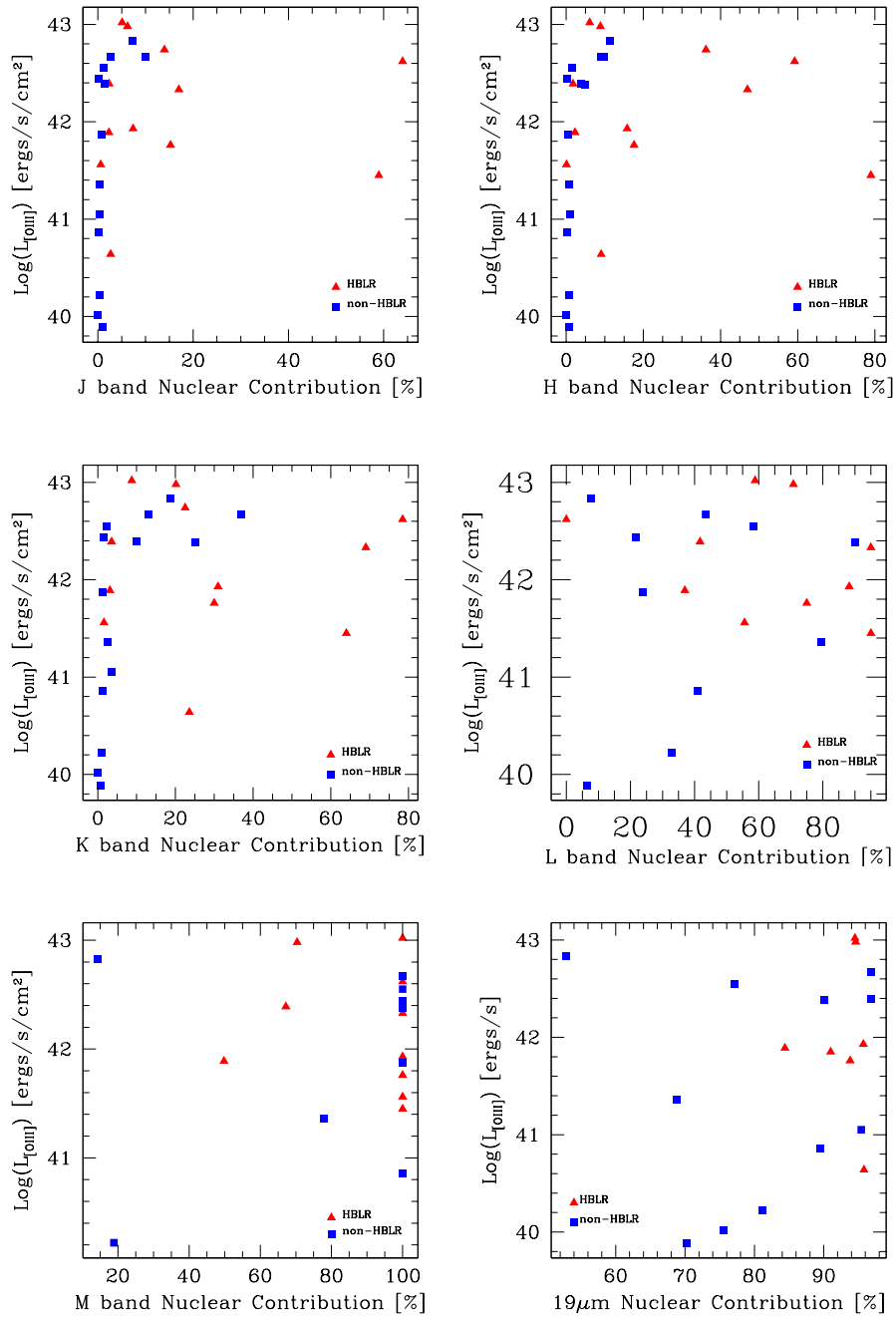


Figure 6.1: Intrinsic [OIII] line luminosities and nuclear contribution in different IR bands. JHKLM bands are determined from our surface brightness profile fitting process. The contribution at 19 μ m comes from Tommasin *et al.* (2009). The spectropolarimetric observations are included through color coding: red triangles represent HBLR objects, blue squares represent non-HBLR objects, and green pentagons represent objects that lack spectropolarimetric observation.

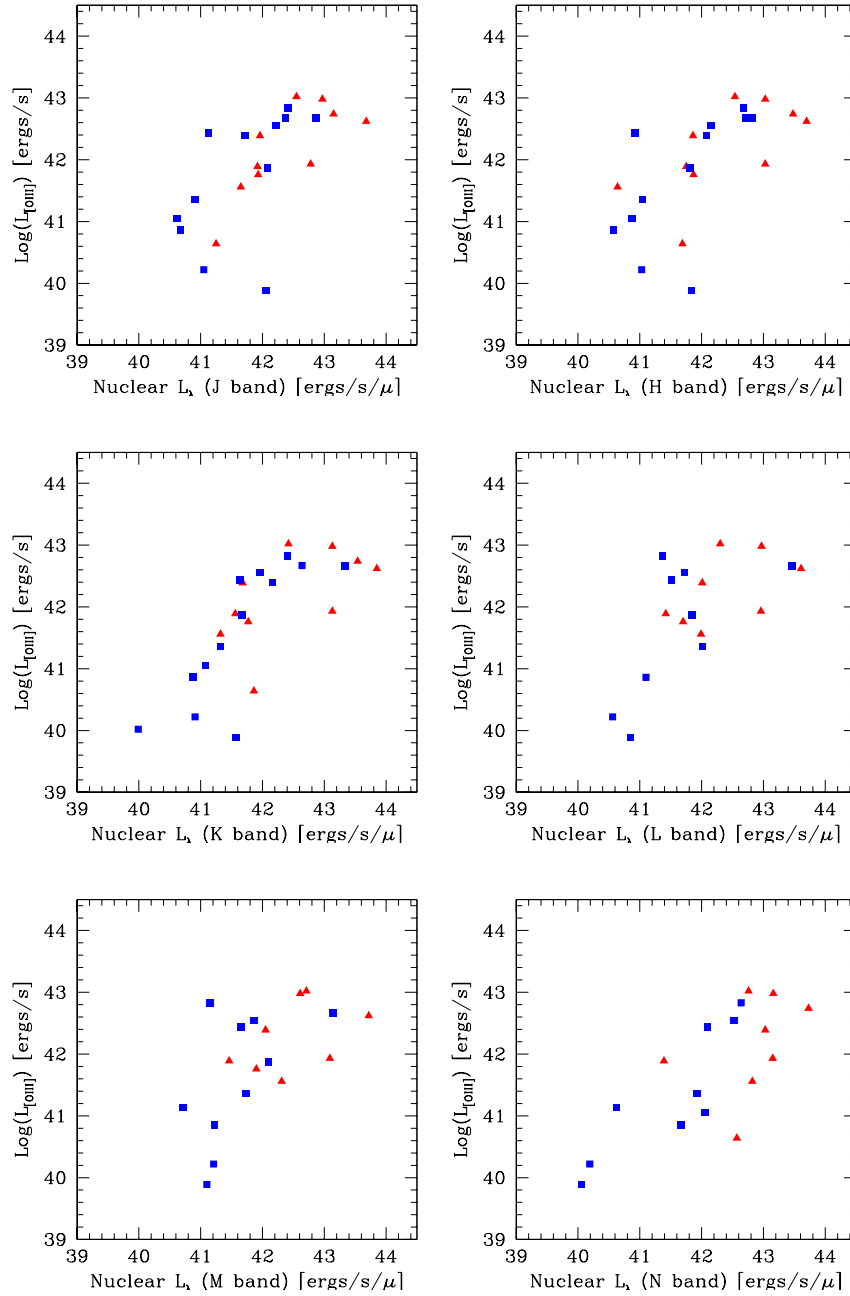


Figure 6.2: Intrinsic [OIII] line luminosities and nuclear contribution in different IR bands. JHKLM bands are determined from our surface brightness profile fitting process. The contribution at $19\mu\text{m}$ comes from Tommasin *et al.* (2009). The spectropolarimetric observations are included through color coding: red triangles represent HBLR objects, blue squares represent non-HBLR objects, and green pentagons represent objects that lack spectropolarimetric observation.

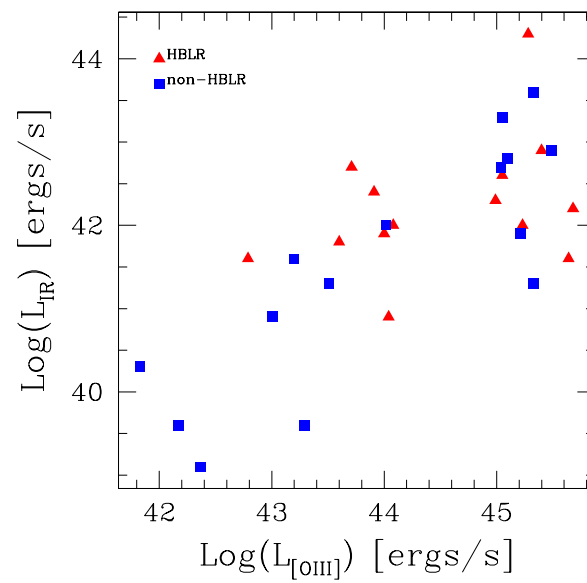


Figure 6.3: Comparison of the AGN bolometric luminosity determined from the observed, extinction corrected [OIII] fluxes and from the torus emission modeling.

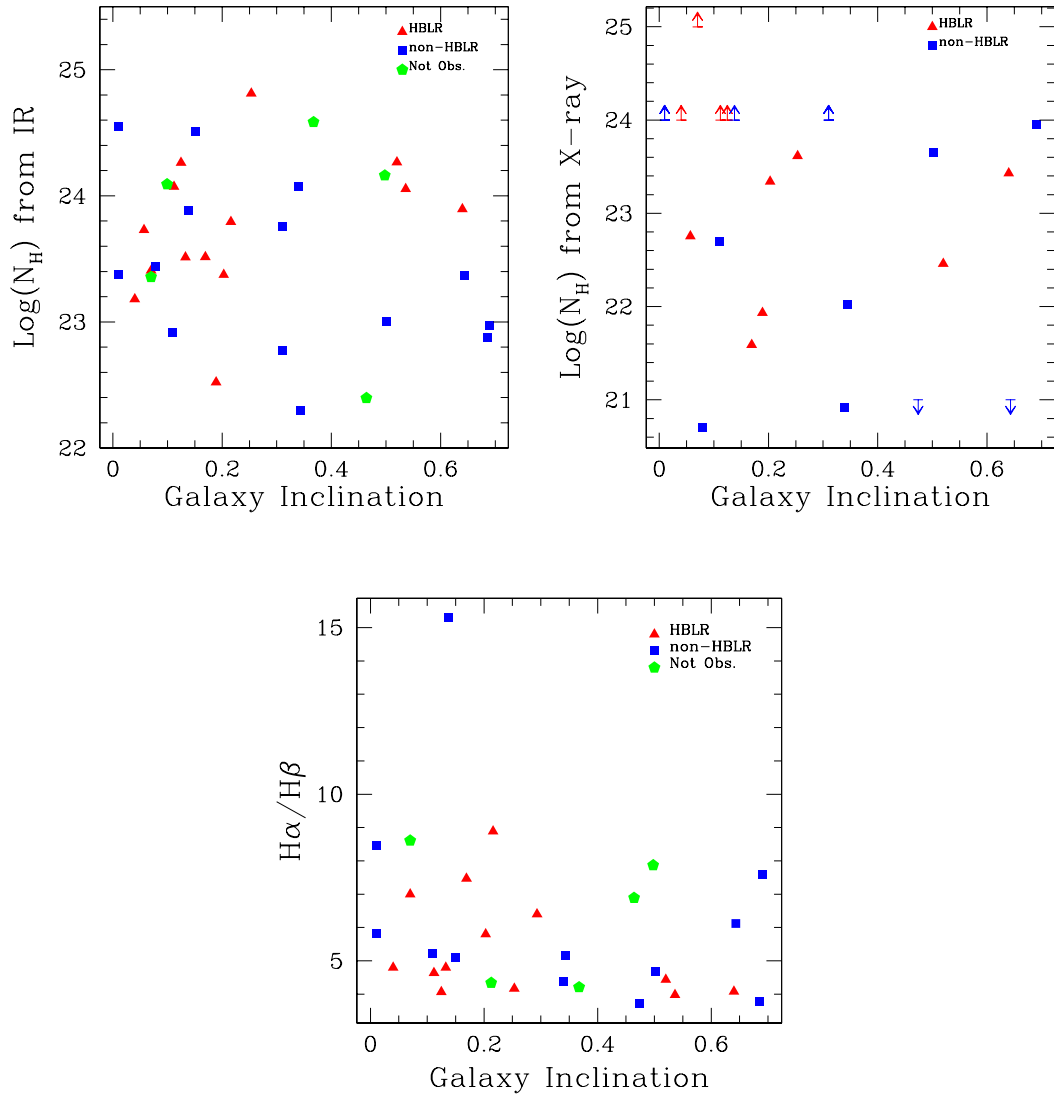


Figure 6.4: Column densities derived from the torus emission modeling (upper left) and from X-ray observations (upper right) versus the galaxy inclination. In the lower panel, the inclination is compared with the extinction obtained from NLR observations. All these plots show that the high extinction found in these galaxies is not produced by the galaxy.

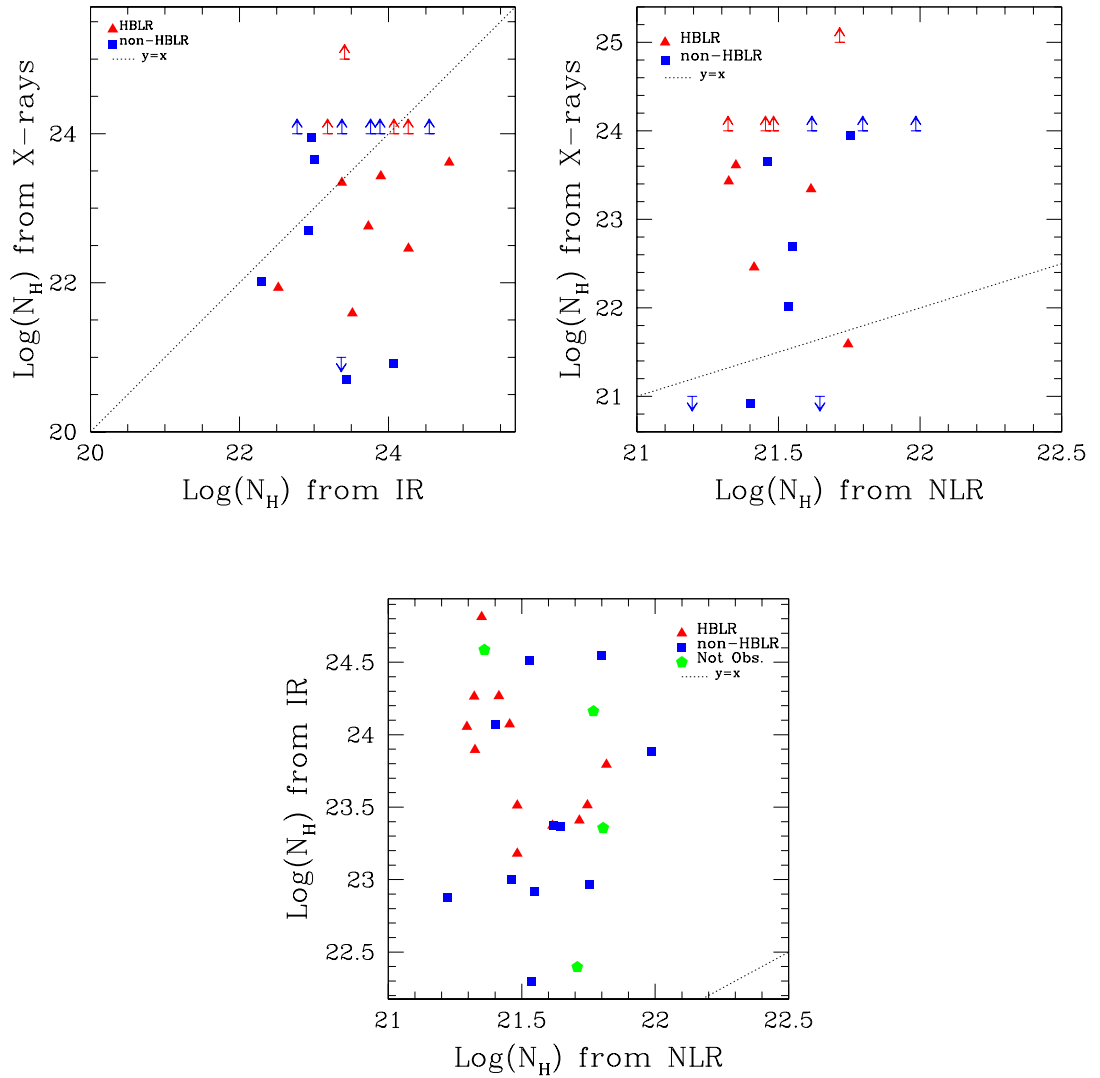


Figure 6.5: Comparison of column densities (N_H) determined through 3 different methods. In the upper panels the column densities obtained from X-ray observations are compared to those obtained from the modeling of the torus emission (left), and to those obtained from the reddened flux of the NLR. Upper limits in the columns derived in the X-rays correspond to optically thick sources. The columns determined through the flux coming from the NLR compared with those obtained from the modeling are shown in the bottom panel.

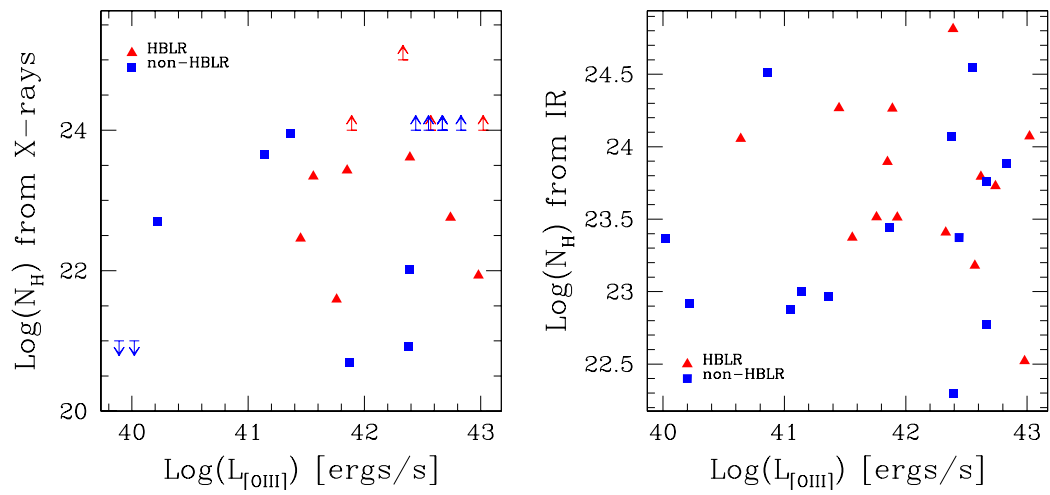


Figure 6.6: Intrinsic luminosity of the AGN compared to the column density determined from X-ray observations and from the torus emission modeling.

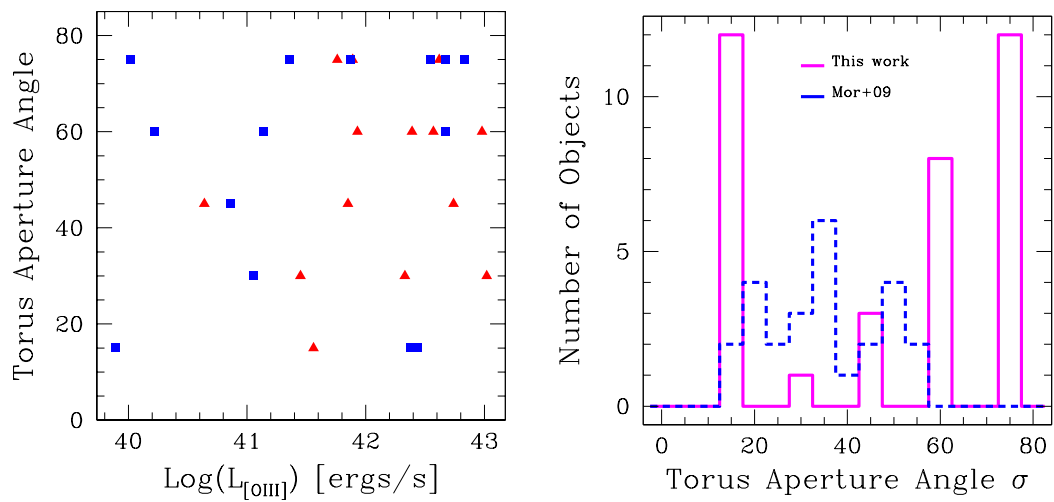


Figure 6.7: Testing a receding torus model. Comparison of the torus aperture angle with the luminosity of the AGN in the left panel. The spectropolarimetric observations are included through the color coding used in all previous figures: red triangles representing HBLR objects, and blue squares representing non-HBLR objects. In the right panel, the distribution of the torus apertures found in high luminosity quasars (from Mor *et al.* (2009)) is shown with a blue dashed line, together with the distribution for less luminous Seyfert galaxies shown with a magenta solid line.

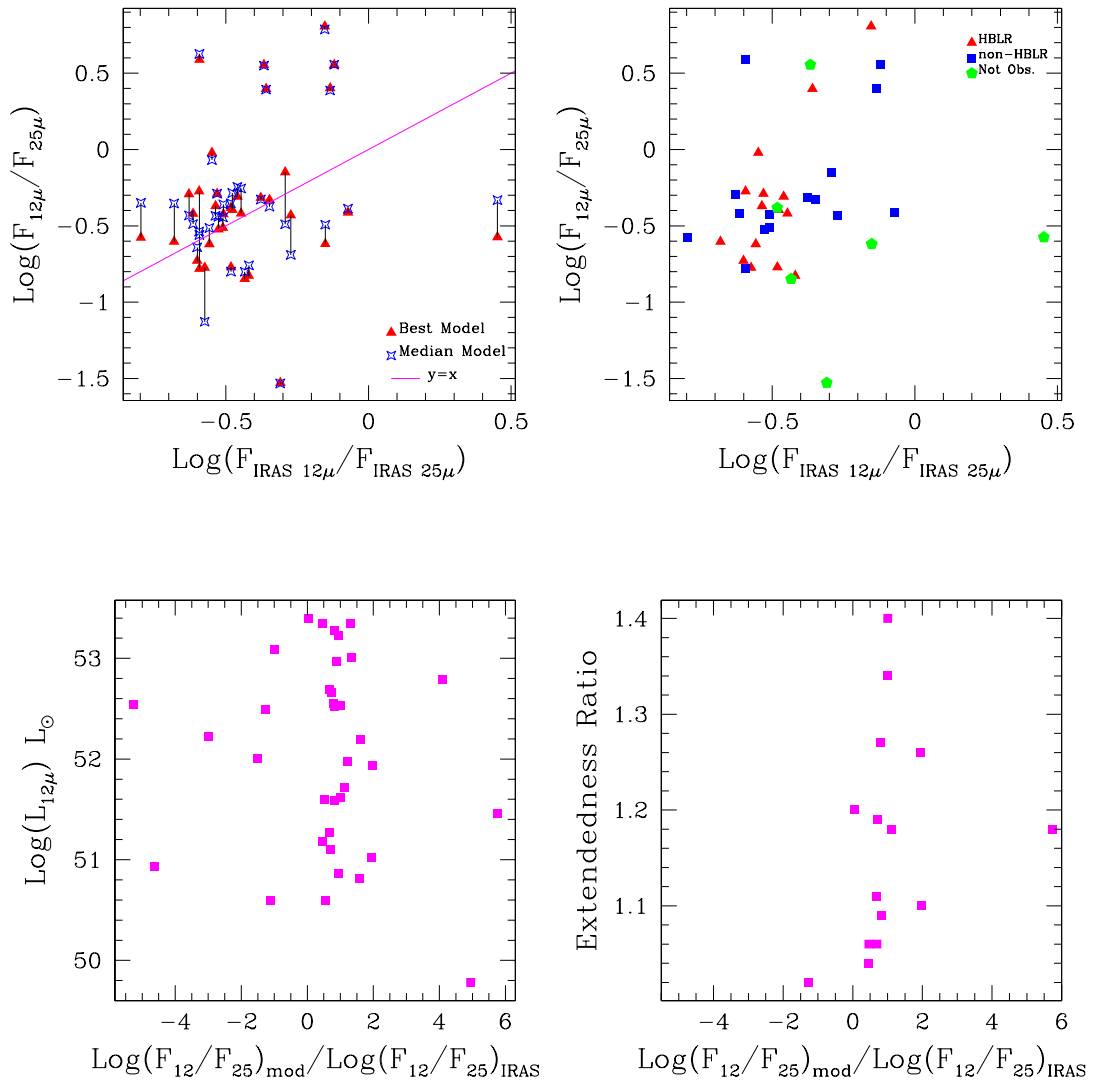


Figure 6.8: Comparison between the IRAS and torus emission modeling $12\mu\text{m}/25\mu\text{m}$ colors. Upper left panel: the red triangles represent the colors obtained from the best model of the observed SED. The blue starred squares represent values obtained from models with the median value of each parameter. The black line joining the points allows to visualize the impact of choosing one or another model as the best representation of the torus emission. The magenta line shows the case $y=x$. Upper right panel: the same plot as in the left, but the spectropolarimetric observations code is used. The ratio of the model $12\mu\text{m}/25\mu\text{m}$ color to the IRAS $12\mu\text{m}/25\mu\text{m}$ color is compared to the luminosity at $12\mu\text{m}$ in the lower left panel. In the lower right panel, the extendedness ratio is compared with the color ratio.

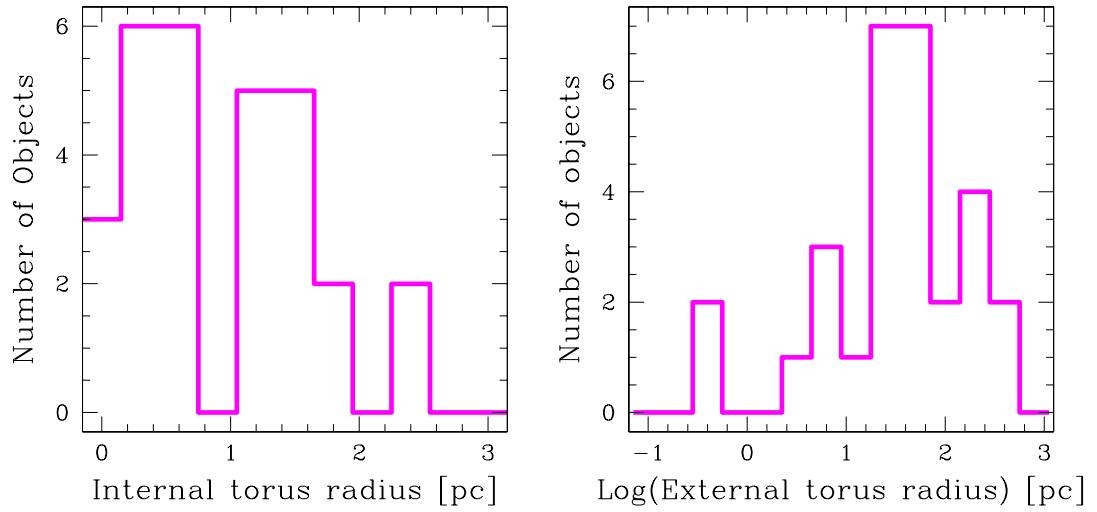
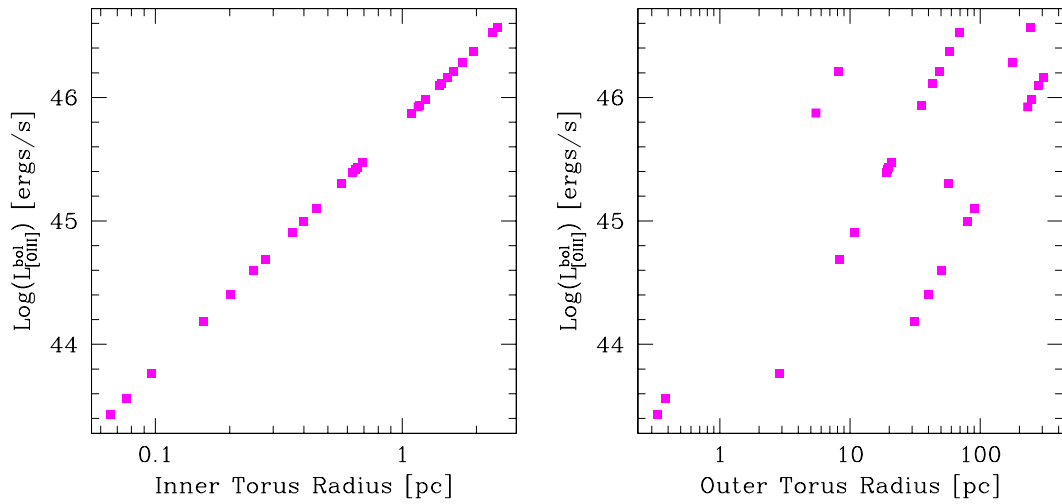


Figure 6.9: Distribution of the physical Torus Radii found through the modeling.

Figure 6.10: Comparison between the bolometric luminosity determined from L_{OIII} and the physical inner and outer torus radii. The inner radius is a function of the luminosity (Eqn. 6.1), and the outer radius is determined through the Y parameter and the inner radius.

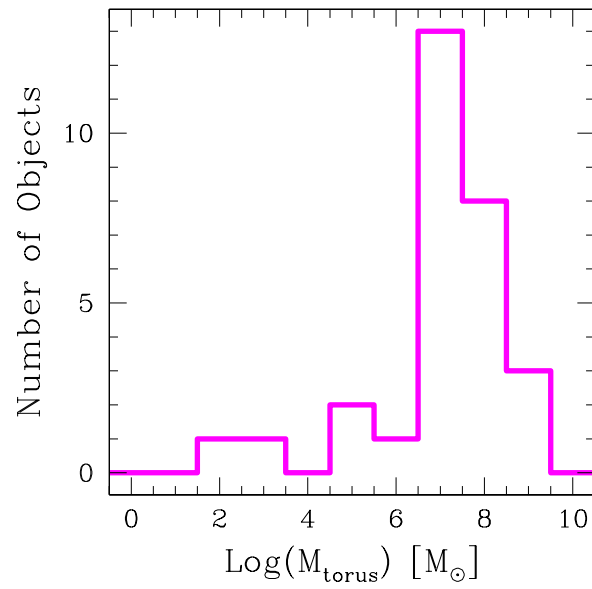


Figure 6.11: Distribution of the torus masses found through the modeling of its emission.

Bibliography

- Alonso-Herrero, A., A. C. Quillen, G. H. Rieke, V. D. Ivanov, and A. Efstathiou 2003. Spectral Energy Distributions of Seyfert Nuclei. *Astron. J.* **126**, 81–100.
- Alonso-Herrero, A., A. C. Quillen, C. Simpson, A. Efstathiou, and M. J. Ward 2001. The Nonstellar Infrared Continuum of Seyfert Galaxies. *Astron. J.* **121**, 1369–1384.
- Alonso-Herrero, A., M. J. Ward, and J. K. Kotilainen 1996. The near-infrared continuum of Seyfert 2s - deconvolution into the stellar and non-stellar components. *MNRAS* **278**, 902–918.
- Antonucci, R. R. J., and J. S. Miller 1985. Spectropolarimetry and the nature of NGC 1068. *Ap. J.* **297**, 621–632.
- Balcells, M., A. W. Graham, L. Domínguez-Palmero, and R. F. Peletier 2003. Galactic Bulges from Hubble Space Telescope Near-Infrared Camera Multi-Object Spectrometer Observations: The Lack of $r_{1/4}$ Bulges. *Ap. J. Lett.* **582**, L79–L82.
- Barmby, P., M. L. N. Ashby, L. Bianchi, C. W. Engelbracht, R. D. Gehrz, K. D. Gordon, J. L. Hinz, J. P. Huchra, R. M. Humphreys, M. A. Pahre, P. G. Pérez-González, E. F. Polomski, G. H. Rieke, D. A. Thilker, S. P. Willner, and C. E. Woodward 2006. Dusty Waves on a Starry Sea: The Mid-Infrared View of M31. *Ap. J. Lett.* **650**, L45–L49.

- Bianchi, S., M. Chiaberge, E. Piconcelli, and M. Guainazzi 2007. A multiwavelength map of the nuclear region of NGC 7582. *MNRAS* **374**, 697–702.
- Buchanan, C. L., J. F. Gallimore, C. P. O’Dea, S. A. Baum, D. J. Axon, A. Robinson, M. Elitzur, and M. Elvis 2006. Spitzer IRS Spectra of a Large Sample of Seyfert Galaxies: A Variety of Infrared Spectral Energy Distributions in the Local Active Galactic Nucleus Population. *Astron. J.* **132**, 401–419.
- Cohen, M., R. G. Walker, B. Carter, P. Hammersley, M. Kidger, and K. Noguchi 1999. Spectral Irradiance Calibration in the Infrared. X. A Self-Consistent Radiometric All-Sky Network of Absolutely Calibrated Stellar Spectra. *Astron. J.* **117**, 1864–1889.
- Dopita, M. A., and R. S. Sutherland 1995. Spectral Signatures of Fast Shocks. II. Optical Diagnostic Diagrams. *Ap. J.* **455**, 468–+.
- Draine, B. T. 2003. Interstellar Dust Grains. *ARA&A* **41**, 241–289.
- Draine, B. T., and H. M. Lee 1984. Optical properties of interstellar graphite and silicate grains. *Ap. J.* **285**, 89–108.
- Dullemond, C. P., and I. M. van Bemmelen 2005. Clumpy tori around active galactic nuclei. *Astron. & Astrophys.* **436**, 47–56.
- Dultzin-Hacyan, D., Y. Krongold, I. Fuentes-Guridi, and P. Marziani 1999. The Close Environment of Seyfert Galaxies and Its Implication for Unification Models. *Ap. J. Lett.* **513**, L111–L114.
- Efstathiou, A., and M. Rowan-Robinson 1995. Dusty discs in active galactic nuclei. *MNRAS* **273**, 649–661.
- Elvis, M., B. J. Wilkes, J. C. McDowell, R. F. Green, J. Bechtold, S. P. Willner, M. S. Oey, E. Polomski, and R. Cutri 1994. Atlas of quasar energy distributions. *Ap. J. Suppl.* **95**, 1–68.

- Falcke, H., A. S. Wilson, and C. Simpson 1998. HST and VLA Observations of Seyfert 2 Galaxies: The Relationship between Radio Ejecta and the Narrow-Line Region. *Ap. J.* **502**, 199–+.
- Ferland, G. J., and H. Netzer 1983. Are there any shock-heated galaxies. *Ap. J.* **264**, 105–113.
- Freeman, K. C. 1966. Structure and Evolution of Barred Spiral Galaxies, I. *MNRAS* **133**, 47–62.
- Fritz, J., A. Franceschini, and E. Hatziminaoglou 2006. Revisiting the infrared spectra of active galactic nuclei with a new torus emission model. *MNRAS* **366**, 767–786.
- Gorjian, V., M. W. Werner, T. H. Jarrett, D. M. Cole, and M. E. Ressler 2004. 10 Micron Imaging of Seyfert Galaxies from the 12 Micron Sample. *Ap. J.* **605**, 156–167.
- Graham, A. W. 2001. An Investigation into the Prominence of Spiral Galaxy Bulges. *Astron. J.* **121**, 820–840.
- Graham, A. W., and S. P. Driver 2005. A Concise Reference to (Projected) Sérsic $R_{1/n}$ Quantities, Including Concentration, Profile Slopes, Petrosian Indices, and Kron Magnitudes. *Publications of the Astronomical Society of Australia* **22**, 118–127.
- Granato, G. L., and L. Danese 1994. Thick Tori around Active Galactic Nuclei - a Comparison of Model Predictions with Observations of the Infrared Continuum and Silicate Features. *MNRAS* **268**, 235–+.
- Greenhill, L. J., R. S. Booth, S. P. Ellingsen, J. R. Herrnstein, D. L. Jauncey, P. M. McCulloch, J. M. Moran, R. P. Norris, J. E. Reynolds, and A. K. Tzioumis 2003. A Warped Accretion Disk and Wide-Angle Outflow in the Inner Parsec of the Circinus Galaxy. *Ap. J.* **590**, 162–173.

- Grosbøl, P., P. A. Patsis, and E. Pompei 2004. Spiral galaxies observed in the near-infrared K band. I. Data analysis and structural parameters. *Astron. & Astrophys.* **423**, 849–859.
- Heckman, T. M., G. Kauffmann, J. Brinchmann, S. Charlot, C. Tremonti, and S. D. M. White 2004. Present-Day Growth of Black Holes and Bulges: The Sloan Digital Sky Survey Perspective. *Ap. J.* **613**, 109–118.
- Herrnstein, J. R., J. M. Moran, L. J. Greenhill, P. J. Diamond, M. Miyoshi, N. Nakai, and M. Inoue 1997. Discovery of a Subparsec Jet 4000 Schwarzschild Radii Away from the Central Engine of NGC 4258. *Ap. J. Lett.* **475**, L17+.
- Hewitt, A., and G. Burbidge 1991. An optical catalog of extragalactic emission-line objects similar to quasi-stellar objects. *Ap. J. Suppl.* **75**, 297–356.
- Huchra, J., and R. Burg 1992. The spatial distribution of active galactic nuclei. I - The density of Seyfert galaxies and liners. *Ap. J.* **393**, 90–97.
- Hunt, L. K., D. Pierini, and C. Giovanardi 2004. Near-infrared observations of galaxies in Pisces-Perseus. V. On the origin of bulges. *Astron. & Astrophys.* **414**, 905–918.
- Jaffe, W., K. Meisenheimer, H. Röttgering, C. Leinert, and A. Richichi 2004. MIDI observations of the nuclear obscuring torus in NGC 1068. In T. Storchi-Bergmann, L. C. Ho, & H. R. Schmitt (Ed.), *The Interplay Among Black Holes, Stars and ISM in Galactic Nuclei*, Volume 222 of *IAU Symposium*, pp. 37–39.
- Joyce, R. R. 1992. Observing With Infrared Arrays. In S. B. Howell (Ed.), *Astronomical CCD Observing and Reduction Techniques*, Volume 23 of *Astronomical Society of the Pacific Conference Series*, pp. 258–+.
- Khachikian, E. Y., and D. W. Weedman 1974. An atlas of Seyfert galaxies. *Ap. J.* **192**, 581–589.

- Kormendy, J., and R. C. Kennicutt, Jr. 2004. Secular Evolution and the Formation of Pseudobulges in Disk Galaxies. *ARA&A* **42**, 603–683.
- Koski, A. T. 1978. Spectrophotometry of Seyfert 2 galaxies and narrow-line radio galaxies. *Ap. J.* **223**, 56–73.
- Kotilainen, J. K., M. J. Ward, C. Boisson, D. L. Depoy, M. G. Smith, and L. R. Bryant 1992. Near-infrared imaging of hard X-ray selected active galaxies. I - Decomposition into nuclear and stellar components. *MNRAS* **256**, 125–148.
- Lamastra, A., S. Bianchi, G. Matt, G. C. Perola, X. Barcons, and F. J. Carrera 2009. The bolometric luminosity of type 2 AGN from extinction-corrected [OIII]. No evidence of Eddington-limited sources. *Astron. & Astrophys.* **504**, 73–79.
- Laor, A., and B. T. Draine 1993. Spectroscopic constraints on the properties of dust in active galactic nuclei. *Ap. J.* **402**, 441–468.
- Laurikainen, E., H. Salo, and R. Buta 2005. Multicomponent decompositions for a sample of S0 galaxies. *MNRAS* **362**, 1319–1347.
- Laurikainen, E., H. Salo, R. Buta, and S. Vasylyev 2004. Bar-induced perturbation strengths of the galaxies in the Ohio State University Bright Galaxy Survey - I. *MNRAS* **355**, 1251–1271.
- Lawrence, A. 1991. The relative frequency of broad-lined and narrow-lined active galactic nuclei - Implications for unified schemes. *MNRAS* **252**, 586–592.
- Lumsden, S. L., and D. M. Alexander 2001. The infrared luminosity of the torus and the visibility of scattered broad line emission in Seyfert 2 galaxies. *MNRAS* **328**, L32–L36.
- Lumsden, S. L., C. A. Heisler, J. A. Bailey, J. H. Hough, and S. Young 2001. Spectropolarimetry of a complete infrared-selected sample of Seyfert 2 galaxies. *MNRAS* **327**, 459–474.

- Lutz, D., R. Maiolino, A. F. M. Moorwood, H. Netzer, S. J. Wagner, E. Sturm, and R. Genzel 2002. Infrared spectroscopy around 4 μ m of Seyfert 2 galaxies: Obscured broad line regions and coronal lines. *Astron. & Astrophys.* **396**, 439–448.
- MacArthur, L. A., S. Courteau, and J. A. Holtzman 2003. Structure of Disk-dominated Galaxies. I. Bulge/Disk Parameters, Simulations, and Secular Evolution. *Ap. J.* **582**, 689–722.
- Maiolino, R. 2001. Obscured active galactic nuclei. *X-ray Astronomy: Stellar Endpoints, AGN, and the Diffuse X-ray Background* **599**, 199–208.
- Maiolino, R., and G. H. Rieke 1995. Low-Luminosity and Obscured Seyfert Nuclei in Nearby Galaxies. *Ap. J.* **454**, 95–+.
- Malkan, M. A., V. Gorjian, and R. Tam 1998. A Hubble Space Telescope Imaging Survey of Nearby Active Galactic Nuclei. *Ap. J. Suppl.* **117**, 25–+.
- Mas-Hesse, J. M., P. M. Rodriguez-Pascual, L. S. F. de Cordoba, and I. F. Mirabel 1994. Multiwavelength analysis of quasars, Seyfert galaxies, and starbursts. *Ap. J. Suppl.* **92**, 599–602.
- Mathis, J. S., W. Rumpl, and K. H. Nordsieck 1977. The size distribution of interstellar grains. *Ap. J.* **217**, 425–433.
- Matthews, T. A., and A. R. Sandage 1963. Optical Identification of 3c 48, 3c 196, and 3c 286 with Stellar Objects. *Ap. J.* **138**, 30–+.
- Miller, J. S., and R. W. Goodrich 1990. Spectropolarimetry of high-polarization Seyfert 2 galaxies and unified Seyfert theories. *Ap. J.* **355**, 456–467.
- Mor, R., H. Netzer, and M. Elitzur 2009. Dusty Structure Around Type-I Active Galactic Nuclei: Clumpy Torus Narrow-line Region and Near-nucleus Hot Dust. *Ap. J.* **705**, 298–313.

- Morris, S., M. Ward, M. Whittle, A. S. Wilson, and K. Taylor 1985. The velocity fields and radio structures of the active galaxies NGC 5643 and NGC 7582. *MNRAS* **216**, 193–217.
- Nenkova, M., Ž. Ivezić, and M. Elitzur 2002. Dust Emission from Active Galactic Nuclei. *Ap. J. Lett.* **570**, L9–L12.
- Nenkova, M., M. M. Sirocky, Ž. Ivezić, and M. Elitzur 2008. AGN Dusty Tori. I. Handling of Clumpy Media. *Ap. J.* **685**, 147–159.
- Nenkova, M., M. M. Sirocky, R. Nikutta, Ž. Ivezić, and M. Elitzur 2008. AGN Dusty Tori. II. Observational Implications of Clumpiness. *Ap. J.* **685**, 160–180.
- Ossenkopf, V., T. Henning, and J. S. Mathis 1992. Constraints on cosmic silicates. *Astron. & Astrophys.* **261**, 567–578.
- Osterbrock, D. E. 1978. Observational Model of the Ionized Gas in Seyfert and Radio-Galaxy Nuclei. *Proceedings of the National Academy of Science* **75**, 540–544.
- Osterbrock, D. E., and A. T. Koski 1976. NGC 4151 and Markarian 6 - two intermediate-type Seyfert galaxies. *MNRAS* **176**, 61P–464P.
- Peng, C. Y. 2002. Assessing Formation Scenarios for the Double Nucleus of M31 Using Two-Dimensional Image Decomposition. *Astron. J.* **124**, 294–309.
- Peng, C. Y., L. C. Ho, C. D. Impey, and H. Rix 2002. Detailed Structural Decomposition of Galaxy Images. *Astron. J.* **124**, 266–293.
- Penston, M. V., and E. Perez 1984. An evolutionary link between Seyfert I and II galaxies? *MNRAS* **211**, 33P–39P.
- Persson, S. E., D. C. Murphy, W. Krzeminski, M. Roth, and M. J. Rieke 1998. A New System of Faint Near-Infrared Standard Stars. *Astron. J.* **116**, 2475–2488.
- Peterson, B. M. 1997. *An Introduction to Active Galactic Nuclei*.

- Pier, E. A., and J. H. Krolik 1992. Infrared spectra of obscuring dust tori around active galactic nuclei. I - Computational method and basic trends. *Ap. J.* **401**, 99–109.
- Pier, E. A., and J. H. Krolik 1993. Infrared Spectra of Obscuring Dust Tori around Active Galactic Nuclei. II. Comparison with Observations. *Ap. J.* **418**, 673–+.
- Pogge, R. W. 1988. Extended ionized gas in the Seyfert 2 galaxy NGC 4388. *Ap. J.* **332**, 702–710.
- Predehl, P., and J. H. M. M. Schmitt 1995. X-raying the interstellar medium: ROSAT observations of dust scattering halos. *Astron. & Astrophys.* **293**, 889–905.
- Press, W. H. 1993. Books-Received - Numerical Recipes in C - ED.2. *Science* **259**, 1931–+.
- Prieto, M., J. A. L. Aguerri, A. M. Varela, and C. Muñoz-Tuñón 2001. Optical surface photometry of a sample of disk galaxies. II. Structural components. *Astron. & Astrophys.* **367**, 405–427.
- Prieto, M., S. T. Gottesman, J. Aguerri, and A. Varela 1997. Structural Components of NGC 5850. *Astron. J.* **114**, 1413–+.
- Prieto, M. A., J. Reunanen, and J. K. Kotilainen 2002. Subarcsecond Emission in Seyfert Galaxies: The Nuclear Component in the L and M Bands. *Ap. J. Lett.* **571**, L7–L11.
- Raban, D., W. Jaffe, H. Röttgering, K. Meisenheimer, and K. R. W. Tristram 2009. Resolving the obscuring torus in NGC 1068 with the power of infrared interferometry: revealing the inner funnel of dust. *MNRAS* **394**, 1325–1337.
- Rieke, G. H., and F. J. Low 1975. The infrared spectrum of NGC 1068. *Ap. J. Lett.* **199**, L13–L17.

- Risaliti, G., M. Elvis, G. Fabbiano, A. Baldi, and A. Zezas 2005. Rapid Compton-thick/Compton-thin Transitions in the Seyfert 2 Galaxy NGC 1365. *Ap. J. Lett.* **623**, L93–L96.
- Risaliti, G., R. Maiolino, and M. Salvati 1999. The Distribution of Absorbing Column Densities among Seyfert 2 Galaxies. *Ap. J.* **522**, 157–164.
- Roche, P. F., and D. K. Aitken 1984. An investigation of the interstellar extinction. I - Towards dusty WC Wolf-Rayet stars. *MNRAS* **208**, 481–492.
- Roche, P. F., and D. K. Aitken 1985. An investigation of the interstellar extinction. II - Towards the mid-infrared sources in the Galactic centre. *MNRAS* **215**, 425–435.
- Roche, P. F., C. Packham, D. K. Aitken, and R. E. Mason 2007. Silicate absorption in heavily obscured galaxy nuclei. *MNRAS* **375**, 99–104.
- Ruiz, M., G. H. Rieke, and G. D. Schmidt 1994. New Infrared Observations of Seyfert 2 Galaxies and Unification Theories. *Ap. J.* **423**, 608–+.
- Rush, B., M. A. Malkan, and L. Spinoglio 1993. The extended 12 micron galaxy sample. *Ap. J. Suppl.* **89**, 1–33.
- Salpeter, E. E. 1964. Accretion of Interstellar Matter by Massive Objects. *Ap. J.* **140**, 796–800.
- Schartmann, M., K. Meisenheimer, M. Camenzind, S. Wolf, and T. Henning 2005. Towards a physical model of dust tori in Active Galactic Nuclei. Radiative transfer calculations for a hydrostatic torus model. *Astron. & Astrophys.* **437**, 861–881.
- Schartmann, M., K. Meisenheimer, M. Camenzind, S. Wolf, K. R. W. Tristram, and T. Henning 2008. Three-dimensional radiative transfer models of clumpy tori in Seyfert galaxies. *Astron. & Astrophys.* **482**, 67–80.

- Schmidt, M., and R. F. Green 1983. Quasar evolution derived from the Palomar bright quasar survey and other complete quasar surveys. *Ap. J.* **269**, 352–374.
- Schmitt, H. R. 1998. The Difference between the Narrow-Line Regions of Seyfert 1 and Seyfert 2 Galaxies. *Ap. J.* **506**, 647–657.
- Shakura, N. I., and R. A. Sunyaev 1976. A theory of the instability of disk accretion on to black holes and the variability of binary X-ray sources, galactic nuclei and quasars. *MNRAS* **175**, 613–632.
- Shu, X. W., J. X. Wang, P. Jiang, L. L. Fan, and T. G. Wang 2007. Investigating the Nuclear Obscuration in Two Types of Seyfert 2 Galaxies. *Ap. J.* **657**, 167–176.
- Siebenmorgen, R., M. Haas, E. Krügel, and B. Schulz 2005. Discovery of 10 μm silicate emission in quasars. Evidence of the AGN unification scheme. *Astron. & Astrophys.* **436**, L5–L8.
- Simons, D. A., and A. Tokunaga 2002. The Mauna Kea Observatories Near-Infrared Filter Set. I. Defining Optimal 1-5 Micron Bandpasses. *PASP* **114**, 169–179.
- Smith, H. J., and D. Hoffleit 1963. Light Variability and Nature of 3C273. *Astron. J.* **68**, 292–+.
- Smith, J. D. T., B. T. Draine, D. A. Dale, J. Moustakas, R. C. Kennicutt, Jr., G. Helou, L. Armus, H. Roussel, K. Sheth, G. J. Bendo, B. A. Buckalew, D. Calzetti, C. W. Engelbracht, K. D. Gordon, D. J. Hollenbach, A. Li, S. Malhotra, E. J. Murphy, and F. Walter 2007. The Mid-Infrared Spectrum of Star-forming Galaxies: Global Properties of Polycyclic Aromatic Hydrocarbon Emission. *Ap. J.* **656**, 770–791.
- Spinoglio, L., and M. A. Malkan 1989. The 12 micron galaxy sample. I - Luminosity functions and a new complete active galaxy sample. *Ap. J.* **342**, 83–99.

- Stasińska, G. 1984. Confrontation of a sample of Seyfert 2 galaxies with photoionized models. *Astron. & Astrophys.* **135**, 341–355.
- Suganuma, M., Y. Yoshii, Y. Kobayashi, T. Minezaki, K. Enya, H. Tomita, T. Aoki, S. Koshida, and B. A. Peterson 2006. Reverberation Measurements of the Inner Radius of the Dust Torus in Nearby Seyfert 1 Galaxies. *Ap. J.* **639**, 46–63.
- Tokunaga, A. T., D. A. Simons, and W. D. Vacca 2002. The Mauna Kea Observatories Near-Infrared Filter Set. II. Specifications for a New JHKL'M' Filter Set for Infrared Astronomy. *PASP* **114**, 180–186.
- Tommasin, S., L. Spinoglio, M. A. Malkan, and G. Fazio 2009. Spitzer-IRS high resolution spectroscopic survey of the 12 micron Seyfert galaxies: II. Results for the Complete Dataset. *ArXiv e-prints*.
- Tran, H. D. 2001. Hidden Broad-Line Seyfert 2 Galaxies in the CFA and 12 μ M Samples. *Ap. J. Lett.* **554**, L19–L23.
- Tran, H. D. 2003. The Unified Model and Evolution of Active Galaxies: Implications from a Spectropolarimetric Study. *Ap. J.* **583**, 632–648.
- Tran, H. D., J. S. Miller, and L. E. Kay 1992. Detection of obscured broad-line regions in four Seyfert 2 galaxies. *Ap. J.* **397**, 452–456.
- Tristram, K. R. W., K. Meisenheimer, W. Jaffe, M. Schartmann, H. Rix, C. Leinert, S. Morel, M. Wittkowski, H. Röttgering, G. Perrin, B. Lopez, D. Raban, W. D. Cotton, U. Graser, F. Paresce, and T. Henning 2007. Resolving the complex structure of the dust torus in the active nucleus of the Circinus galaxy. *Astron. & Astrophys.* **474**, 837–850.
- Tristram, K. R. W., D. Raban, K. Meisenheimer, W. Jaffe, H. Röttgering, L. Burtscher, W. D. Cotton, U. Graser, T. Henning, C. Leinert, B. Lopez, S. Morel, G. Perrin, and M. Wittkowski 2009. Parsec-scale dust distributions

- in Seyfert galaxies. Results of the MIDI AGN snapshot survey. *Astron. & Astrophys.* **502**, 67–84.
- Urry, C. M., and P. Padovani 1995. Unified Schemes for Radio-Loud Active Galactic Nuclei. *PASP* **107**, 803–+.
- van der Blik, N. S., J. Manfroid, and P. Bouchet 1996. Infrared aperture photometry at ESO (1983-1994) and its future use. *Astron. & Astrophys. Sup.* **119**, 547–557.
- Veron-Cetty, M.-P., and P. Veron 1991. A catalogue of quasars and active nuclei. *European Southern Observatory Scientific Report* **10**, 1–199.
- Wu, Y., V. Charmandaris, J. Huang, L. Spinoglio, and S. Tommasin 2009. Spitzer/IRS 5-35 μm Low-resolution Spectroscopy of the 12 μm Seyfert Sample. *Ap. J.* **701**, 658–676.
- Zakamska, N. L., G. D. Schmidt, P. S. Smith, M. A. Strauss, J. H. Krolik, P. B. Hall, G. T. Richards, D. P. Schneider, J. Brinkmann, and G. P. Szokoly 2005. Candidate Type II Quasars from the Sloan Digital Sky Survey. III. Spectropolarimetry Reveals Hidden Type I Nuclei. *Astron. J.* **129**, 1212–1224.
- Zel'Dovich, Y. B. 1964. The Fate of a Star and the Evolution of Gravitational Energy Upon Accretion. *Soviet Physics Doklady* **9**, 195–+.
- Zitelli, V., G. L. Granato, N. Mandolesi, R. Wade, and L. Danese 1993. A near-infrared study of a homogeneous sample of optically selected active galactic nuclei. I - The observations. *Ap. J. Suppl.* **84**, 185–199.